Quantum gases in box potentials: Sound and light in bosonic Flatland

Jean-Loup Ville

THÈSE DE DOCTORAT

de l'Université de recherche Paris Sciences et Lettres
PSL Research University

Préparée à l'École Normale Supérieure
au sein du Laboratoire Kastler-Brossel

Quantum gases in box potentials: Sound and light in bosonic Flatland

Fluides quantiques dans des boîtes : Son et lumière dans un gaz de Bose bidimensionnel

École doctorale n°564
"PHYSIQUE EN ÎLE-DE-FRANCE"

Spécialité PHYSIQUE QUANTIQUE

Soutenue le
13 avril 2018 par
Jean-Loup VILLE

Dirigée par **Jean DALIBARD**
et par **Jérôme BEUGNON**

COMPOSITION DU JURY :

M. Antoine BROWAEYS
Institut d'Optique, Rapporteur

M. Henning MORITZ
Hamburg University, Rapporteur

Mme Jacqueline BLOCH
Université Paris Sud, Présidente du jury

M. Jean DALIBARD
Collège de France, Directeur de thèse

M. Jérôme BEUGNON
Sorbonne Université, Membre invité

Abstract

Ultracold atoms have proven to be a powerful platform for studying many-body physics. However the inhomegeneity of atomic clouds induced by potentials commonly used to trap the atoms constitutes a limitation for studies probing large length scales. Here we present the implementation of a new versatile setup to study two-dimensional Bose gases, combining a tunable in-plane box potential with a strong and efficient confinement along the third direction. We study different excitations of the system, either of internal degrees of freedom of the atoms with light scattering, or of their collective motion with phonon propagation.

The slab geometry is particularly well suited for light scattering studies. It allows one to probe high atomic densities, leading to strong induced dipole-dipole interactions, while keeping a good enough light transmission for measurements. We monitor the deviation from the single atom behavior for near resonant light by varying the atomic density. We additionally monitor the spreading of photons inside the slab by injecting light only at the center of a disk of atoms.

We also investigate collective excitations of the atomic gas. We measure the speed of sound which is linked to the superfluid density of the cloud and compare our results to a two-fluid hydrodynamic model predictions. Using a relevant geometry, we additionally study how an isolated system goes back to equilibrium. This is done by imaging the phase of the resulting Bose-Einstein condensate (BEC) after merging up to twelve BECs.

Résumé

Les atomes ultrafroids constituent depuis une vingtaine d'années un domaine fructueux pour l'étude de la physique à N corps. Cependant l'inhomogénéité des nuages atomiques, induite par les méthodes de piégeage utilisées habituellement, constitue une limite pour les études portant sur de grandes échelles de longueur. Nous reportons ici la mise en place d'un nouveau dispositif expérimental, combinant un potentiel modulable à bords raides et fond plat dans le plan atomique, avec un confinement versatile dans la troisième direction. Nous nous intéressons à différentes excitations du système, premièrement des degrés de liberté internes des atomes via leur interaction avec la lumière, puis deuxièmement de leur mouvement collectif avec la propagation de phonons.
La répartition des atomes dans un plan est particulièrement adaptée aux études de diffusion de la lumière. Elle permet en effet de sonder de fortes densités atomiques, entraînant de fortes interactions dipôle-dipôle induites, tout en gardant un signal transmis suffisant pour effectuer des mesures. Nous avons mesuré la déviation au comportement d'un atome isolé pour de la lumière proche de résonance lorsque la densité atomique est modifiée. Nous avons également étudié la diffusion de photons dans un disque d'atomes en injectant de la lumière seulement au centre du disque.
Nous nous sommes ensuite intéressés aux excitations collectives du gaz. Nous avons mesuré la vitesse du son dans le milieu, qui est liée à la fraction superfluide du système, et comparé nos résultats aux prédictions d'un modèle hydrodynamique à deux fluides. En utilisant une géométrie adaptée, nous avons en outre étudié la dynamique de retour à l'équilibre d'un système isolé, en imageant la phase du condensat de Bose-Einstein résultant de la fusion de jusqu'à douze condensats.

Acknowledgments

I first would like to thank the English speaking reader who will forgive me for writing my acknowledgements in French.

Je voudrais tout d'abord remercier mes directeurs de thèse Jean Dalibard et Jérôme Beugnon. Déjà pour m'avoir accepté sur le projet Rubidium 3, puis pour tout le temps qu'ils m'ont consacré lors de ces trois années et demi. C'était un honneur de travailler avec Jean, suite à une conférence que j'avais suivie à Cambridge. Les moments où je suis allé te poser des questions plus ou moins pertinentes dans ton bureau à la porte toujours ouverte, ou tes arrivées dans la salle de manip avec une nouvelle idée resteront des moments forts de mon passage ici. Je remercie très sincèrement Jérôme pour son encadrement quotidien et bienveillant. Je ressors de cette thèse en ayant énormément appris sur les plans scientifique, technique et méthodologique, et c'est en grande partie grâce à lui. Merci de m'avoir fait bénéficier de ta très grande culture expérimentale, de ton efficacité mais aussi de ta confiance, qui ont fait du laboratoire un endroit agréable où il est possible d'entreprendre des choses de notre propre initiative. Merci également à Sylvain, pour ses calculs rapides et efficaces, et sa pensée très vive, qui apportent beaucoup à l'équipe.

Je voudrais ensuite remercier le jury: Jacqueline Bloch, Henning Moritz et Antoine Browaeys pour leur lecture attentive de ce manuscript, et pour leurs questions lors de la soutenance.

Un thèse en atomes froids aujourd'hui c'est d'abord un gros travail d'équipe, avec des gens avec qui l'on passe beaucoup de temps. Merci d'abord à Laura et Tom, et également Lauriane à mon arrivée, pour tout ce qu'ils ont fait pour la construction de cette manip extrêmement robuste, et surtout de m'avoir si bien accueilli dans l'équipe. Merci Laura pour ta rapidité à faire les mille choses que tu sais faire et Tom pour m'avoir enseigné les « gammes » de la manip qui ont surement contribué à ce qu'elle marche presque sans discontinuité durant ces années. Je remercie également Katharina et David qui ont travaillé sur les premières étapes de la manip et qui ont permis que mon travail de thèse commence rapidement. Merci bien sûr ensuite à Raphaël, mon principal binôme, qui a commencé peu de temps après moi, et avec qui j'ai donc passé presque toute ma thèse. Tes grandes capacités scientifiques et mathématiques ont très souvent contribué à résoudre les nombreux problèmes que nous avons rencontrés, et je ne doute pas que tu continueras à bien les utiliser par la suite. Merci à Monika, qui m'a impressionné par sa capacité à toujours trouver très rapidement ce qu'il fallait faire ensuite. Son passage même si de seulement une année aura été d'une grande valeur. Merci aux différents stagiaires, Victor, Charlie et Andres, qui nous ont aidé chacun à leur manière, et à Marius qui en plus de sa bonne humeur communicative nous a beaucoup avancés lors de son stage plus long. C'était également un grand plaisir de travailler avec Patricia, Édouard et Brice, qui

s'occupent maintenant de la suite avec Raphaël. Les discussions avec toutes ces personnes aussi bien sur la physique que sur nos vies respectives resteront parmi les meilleurs moments de cette thèse, avec les résolutions de bugs souvent en musique ! Je remercie toutes les autres personnes de l'étage pour la bonne ambiance qu'il y règne, avec le paper club qui aura finalement réussi à perdurer, et également le BCBP qui a su rassembler les doctorants dans les moments notamment de vacances où les labos étaient plus vides. J'ai aussi une pensée spéciale pour les nuits de la physique que nous avons passées avec Manel et Chayma à étudier les cours au Collège de France de Claude Cohen Tannoudji (en plus bien sûr de ceux de Jean) tout en mangeant des pizza. Merci aussi à Raphaël Yb pour ses connaissances solides et ses avis réfléchis lors de nos différentes discussions. Merci à Thomas d'avoir été aussi nul que moi avec le bitcoin. Merci à Leonid pour les discussion sur l'étude du son dans notre gaz. Et merci à tous les autres notamment tous ceux avec qui nous avons fait la rando de la physique avant les Houches. J'apprécie au passage les différents séminaires de l'ERC UQUAM que nous avons pu avoir, qui ont été un moment privilégié de partage avec les groupes partenaires.
Merci à l'équipe des italiens avec Davide, qui m'a fait découvrir sa merveilleuse région du Friuli, Andrea, qui m'a montré ce que c'était de rédiger, j'ai aussi envie de mettre Camille, pour son aide en électronique même tard le soir quand je n'y croyais plus, Lorenzo, Fabrizio et Elisa pour toute la bonne humeur et l'ambiance qu'ils ont apporté au cours de ces années. Merci également aux autres membres permanents de l'équipe, Fabrice et le tout dernier Raphaël, pour les discussions de physique aussi bien que sur d'autres sujets.
Je tiens à dire également que le groupe condensats de Bose-Einstein au sein du Collège de France est un formidable endroit pour effectuer sa thèse. D'abord avec la proximité d'autres équipes de physique comme celles de Quantum photonics d'Alexei et d'Électrodynamique quantique en cavité du rez-de-chaussée, mais également avec toutes les autres équipes de biologie, chimie ou littérature avec lesquelles nous avons pu interagir. C'était également une superbe opportunité de suivre des cours ou séminaires sur d'autres sujets.
Je remercie l'ensemble du personnel du Laboratoire Kastler Brossel et du Collège de France, avec notamment les services techniques et administratifs, et les ateliers électroniques et mécaniques. Je remercie également l'école doctorale et Sylvain Gigan d'avoir accepté d'être mon parrain. Enfin je remercie Danijela Markovic et Zaki Leghtas pour le travail que nous avons fait pour les élèves du CPES de Paris Sciences et Lettres et pour leur aide dans mon passage vers un nouveau domaine.
Pour finir je remercie bien sûr ma famille pour m'avoir toujours encouragé, mes amis dont les colocataires (la coloc d'Ancenis au KB) pour tous les moments partagés et leur aide jusqu'au bout, la fanfare Rolland Merguez pour les délicieux moments en festival ou en tournée lors des vacances, et enfin Elsa pour me faire découvrir un nouveau monde.

Contents

Introduction

The invention of lasers has had a huge impact in many sections of modern society. They can be found for example at home in optical disk drives, in medicine for laser surgery, or in the industry for cutting or welding materials. They furthermore improved the internet transmission system with fiber-optic communication. Their use is also fruitful on atomic physics. They allow to act mechanically on atoms, slowing them down to speeds of a few millimeters per second, corresponding to temperatures a few hundreds of nanokelvins above absolute zero. Since the first demonstration of the mechanical action of light on atomic beams by R. Frisch in 1933 [1], atoms are now routinely trapped and can even be individually manipulated. This cooling down of atoms led to advances in the understanding of quantum mechanics. One root of the theory is that matter exhibits wave-like properties. This is not visible in our everyday life because the energies are usually too high, leading to too small wavelengths for these wave properties to become apparent. With atomic cooling techniques however, it is possible to reduce so much the temperature and thus the energy of the atoms that the wavelength associated with the particles becomes of the order of the distance between atoms. This corresponds to the regime of quantum degeneracy, and for bosonic atoms leads to the phenomenon of Bose-Einstein condensation predicted in 1924 [2], and corresponding to a macroscopic accumulation of bosons in the lowest energy state of the system. This was observed in dilute atomic vapors in 1995 [3, 4, 5], opening the way to a wide domain in atomic physics.

Before that, for a long time, the only experimental manifestation of Bose-Einstein condensation was in superfluid ^{4}He. But when its condensed fraction was measured in 1979 [6], it was found to be only 10%, whereas the whole system is superfluid. This is due to the very strong interactions between particles in the system, which is different from the situation of non-interacting bosons considered in [7, 2]. Interactions in dilute atomic vapors are usually small, making these systems much closer experimental realizations of the initial idea.

A good quantitative description of these systems is provided by considering an average effect of the interactions between atoms, *ie* using a mean-field theory. The gas is then well described by a single wavefunction, whose behaviour is governed by a nonlinear Schrödinger equation: the Gross-Pitaevskii equation [8, 9]. During the years following 1995, the research was mainly directed towards the exploration of phenomena well described within this framework. The ondulatory nature of the Bose-Einstein condensate (BEC) was demonstrated through matter-wave interference [10]. The long range coherence of this system (observed in [11]) led to the experimental realization of a atom lasers [12, 13, 14]. The excitation spectrum of a BEC predicted by the Bogoliubov theory [15] was measured [16]. The superfluid character of the BEC was demonstrated through the observation of vortices [17, 18], and of their

arrangement in Abrikosov lattices [18, 19]. Only four years after the observation of a BEC, Fermi gases (the only other type of quantum statistics available in nature) were also brought to degeneracy with similar experimental techniques [20, 21, 22]. In this case it is of course not a BEC which is observed, as Pauli exclusion principle prevents the particles from occupying the same state, but the atoms occupy the ladder of available energy states starting from the lowest one, up to a maximum value (the Fermi energy). This has many realisations in nature, such as for example electrons in a ordinary metal and white dwarfs or neutron stars.

The cold atoms toolbox: studying many-body physics

The domain of cold atoms could have stayed limited to systems of almost non-interacting particles, as it is expected for dilute gases. But major developments considerably enlarged the range of physics accessible with these systems, allowing the study of strong-correlation aspects [23], *ie* phenomena that are not captured by weak-coupling descriptions like the Gross-Pitaevskii or Bogoliubov theory, and are much more involved to solve numerically.

One development is the ability to tune interparticle interactions for certain atomic species using Feshbach resonances [24]. It allows to access strongly interacting regimes for bosons [25] and fermions [26]. In Fermi gases, Feshbach resonances led to the observation of the crossover from a BEC of weakly bound molecules to a superfluid of Cooper pairs [27, 28], as described by the Bardeen-Cooper-Schrieffer theory of superconductors. These correspond to short-range interactions, but long-range interactions such as dipolar magnetic ones are also available for cold atoms. It requires working with species having an important magnetic moment, such as Chromium, Erbium or Dysprosium for example, which have now been brought to quantum degeneracy.

A second development is the ability to tune the potential felt by the atoms. This allows to study low-dimensional physics by confining the gas strongly in one or two directions. An interest of this type of physics is that in reduced dimensions such as for 2D and 1D systems, the thermal and quantum fluctuations are very important and destroy long-range order [29, 30, 31]. Confining a Bose gas in 1D traps, the Tonks-Girardeau regime was realized [32, 33], and in a two-dimensional trap the famous Berezinskii-Kosterlitz-Thouless (BKT) transition was observed [34]. As the study of this transition constitutes an important part of this thesis we will come back to it later, and first briefly describe a type of potential which led to a lot of important results: the optical lattices.

It is possible to use interfering light beams to force the atoms to arrange themselves periodically. This constitutes a very pure realization of the Bose and Fermi-Hubbard models [35], the fermionic case describing electrons in condensed matter systems. It is very easy with cold atoms to obtain information about their momentum distribution and coherence properties by probing the gas after time-of-flight. This led to the observation of the quantum phase transition between a superfluid and a Mott insulating phase in bosonic systems [36, 37, 38, 39], and to the observation of a crossover with fermions [40, 41]. Different lattice geometries have been engineered [42, 43, 44, 45, 46] showing the variety of potentials which can be realized. One step further was realized with the “quantum gas microscopes”, a new generation of

experiments in which it is possible to image individual atoms from different sites of a lattice. Even the spin of the atoms can be read from these microscopes [47, 48].
A limitation of cold atoms could be that their charge neutrality prevents a direct application of the Lorentz force, making out of reach the study of some strongly correlated states such as quantum Hall states, which require the implementation of a large magnetic field. Solutions to overcome this problem are now being developed, to engineer artificial magnetic fields which mimic the effect of real magnetic fields [49, 50, 51, 52, 53].
Cold atoms are also suitable for performing precision measurements and can be used for example to realize very sensitive gravimeters [54]. Some companies even start to emerge using them in this direction. Today's most stable atomic clock [55] uses a degenerate Fermi gas in a 3D optical lattice, and has a precision of $5\,10^{-19}$ in one hour of averaging time. This offers amazing perspectives by providing new ways to study many-body physics but also other types of physics by measuring tiny shifts of frequency.
A natural extension of these works done for systems at equilibrium is the study of out-of-equilibrium physics. In cold atoms systems all energy scales are low, meaning that their evolution is slow, on the order of milliseconds to seconds, which is easily tractable in an experiment. They in addition are well isolated from perturbations from the environment. We just give here some examples such as the study of supercurrents in rings in the presence of a weak-link [56], the study of prethermalization in one-dimensional systems [57], or transport experiments [58, 59, 60, 61]. The dynamical study of atoms in tailored optical potential has led to a whole new field called "atomtronics" [62], aiming at creating atom analogs of electronic materials, devices and circuits.

About the 2D Bose gas

A part of this thesis focusses on properties of 2D Bose gases. A major interest of these systems is the existence of a superfluid BKT phase, supporting a quasi long-range coherence. This is microscopically enabled by the pairing of topological defects (called vortices) in the gas. The transition from a normal state to this state does not rely on the breaking of a symmetry, making all thermodynamical variables continuous at the critical point. For this reason the transition is said to be of infinite order.
This transition has been observed through the analysis of the contrast in the interference patterns of atoms emerging from two traps as a function of the spatial range in [34]. The authors identified a sudden decrease in the degree of phase order, indicative of a jump in the superfluid density at the transition temperature. They observed simultaneously the appearance of dislocation lines, corresponding to the presence of isolated vortices. Below T_c, the vortices are expected to group in close pairs, thus conserving the phase order. These thermally activated vortex pairs have been observed in [63], but the authors have to apply a radial compression to the gas before releasing it to be able to observe these pairs.
Other previous experimental investigations of this subject led to the following results. The equation of state has been measured [64, 65] and its approximate scale-invariance in the weakly interacting regime has been experimentally verified [66]. The "pre-

superfluid" or "quasi-condensate" state required for the BKT transition to occur has been studied in [67, 68, 69], and the quasi-condensate density measured in [66]. They had to take into account the finite imaging resolution of their system, as explained in [70], where they also measure the static structure factor of the gas in different regimes. Density and phase fluctuation scalings within the critical region were also investigated [71, 72].
All these experiments were performed in harmonically trapped gases, and their results were linked back to the homogeneous system by considering the gas as locally equivalent to a uniform one (local density approximation). In this thesis, a Bose gas in a flat-bottom box-like potential is realized, avoiding the need for this approximation. This should also enable us to measure correlations in the gas which are blurred in harmonically trapped systems [73, 74].

Studying light scattering

Another part of this thesis focusses on the study of light scattering. This might seem less linked to what was described until here, but cold atoms offer a very interesting platform for this kind of studies. The understanding of some of these phenomena is furthermore required to properly characterize the trapped gases. It is indeed not obvious from absorption imaging, the usual way of probing cold atoms, to infer correctly the number of atoms in the image.
The study of light scattering is also an extremely interesting topic in itself. A broader introduction to the subject will be done in chapter 3, but the main idea is that due to the important cross-section that the atoms have with resonant light, "simple" descriptions, either with a mean-field refractive index or by random walks of photons break down for samples in which the distance between scatterers is comparable with the light wavelength. This allows the study of interesting effects such as superradiance, corresponding to the emission of light by a collection of scatterers faster than for a single scatterer, or coherent backscattering, the manifestation of a robust interference effect of light propagating backwards. Atoms furthermore have the advantage of being non-absorptive materials, *ie* all photons entering the sample have to be re-emitted. This is in contrast with solid state materials in which some might be absorbed by the sample, which complicates the interpretation of results. For systems of molecules as well, some energy might be transferred to excitation of rotational levels.
The ability to tune the geometry is an important tool for these studies as well. A particularly interesting one is the slab geometry, as is realized in this work. It indeed has the advantage of keeping a high density for the scatterers, while the light propagates for only a short distance in the material, thus having its intensity not too reduced. Atomic densities up to 10^{14} cm^{-3}, *ie* an average atomic distance $\approx \lambda_{\text{optical}}/10$, can be reached in our samples, making them dense even if much less dense than condensed matter systems.

Thesis outline

This thesis is organised in three parts. **The first part** contains two chapters. Chapter 1 describes the theory of the 2D Bose gas and contrasts it with the 3D case. The notions of superfluidity and superfluid fraction will be introduced, and

the classical field formalism explained. It allows a description of the gas at finite temperature, and thus beyond Gross-Pitaevskii. The experimental setup to create a dense and thin slab of atoms is described in Chapter 2, with the first tools we had to characterize the gas.

The second part of the thesis is about light scattering in a gas of cold atoms. It is of importance here as in dense samples as we have, induced dipole-dipole interactions modify deeply the response of the gas compared to the single atom case. To correctly measure the atom number in the gas, some effects had to be understood. Chapter 3 is an introductory chapter for the projects of chapter 4 and 5. It introduces different notions relevant for the description of light scattering, and briefly reviews different regimes probed in cold atom experiments. Chapter 4 studies the absorption of close to resonance light by the slab. The density is varied in a controlled way and allows to probe the response of the gas from a dilute regime where it is close to the single-atom case, to a dense regime where the behaviour is very different. Another experiment is described in chapter 5, investigating the propagation of photons in the slab thanks to fluorescence imaging. A focused beam in the center of the slab is a source of photons which then propagate in it. The study is done varying the density and the detuning of the light.

The third part of the manuscript presents experiments probing superfluid aspects of the gas. Chapter 6 studies how the phase of a system put out of equilibrium relaxes. Several independent condensates are realised and merged together in a ring geometry, from which the phase is inferred through interferometric measurements. The expected distribution of supercurrents is recovered and a timescale for this homogeneisation is measured. Chapter 7 describes better characterizations of the gas, which are useful for the next chapter. Chapter 8 studies sound propagation in a 2D Bose gas, aiming at implementing the proposal [75].

Finally, chapter 9 concludes this work and discusses prospective experiments. It also tries to give a broader view of the remaining topics to be studied in the 2D Bose gas.

Theory and experimental setup

1

Overview of the two-dimensional Bose gas

The two-dimensional Bose gas is a rich system in the sense that it can undergo more complexe phase transitions than in the three dimensional case. It has already been reviewed for example in [76, 77], but in this chapter we will explain and contrast different selected notions and important features that will be used in the following of this work. The intention is to give an overview of the two-dimensional Bose gas to the reader, without aiming for exhaustivity. We will focus only on the now experimentally available uniformly trapped systems.

We first have to address a very important point which is the definition of condensation. Einstein's argument for BEC [2, 7] requires to know what is the lowest single-particle energy eigenstate of the Hamiltonian. But an effect of the interactions is to modify the eigenstates of the system, which are no longer the ones of the single-particle Hamiltonian. This rises the fundamental question of what does Bose-Einstein condensation then mean.

A generalized criterion has been proposed by Oliver Penrose and Lars Onsager in 1956 [78], initially in the context of the study of liquid Helium. Their idea is to use the reduced von Neumann's statistical operator [79] which will be described later. The criterion for Bose-Einstein condensation to occur is then that the largest eigenvalue of this operator has a finite value when taking the thermodynamic limit, *ie* $N \to \infty$ with N/V being kept constant. We will see how condensation is recovered in our finite-size samples according to this generalized criterion.

The chapter is articulated as follows. Starting with the ideal case, the infinite uniform two-dimensional Bose gas does not condense. Indeed, except at exactly zero temperature, thermal fluctuations kill any long-range order [80, 81, 82]. This will be the object of the first section. The second section will describe theoretical ways to model the interacting 2D Bose gas, and some simplified descriptions such as the classical field formalism. In the third section we will describe how density fluctuations tend to be reduced by the interactions, giving rise to quasi-condensates [83, 84, 85]. These do not directly allow to recover a phase coherence in the system, but are required for another type of transition to occur: the Berezinskii-Kosterlitz-Thouless (BKT) transition [86, 87, 88], which tends to extend further the correlations. It is also a transition to a superfluid regime and will be described in the fourth section. Analytical calculations nevertheless do not allow to calculate the full equation of state of the gas, and Monte Carlo simulations are required to compute it quantitatively. We thus describe the principle of these simulations and their results on important quantities in the fifth part, and finally describe the equation of state in the last part.

1.1 The ideal uniform Bose gas in three and two dimensions

1.1.1 Does condensation occur?

Bose-Einstein condensation occurs because of the saturation of the number of bosons which can occupy the excited states of a system at thermal equilibrium. Its derivation for the 3D ideal gas is derived in numerous statistical physics books. We will nevertheless rederive it here in the case of a uniform system with periodic boundary conditions to contrast it with the 2D uniform case. We also derive the coherence length, which will be an important quantity in the following. More general derivations in other potentials can be found in [89].

3D case

Consider N non-interacting bosons of mass m in a cubic box of side L. The Hamiltonian is then simply composed of the kinetic energy, and the eigenstates for periodic boundary conditions are the plane waves of momentum $\boldsymbol{p}$:

$$\psi_{\mathbf{p}}(\boldsymbol{r}) = \mathrm{e}^{\mathrm{i}\boldsymbol{p}\cdot\boldsymbol{r}/\hbar}, \quad \boldsymbol{p} = \frac{2\pi\hbar}{L}\boldsymbol{n}, \quad \boldsymbol{n} = (n_x, n_y, n_z) \in \mathbb{Z}^3. \tag{1.1}$$

The energy of a plane wave of momentum $\boldsymbol{p}$ is $E_{\boldsymbol{p}} = \boldsymbol{p}^2/2m$, and the Bose-Einstein (BE) law gives the mean population of a state $\psi_{\boldsymbol{p}}$ in the grand canonical ensemble:

$$N_{\boldsymbol{p}} = \frac{1}{\mathrm{e}^{(E_{\boldsymbol{p}}-\mu)/k_{\mathrm{B}}T} - 1}, \tag{1.2}$$

where we introduced the thermodynamic variables T and μ, respectively the temperature and chemical potential. The total atom number N is then simply the sum of these populations over all states

$$N = \sum_{\boldsymbol{p}} N_{\boldsymbol{p}}. \tag{1.3}$$

One important property of the distribution (1.2) is that all $N_{\boldsymbol{p}}$ have to be positive, thus imposing $\mu < E_0$. Taking $E_0 = 0$ we thus have $\mu < 0$. It is then useful to separate the sum (1.3) in two parts, the first being the fundamental state $\boldsymbol{p} = 0$ and the second all the excited states $\boldsymbol{p} \neq 0$:

$$N = N_0 + N_{\mathrm{exc}}, \quad N_0 = \frac{z}{1-z}, \quad N_{\mathrm{exc}} = \sum_{\boldsymbol{p}\neq 0} N_{\boldsymbol{p}}, \tag{1.4}$$

where we introduced the fugacity $z = \mathrm{e}^{\mu/k_{\mathrm{B}}T}$ which is thus bounded between 0 and 1. As the $N_{\boldsymbol{p}}$ are increasing functions of μ, the sum N_{exc} is maximal for $\mu = 0$ *ie* $z = 1$. As we will see just after, switching to a continuous momentum distribution, the sum always converges for a finite box of size L. This is the famous saturation of the excited states giving rise to the accumulation of atoms in the fundamental state once the saturation number is reached.
We have to check that the saturation holds in the thermodynamic limit, meaning:

$$L \to \infty, \quad N \to \infty, \quad \rho^{(3\mathrm{D})} = \frac{N}{L^3} = \text{constant}. \tag{1.5}$$

The useful quantity is now $\rho_{\rm exc}^{(3D)} = N_{\rm exc}/L^3$. It can be computed substituting the sum by an integral according to

$$\sum_{\boldsymbol{p}} ... \to \left(\frac{L}{2\pi\hbar}\right)^3 \int \mathrm{d}^3p \, ... \tag{1.6}$$

This gives

$$\rho_{\rm exc}^{(3D)} = \frac{1}{(2\pi\hbar)^3} \int \mathrm{d}^3p \, \frac{z}{\mathrm{e}^{\boldsymbol{p}^2/2mk_{\rm B}T} - z}, \tag{1.7}$$

which can be rewritten for $z < 1$, and after inverting the sum and the integral

$$\rho_{\rm exc}^{(3D)} = \frac{1}{(2\pi\hbar)^3} \sum_{n=1}^{\infty} z^n \int \mathrm{d}^3p \, \mathrm{e}^{-n\boldsymbol{p}^2/2mk_{\rm B}T}. \tag{1.8}$$

As the integral is over the three directions of momenta, it can be decomposed into three 1D gaussian integrals. This leads to

$$\rho_{\rm exc}^{(3D)} = \lambda_T^{-3} \, \mathrm{Li}_{3/2}(z), \tag{1.9}$$

where we introduced the thermal wavelength λ_T and the polylog function Li_α:

$$\lambda_T = \frac{h}{\sqrt{2\pi m k_{\rm B} T}}, \quad \mathrm{Li}_\alpha(z) = \sum_{n=1}^{\infty} \frac{z^n}{n^\alpha}. \tag{1.10}$$

It is then convenient to use the phase-space density of the excited states $\mathcal{D}_{\rm exc}^{(3D)} = \rho_{\rm exc}^{(3D)} \lambda_T^3$:

$$\mathcal{D}_{\rm exc}^{(3D)} = \mathrm{Li}_{3/2}(z). \tag{1.11}$$

The important result of Einstein's derivation is that this polylog saturates at a certain value when the fugacity z goes to 1:

$$\mathcal{D}_{\rm exc}^{(3D,\max)} = \mathrm{Li}_{3/2}(1) = 2.612... \tag{1.12}$$

To describe the total atom number, one must then separate two cases depending if the condensation threshold has been reached or not:

$$\mathcal{D}^{(3D)} = \begin{cases} \mathrm{Li}_{3/2}(z) & \text{if } \mathcal{D}^{(3D)} < D_{\rm exc}^{(3D,\max)} \\ \mathcal{D}_0^{(3D)} + \mathrm{Li}_{3/2}(1) & \text{if } \mathcal{D}^{(3D)} > D_{\rm exc}^{(3D,\max)}, \end{cases} \tag{1.13}$$

where $\mathcal{D}_0^{(3D)}$ corresponds the bosons accumulated in the lowest energy state, which form the condensate.

2D case

The difference in the 2D case is that this saturation, even at the thermodynamic limit, does not occur. The derivation is very similar, except that the substitution of the sum by an integral is now

$$\sum_{\boldsymbol{p}} ... \to \left(\frac{L}{2\pi\hbar}\right)^2 \int \mathrm{d}^2p \, ... \tag{1.14}$$

which makes the equation (1.8) become

$$\rho_{\mathrm{exc}}^{(2\mathrm{D})} = \frac{1}{(2\pi\hbar)^2} \sum_{n=1}^{\infty} z^n \int \mathrm{d}^2 p \; \mathrm{e}^{\frac{-n\boldsymbol{p}^2}{2mk_{\mathrm{B}}T}}. \tag{1.15}$$

The integral now decomposes only into two 1D gaussian integrals, leading to, with $\mathcal{D}_{\mathrm{exc}}^{(2\mathrm{D})} = \rho_{\mathrm{exc}}^{(2\mathrm{D})} \lambda_T^2$ the phase-space density in 2D

$$\mathcal{D}_{\mathrm{exc}}^{(2\mathrm{D})} = \mathrm{Li}_1(z) = -\ln(1-z). \tag{1.16}$$

In this case $\mathcal{D}_{\mathrm{exc}}^{(2\mathrm{D})}$ is not bounded when z goes to 1. There is no saturation of the excited levels and thus no Bose-Einstein condensation. As the atom number in the ground state never becomes macroscopic, one can approximate $\mathcal{D}^{(2\mathrm{D})} \simeq \mathcal{D}_{\mathrm{exc}}^{(2\mathrm{D})}$ and we have the equation of state for the 2D ideal Bose gas:

$$\mathcal{D}^{(2\mathrm{D})} = -\ln(1-z). \tag{1.17}$$

The fact that a uniform 2D Bose gas cannot undergo Bose-Einstein condensation is actually a special case of the Mermin-Wagner-Hohenberg theorem [80, 81, 82] that states that in a 2D system with contact interaction, it is not possible to have long-range order provided by the breaking of a continuous symmetry.

1.1.2 Coherence length

We now look at the effect of Bose-Einstein condensation on another observable than the population of the lowest single-particle energy eigenstate which corresponds to the historical definition of condensation by Einstein. We consider the coherence length of the gas, which is more linked to the Penrose-Onsager definition of condensation. We will adopt the broader formalism of density operators to be able to generalize later the results to the case of an interacting gas.
The density operator of the gas at thermal equilibrium is in the canonical ensemble

$$\hat{\rho} = \frac{1}{Z} \mathrm{e}^{-\hat{H}/k_{\mathrm{B}}T}, \tag{1.18}$$

with $Z = \mathrm{Tr}(\mathrm{e}^{-\hat{H}/k_{\mathrm{B}}T})$ the partition function. This operator corresponds to the von Neumann's statistical operator [79]. Let's now define the one-body density operator, obtained by taking the partial trace on $N-1$ particles:

$$\hat{\rho}_1 = N \, \mathrm{Tr}_{2,\ldots,N}(\hat{\rho}). \tag{1.19}$$

It corresponds to the reduced von Neumann's statistical operator used by Penrose and Onsager for their new definition of condensation [78]. It is also used to define the first-order correlation function [90]:

$$G_1(\boldsymbol{r}, \boldsymbol{r'}) = \langle \boldsymbol{r} | \, \hat{\rho}_1 \, | \boldsymbol{r'} \rangle \,, \tag{1.20}$$

which can be rewritten in our case taking advantage of the translational invariance with $\boldsymbol{u} = \boldsymbol{r} - \boldsymbol{r'}$

$$G_1(\boldsymbol{u}) = \langle \boldsymbol{r} | \, \hat{\rho}_1 \, | \boldsymbol{r'} \rangle \,. \tag{1.21}$$

Noting that

$$\begin{aligned} N(\boldsymbol{p}) &= \langle \boldsymbol{p}| \, \hat{\rho}_1 \, |\boldsymbol{p}\rangle \\ &= \iint \langle \boldsymbol{p}|\boldsymbol{r}\rangle \, \langle \boldsymbol{r}| \, \hat{\rho}_1 \, |\boldsymbol{r'}\rangle \, \langle \boldsymbol{r'}|\boldsymbol{p}\rangle \;\; \mathrm{d}^3 r \; \mathrm{d}^3 r' \\ &= \int \mathrm{e}^{-i\boldsymbol{u}\cdot\boldsymbol{p}/\hbar} \; G_1(\boldsymbol{u}) \; \mathrm{d}^3 u, \end{aligned} \tag{1.22}$$

where the integration is over the volume L^3 and we used the translational invariance, writing $G_1(\boldsymbol{u}, 0) = G_1(\boldsymbol{u})$. The correlation function G_1 is thus the Fourier transform of the momentum distribution. We note that this result is independent of the dimension. And as we did not use the fact that we supposed the gas ideal, this will hold when we add interactions.
On can then obtain G_1 as the inverse Fourier transform of the momentum distribution. Following the same spirit as in the beginning of this chapter, we can rewrite it as an infinite sum. This gives in the 2D case:

$$G_1(\boldsymbol{r}) = \frac{1}{(2\pi\hbar)^2} \int \mathrm{e}^{\mathrm{i}\boldsymbol{r}\cdot\boldsymbol{p}/\hbar} \; N(\boldsymbol{p}) \; \mathrm{d}^2 p \tag{1.23}$$

$$= \frac{1}{\lambda_T^2} \sum_{n=1}^{\infty} \frac{z^n}{n} \mathrm{e}^{-\pi \boldsymbol{r}^2 / 2n\lambda_T^2}. \tag{1.24}$$

In the 3D case we have to separate the macroscopically occupied lowest state:

$$G_1(\boldsymbol{r}) = \frac{N(0)}{L^3} + \frac{1}{(2\pi\hbar)^3} \int \mathrm{e}^{\mathrm{i}\boldsymbol{r}\cdot\boldsymbol{p}/\hbar} \; N(\boldsymbol{p}) \; \mathrm{d}^3 p \tag{1.25}$$

$$= \frac{N(0)}{L^3} + \frac{1}{\lambda_T^3} \sum_{n=1}^{\infty} \frac{z^n}{n^{3/2}} \mathrm{e}^{-\pi \boldsymbol{r}^2 / 2n\lambda_T^2}. \tag{1.26}$$

A natural way to normalize this correlation function is [90]:

$$g_1(\boldsymbol{r}) = \frac{G_1(\boldsymbol{r})}{\sqrt{G_1(\boldsymbol{r})}\sqrt{G_1(\boldsymbol{0})}}. \tag{1.27}$$

We can then compare the behaviour of the g_1 functions in the 3D and 2D cases. The result is shown figure 1.1.
Qualitatively, we see that for a high enough $\mathcal{D}^{(3\mathrm{D})}$, the limit where $\boldsymbol{r} \to \infty$ of g_1 is finite in the 3D case. This is an important result because it means that the atomic field has correlations for any two points separated in space. This property is called *off-diagonal long-range order* and as can be seen taking the thermodynamic limit in equation (1.26) fulfills the condensation criterion of Penrose and Onsager. This first-order correlation function for a uniform 3D gas has been measured with Bragg beams in the group of Zoran Hadzibabic [91].
In the 2D case we recover the fact that there is no condensation as g_1 goes to 0 when $\boldsymbol{r} \to \infty$. But the asymptotic behaviour in the degenerate case is still interesting. We first go back to the BE distribution (1.2) to identify two limits of the mode populations when one compares $E - \mu$ and $k_\mathrm{B}T$ (see also figure 1.2):

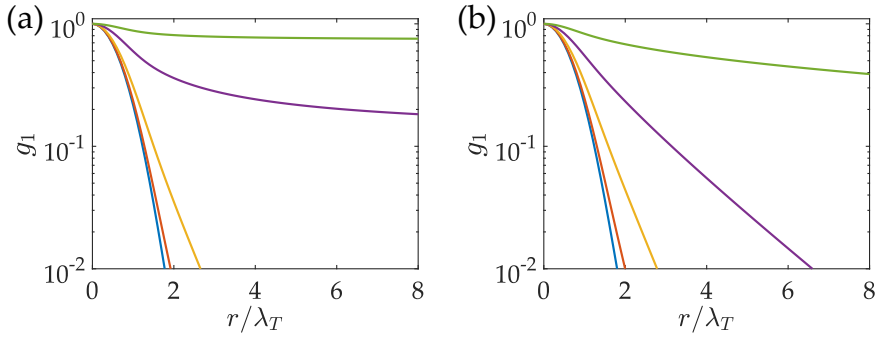

Figure 1.1 *– Behaviour of the normalized g_1 fonctions for different values of the phase-space density $\mathcal{D}$: $0.1, 0.3, 1, 3$ and 10. (a) shows the results in the 3D case and (2) in the 2D case. The sums are computed up to $n = 10^4$.*

- If $E - \mu \gg k_{\mathrm{B}}T$, we find that the population of the mode of energy E is

$$N(E) \approx \mathrm{e}^{-(E-\mu)/k_{\mathrm{B}}T}, \tag{1.28}$$

  corresponding to the Boltzmann's law. Looking back at (1.2), this limiting case implies that the exponential is bigger than the one at the denominator, meaning that this limit corresponds to $N(E) < 1$.
- If $E - \mu \ll k_{\mathrm{B}}T$, we find that the population of the mode of energy E

$$N(E) \approx \frac{k_{\mathrm{B}}T}{E - \mu}, \tag{1.29}$$

  and $N(E) > 1$. This will correspond to the domain of validity of the classical field approximation that we will use later.

The high energy states correspond to the first limiting case. They will thus always lead to a gaussian decay of the first order correlation function. When z is close to one, the occupation numbers of the low energy states however correspond to the second limiting case

$$N_{\boldsymbol{p}} = \frac{k_{\mathrm{B}}T}{E_{\boldsymbol{p}} + |\mu|} = \frac{4\pi}{\lambda_T^2} \frac{\hbar^2}{p^2 + p_{\mathrm{c}}^2}, \tag{1.30}$$

where $p_{\mathrm{c}} = \sqrt{2m|\mu|}$. The correlation function $g_1(\boldsymbol{r})$ is then bimodal. At short distances up to $r \simeq \lambda_T$ corresponding to high energy states, the correlations are gaussian, and at larger distances $r \gg \lambda_T$ the Lorentzian form of equation (1.30) corresponds to an approximately exponential decay[a]

$$G_1(\boldsymbol{r}) \propto \frac{1}{\sqrt{|\boldsymbol{r}|}} \mathrm{e}^{-|\boldsymbol{r}|/\ell}, \quad \text{with} \quad \ell = \frac{\hbar}{p_{\mathrm{c}}}. \tag{1.31}$$

[a] More precisely the Fourier transform of the 2D Lorentzian distribution is proportional to the Bessel function of imaginary argument $K_0(k_{\mathrm{c}}r)$, whose asymptotic behaviour is $\mathrm{e}^{-k_{\mathrm{c}}r}/\sqrt{r}$.

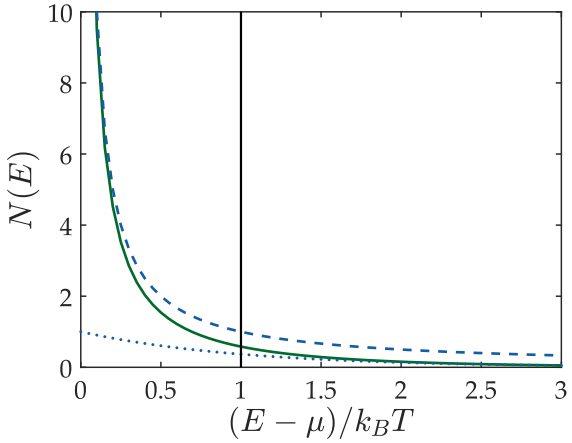

Figure 1.2 *– Distribution of Bose-Einstein of the atoms in green solid line. The dotted blue line is the Maxwell-Boltzmann distribution. The dashed line corresponds to the distribution for a classical field. We already see here that this distribution goes more slowly to zero than the BE distribution. This will lead, as explained later in the text, to the introduction of a cutoff, shown here as a vertical black line.*

This is very important because when $\mathcal{D}^{(2D)} > 1$, the correlation length $\ell \propto e^{\mathcal{D}^{(2D)}/2}$ grows exponentially[a]. When its size becomes of the order of the size of the sample, the atomic field shows correlations over the whole sample. This corresponds to a macroscopic value for the largest eigenvalue of the position representation of the reduced statistical operator, and the Penrose-Onsager criterion for condensation is fulfilled. This is also visible figure 1.1, where for $\mathcal{D}^{(2D)} = 10$, the coherence is still very high after several λ_T.
A threshold for this finite-size condensation to appear can be estimated, with L the linear size of the sample as

$$\ell \geq L \quad \rightarrow \quad e^{\mathcal{D}^{(2D)}/2} \geq \frac{L}{\lambda_T}, \quad \text{or equivalently,} \quad \mathcal{D}^{(2D)} \geq \ln\left(\frac{L^2}{\lambda_T^2}\right). \tag{1.32}$$

A more rigorous calculation for a square and a circular box can be found in [92], which shows that the formula above gives a good estimate of when this "transition" occurs. We will now see that interactions tends to make the coherence length decay even slower, achieving a *quasi-long-range order*.

1.2 The weakly interacting 2D Bose gas: fundamental equations

To go further than the ideal case which shows only a transition driven by bosonic statistics, we need to take into account interactions between atoms. As we will now consider only the 2D case, we now use the notation n for the atom number density.

[a] This result is obtained using equation (1.31), the definition of p_c and the limiting case $z \approx 1$ of the EoS of the ideal 2D Bose gas.

1.2.1 Adding interactions

In 3D and at low densities, the interaction between two bosons described by their positions $\boldsymbol{r}_i$ and $\boldsymbol{r}_j$ is well described by [93]:

$$U(\boldsymbol{r}_i - \boldsymbol{r}_j) = g^{(3\mathrm{D})}\delta^{(3\mathrm{D})}(\boldsymbol{r}_i - \boldsymbol{r}_j), \tag{1.33}$$

where $g^{(3\mathrm{D})} = 4\pi\hbar^2 a/m$ is the coupling strength, which is characterized by the s-wave scattering length $a = 5.3$ nm for ^{87}Rb [94]. This simple expression comes from the fact that the scattering amplitude $f_{3\mathrm{D}}(\boldsymbol{k})$ characterizing the scattering state between two particles with relative wave vector $\boldsymbol{k}$ tends towards a constant for low energy collisions.
When treating the scattering problem in a 2D geometry, the scattering amplitude $f_{2\mathrm{D}}(\boldsymbol{k})$ keeps a dependence in $\boldsymbol{k}$ at small wave vectors. However in the case of the quasi-2D regime which is relevant for us and which will be described later, the scattering amplitude can be approximated by a constant to a very good approximation.

1.2.2 From the quantum Hamiltonian to classical field

Let's consider a fluid composed of identical bosons with binary interactions $U(\boldsymbol{r}_i - \boldsymbol{r}_j)$. These bosons are trapped in the potential:

$$V_{\mathrm{trap}}^{(3\mathrm{D})}(\boldsymbol{r}) = V_{\mathrm{trap}}^{(1\mathrm{D})}(z) + V_{\mathrm{trap}}^{(2\mathrm{D})}(x, y), \tag{1.34}$$

where

- The strong confinement along the z axis $V_{\mathrm{trap}}^{(1\mathrm{D})}(z)$ freezes the motion along this axis and makes the gas bi-dimensional.
- The confinement in the plane is, for example, a hard-wall confinement in a flat-bottom box of size $L \times L$.

The Hamiltonian of the system can then be written in the formalism of the first quantification:

$$\hat{H} = \sum_{j=1}^{N}\left(\frac{\hat{\boldsymbol{p}}_j^2}{2m} + V_{\mathrm{trap}}^{(3\mathrm{D})}(\hat{\boldsymbol{r}}_j)\right) + \frac{1}{2}\sum_{i\neq j} U(\hat{\boldsymbol{r}}_i - \hat{\boldsymbol{r}}_j), \tag{1.35}$$

or in the second quantification:

$$\begin{aligned}\hat{H} = &\int\left(\frac{\hbar^2}{2m}\nabla\hat{\Psi}^\dagger(\boldsymbol{r})\cdot\nabla\hat{\Psi}(\boldsymbol{r}) + \hat{\Psi}^\dagger(\boldsymbol{r})V_{\mathrm{trap}}^{(3\mathrm{D})}(\boldsymbol{r})\hat{\Psi}(\boldsymbol{r})\right)\mathrm{d}^3 r \\ &+ \frac{1}{2}\iint \hat{\Psi}^\dagger(\boldsymbol{r})\hat{\Psi}^\dagger(\boldsymbol{r'})U(\boldsymbol{r}-\boldsymbol{r'})\hat{\Psi}(\boldsymbol{r'})\hat{\Psi}(\boldsymbol{r})\,\mathrm{d}^3 r\,\mathrm{d}^3 r',\end{aligned} \tag{1.36}$$

where $\hat{\Psi}(\boldsymbol{r})$ is a field operator destroying a particle at position $\boldsymbol{r}$ and its hermitian conjugate $\hat{\Psi}^\dagger(\boldsymbol{r})$ creates one at this point.
According to the previous paragraph, we would like to treat the interaction between atoms as a contact interaction: $U(\boldsymbol{r}) = U_0\delta(\boldsymbol{r})$. The problem with this Hamiltonian is that in two and three dimensions this leads to mathematical inconsistencies in the quantum framework. An advantage of the classical field formalism used in the following is that this problem does not arise.

1.2.3 Classical field formalism

A N-body quantum system is described by its wave function $\Phi(\boldsymbol{r}_1, ..., \boldsymbol{r}_N)$ or more generally by its density operator $\hat{\rho}$. The idea of the classical field formalism is to approach this quantum state by a statistical mixture of states characterized by a field $\psi(\boldsymbol{r})$, which is the same for all particles:

$$\Phi(\boldsymbol{r}_1, ..., \boldsymbol{r}_N) \approx \psi(\boldsymbol{r}_1)...\psi(\boldsymbol{r}_N). \tag{1.37}$$

This is called the *Hartree's ansatz*. The problem is then to find a distribution of probabilities $\mathcal{P}[\psi]$ which reproduces as nicely as possible the state Φ or the density matrix $\hat{\rho}$. This means that for any observable $\hat{A}$ we would like to have, using the functional integral formalism for the field ψ,

$$\mathrm{Tr}(\hat{A}\hat{\rho}) = \int \langle \psi(\boldsymbol{r}_1)...\psi(\boldsymbol{r}_N)| \, \hat{A} \, |\psi(\boldsymbol{r}_1)...\psi(\boldsymbol{r}_N)\rangle \, \mathcal{P}[\psi]\mathrm{d}[\psi]. \tag{1.38}$$

This treatment is not exact as it is not always possible to find such a distribution of probabilities (for a counterexample, and to see how this treatment falls down when the granularity of the field has to be taken into account, see [77], chapter 3). In fact, the range of validity of this approximation is when the populations of the modes considered are much bigger than one particle. In this case, as was shown in equation (1.29), the population of the mode is well approximated by

$$N(E) \approx \frac{k_{\mathrm{B}}T}{E-\mu}. \tag{1.39}$$

This will be used for example in our Monte Carlo simulations.
It may seem weird to simulate quantum phenomena with classical fields. However it is not the particles that are modelled as classical here, but the field. This is deeply different because we keep the fundamental ingredient of quantization of the circulation, which is enough to derive all behaviours obtained here. This is analogous to the classical field study of light, with the Maxwell equations, which gives the correct behaviour of electro-magnetic fields for all phenomena which do not require to take the "granularity", *ie* the photons into account.

1.2.4 Factorization of the "frozen direction"

We now use this approximation for the Hamiltonian (1.36). We call $\psi_{3\mathrm{D}}$ the wave function for the Hartree ansatz. We compute the energy $E(\psi_{3\mathrm{D}})$ from $\langle\Phi| \, \hat{H} \, |\Phi\rangle$ by injecting $\psi_{3\mathrm{D}}$ in it. We also replace the interaction term by the contact interaction of (1.33):

$$E(\psi_{3\mathrm{D}}) = \int \left(\frac{\hbar^2}{2m}|\nabla\psi_{3\mathrm{D}}(\boldsymbol{r})|^2 + V_{\mathrm{trap}}^{(3\mathrm{D})}|\psi_{3\mathrm{D}}(\boldsymbol{r})|^2 + \frac{g^{(3\mathrm{D})}}{2}|\psi_{3\mathrm{D}}(\boldsymbol{r})|^4 \right) \mathrm{d}^3r \, . \tag{1.40}$$

To take into account the frozen movement along z, we use an additional *ansatz*:

$$\psi_{3\mathrm{D}}(\boldsymbol{r}) = \psi(x,y) \; \chi_0(z), \tag{1.41}$$

where $\chi_0(z)$ is the ground state of the motion of one particle along z

$$-\frac{\hbar^2}{2m}\frac{\mathrm{d}^2\chi_0(z)}{\mathrm{d}^2 z}+V_{\mathrm{trap}}^{(1\mathrm{D})}\chi_0(z)=\varepsilon_0\chi_0(z). \tag{1.42}$$

This factorization ansatz is valid if the interaction and thermal energies are both small compared to the difference of energy between the ground state and the first excited level of the trapping along z. This is the condition to experimentally realize a two-dimensional gas.
We get for ψ (up to a meaningless additive constant):

$$E(\psi)=\int\left(\frac{\hbar^2}{2m}|\nabla\psi|^2+V_{\mathrm{trap}}^{(2\mathrm{D})}|\psi(\boldsymbol{r})|^2+\frac{g^{(2\mathrm{D})}}{2}|\psi(\boldsymbol{r})|^4\right)\mathrm{d}^2 r, \tag{1.43}$$

with

$$g^{(2\mathrm{D})}=g^{(3\mathrm{D})}\int|\chi_0(z)|^4\,\mathrm{d}z. \tag{1.44}$$

In the case of a harmonic vertical confinement ω_z, this leads to $g^{(2\mathrm{D})}=\hbar^2\sqrt{8\pi}a/m\ell_z$, with the harmonic oscillator length $\ell_z=(\hbar/m\omega_z)^{1/2}$ which constitutes an additional characteristic length to the problem. This will lead to the scale invariance of the system as we will see later in this chapter.
We can wonder if we could not make a better choice for $\chi_0(z)$. We indeed expect that when the interaction energy $g^{(2\mathrm{D})}n$ is not negligeable compared to $\hbar\omega_z$, different levels of the vertical harmonic oscillator will be populated. This has been analytically solved in a self-consistent manner in [95], section 4.4.2, and led to the conclusion

$$g^{(2\mathrm{D})}\approx g_{n=0}^{(2\mathrm{D})}(1-1.39\,a\,\ell_z\,n), \tag{1.45}$$

where $n=|\psi|^2$ is the 2D atomic density. As we will see, n can reach up to 50 atoms/µm^2 for the vertical confinement $\omega_z=2\pi\times 4.0$ kHz, which leads to a reduction of $g^{(2\mathrm{D})}$ of 5 %.

1.2.5 The quasi-2D regime

The change of the interaction parameter from $g^{(3\mathrm{D})}$ to $g^{(2\mathrm{D})}$ is a bit more complicated than the heuristic derivation we made just above. This comes from the fact that contrarily to $f_{(3\mathrm{D})}(\boldsymbol{k})$, $f_{(2\mathrm{D})}(\boldsymbol{k})$ does not tend towards a constant at low k.
To be more rigorous we need to distinguish two different regimes, depending on the thickness of the system ℓ_z:

- The true 2D regime for which the motion of the atoms is strictly confined to the xy plane. This occurs when the effective range of the interaction potential R_e, which is very close to a in our case, is much bigger than the length of the harmonic oscillator along z. In this case the scattering amplitude is energy-dependent, and there is no additional constant characteristic length in the system.
- The quasi-2D regime where the microscopic motion of the atoms along z is still possible, which corresponds to $\ell_z\gg R_e$. This is the case relevant for us because $R_e\simeq a\ll l_z$. We note that the term "quasi-2D" in the cold atom

domain also has another meaning. It sometimes refers to the fact that $k_{\mathrm{B}}T$ is usually not so small compared to $\hbar\omega_z$ the vertical confinement, meaning that some atoms are in the excited levels of the harmonic oscillator in the z direction[a].

In this second regime, the interactions can be expressed as a contact potential

$$U(\boldsymbol{r}_i - \boldsymbol{r}_j) = g^{(2\mathrm{D})}\delta^{(2\mathrm{D})}(\boldsymbol{r}_i - \boldsymbol{r}_j), \tag{1.46}$$

with a two-dimensional coupling constant derived by Petrov *et al.* [85, 96]:

$$g^{(2\mathrm{D})} = \frac{\sqrt{8\pi}\hbar^2}{m}\frac{1}{\ell_z/a - \ln(\pi q^2\ell_z^2)/\sqrt{2\pi}}, \quad \text{where} \quad q^2 = \frac{2m\mu}{\hbar^2}. \tag{1.47}$$

The energy dependence is only in the logarithm, and is negligible for our experimental parameters. In the usual case of a harmonic trapping potential along z, we thus rather characterized the interactions with the parameter $\tilde{g}$ defined as:

$$g^{(2\mathrm{D})} = \frac{\hbar^2}{m}\tilde{g}, \quad \text{where}\, \tilde{g} = \sqrt{8\pi}\frac{a}{\ell_z}. \tag{1.48}$$

The interaction energy is then:

$$E_{\mathrm{int}} = \frac{g}{2}\int \langle n^2(\boldsymbol{r})\rangle \, \mathrm{d}^2 r = \frac{\hbar^2\tilde{g}}{2m}\int \langle n^2(\boldsymbol{r})\rangle \, \mathrm{d}^2 r \, . \tag{1.49}$$

The integration we did in the previous section would lead to the same formula for E_{int}, but the requirement $a \ll \ell_z$ was hidden in the procedure.

The 2D healing length ξ, which gives the characteristic length scale corresponding to the interaction energy, and thus the distance at which the wave function takes its normal value if we impose it to be zero at one point is given by:

$$\xi = \frac{\hbar}{\sqrt{mgn}} = \frac{1}{\sqrt{\tilde{g}n}}. \tag{1.50}$$

As done in [76] we can quantitatively define the strongly interacting limit by the value of $\tilde{g}$ for which the energy of N particles, E_{int}, reaches the kinetic energy E_{K} of N non-interacting particles equally distributed over the lowest N single-particle states. This leads to

$$E_{\mathrm{int}} = E_{\mathrm{K}} \Rightarrow \tilde{g} = 2\pi. \tag{1.51}$$

Degenerate quasi-2D Bose gas have been realized experimentally with values of $\tilde{g}$ from 0.01 to 3 [34, 68, 64, 67, 97, 98, 99]. This parameter is also expected to be of the order of 1 for 2D layers of liquid helium. We note that for values of $\tilde{g} \geq 1$, the logarithmic contribution in equation (1.47) is no longer negligeable and there is a k dependence of $\tilde{g}$. But for for the experiment described in this thesis, $\tilde{g} \approx 0.1$, and it thus stays independent of k to a very good approximation and scale invariance which we describe now occurs.

[a]The effects of atoms in the excited levels of the z harmonic oscillator were the object of long developments in the study of harmonically trapped 2D Bose gases. We won't consider them a lot in the rest of this work because their effect in hard walls flat-bottom box potentials will be the same everywhere in the trap, and thus won't modify much the physics of the system.

1.2.6 Scale invariance

The type of scale invariance we are interested in occurs when the energies of a system behave in a certain way for a dilatation of the lengths of the system. More precisely, it can be shown [77] that if the following relation is verified:

$$\left.\begin{array}{l}\text{lengths: } \ell \to \lambda\ell \\ \text{time: } t \to \lambda^2 t\end{array}\right\} \quad \Rightarrow \quad \text{Energy: } E \to \frac{1}{\lambda^2}E, \tag{1.52}$$

then the equation of state of the system can be expressed as

$$\mathcal{D} = \mathcal{G}\left(\frac{\mu}{k_{\mathrm{B}}T}\right), \tag{1.53}$$

with $\mathcal{G}$ a function to be determined. This means that the state of the system is characterized by a single parameter $\alpha = \mu/k_{\mathrm{B}}T$ and not anymore μ and T separately. For the 2D Bose gas, the condition (1.52) is fulfilled for the kinetic energy (see [77] for the quantum derivation). It is also the case for the interaction energy as we consider a contact interaction which satisfies $\delta^{(2)}(\lambda\boldsymbol{r}) = \delta(\boldsymbol{r})/\lambda^2$. Other systems exhibiting this scale invariance are for example liquids with interactions in $1/r^2$ ([100] §35). These conditions for scale invariance can alternatively be viewed as the fact that the equation of state has to be expressed in terms of dimensionless parameters. In the 3D Bose gas, there are at least three dimensioned parameters: μ, $k_{\mathrm{B}}T$ and the scattering length a. Introducing the energy linked to a, $\epsilon = \hbar^2/ma^2$, the equation of state must then have a form like

$$\mathcal{D} = \mathcal{G}\left(\frac{\mu}{\epsilon}, \frac{k_{\mathrm{B}}T}{\epsilon}\right). \tag{1.54}$$

Going to the quasi-2D regime, ℓ_z can be combined with a to form $\tilde{g}$ which is a dimensionless parameter. The equation of state then becomes

$$\mathcal{D} = \mathcal{G}\left(\frac{\mu}{k_{\mathrm{B}}T}, \tilde{g}\right). \tag{1.55}$$

As for our system $\tilde{g}$ is constant, this is equivalent to (1.53). With this condition we see that the unitary Fermi gas for which the scattering length diverges also exhibits this scale invariance.

1.3 The weakly interacting 2D Bose gas: some properties

Now that we introduced the theoretical framework to study the uniform 2D Bose gas, we turn in this part to some important analytical results which can be derived.

1.3.1 Reduction of density fluctuations and quasi-condensate

Compared to the ideal gas, we will see here that repulsive interactions between particles tend to reduce density fluctuations. The interaction energy is indeed, as we saw in equation (1.49), and considering a system of size L:

$$E_{\rm int} = \frac{\hbar^2 \tilde{g}}{2m} \int \langle n^2(\boldsymbol{r}) \rangle \, \mathrm{d}^2 r = \frac{\hbar^2 L^2}{2m} \, \tilde{g} \, \langle n^2(\boldsymbol{r}) \rangle, \tag{1.56}$$

so that the cost in interaction energy compared to the zero temperature gas is directly proportional to the density fluctuations characterized by [101]:

$$(\Delta n)^2(\boldsymbol{r}) = \langle n^2(\boldsymbol{r}) \rangle - n^2(\boldsymbol{r}) = (g_2(0) - 1) n^2(\boldsymbol{r}), \tag{1.57}$$

where $g_2(\boldsymbol{r}) = \langle n(\boldsymbol{r}) n(0) \rangle / n^2$ is the *normalized* second order (density-density) correlation function. In the case of the uncondensed ideal Bose gas, $g_2(0) = 2$, while if the density fluctuations are completely suppressed $g_2(0) = 1$.
For an interacting gas, the interaction energy will always dominate when a low enough temperature is reached. The mean-field interaction energy per particle $E_{\rm int}/N = \hbar^2 \tilde{g} n / 2m$ will indeed become bigger than $k_{\rm B} T$ when T is low enough, which can be expressed in terms of the phase-space density D:

$$\frac{E_{\rm int}/N}{k_{\rm B} T} = \frac{\tilde{g}}{4\pi} \mathcal{D} \gg 1, \quad \text{or} \quad \mathcal{D} \gg \frac{4\pi}{\tilde{g}}. \tag{1.58}$$

In fact calculations done by Nikolay Prokof'ev and Boris Svitsunov [102] which will be briefly described later show that these density fluctuations are significantly suppressed already for $D \gg 1$. This reduction of density fluctuations is also described as the appearance of a *quasi-condensate* or a *pre-superfluid state*. The notion of quasi-condensate has first been introduced in [83] and extended in [85]. It has been experimentally observed in two-dimensional atomic hydrogen by [103], looking at three-body dipole recombinations. It has also been observed in cold atom systems for example by [67, 68, 66].
It is interesting to give a definition of the quasi-condensate as done in [102]:

$$n_{\rm qc} = \sqrt{2n^2 - \langle n^2 \rangle}, \tag{1.59}$$

which corresponds to non-gaussian fluctuations of the atomic density. It thus also quantifies the reduction of density fluctuations, and its value increases from zero to a value close to one before the superfluid transition. We will show the results obtained with Monte Carlo simulations in section 1.6.2.
It is important to stress that the word "quasi-condensate" might be misleading. It indeed corresponds only to a reduction of density fluctuations and does not imply an extended phase coherence as is the case for a true condensate. A nice result of the paper [67] is that they show that even if a quasi-condensate is present, there is no extended phase coherence in the system between the quasi-condensate and superfluid thresholds. The reduction of density fluctuations is necessary for a BKT-type superfluid transition to happen.

1.3.2 Bogoliubov analysis

The idea of the 3D Bogoliubov analysis is to start with the assumption that at zero temperature the state of a weakly interacting gas is described by the uniform order parameter $\psi = \sqrt{n} \mathrm{e}^{\mathrm{i}\theta}$, find the excitation spectrum, and then consider the effects of the thermal occupation of the excitation modes. It is thus a purely phononic

treatment which does not take for example vortices into account. We might think that this treatment is not justified in 2D because thermal fluctuations destroy the order parameter. But the long-wavelength phase fluctuations destroy it only at long distances and locally the order parameter stays well defined. The applicability of the Bogoliubov approach was formally justified by C. Mora and Y. Castin for quasi-condensates in 2D in [104, 105].
The Bogoliubov treatment then is not very different from the 3D case, the detailed calculations can be found in [76], and one recovers the BEC excitation spectrum:

$$\omega_k = \sqrt{\frac{\hbar k^2}{2m}\left(\frac{\hbar k^2}{2m} + \frac{2g^{(2D)}n}{\hbar}\right)}. \tag{1.60}$$

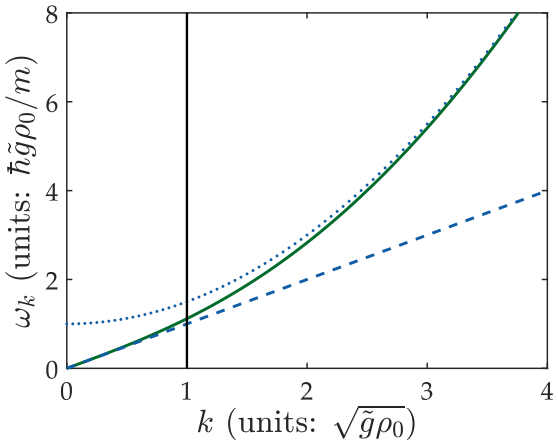

Figure 1.3 *– Excitation spectrum of Bogoliubov in green solid line. The dashed line corresponds to the linear approximation for low k, corresponding to the phononic regime. The dotted parabolic curve matching the dispersion relation at high k corresponds to the free-particle regime. The vertical black line shows $k = 1/\xi$, the limit between the two regimes.*

According to the Landau criterion [89], we thus expect the system to be superfluid with a critical velocity $v_c = \sqrt{g^{(2D)}n/m}$ as shown figure 1.3. This excitation spectrum has been precisely measured for a 3D BEC with Bragg excitation in [16].
With the Bogoliubov analysis, it is also possible, introducing a cutoff in the population of the excitation modes and considering the Fourier coefficients of the expansion of the density variations, to find an analytical formula for the density fluctuations:

$$\frac{\Delta n^2}{n^2} \approx \frac{2}{n\lambda^2}\ln\left(\frac{k_B T}{2gn}\right). \tag{1.61}$$

1.3.3 Algebraic decay of correlations

We will give here the result for the first-order correlation function obtained within the Bogoliubov treatment. The idea of the derivation is the same as the one to get the density fluctuations, also introducing a cutoff in the population of the excitation

modes, but this time considering the Fourier coefficients of the expansion of the phase variations. We get [76]:

$$g_1(r) \approx n_s \left(\frac{\xi}{r}\right)^{1/n_s\lambda_T^2}. \tag{1.62}$$

This algebraic decay of correlations is called *quasi-long-range order*, because it still vanishes for $r \to \infty$, consistently with the Mermin-Wagner theorem, but much slower than the exponential behaviour found for the ideal 2D Bose gas (1.31). This has important effects on finite-size systems, which will condense in the sense of Penrose and Onsager for much lower phase-space densities than what would be required without the interactions leading to this algebraic decay. One then talks about *interaction-driven condensation*.

1.4 Superfluid transition in the 2D Bose gas

Superfluidity has not been directly addressed yet in this chapter. It is an important property which can lead to spectacular effects such as the fountain effect for liquid helium. In this section we will first give definitions of superfluidity and of the superfluid fraction. We will then recover by a simple thermodynamic calculation the superfluid jump which occurs in a BKT-type transition and which is the only sharp modification of the system happening at the critical point. We will finally give the parameters at which this transition should occur, which were calculated with Monte Carlo simulations.

1.4.1 Definition of superfluidity and superfluid fraction

We said in section 1.3.2 that according to the Landau criterion, the equation (1.60) was implying that the system is superfluid. The occurrence of superfluidity is in fact a very subtle question, and one must be a bit more careful.
Superfluidity is characterized by at least two distinct properties [106, 107]:

- A superfluid state must have a certain phase stiffness. For example if one puts the superfluid in a cylindrical box that one sets into rotation at the angular frequency $\boldsymbol{\Omega}$, the superfluid will stay at rest in the Galilean frame of the laboratory, at least for low rotation speeds. On the contrary, a normal fluid would acquire a field of speed $\boldsymbol{\Omega} \times \boldsymbol{r}$ even for small $\boldsymbol{\Omega}$.
- A superfluid current must be metastable. This means that if the superfluid is in motion inside a static cylindrical box, this movement can continue for a very long time, whereas the rugosity of the walls of the box would stop the current of a normal fluid. This might also depend of the speed of the supercurrent.

The difference between the two may not seem obvious at first view, but can be understood on the example of the ideal Bose gas which satisfies the first but not the second criterion as explained in [108], chapter 2. The Landau criterion satisfied by the condensed Bose gas is thus a necessary, but not a sufficient condition for the existence of a superfluid state.

A quantitative definition of the superfluid fraction consists in evaluating the cost in free energy of a small distortion of the boundary conditions of the system (see [108] and the annexe of [23]). More precisely, starting from a system with periodic boundary conditions, we impose:

$$\psi(x+L,y) = \mathrm{e}^{\mathrm{i}\Theta}\psi(x,y), \quad \psi(x,y+L) = \psi(x,y), \quad \Theta \ll 1, \tag{1.63}$$

and the superfluid density n_s is defined as

$$F(\Theta) = F(0) + \frac{\hbar^2\Theta^2}{2m} n_\mathrm{s} + O(\Theta^4). \tag{1.64}$$

The exact computation of the superfluid fraction for our system then requires to compute the kinetic energy for the different contributions to the velocity field. The tricky point is that for the integration one has to choose a length β and to consider only vortices separated by a distance greater than β. The contribution of vortices separated by a distance lower than β is not forgotten, but taken into account via the superfluid density. The proper way to do this is an important technique of statistical theory of fields, called renormalization (see for example [109]).

One can also wonder if superfluidity is equivalent to condensation. This is the object of the appendix of [23]), which shows that, at least for experiments with ultracold gases, there is equivalence between the appearance of a condensate or quasi-condensates and the occurrence of superfluidity. These two phenomena are thus "two faces of the same coin". But as we see for example in the Monte Carlo simulations, the quasi-condensate and superfluid fractions are not equal for the two-dimensional case, whereas the condensate and superfluid fraction are essentially equal for a weakly interacting three-dimensional Bose gas. Another example for which the two fractions are different is the liquid ^{4}He in its low-temperature limit, which is totally superfluid whereas its condensate fraction is only of 10 %.

1.4.2 The superfluid universal jump

For our atomic gas described by a classical wave function $\psi(\boldsymbol{r})$, a vortex is a zero of this function. Around this zero, the phase must roll in an integer multiple of 2π because the wavefunction must be single valued everywhere. The integer is the topological charge Q of the vortex. We say that this charge is topological because the wave function cannot be continuously deformed to create or annihilate a vortex. Vortices can only be created on the side of the sample or by pairs of opposite charge.

The aim of this section is to go beyond the Bogoliubov model we developed before, which is purely phononic, by taking vortices into account. Intuitively, they can have a big impact on the phase coherence of the system. Imagine indeed that for two points A and B which had a certain phase coherence according to the treatment above, a vortex could be introduced between them with a certain probability. The difference of phase between the two points will then switch from ϕ to $\phi + \pi$ when the vortex is here. This would destroy the quasi-order in phase which was present. We now follow the derivation of the superfluid jump done in [77], chapter 4.

Properties of a vortex

It is interesting to compute the energy of a single vortex. Together with a small thermodynamical study, it will allow us to derive the universal jump of the superfluid fraction at the BKT transition. An alternative derivation, which is also the historical one, can be done using the free energy of the configuration with one vortex [110]. The velocity field created by the vortex is orthoradial and such that the circulation around the center is h/m, which gives if we assume cylindrical symmetry

$$\boldsymbol{v}(\boldsymbol{r}) = \frac{\hbar}{mr}\boldsymbol{u}_\phi, \quad \text{with} \quad \boldsymbol{u}_\phi = \boldsymbol{u}_z \times \frac{\boldsymbol{r}}{r}. \tag{1.65}$$

If for simplicity we model the vortex core by a step function of size ξ, the kinetic energy of a vortex is

$$\begin{aligned} E_{\text{kin}} &= \frac{1}{2}m\int n(\boldsymbol{r})\boldsymbol{v}^2(\boldsymbol{r})\,\mathrm{d}^2r \\ &\approx \frac{1}{2}mn\frac{\hbar^2}{m^2}\int_\xi^R \frac{1}{r^2}2\pi r dr \\ &\approx \pi\frac{\hbar^2 n}{m}\ln\left(\frac{R}{\xi}\right). \end{aligned} \tag{1.66}$$

The important point is that the energy of a single vortex goes to infinity when the size of the system goes to infinity. As this energy is linked to the phase stiffness, the atomic density n has to be replaced by the superfluid density n_{s} in the above formula. The interaction energy however does not increase when the size of the system is increased.

Simple thermodynamics of an ensemble of vortices

To derive the superfluid jump, we will now ask ourselves the question: *Is the observation of a single vortex probable?*
As the size of the core of the vortex is $\pi\xi^2$, we can consider that there are $W = \pi R^2/\pi\xi^2$ independent states for a single vortex in a disk of radius R. The probability for one state to be realized is then:

$$p \approx \mathrm{e}^{-E_{\text{kin}}/k_{\text{B}}T}, \tag{1.67}$$

which using equation (1.66) gives

$$p \approx \left(\frac{\xi}{R}\right)^{\mathcal{D}_{\text{s}}/2}. \tag{1.68}$$

The probability for a vortex to be present in the sample independently of its position is then

$$Wp = \frac{R^2}{\xi^2}p \approx \left(\frac{\xi}{R}\right)^{-2+\mathcal{D}_s/2}. \tag{1.69}$$

There are then two different cases which can occur:

1. If $\mathcal{D}_\mathrm{s} > 4$, the probability Wp goes to zero for samples of big size: vortices are very rare. In fact they exist only in bound pairs, and have little influence on the coherence properties of the system. We found that the phonons lead to an algebraic decay of the correlations, which is not prevented by the pairs of vortices, and thus to the appearance of superfluidity. A quantitative calculation of the superfluid fraction can be done using Monte Carlo simulations.
2. If $\mathcal{D}_\mathrm{s} < 4$, Wp diverges at the thermodynamic limit. Vortices of random charge then proliferate in the system and prevent any phase coherence to occur. The system is thus not superfluid and the renormalization framework leads to $\mathcal{D}_\mathrm{s} = 0$.

It is impressive that with such a simple model one can recover quantitatively the value of the superfluid jump [110]:

$$\begin{cases} n_\mathrm{s}(T_\mathrm{BKT})\lambda^2_{T_\mathrm{BKT}} = 4 & \text{if } \mathcal{D} = \mathcal{D}_\mathrm{c}^+ \\ n_\mathrm{s} = 0 & \text{if } \mathcal{D} = \mathcal{D}_\mathrm{c}^-. \end{cases} \tag{1.70}$$

1.4.3 Connexion to the Berezinskii-Kosterlitz-Thouless transition

The transition to a superfluid state studied here is the BKT transition, originally derived for the two-dimensional XY model [86, 87, 88]. The mapping of this model to the 2D Bose gas is possible if and only if the density fluctuations are completely absent. In this case the kinetic energy arises only from the variation of the phase θ. One can then introduce an effective *low-energy Hamiltonian*:

$$H_\theta = \frac{\hbar^2}{2m} n_\mathrm{s} \int (\nabla\theta)^2 \, \mathrm{d}^2 r, \tag{1.71}$$

which supports a BKT transition[a]. As the speed of a superfluid is expressed in terms of its phase $v_s = \hbar\nabla\theta/m$, we see that this Hamiltonian corresponds to the kinetic energy of a superfluid. This is why we wrote n_s instead of n in equation (1.71). It can be shown with a Bogoliubov analysis that by using this low energy Hamiltonian, we are introducing a cutoff at $k_\mathrm{max} = 1/\xi$. Replacing n by n_s is thus a heuristical way of incorporating short-distance physics in this description.
The absence of density fluctuations is essentially fulfilled for $\mathcal{D} \gg 2\pi/\tilde{g}$, but it is not satisfied at the critical point of the gas. This is why a microscopical description of the 2D Bose gas around this transition is very difficult and why one still relies on Monte Carlo simulations. Since the transition is still driven by the dissociation of vortex pairs, we will nevertheless continue to call this transition in our gas the BKT transition.

1.4.4 Critical temperature of the transition

The relation obtained just above for the superfluid jump is universal in the sense that it is independent of $\tilde{g}$, but it does not give the relation between the total density n and the critical temperature T_BKT. Fisher and Hohenberg [111] found that the

[a] But this Hamiltonian cannot be the true one as it has a temperature dependence through the superfluid density n_s.

chemical potential and phase-space density at the transition should be written in the form:

$$\mathcal{D}_{\mathrm{BKT}} = \ln\left(\frac{\xi_{\mathcal{D}}}{\tilde{g}}\right), \tag{1.72}$$

$$\left(\frac{\mu}{k_{\mathrm{B}}T}\right)_{\mathrm{BKT}} = \frac{\tilde{g}}{\pi}\ln\left(\frac{\xi_{\mu}}{\tilde{g}}\right). \tag{1.73}$$

Prokof'ev, Ruebenacker and Svitsunov [102] with their Monte Carlo simulations described in 1.5.3 found the constants to be: $\xi_{\mathcal{D}} = 380 \pm 3$ and $\xi_{\mu} = 13.2 \pm 0.4$.

1.5 Classical field Monte Carlo simulations

The analytical results presented in section 1.3 are very important, but do not provide quantitative predictions of for the quasi-condensate or the superfluid fractions, for example. We now turn to a numerical implementation of the classical field approach, which allows us to recover some interesting features such as the transition of the first-order correlation function from an exponential to an algebraic decay, and the prediction of the quasi-condensate fraction. We will then briefly describe the Monte Carlo simulations done by N. Prokof'ev and B. Svitsunov which we use for the equation of state of the 2D Bose gas.

1.5.1 One way to implement the classical field Monte Carlo approach

The idea of a Monte Carlo simulation in statistical physics is to compute a lot of microscopical states and evaluate thermodynamic quantities on these states. If the states are well sampled, an average of these values constitutes a thermal average of the thermodynamic quantity. A good sampling requires ergodicity, meaning that the process used for computing the microscopical states should be able to create all the possible states.
When the work is done in the canonical ensemble, an efficient and often used way of sampling the states has been introduced by Metropolis, Rosenbluth and Teller [112] and consists in sampling the system by modifying it slightly around equilibrium and attributing different weights to the obtained states. The weights are simply the Boltzmann's factor between the computed energy of the states.
In the simulations described in this section, we choose a certain energy of the system which we keep constant along the evolution to get the different microscopical states. We are thus working in the microcanonical ensemble, and all the states have equal probabilities. The bench of states obtained this way corresponds to a sampling of all the microscopical states which we hope is representative.

Principle of computation of the microscopical states

We do our simulations on a grid of size $N_{\mathrm{S}} \times N_{\mathrm{S}}$. We compute the microscopical states from a state $\psi(\boldsymbol{r})$ with white noise, corresponding to the energy put into the system, with Dirichlet boundary conditions. We thus are simulating a finite size

system. We then do a time evolution of this system by the splitting method, using $\psi(\boldsymbol{r})$ for the evolution with the interaction energy, and its discrete sine transform $\phi(\boldsymbol{q})$ for the kinetic energy evolution. We let this state evolve so that it "thermalizes" thanks to the non-linearity in the interaction energy evolution. We then compute the phase-space density $\mathcal{D}$ and post select the states so that the $\mathcal{D}$ found after evolution is compatible with the initial $\mathcal{D}$ used for the evolution with a relative error of less than 10%. The full process is described with more details in the Annexe A.

Choice of the ultraviolet cutoff

As all classical field theories, the modelisation of the fluid by the wave function ψ induces a problem of ultraviolet divergence. This is the famous "black-body" problem. There are indeed modes of arbitrarily high $\boldsymbol{q}$ which cause a divergence of the integrals over the energy giving physical quantities. This has been understood a long time ago and we know that the solution is to quantize the field. In our case we are only interested in the long-distance behaviour of the correlation functions of the fluid, associated to the small $\boldsymbol{q}$'s. We will thus only introduce "by hand" a cut-off in the energies as

$$\epsilon_{q_{\mathrm{cut}}} \simeq k_{\mathrm{B}} T. \tag{1.74}$$

The position of the cutoff influences the result of the simulations. For a precise discussion of the position of the cutoff, see [113] chapter 12[a].
Our analysis will then not allow the study of momenta bigger than $q_{\mathrm{cut}} = \sqrt{2mk_{\mathrm{B}}T}/\hbar$, or equivalently of phenomena of length smaller than λ_T.

1.5.2 Result on correlation functions

We saw section 1.3.3 that an important feature of the superfluid transition in 2D is that the correlation function should switch from an exponential to an algebraic decay. We tested this in our simulations on a grid of 64×64 for two different $\tilde{g}$. The first order correlation function was computed and its decay with the distance fitted by an exponential or a power law. The results are shown figure 1.4. One clearly see that for $\mathcal{D}$ below $\mathcal{D}_{\mathrm{BKT}}$ the decay is close to being exponential, corresponding to no long-range order. But for $\mathcal{D}$ above $\mathcal{D}_{\mathrm{BKT}}$, the decay is better approximated by an algebraic function, corresponding to what was found section 1.3.3. It is also nice that the value of $\mathcal{D}$ at which it happens is close to the expected one. This means that our cutoff is not too bad. This result for the fit of g_1 functions has been seen experimentally by the group of Selim Jochim on fermionic atoms in [73], but the fitted exponents they obtained were not the expected ones.
We also used these simulations to compute the quasi-condensate fraction. The result will be shown together with the result of Prokof'ev and Svitsunov in figure 1.6 in section 1.6.2.

[a] This is also why Prokof'ev and Svitsunov compute only quantities relative to the critical ones, using a universality which will be briefly described later, so that their calculations are cutoff independent.

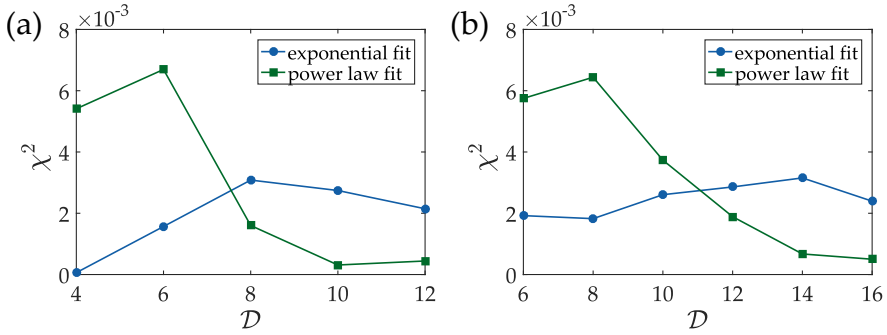

Figure 1.4 *– Goodness of the fits of the first order correlation functions obtained from the Monte Carlo simulations for exponential (blue disks) and power-law (green squares) functions, for $\tilde{g} = 0.1$ in (a) and $\tilde{g} = 0.01$ in (b). A crossing from exponential to power-law is clearly visible for both $\tilde{g}$. From formula (1.73) we expect the transition to occur at $\mathcal{D}_{\mathrm{BKT}} = 8.2$ for $\tilde{g} = 0.1$ and $\mathcal{D}_{\mathrm{BKT}} = 10.5$ for $\tilde{g} = 0.01$.*

1.5.3 Monte Carlo simulations of Prokof'ev and Svitsunov

We will not try here to explain fully their simulations. Further explanations are given in their book [114]. We will just try to stress the main differences with our simulations. This is important because we will use the values they found for the equation of state of the 2D Bose gas later in this thesis.

We said that we compute states all with the same energy, and that we are working in the microcanonical ensemble. They on the contrary use states with different energies, and are thus in the grand canonical ensemble. They then need a powerful process to sample their states, that they call *Worm algorithm* and which they describe in [102].

As discussed section 1.5.1, the results of our simulations are cutoff dependent. To have cutoff independent results, Prokof'ev and Svitsunov use an other type of universality that we did not describe yet. It can be shown that close to the critical point, all the differences between a physical quantity and its value at the critical point, for example $\mathcal{D} - \mathcal{D}_{\mathrm{c}}$, can be expressed as a function of one variable:

$$\frac{1}{\tilde{g}}\left[\frac{\mu}{k_{\mathrm{B}}T} - \left(\frac{\mu}{k_{\mathrm{B}}T}\right)_{\mathrm{c}}\right]. \tag{1.75}$$

They thus perform all their calculations as a function of the parameter $X = (\mu - \mu_{\mathrm{c}})/\tilde{g}k_{\mathrm{B}}T$, and get results independent of the cutoff. This universality has been tested for the phase-space density in the group of Cheng Chin in Chicago in [66] for values of $\tilde{g}$ up to 0.26. The Monte Carlo simulations were also performed for systems of different sizes to eliminate finite-size effects. Note however that this universality seems to give unphysical results for the quasi-condensate fraction for values of $\tilde{g} \geq 1$, as will be shown in section 1.6.2. We now turn to an important result of their simulations which is the numerical determination of the equation of state of the weakly-interacting 2D Bose gas.

1.6 Equation of state

The knowledge of the equation of state (EoS) of a system is enough to derive all thermodynamic variables. Taking advantage of the scale invariance described in section 1.2.6, all thermodynamic variables can be expressed only in terms of $\mu/k_{\mathrm{B}}T$. The EoS is now a well-established result, theoretically and experimentally [102, 65], and we will use it to measure the phase-space density of our gas as described in the next chapter. We now describe the different regimes of validity of the possible approximations used to derive it.

1.6.1 Limiting cases of equation of state

Thomas-Fermi regime

Starting from equation (1.43), and minimizing the fonctional energy, one gets the 2D Gross-Pitaevskii equation:

$$\left(-\frac{\hbar^2}{2m}\nabla^2 + g^{(2\mathrm{D})}n(\boldsymbol{r})\right)\psi(\boldsymbol{r}) = \mu\psi(\boldsymbol{r}), \tag{1.76}$$

where the chemical potential μ arises in the minimization as a Lagrange multiplier to keep the normalization of $\psi(\boldsymbol{r})$ constant. In the limit of zero (or very low) temperature, using the Thomas-Fermi approximation which consists in neglecting the kinetic energy term, one gets

$$g^{(2\mathrm{D})}n = \mu\,, \text{ which can be rewritten } \mathcal{D} = \frac{2\pi}{\tilde{g}}\frac{\mu}{k_{\mathrm{B}}T}. \tag{1.77}$$

This is the regime valid for very low temperature, or $\mathcal{D} \gg 1$.

Hartree-Fock regime

In the opposite regime of low $\mathcal{D}$, one has to consider the interactions in and between the condensate and the thermal parts. The effect of considering the thermal part is to effectively change the chemical potential: $\mu \to \mu - 2g^{(2\mathrm{D})}n$.
Replacing the chemical potential in the equation of state of the ideal 2D Bose gas that we got equation (1.17), we get:

$$\mathcal{D} = -\ln\left(1 - z\mathrm{e}^{-\tilde{g}\mathcal{D}/\pi}\right). \tag{1.78}$$

The approximations break down when the density fluctuations are reduced, and one then has to link the two regimes thanks to the Monte Carlo simulations. The whole curve is shown in figure 1.5.

1.6.2 Quasi-condensate and superfluid fractions

We now look at the different components of the gas as defined by Prokof'ev and Svitsunov: the quasi-condensate and superfluid fractions. Both quantities can be computed from their simulations, and the results are shown in figure 1.6 together with the result of our simulations for the quasi-condensate fraction. The quasi-condensate

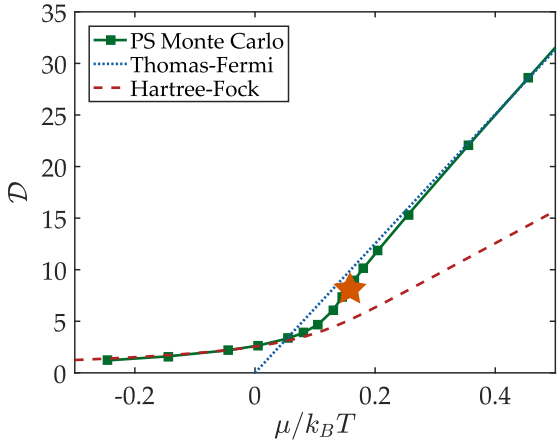

Figure 1.5 *– Equation of state of the 2D Bose gas for $\tilde{g} = 0.1$ computed by Prokof'ev and Svitsunov, with the two asymptotic regimes. The position of the superfluid transition described section 1.4.4 is shown by the orange star.*

grows well before $\mathcal{D}_{\mathrm{BKT}}$, showing the reduction of density fluctuations required for the BKT transition to occur. The superfluid jump is clearly visible at the transition for the two different $\tilde{g}$. We note that the quasi-condensate fraction has been measured in [66]), but no precise measure of the superfluid fraction has been reported until now for cold gases.

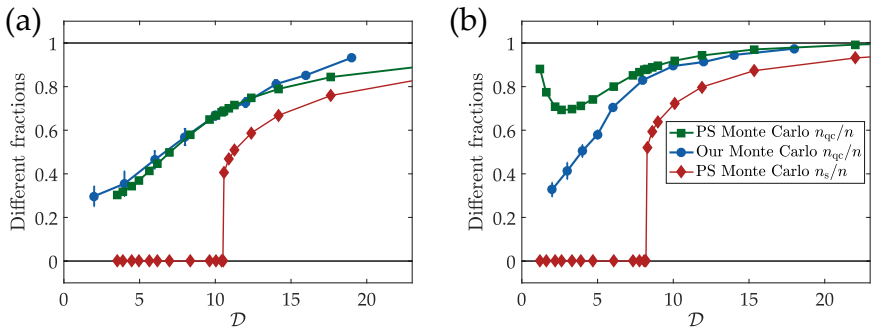

Figure 1.6 *– Computed superfluid and quasi-condensed fractions of the gas for $\tilde{g} = 0.1$ in (a) and $\tilde{g} = 0.01$ in (b). The green squares correspond to the quasi-condensate fraction computed by Prokof'ev and Svitsunov, and the blue disks to the results of our simulations. The red diamonds correspond to the superfluid fraction computed by Prokof'ev and Svitsunov.*

The discrepancy between our simulations and what they obtain for $\tilde{g} = 0.1$ might be due to the "universality" they use. They indeed say that their result must be valid for $\tilde{g} < 0.1$ we are thus already at their limit for the computation of the quasi-condensate density. Our simulations however suffer from not being cutoff independent.

1.6.3 Summary of transitions crossed by a finite-size 2D uniform Bose gas

We now briefly summarize the different transitions or cross-over which can be expected for our system.
We consider our typical square box of size $40\,\mu\text{m} \times 40\,\mu\text{m}$ and a typical temperature of 100 nK. According to the equation (1.32), we found that the system will be coherent over the whole sample simply due to the bosonic statistics (without interactions) for $\mathcal{D}_\text{c} = \ln(L^2/\lambda_T^2) = 11.3$[a].
According to equation (1.73), the BKT transition in an infinite system with our value of $\tilde{g}$ of 0.15 should happen at $\mathcal{D}_\text{BKT} = 7.8$. We thus expect when $\mathcal{D}$ is increased that we will first cross the BKT transition before getting the condensate that would have been obtained for this finite-size system even without interactions.
It can however be shown that above that just before crossing the BKT transition, the first order correlation function behaves as $g_1(r) \approx \mathrm{e}^{-r/\ell}$, with

$$\ell = \exp\left(\frac{\sqrt{\gamma T_\text{BKT}}}{\sqrt{T - T_\text{BKT}}}\right), \tag{1.79}$$

where γ is a model-dependent constant. This exponential divergence of the correlation length, contrary to the second-order phase transitions which exhibit a polynomial divergence leads to a larger critical region. We also notice that for finite-size systems, there will be a temperature slightly higher than T_BKT for which the coherence length ℓ will be already of the order of the sample size. Using equation (1.79) and taking $\ell = L$ and $\gamma = 1$, we estimate that

$$\frac{\Delta T}{T_\text{BKT}} \approx \left(\frac{\gamma}{\ln(L/\lambda_T)}\right)^2 \approx 0.05. \tag{1.80}$$

There will thus always be an effective quasi long-range order over our sample size before that the BKT transition occurs. Extremely big samples would be required to avoid this effect. We note that this "interaction-driven condensation' has been studied experimentally varying the interactions between atoms but in the case of harmonic trap in the group of Zoran Hadzibabic [115].

[a] Or with the correction for a square box as computed in [92] for $\mathcal{D}_\text{c} = 10.5$

2

Experimental Setup

This chapter is dedicated to the description of our experimental setup enabling the preparation of a two-dimensional BEC and of the tools we have to manipulate it. It is the third generation of setups realized in the team to study degenerate two-dimensional gases of ^{87}Rb. Its design thus benefited from the previous experiments and has been improved in several ways. The main advantages of our setup are that it does not require any transport of the atoms while keeping an important optical access to the science cell, which could be used, for instance, in the future to install square or triangular lattices in the atomic plane.

The final trap configuration is shown in figure 2.1. The interfering blue-detuned dipole trap beams coming from the right provide the vertical confinement and the vertical beam passing through the microscope objective provides the in-plane confinement. The atoms are depicted in blue. The choice of an all-optical repulsive final trap leads to a very small heating of the gas as it stays in the dark regions of the beams. Contrary to most experiments, the atoms are trapped in a hard-wall flat-bottom potential. In addition, the tunability of the in-plane trapping due to a Digital Micromirrors Device (DMD) and to the vertical trapping thanks to an accordion lattice make the experiment suitable for the study of a wide range of topics.

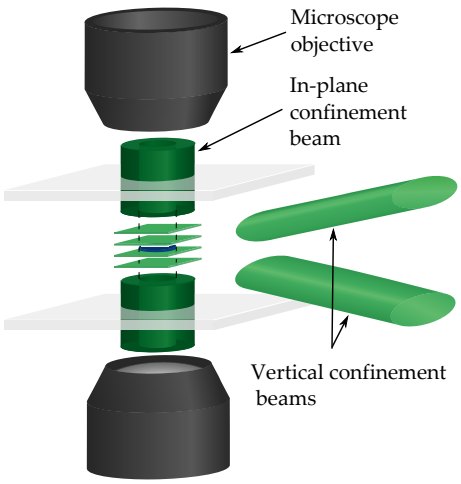

Figure 2.1 *– Schematic view of the final trap configuration. Figure extracted from [116].*

As shown in figure 2.1, the atoms are in the middle of two microscope objectives. They are custom made by Nachet and have been optimized to have a numerical aperture of 0.45 at a working distance of 14 mm, including the crossing of the glass slab of 5 mm.

We achieved a very stable experiment able to produce a condensate in the final trap every 30 s and working from the first shots of the day. Typically one hour of warming up is required to obtain a stable configuration. We first briefly describe the different steps to reach the degenerate regime. We then describe the absorption imaging we use to probe the gases and we characterize the final trap. We then explain how

we manipulate the internal states of the atoms and finally how we measured the temperature of the gas for the first projects of this thesis.

2.1 Reaching the degenerate regime

When I arrived in the lab, the vacuum system was already prepared and the laser systems with their locks were mounted but nothing was aligned on the experiment. I thus will not describe in details all apparatus, beam paths, AOM frequencies, *etc* here, but these can be found in Laura's thesis [117], who took care to write most of the information in her chapter 4. Further information can also be found in Katharina's report [118] who worked on the laser systems and on early stages of the experiment such as the computer control. I will nevertheless briefly explain the sequence used to reach the degenerate regime, as some of the tools will be reused later in the sequence for other purposes.

2.1.1 Experimental sequence to load the final trap

The experiment is designed to be as simple as possible. A pressure on the order of 10^{-7} mbar is obtained by heating a piece of solid rubidium up to 65 °C. This loads a commercial two-dimensional magneto-optical trap (MOT), from which atoms are pushed by a laser beam to the lower pressure science cell (less than 10^{-11} mbar) where they are captured in a 3D MOT. This loading is maintained for 7 s, to get about 10^9 atoms at 250 µK. The MOT is then compressed for 15 ms before cutting the magnetic gradient to further cool the atoms in an optical molasses stage. This leads to 6 10^8 atoms at about 15 µK.
They are then transferred to a magnetic quadrupole trap for radio-frequency evaporation. The MOT and quadrupole coils have been carefully designed and mounted so that the zeros of their gradient coincide at less than one millimeter. We want to trap only atoms in $|\mathrm{F}=1,\mathrm{m_F}=-1\rangle$ state in the quadrupole. The MOT beams are then detuned closer to the $|\mathrm{F}=2\rangle \rightarrow |\mathrm{F}'=2\rangle$ transition and the sidebands (which will be described in the next section) cut for 1 ms[a]. The loading happens at low magnetic gradient (58 G/cm) before it is ramped up to 240 G/cm to get a higher collision rate for an efficient thermalization. The radio-frequency (RF) field is provided by an interface bus (GPIB) controlled generator Rigol DG5070. This signal is amplified by a 4 W amplifier from HD communications (model HD19153). The evaporation consists of a linear ramp from 34 to 2.5 MHz in 12 s. The field is sent onto the atoms with a home-made two-turn antenna of 7 cm radius. This leads to 2.5 10^7 atoms at a temperature of 16 µK, which can be efficiently loaded into the crossed dipole trap. The evaporation is stopped at this point to avoid Majorana losses.
Two perpendicularly crossed dipole beams (elliptical beams of horizontal waist 90 µm, vertical waist 30 µm and wavelength 1064 nm) are then shone at their full power (2 W each on the atoms) from the middle of the RF evaporation. The quadrupole is decompressed at the end of the evaporation and 1.3 10^7 atoms at about 8 µK are

[a] We note that some atoms in $|\mathrm{F}=2\rangle$ are still trapped but we checked that they are lost before the loading of the final trap.

subsequently trapped in the dipoles. The magnetic force from the quadrupole field still compensates one third of the gravity until the end of the sequence. The power of the dipole beams is then reduced exponentially for 3 s, decreasing the power of one beam more than the other one so that the two in-plane frequencies stay equal[a]. At the end of the evaporation we have a quasi-pure BEC of 3 10^5 atoms, which can be loaded in the final trap detailed below. The total sequence duration is less than 30 s and what is done in the final trap takes usually less than 2 s.

2.1.2 Computer control

The experimental sequence is controlled thanks to the Cicero Word Generator software[b] which provides a graphical user interface. This is convenient to prepare the sequences which can be quite complicated. The sequences prepared this way are then read by an other program called Atticus, which generates output buffers which are sent to the hardware cards.
We have five National Instruments hardware cards. One NI PXI 6534 delivers 32 digital channels, that we use as on/off switches. The analog channels are delivered by four NI PCI 6713 cards, which provide each 8 channels of 12 bits, able to supply voltages between -10 V and +10 V. These cards communicate with the computer via a NPI PXI-ExpressCard 8360. They are all synchronized thanks to an Opal Kelly FPGA Module XEM3001, for which the trigger frequency is set to 10 MHz, leading to a maximal time resolution of 200 ns. Further information can be found in [118].
The cameras are controlled by a Python program (see [117] for more details) made to work together with Cicero. We also modified the programs so that pictures with different cameras can be taken during the experimental sequence to monitor the positions of the dipole trap laser beams.

2.1.3 Laser system

We are using for now 5 different lasers on the experiment.

- A 3 W Toptica TA pro laser at 780 nm, used for the 2D and 3D MOTs, the imaging beam and the depumping light. The beam passes through an electro-optical modulator (EOM) working around the frequency of 6.6 GHz. This creates sidebands in the beam, each one having up to 8% of the total power. One of the sideband is used to repump the fraction of atoms which left the closed transition, by transferring them back from the $|F = 1\rangle$ to the $|F = 2\rangle$ ground state. The microwave in the EOM can be switched off for example when one wants to use depumping light[c].
- A Radiant Dyes Narrow Diode laser at 780 nm which can also be used to repump the atoms.

The frequencies of these two lasers are locked using saturated absorption spectroscopy of a rubidium cell.

[a] It is not clear why the two arms do not behave the same way.
[b] http://akeshet.github.io/Cicero
[c] for example before loading the quadrupole or between the two images required for absorption imaging.

We have three far detuned lasers used as dipole traps. Two red-detuned used for the crossed dipole trap and one blue-detuned laser used for the final trapping:

- A 10 W multi-mode IPG laser at 1070 nm.
- A 8.4 W single-mode Azurlight system 1064 nm laser working at 5 W.
- A 10 W Verdi V_{10} laser from which we separate three arms, for two different vertical beams and one horizontal one.

They are all fiber-coupled to filter the spatial mode and reduce position drifts of the beams.

2.1.4 Magnetic field control

The cooling steps require by themselves a good magnetic field control on the experiment, but the radio-frequency and microwave transitions that we will use in the following require an even better control of it. We first describe here the different coils we have and how they are used in the experiment.
There are 3 large coils (about 1 meter diameter) around the experiment table to compensate residual magnetic fields. Their currents were optimized looking at the isotropy of the "explosion" of the molasses when one removed the laser-cooling beams.
The MOT coils are wound on a water-cooled mount and provide a gradient of 22 G/cm at 20 A. They are powered by a Delta Elektronika SM 7020D power supply.
The quadrupole coils are made of 14 turns of hollow copper wire and are also water-cooled. They stand a current of 400 A which creates a gradient of 240 G/cm. They are powered by two Delta Elektronika SM 15-200D power supplies in parallel. They are conical to maximize the optical access on the science cell. Their current is switched off using an insulated gate bipolar transistor (IGBT). This allows a switching off of the current in about 30 µs. There are still eddy currents after the switching off in the system but we estimate that they have no effect after 2 ms. They are shown together with the MOT coils in figure 2.2 (a).
A particularity of our setup is the *cage system* mounted directly on the science cell (in black figure 2.2 (b)) which holds 10 independent coils: two pairs for the z axis, two pairs for the y axis and one pair for the x axis. All these pairs create about 1G/A at the center of the science cell[a]. The advantage of this configuration is that controlling the two pairs of coils of an axis with two different power supply one can switch from a positive to a negative magnetic field. It is also possible to change the plugging of the coils to switch them from Helmholtz to anti-Helmholtz configuration and create gradients. They are powered by Delta Elektronika ES030-5 specified at 10^{-4} RMS noise in current control. With these power supplies one can reach about 10 G along the y and z directions.

2.2 Absorption imaging of the cloud

Before explaining further our experimental sequence, we first describe the way we probe the atoms.

[a] More turns were done for the pair of the x axis as it is further away.

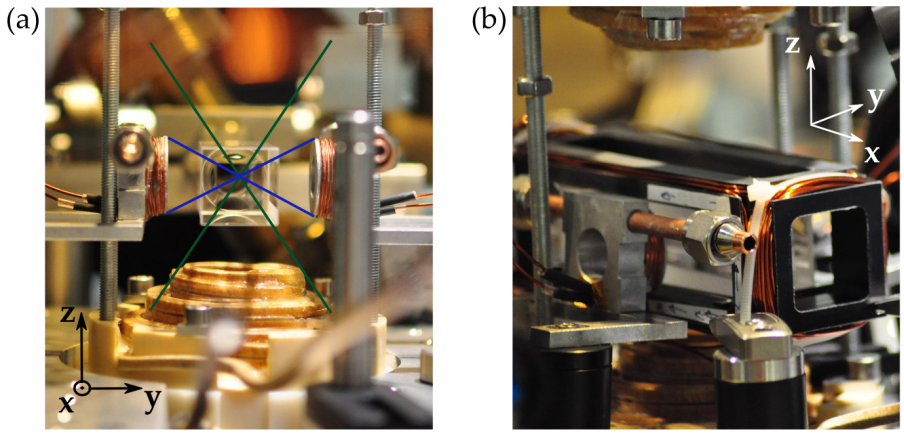

Figure 2.2 *– Main coils of the setup around the science cell. In (a) are shown the MOT coils and one of the quadrupole coils creating the gradients (symbolized in blue and green respectively) and in (b) the cage system holding coils for creating fields in the three directions.*

2.2.1 Brief description

A cloud of atoms in a beam of resonant light scatters a part of it. The principle of absorption imaging is to illuminate the atoms and image their shadow on a camera. The more photons the atoms scatter, the easier it will be to detect atoms[a]. We thus use the $|F = 2\rangle$ to $|F' = 3\rangle$ cycling transition: the atoms cycle between these two states at a certain rate (depending on the intensity of the beam, the detuning, the polarization of the light and the level structure of the atoms) and one can recover the number of atoms in the cloud.
According to the Beer-Lambert law, light travelling along the z direction and passing through a thin sheet of atoms with thickness $\mathrm{d}z$ is absorbed, such that the light intensity is decreased by a small fraction

$$\frac{\mathrm{d}I}{I} = -n(z)\sigma(I)\mathrm{d}z, \tag{2.1}$$

where $n(z)$ is the atomic density in the z plane and $\sigma(I)$ the intensity dependent scattering cross section. Describing simply an atom by a two-level system, and using the optical Bloch equations, the cross section can be written

$$\sigma = \frac{\sigma_0}{1 + I/I_{\mathrm{sat}} + (2\delta/\Gamma)^2}, \quad \text{with} \quad \sigma_0 = \frac{3\lambda^2}{2\pi}, \quad I_{\mathrm{sat}} = \frac{\hbar\omega\Gamma}{2\sigma_0}, \tag{2.2}$$

where λ is the optical wavelength and Γ the linewidth of the excited level. At resonance and in the low saturation limit ($I \ll I_{\mathrm{sat}}$), the integration of (2.1) gives

$$n^{(2\mathrm{D})} = -\frac{1}{\sigma_0}\ln\left(\frac{I_{\mathrm{out}}}{I_{\mathrm{in}}}\right), \tag{2.3}$$

[a]But too many scattered photons also leads to complications which will be studied later.

where $n^{(2D)}$ is the atomic density integrated along z. But the rubidium atom does not have a two-level structure. It is possible to isolate a transition between only two states by imaging with circularly polarized light and polarizing conveniently the atoms [119], but creating perfectly circularly polarized polarized light aligned with the residual magnetic field is not easy. We made the choice to image the atoms with linearly polarized light propagating along the vertical axis, and to use an effective cross-section

$$\sigma_{\text{eff}} = \frac{7}{15}\sigma_0, \tag{2.4}$$

where the 7/15 factor comes from the average of the Clebsch-Gordan coefficients for the π transitions (see appendix C). In a small enough magnetic field, the atoms should indeed spread among all the Zeeman sublevels and all the π transitions have equal probabilities to happen. Note that we described an imaging process for which the atoms have to be in the $|F = 2\rangle$ state. We thus have to repump them from the $|F = 1\rangle$ state prior to imaging, which can be done either optically, or as will be described in section 2.4.4 with a micro-wave pulse.

We note that an often used quantity for experimental images is the optical depth (OD)

$$\text{OD} = -\ln\left(\frac{I_{\text{out}}}{I_{\text{in}}}\right). \tag{2.5}$$

2.2.2 Imaging axes of the setup

We built several imaging paths on the experiment to be able to probe the cloud in different directions. I will describe only the horizontal and vertical ones which are the most used now on the experiment. Two additional Lumenera cameras LM135M are mainly used to image the atoms in the MOT or in the quadrupole.

- The horizontal axis corresponds to the imaging light propagating along the x direction. The absorption picture is taken by a Pixelfly PF-M-QE-PIV with a magnification 3 used in *interframed* mode. This axis allows us to check the vertical confinement of the atoms. An example of picture is shown in figure 2.4 (a).
- For the vertical axis, the imaging light propagates in the z direction (downwards). The absorption picture is taken by a Princeton Instrument PIXIS 1024 Excelon with a magnification of 11 used in *frame-transfer* mode. Its quantum efficiency is of 0.95. This axis has a high numerical aperture of 0.45 thanks to the use of a microscope objective described in the following. The imaging light is linearly polarized and examples of pictures are shown in figure 2.6.

We have in addition 4 Chameleon cameras from Point Grey allowing to monitor the drifts of the different beams. The most used is the one monitoring the position of the accordion fringes which is used for a feedback as explained section 2.3.1. In the next paragraph we focus on the vertical imaging axis which provides the highest quality pictures for the experiment.

2.2.3 Optical resolution of the vertical axis

One difficulty for measuring the optical resolution directly on the setup is that we must look at the resolution of an imaged object at the position of the atoms. The best way would be to use an object of size well below the expected resolution, but we do not have such an object inside the science cell. The simplest way is then to image the atoms directly, but the resolution of the imaging system cannot be isolated from the sharpness of the potential trapping the atoms.
An optical study of the custom made NACHET microscope objectives was nevertheless done in [95] with a calibrated target, which showed that two thin lines spaced by 1 µm could be separated after imaging whereas two lines spaced by 0.75 µm could not. This means that the best resolution we can have on our setup is between these two values. We note that a study of correlations between pixels in section 7.3 leads to an estimation of the resolution of the system. The depth of field of the microscope objectives will also be measured in section 2.3.3.

2.2.4 Calibration of intensity on the atoms

As seen in equation (2.2), the light scattering cross-section of an atom depends on the intensity of the light. To recover the number of atoms from an absorption image, one must thus know the saturation parameter I/I_{sat} in the atomic plane. We calibrated it by measuring the power of the imaging beam before and after the microscope objectives. We measured a loss of power of 40%, which is compatible with attenuations of the beam of 15% through each microscope objective and of 4% on each glass cell interface, as expected.
We note that another method, measuring the momentum transferred to the atoms by the imaging light while varying its intensity as described in [120], could be used to make a better calibration.

2.3 Description of the final trap

We now describe the final trap in which the experiments are done. It is an all optical blue-detuned trap, such that the atoms are in the dark regions of the beams and are thus not heated through spontaneous emission. The beams are schematically represented in figure 2.3.
We create a vertical optical lattice that we call *optical accordion* following the design of [121]. A beam is separated into two beams thanks to the two polarizing beam splitters (PBS), which then interfere in the focal plane of the lens of focal length f_0. The period of the optical lattice can be tuned by moving the incoming beam along the blue arrow of figure 2.3.
Two digital micromirror devices (DMD1 and DMD2) are imaged onto the atoms. One DMD is enough to provide the in-plane confinement. The second one was added to enable other manipulations as will be explained in chapter 8. As the atoms are in the dark regions of the beam, they feel the same potential everywhere in between the walls, and this constitutes a hard-wall flat-bottom trap.

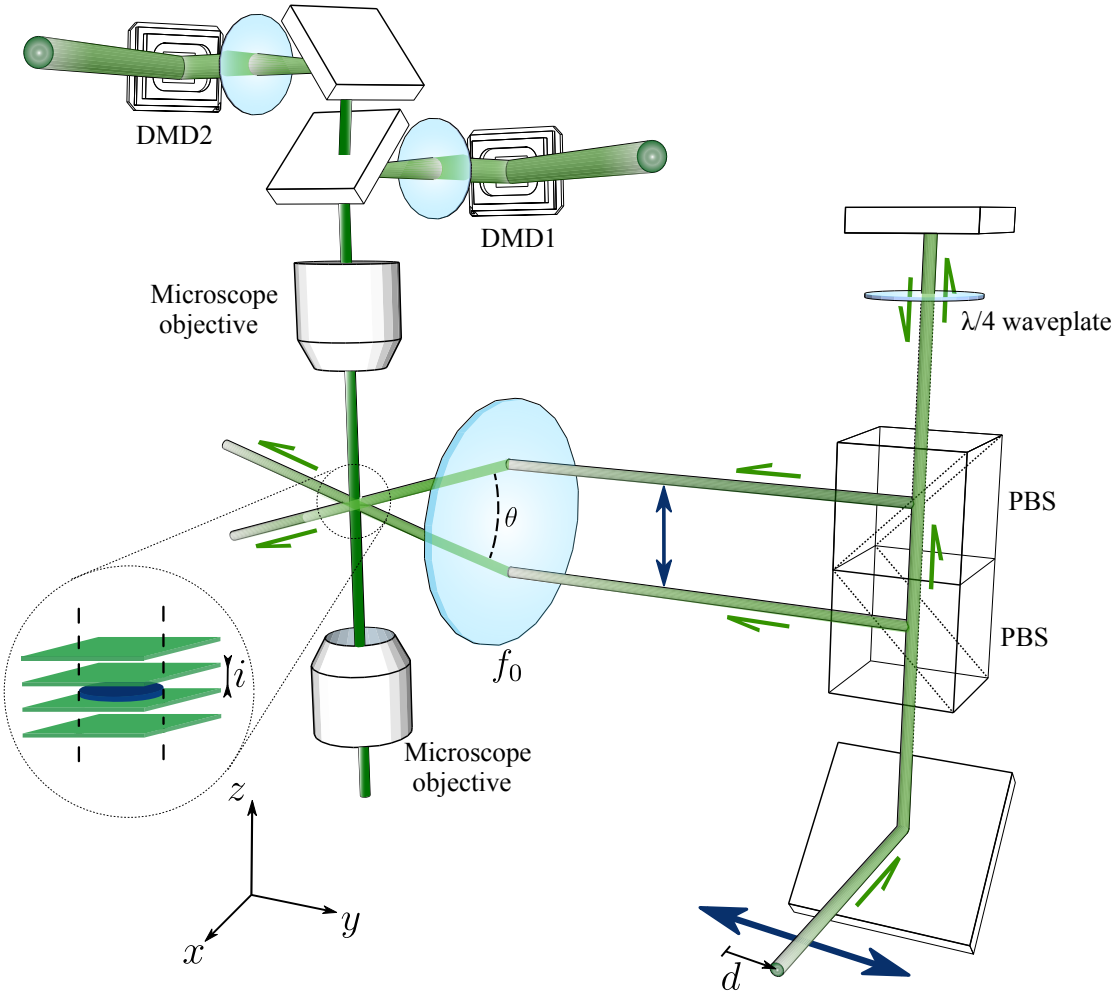

Figure 2.3 *– Schematic view of the whole final trapping setup.*

2.3.1 Loading of the atoms in a single fringe

The loading of the final trap starts from the quasi-pure BEC obtained as described in section 2.1.1. The measured frequencies of the crossed optical dipole trap are 85 Hz vertically and 35 Hz horizontally after evaporation. For 3 10^5 atoms in the condensate, this leads to a vertical Thomas-Fermi radius of about 6 µm. The maximal spacing between two fringes of the accordion being of 12 µm, we are in the limit case where even if the beams are perfectly aligned, shining directly the optical lattice on the BEC tends to populate several planes. This was confirmed experimentally. We thus present the technique that we use to load the atoms in a single node of the accordion.

- The in-plane trapping is first ramped to full power around the BEC in 300 ms.
- One of the dipole arms is then ramped to its maximal power in 125 ms to reduce the vertical size of the cloud[a]. The horizontal size is limited by the in-plane trapping. The other dipole arm is shut down.
- The power of the accordion lattice is then ramped up to its maximum value in

[a]We empirically found that it was better to do it only for one dipole arm rather than for both.

25 ms.

- The power of the remaining dipole arm is ramped down. The atoms are now trapped only by blue-detuned beams.

One advantage of the optical accordion is the possibility to compress the gas along the z direction once the atoms are loaded in a single node of the lattice. As the loading is usually done in the largest spacing configuration, this allows to load a lot of atoms in a single plane without having to remove atoms from the other planes, while keeping a strong vertical confinement after compression. An image of the result is shown in figure 2.4.

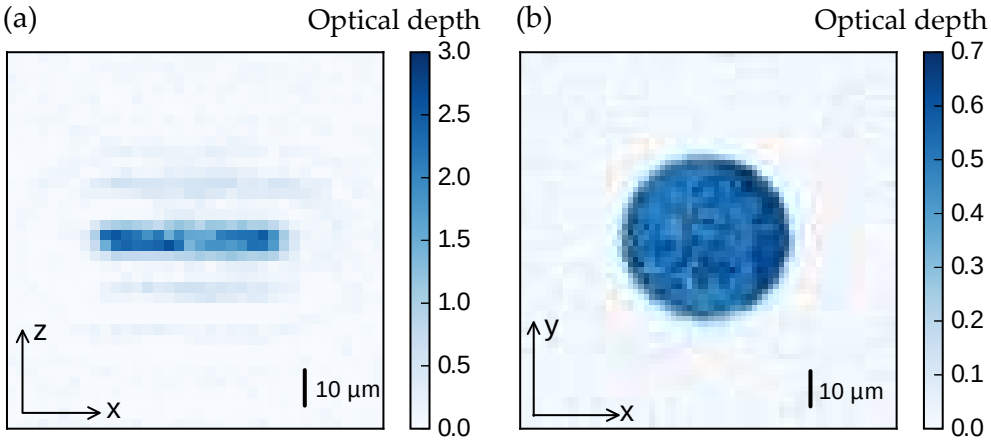

Figure 2.4 *– In situ absorption images from the horizontal axis in (a) and vertical axis in (b). They correspond to the average of 5 and 35 images respectively. For (b), only 3% of the atoms are transferred to the $|F = 2\rangle$ state by a MW pulse to avoid saturating the image. Figures extracted from [116].*

The relative phase between the two beams, which determines the absolute position of the fringes, is controlled by a piezoelectric stack glued on the mirror reflecting the top beam. One problem we had was that during the day the fringes drifted, thus degrading the loading of a single plane. We counter this effect by measuring the position of the fringes at each cycle of the experiment and correcting the drift thanks to a feedback on the piezoelectric stack. This closed-loop control is done in Python and using an ARM mbed.

2.3.2 Compression in the accordion

The characterization of the accordion setup, which was first studied optically by Raphaël [122], has been the object of an article (see [116] or appendix B) after its implementation on the experiment. We only discuss here the strongest vertical confinement reachable in our setup.

To be in the quasi-2D regime, the temperature of the gas has to be low compared to the vertical confinement frequency ($k_{\mathrm{B}}T \ll \hbar\omega_z$). Increasing the confinement thus allows to have gases at higher temperatures and still quasi-2D. Modifying the vertical confinement also changes the strength of the interactions $\tilde{g}$ (as explained in section 1.2.5).

The frequency which characterizes the strength of the vertical confinement is determined as follows. The center of mass (COM) motion of the cloud along the z direction is excited by suddenly changing the power of the accordion beams. We then let the cloud oscillate, and measure the vertical position of the atomic cloud after time of flight (TOF). The trapping frequency is given by a sinusoidal fit of the data as shown in figure 2.5 (a).
We repeated the measurements for different compressions, corresponding to different lattice spacings (from 11 to 2 µm). The results are shown in figure 2.5 (b). We observe an increase of the oscillation frequency from 2.15(5) to 11.2(3) kHz. We also plot in figure 2.5 (b) the expected frequency calculated with the measured power, waists and lattice spacing.

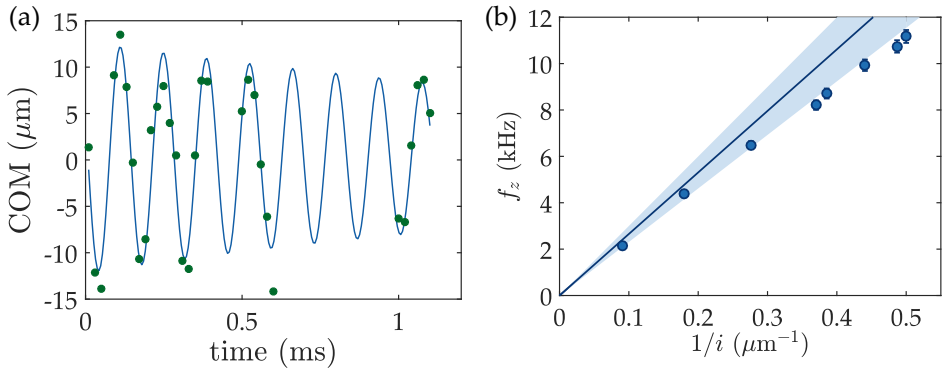

Figure 2.5 *– Measured vertical oscillation frequencies. In (a) is shown an example of measure of frequency after a TOF of 12.7 ms. It leads to a frequency of 7.26(7) kHz. In (b) are shown the frequencies f_z measured for different inverse lattice spacings $1/i$. The solid line is the frequency computed with the independently measured parameters of the beams and the shaded area corresponds to the uncertainty on the calibration of the beam parameters (figure extracted from [116]).*

In practice we did not use such high frequencies for the projects done in this thesis, but the compression was still very useful as it allowed us to reduce the power of the accordion beams while keeping a frequency sufficient to stay in the quasi-2D regime. We found that this procedure reduces inhomogeneities in the potential felt by the atoms due to the accordion.

2.3.3 In-plane confinement: Potentials of arbitrary shape

We now describe the in-plane confinement. As shown in figure 2.3, a blue-detuned beam is reflected on a DMD, and the confinement is provided by the image of the screen of the DMD onto the atoms[a]. The DMD, bought from Vialux[b], is an array of 1024 × 786 micromirrors of size 13.68 µm, which can reflect light in one angle or

[a]There are 2 DMDs on the experiment but we describe only one here. The second one is working the same way.

[b]We bought the DLP V4100 Controller Board from Vialux which drives a 0.7 XGA 2xLVDS DMD by using the Texas Instruments Discovery 4100 chipset.

another one (corresponding to on or off). The magnification between the screen of the DMD and the atomic plane is of 1/70[a], leading to an effective size of a micromirror on the atoms of 0.2 µm, below the optical resolution of the system[b]. The waist of the beam on the atoms when all mirors are on is of 45 µm. For the maximal power, corresponding to about 300 mW on the atoms, the potential height at the center of the beam is thus of $k_B \cdot 6\,\mu K$.
The advantage of using a DMD is that one can tune almost at will the image projected onto the atoms[c]. Examples of single-shot images are shown in figure 2.6.
The mirrors can only be turned on or off, which means that having them in direct imaging, there is no intermediate level: we either send light or no light onto the atoms. But as the effective size of the mirrors is below the optical resolution, one could think that switching on a randomly distributed percentage of the mirrors will average the light and that one could get an intermediate level this way. We did not use this possibility yet, as it requires a correction algorithm to reduce the speckle pattern that results from the diffraction of randomly positioned micromirrors.

Flatness of the potential

The condition for a potential to be flat enough for the gas to be considered homogeneous is that its unavoidable corrugations are small compared to the energy scales of the atomic cloud: temperature and chemical potential. An optical study of the trapping system was realized to characterize the resulting potential [123, 117]. For a disk of 25 µm radius on the atoms, it led to the conclusion that the peak-to-peak variations of the remaining light intensity in the dark zone were less than 5% of the height of the barrier. As the temperature and chemical potential usually correspond to a higher fraction of the barrier, we found that the optical potential should be good enough for the cloud to be approximately homogeneous.
We experimentally found that the atoms were very sensitive to residual magnetic gradients, which is why the projects of the third part of the thesis were done with the atoms in the $|F = 1, m_F = 0\rangle$ state, which is almost insensitive to magnetic fields.
We then found that the main inhomogeneities of the potential came from the accordion beams. Reducing their power seems to improve the flatness of the potential but one has to keep a strong enough vertical confinement to be in the quasi-2D regime. In practice we change the relative power between the two beams thanks to a motorized half-wave plate several times a day to optimize the trapping potential when gases of small chemical potential are used.

Spatial stability

The microscope objective used to image the DMDs onto the atoms is hold by a mount fixed on a breadboard above the experiment. We found that this leads to drifts of the order of 0.2 to 0.3 µm for 2 hours. We remove this drift from the analysis of

[a] This is an estimate from nominal values of the lenses we use. A precise calibration is done in 7.1.

[b] We thus have roughly 25 pixels in the extent of the point spread function.

[c] The DMD could also be used in the Fourier plane, to modify the beam holographically. We chose not to use this technique even if it could lead to a better resolution of the system thanks to wavefront correction, because less power is then transmitted onto the atoms.

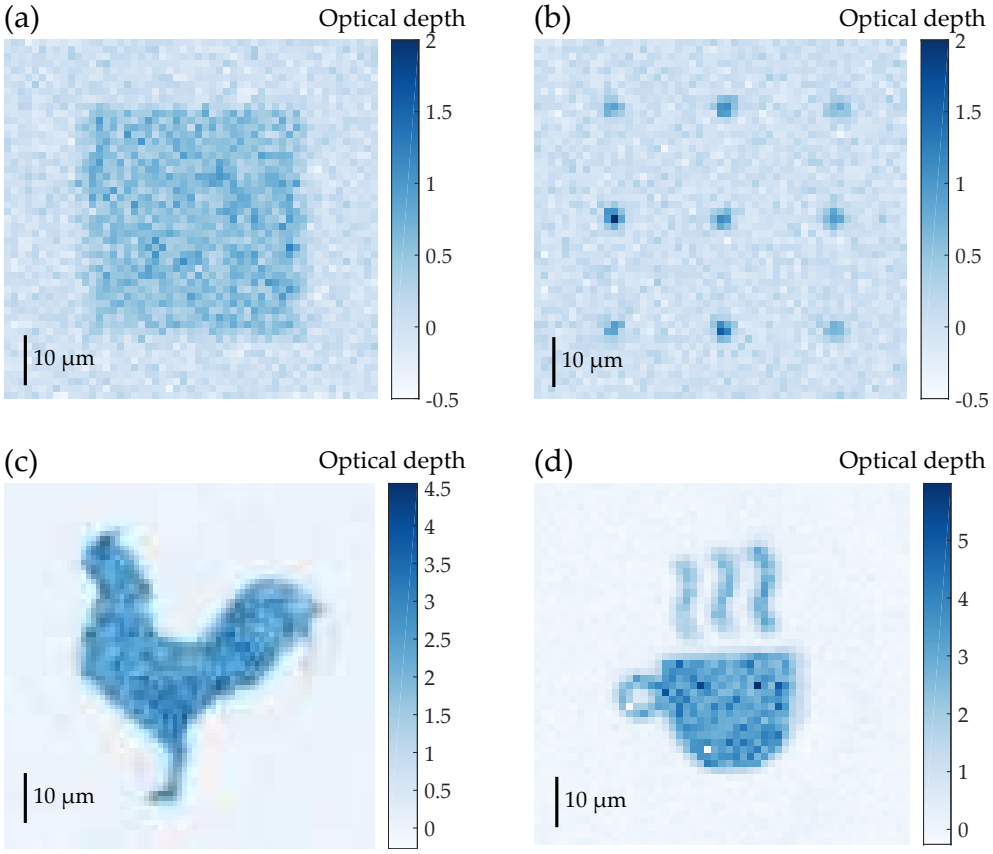

Figure 2.6 *– Result of different in-plane trapping potentials on the atoms. All images are single-shots. Image (a) corresponds to partial imaging of the atoms, as described in section 2.4.4, whereas the three other images correspond to an image of all the atoms.*

the pictures when this is needed by fitting the edges of the cloud and centering the image according to that. This was done for chapter 8.

Could we get tunnelling between adjacent condensates?

It is an interesting feature to know if we could we get tunnelling for sufficiently close condensates. This would allow us to study interesting condensed matter models without adding new lattice beams. A simple way to estimate the tunnelling rate we could get taking into account our resolution is to use the formula found for a sinusoidal potential [23], valid when the recoil energy is small compared to the height of the potential:

$$\frac{J_0}{E_\mathrm{R}} = \frac{4}{\sqrt{\pi}} \left(\frac{V_0}{E_\mathrm{R}}\right)^{3/4} \mathrm{e}^{-2\sqrt{\frac{V_0}{E_\mathrm{R}}}}, \tag{2.6}$$

where J_0 is the tunnelling rate, V_0 the height of the potential, and E_R the recoil energy associated with the lattice. Assuming a distance between two sites of 1.5 µm (corresponding to a recoil energy of $k_\mathrm{B} \cdot 12$ nK) and a height of the potential of $k_\mathrm{B} \cdot 100$ nK, we get a tunnelling rate of 10 Hz. To reach the hundreds of Hz, one would need to put the two condensates closer. We did not try yet to reach this

regime but according to our measured combined resolution this would be clearly at the limit of our system.

Focus and Depth of field of the imaging microscope objective

We studied the depth of field of the imaging microscope objective with the nine dots of figure 2.6b. These samples have a very small size (2×2 µm^2) according to the magnification between the DMD and the atomic plane. It is possible to focus the imaging system by looking at such small samples and fitting their size while moving the imaging microscope objective as shown figure 2.7. Iterating with focussing the in-plane potential thanks to a lens in the DMD path, one can have both systems at focus[a]. This leads to a best fitted waist w of 1.5 µm (fit using e^{-2r^2/w^2}), which combines the resolution of both systems and the size of the pattern trapping the atoms. This focussing also allows us to extract a depth of focus of the microscope objective for the 780 nm light, using

$$w^2(z) = w^2(0)\left(1 + \frac{z}{z_\mathrm{R}}\right), \tag{2.7}$$

where z_R is the Rayleigh length, whose expected value for a coherent beam of waist $w(0) = 1.5$ µm is $z_\mathrm{R} = \pi w^2(0)/\lambda = 9\,\mu\mathrm{m}$. The measured values on figure 2.7 give rather $z_\mathrm{R} = 6\,\mu\mathrm{m}$.

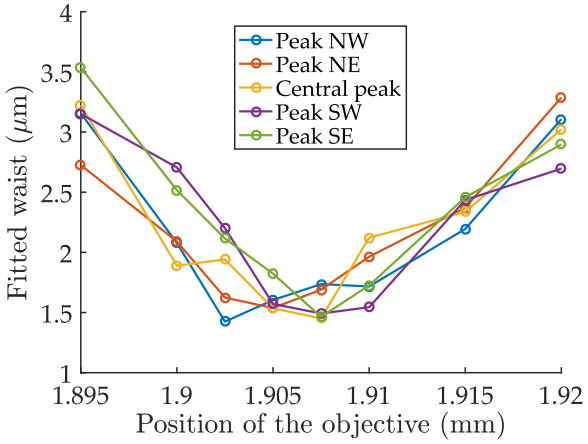

Figure 2.7 *– Fitted waists of five of the nine spots of figure 2.6b for different positions of the imaging microscope objective.*

Vortex detection

We also show that we are able to detect vortices in our setup. Picture 2.8 shows vortices obtained by exciting the cloud with a movie on the DMD, with the gas in the very degenerate regime. The picture is taken after 3 ms of release of the in-plane trapping and 3 ms of time of flight. This gives a good contrast for the vortices. We did not manage to see them in situ, as their size is then comparable to our imaging

[a]We however notice that all 9 spots are not focussed exactly for the same position, due to small misalignments in the optical setup.

resolution. We also note that seeing them around the BKT transition is much harder as the phase and density fluctuations make the image harder to interpret.

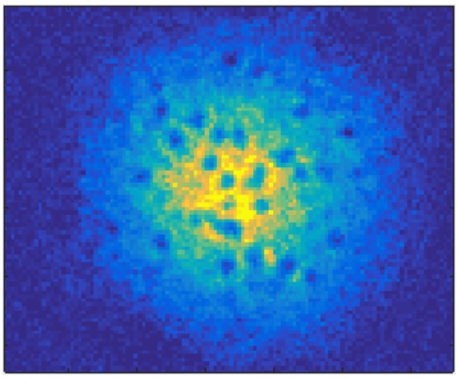

Figure 2.8 *– Example of vortex detection after TOF, with a very degenerate cloud and the gas excited by a movie on the DMD.*

2.4 Manipulation of hyperfine states

One advantage of being in a full optical trap[a] is that one can change the magnetic field on the atoms at will. After loading the atoms in the final trap, they are in the $|F = 1, m_F = -1\rangle$ state. After reminding the hyperfine structure of ^{87}Rb atoms, we describe how we can transfer the atoms between different internal states.

2.4.1 Hyperfine structure and Breit-Rabi formula

An accurate description of the $5^2S_{1/2}$ ground state of ^{87}Rb atoms in a static magnetic field is provided by the Hamiltonian [124]

$$H = A_{\text{hfs}}\mathbf{I}\cdot\mathbf{J} + \mu_{\text{B}}B(g_J J_z + g_I I_z). \tag{2.8}$$

The first term corresponds to the hyperfine interaction between the nuclear angular momentum $\mathbf{I}$ and the electron angular momentum $\mathbf{J}$ with a coupling A_{hfs}, while μ_{B} is the Bohr magneton and g_J and g_I describe the couplings of respectively $\mathbf{J}$ and $\mathbf{I}$ to the magnetic field (here taken along the z-axis). At high magnetic fields, the hyperfine interaction can be neglected and the eigenstates can be labelled as $|m_J, m_I\rangle$. Their energy shift versus magnetic field is shown in figure 2.9 (b).
Since $I = 3/2$ and $J = 1/2$, the total atomic angular momentum $\mathbf{F} = \mathbf{J} + \mathbf{I}$ can take the values $F = 2$ and $F = 1$. At low magnetic fields, the hyperfine interaction has to be taken into account and the eigenstates are the $|F, m_F\rangle$ states. Computing perturbatively their energy shift versus magnetic field leads to the Zeeman effect

$$\Delta E = \mu_{\text{B}} g_F m_F B, \tag{2.9}$$

[a] The vertical confinement is strong enough to hold the atoms against gravity.

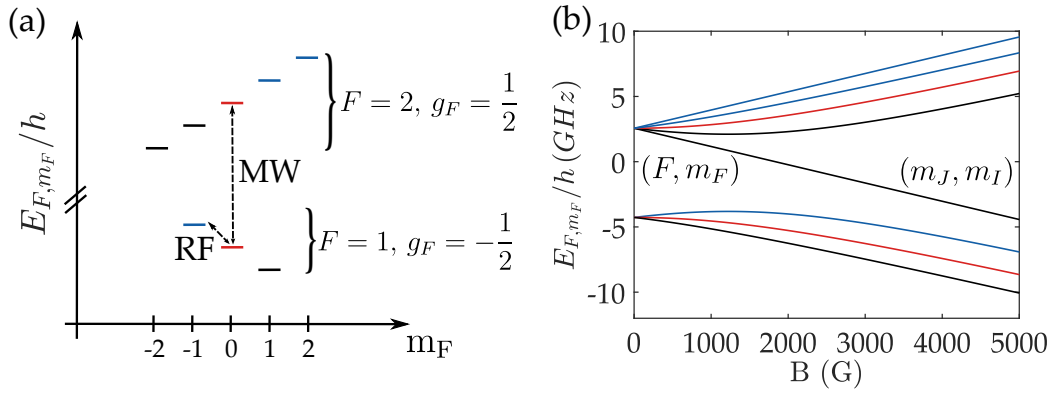

Figure 2.9 *– Energy levels of the $5^2S_{1/2}$ ground state of ^{87}Rb atoms. In (a) is shown the limit of small magnetic fields also known as the Zeeman effect. The magnetically trappable states are shown in blue and the ones insensitive to magnetic fields at first order in red. In (b) is shown the full solution, with for small magnetic field the good quantum numbers being F, m_F and for high magnetic fields m_J, m_I.*

with $g_F = \pm 1/2$, as depicted schematically in figure 2.9 (a).
In the intermediate regime, the eigenstates have in general to be solved numerically, but in the case $J = 1/2$ an analytical solution can be found, called the *Breit-Rabi formula*:

$$E_{F,m_F} = -\frac{E_{\text{hfs}}}{2(2I+1)} + \mu_B g_I m_F B \pm \frac{E_{\text{hfs}}}{2} + \left(1 + \frac{4m_F\xi}{2I+1} + \xi^2\right)^{1/2}, \qquad (2.10)$$

$$\text{where} \quad \xi = \frac{\mu_B(g_J - g_I)B}{E_{\text{hfs}}}.$$

Here $E_{\text{hfs}} = A_{\text{hfs}}(I + 1/2)$ and the energies E_{F,m_F} are measured with respect to the "center of gravity" of the hyperfine levels. This formula[a] allows to plot the energy levels for all magnetic fields as shown in figure 2.9 (b).
It also allows to compute second order effects in magnetic field. It leads for example to a quadratic shift of 525 Hz/G^2 for the clock transition $|F = 1, m_F = 0\rangle \rightarrow |F = 2, m_F = 0\rangle$ and of 72 Hz/G^2 for the $|F = 1, m_F = 0\rangle \rightarrow |F = 1, m_F = -1\rangle$ and the $|F = 1, m_F = 1\rangle \rightarrow |F = 1, m_F = 0\rangle$ transitions.

2.4.2 Stabilisation of the magnetic field

Working in the center of Paris has its advantages but also some drawbacks. While implementing the micro-wave (MW) transfers on the experiment, we noticed that it did not work for certain shots, and that this did not happen during the night. We thus found out that this was due to the 10$^{\text{th}}$ line of the metro (or to the RER B) which passes closeby and creates variations mainly on the vertical magnetic field.
We compensate these variations by implementing an open-loop correction on the vertical magnetic field. We use a Bartington probe in a room next to the experiment

[a] There is a sign ambiguity which has to be taken into account as in [125].

to monitor the ambient magnetic field. The signal obtained is used to control the current flowing in the vertical coils of the cage system described in 2.1.4. Without compensation, the peak-to-peak variations of the magnetic field measured on the experiment were of 15 mG, and 2.6 mG RMS, whereas after compensation it is of 1.8 mG peak-to-peak, and 0.31 mG RMS. These measurements were done during one hour in day time.

2.4.3 Radio-frequency transfers

In a flat bottom optical potential, any gradient of magnetic potential would make the atoms fall to one side of the box if their chemical potential is low. This is why we chose to work with the $|F = 1, m_F = 0\rangle$ state which is insensitive to magnetic fields. As shown in figure 2.9, the transfer from $|F = 1, m_F = -1\rangle$ to $|F = 1, m_F = 0\rangle$ corresponds to a radio frequency (RF).

To make this transfer, the RF field is provided by the same antenna as the one of section 2.1.1 used for the evaporation in the quadrupole trap. As can be seen in figure 2.9, the energies of the two transition between the $|F = 1\rangle$ states are degenerate, which makes it impossible to transfer the totality of the atoms towards only one other state. We thus have to lift the degeneracy thanks to the quadratic Zeeman shift discussed in section 2.4.1. Applying a 10 G field as we do separates the two transitions by 14.4 kHz.

But the low Rabi frequency obtained for this transition made the efficiency of the transfer too low due to residual variations of the magnetic field. We thus chose to use a rapid-adiabatic-passage by making a sweep of the RF frequency to transfer the atoms more efficiently. We found the best parameters to be a sweep of 22 kHz, starting around 5.865 MHz and reducing the frequency in 40 ms.

Performing a Stern-Gerlach measurement, we can extract the populations in the different states after the sweep. One can then optimize the transfer by tuning the starting frequency of the sweep, as shown figure 2.10.

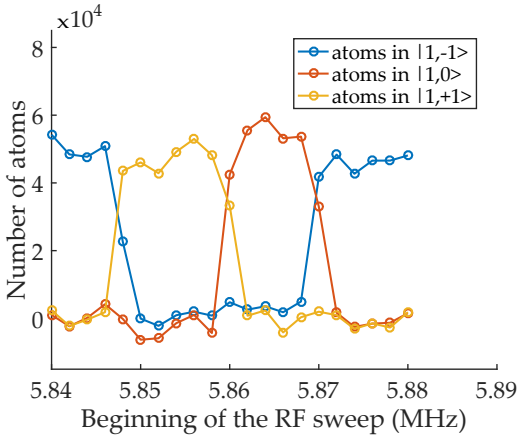

Figure 2.10 *– Number of atoms in the different Zeeman states after the RF sweep for different starting frequencies*

2.4.4 Micro-wave transfers

We saw in section 2.2 that the atoms have to be in the $|F = 2\rangle$ state to be imaged. A first way to transfer them from the $|F = 1\rangle$ state in which they are at the end of the experimental sequence is to use an optical repumper, which sends light resonant with the $|F = 1\rangle$ to $|F' = 2\rangle$ transition. This way they can decay only to $|F = 1\rangle$ and $|F = 2\rangle$ states and they are optically pumped to the $|F = 2\rangle$ state. But this transfers momentum to the atoms, which can be enhanced a lot by induced dipole-dipole coupling. A direct effect of this acquired momentum is to "blur" the edges of the cloud on the camera, making them less sharp as they are in reality.
Another method, which circumvents this problem, is to drive the transition directly at the good frequency. This constitutes a very useful tool as will be seen in the next. When a two-level system is driven at its transition frequency, it undergoes the well-known Rabi oscillation[a]. Its state is a coherent superposition of the two unperturbed eigenstates, and the probability to be measured in state $|2\rangle$ if the system starts in state $|1\rangle$ varies with time as

$$P_{1\to 2} = \frac{\Omega^2}{\Omega^2 + \Delta^2} \sin^2\left(\frac{\sqrt{\Omega^2 + \Delta^2}t}{2}\right), \tag{2.11}$$

where Ω is the Rabi frequency and Δ the detuning of the driving beam to the transition. Performing these oscillations on an ensemble of atoms, with for example the $|F = 1, m_F = 0\rangle$ and $|F = 2, m_F = 0\rangle$ states leads to oscillations of the atom number measured in $|F = 2\rangle$ following the same formula, as shown in figure 2.11.

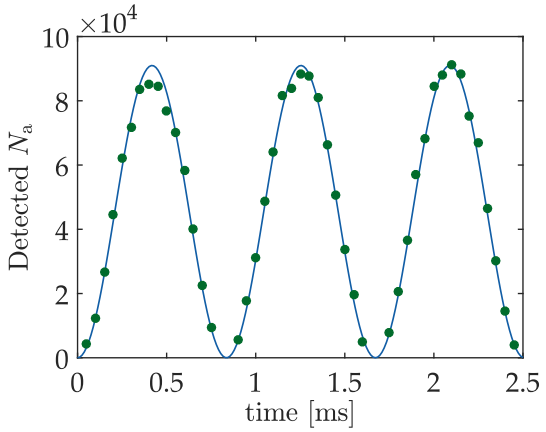

Figure 2.11 *– Number of atoms measured in $|F = 2\rangle$ for different durations of MW pulse at resonance. The atom number is measured after TOF to avoid induced dipole-dipole effects. The data are fitted following equation 2.11.*

The micro-wave (MW) field is generated as the sum of a signal at 6.8 GHz done with an oscillator (NEXYN NXPLOS 0680-02778) and the one of a controllable function generator (Tektronix TDS 1002). The sum is done the same way as described in [126]. The signal is then sent to a 10 W amplifier (Kuhne KU PA 7000), and radiated onto

[a] A brief description from the framework of perturbation theory is done in appendix C.

the atoms through an antenna which controls its polarization. We had it polarized along x for the projects of the second part of the thesis and polarized along z for the projects of the third part.

The time during which the MW is applied onto the atoms has to be very precise. The amplifier has an internal switch but it seems that it has to be switched on at least 10 ms before the sending of the signal so that the power is the desired one. We thus added two switches (ZYSWA 2-50DR) for the two signals from the Tektronix generator which precisely control the duration of the MW pulses. The Rabi frequency is dependent on the power sent onto the atoms, on the polarization of the wave, but also on the Clebsch-Gordan coefficients which are shown in appendix C.

Choosing the time during which the MW is sent allows to choose the fraction of atom transferred to the $F = 2$ state. This technique thus allows to perform partial-transfer absorption imaging [127]. The idea is to repump to a light sensitive state only a small fraction of atoms, which are then in the same spatial mode as the whole cloud. Due to the low density of atoms sensitive to light, problems of saturation of optical depth (mainly due to multiple scattering effects as will be described chapter 4) are avoided. It also allows precise measurements of the magnetic field on the atoms[a]. Changing the power of the radiated MW we manage to tune the Rabi frequency of the $|F = 1, m_F = 0\rangle$ to $|F = 2, m_F = 0\rangle$ transition between 20 kHz and 80 Hz.

2.5 Crossing the condensation threshold of the gas

While the Bose-Einstein condensation threshold is very clear in 3D harmonic traps, where a bimodal fit after TOF gives a good indication of the fraction of condensed atoms, this is less obvious in 2D uniform traps. Looking along the vertical axis, one indeed expect the condensate to fall 'as a brick' during the TOF, without much modification of its shape in the plane[b], whereas the thermal atoms should expand. The resulting profile is then the sum of the shape of the condensate and of the convolution of the initial position of the thermal atoms with the gaussian profile of their thermal expansion during the TOF. This makes a bimodal fit rather difficult, and the determination of a condensation threshold not obvious.

The condensation can be investigated through the presence of interference fringes between two adjacent condensates. Such interference fringes will be shown in chapter 6, but a precise determination of a threshold is still hard with this method as contrast reductions can also be due to the method of detection. We thus first explain the way we chose to vary the degeneracy of the system, and then describe a tool which reveals the crossing of the BEC transition.

[a] Following a magnetic-field dependent transition while changing the homogeneous bias field on the cloud, we were able to measure precisely the position of the center of the quadrupole. We found that it is 85 µm above the final trap. We also did some Ramsey measurements to measure residual magnetic field gradients on the cloud, which are not described here.

[b] The condensate expands a lot vertically due to the strength of the confinement, but this is the direction of integration while taking the picture.

2.5.1 Blasting

To change the phase-space density $\mathcal{D}$ of the system, we chose to keep the gas at roughly the same temperature as the one reached by evaporation, reduce the atom number and let the remaining atoms thermalize. This can be done by transfering a part of the atoms to the $|F = 2\rangle$ state with a MW pulse, and then to blast them with a resonant light beam. The momentum they acquire by absorbing several photons makes them leave the trap. The remaining atoms in $|F = 1\rangle$ are insensitive to the light and are still trapped. The result of this method on the degeneracy of the gas is shown via the condensate focussing technique described below. It will also be used in chapter 8 with a more precise measurement of $\mathcal{D}$.

2.5.2 Making a thermal 2D Bose gas

It is not a simple task to realize a thermal 2D Bose gas. The gas should indeed not be condensed, but its temperature T should still be well below the vertical frequency of the accordion times h/k_{B}.
A simple way we could think of is to reach a temperature below 200 nK, then stop the evaporation and wait long enough so that atoms leave the trap (due to collisions with residual particles of the vacuum for example), thus reducing D. But this random removing of atoms leads to cooling of the gas due to the bosonic statistics of the atoms (see [128, 129]). We thus chose to use the blasting method. We proved its efficiency to create a thermal two-dimensional Bose gas using the condensate focussing technique.

2.5.3 Condensate focussing

The problem of doing a simple TOF to extract the momentum distribution of the atoms is that one needs it to be very long so that the initial position distribution has no large effect. We describe here another method, used in [130, 68, 131, 69, 115, 132], called condensate focussing and allowing in principle to extract exactly the momentum distribution. The idea is to let the atoms evolve in plane in a harmonic potential so that after a quarter of oscillation period, the position distribution of the atoms reflects their initial momentum distribution.

Principle

The mapping of the in-plane momentum distribution and the in-plane position distribution can be understood with a simple classical harmonic oscillator model. This model works well for describing the in-plane motion of a 2D Bose gas since the interaction between atoms is greatly suppressed soon after the optical lattice is turned off. Noting r the in-plane radial position of an atom, its equations of motion with an initial velocity $\dot{r}(0)$ and an initial position $r(0)$ in a harmonic potential are

$$r(t) = r(0)\cos(\omega_r t) + \frac{\dot{r}(0)}{\omega_r}\sin(\omega_r t), \tag{2.12}$$

$$\dot{r}(t) = -r(0)\omega_r \sin(\omega_r t) + \dot{r}(0)\cos(\omega_r t), \tag{2.13}$$

where ω_r is the horizontal trapping frequency of the confining harmonic potential. At the focused time $t_f = \pi/2\omega_r$, one gets

$$m\dot{r}(0) = m\omega_r r(t_f), \tag{2.14}$$

$$\omega_r r(0) = -\dot{r}(t_f). \tag{2.15}$$

From equations 2.14 and 2.15, we see that the initial radial momentum-space distribution is mapped onto the coordinate-space distribution at the focused time t_f, and vice versa, with a scaling factor $m\omega r$.

Implementation

We created this harmonic potential on the experiment using the already present quadrupole coils. The attractive potential felt by the atoms in $|F = 1, m_F = -1\rangle$ is indeed proportional to the quadrupolar magnetic field $\boldsymbol{B}$

$$\boldsymbol{B} = b' \begin{pmatrix} -x/2 \\ -y/2 \\ z \end{pmatrix}. \tag{2.16}$$

At fixed z, and noting $r = \sqrt{x^2 + y^2}$, one then get that the potential for the atoms is of the form

$$V \propto \sqrt{z^2 + \frac{r^2}{4}}, \tag{2.17}$$

which can be developped if $r \ll z$,

$$V(r) \propto z \left(1 + \frac{r^2}{8z^2}\right). \tag{2.18}$$

This constitutes a harmonic potential, at least at this order. We note that as the vertical optical lattice has to be removed during the evolution in the harmonic potential (to remove interactions), the atoms have to be levitated. This can also be done by the quadrupole field, but it fixes the value of the vertical magnetic gradient b'.

For the other groups who implemented this method, the harmonic potential was already present during the sequence, whereas it cannot be for us as we want the atoms to be in a uniform trap. We thus transfer the atoms which are in the $|F = 1, m_F = 0\rangle$ state for the trapping, to the $|F = 2, m_F = 1\rangle$ just before removing the optical lattice. This way the quadrupole field can always be present but is felt by the atoms only when we want them to evolve in the harmonic potential. Examples of images taken before and after this condensate focussing are shown figure 2.12.

The high peak of figure 2.12 (b) shows an accumulation of atoms in the lowest momentum state, which is a signature of Bose-Einstein condensation. We plot in

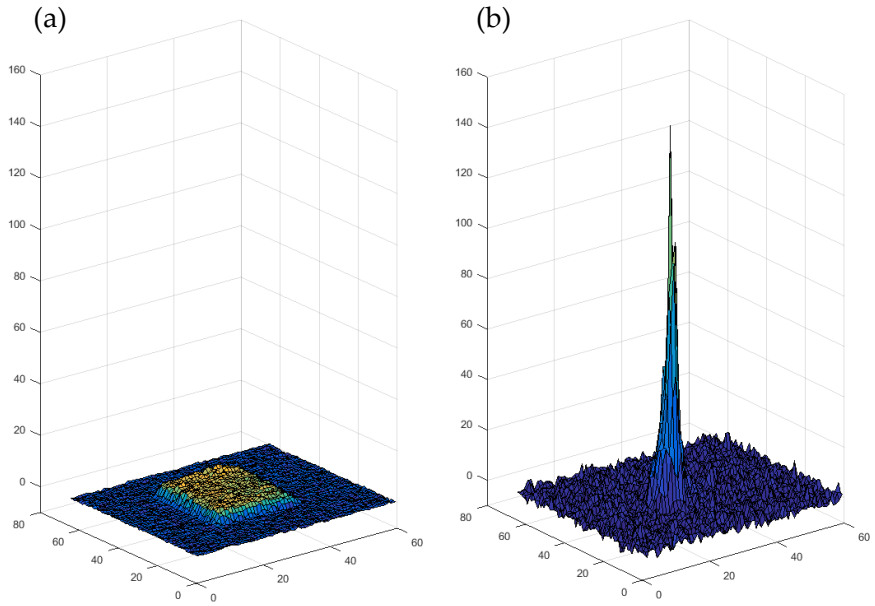

Figure 2.12 *– In-situ (a) and after condensate focussing (b) images of a very degenerate gas in a rectangular box. The OD displayed is obtained using partial-transfer absorption imaging and rescaled according to the duration of the MW pulse.*

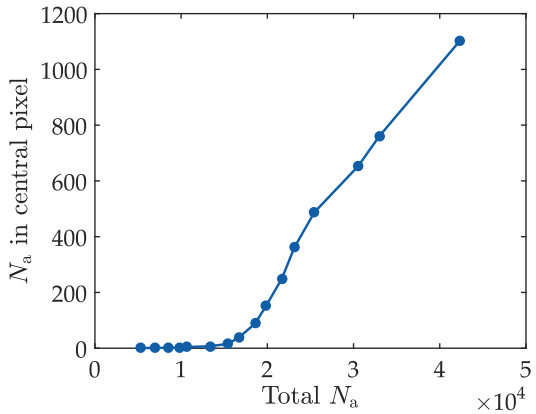

Figure 2.13 *– Number of atoms in the central pixel after condensate focussing.*

figure 2.13 the number of atoms in the central pixel. This allows us to qualitatively see a difference of behaviour around the transition.

This method can be pushed further [133], to extract for example the temperature of the gas. But in our case, the vertical expansion of the atoms due to the strong confinement combined with the short depth of field of the microscope objective prevented us to extract quantitative information about the temperature of the gas. We will nevertheless see how we plan to improve this method in the prospective

experiments section 9.3.1. We now describe other methods we used which give a more quantitative determination of the degeneracy of the system.

2.6 Thermometry of the gas

We want to be able to characterize precisely the degeneracy and the temperature of the gas. The degeneracy will in particular be very important for chapter 8 where it will be varied and the speed of sound measured for its different values. The temperature is also an important parameter as for the gas to be quasi-2D, its temperature has to be well below the frequency of the vertical confinement, $k_{\mathrm{B}}T \ll \hbar\omega_z$.

2.6.1 Difficulty for the uniform 2D Bose gas

The usual way in cold bosons experiments to measure a temperature is to look at the atom distribution after TOF and to fit the thermal wings with a Boltzmann or Bose distribution. This works nicely at high temperature, but when the system is degenerate one has to separate the condensate part from the thermal atoms part. This works still nicely in 3D as the shape of the saturated Bose distribution, fitting the thermal atoms, depends only on the temperature (It is a good approximation to fix the fugacity z to one). But in 2D uniform infinite systems, there is no saturation of the Bose distribution, and the shape of the momentum distribution depends on two parameters: the temperature T and the chemical potential μ.
In our case the finite size of the system restores a condensation but it is not clear that this should allow to fix z at one. Furthermore, in the presence of a condensate due to the finite size of the system, we already said that the atomic distribution after TOF is the sum of the shape of the condensate and of the convolution of the initial position of the thermal atoms with the profile of their thermal expansion during the TOF. To avoid the condensed atoms which should not be included in the profile of the thermal atoms, one thus has to fit only in the wings of the distribution. This reduces the signal compared to harmonically trapped 2D Bose gases (for which the condensate occupies a smaller region), and the fits are rather unstable [134].

2.6.2 Improved thermometry

We present here the method we were using at the time of the projects of chapters 4, 5 and 6. Another method used for the project of chapter 8 will be presented in section 8.4.2.
To circumvent the problem of a condensed part in the atoms profile after TOF, we use a "thermometer" as done in [135]. In the final trap, we repump with a MW pulse from a $|\mathrm{F}=1\rangle$ to a $|\mathrm{F}=2\rangle$ state a fraction of the atoms and let them thermalize with the rest of the cloud[a], for a time of about 500 ms.
We then release all atoms and image them without further repumping. We thus only see the repumped atoms which thermalized and are thus at the same temperature as

[a] As the repumped atoms are not in the same hyperfine state we are not using magnons as in [135] but this does not make a difference as long as we checked that the two species mix together.

the rest of the cloud. The repumped fraction is chosen such that we have enough signal after a TOF of typically 8 ms, and an atom number in the thermometer below the condensation threshold of the temperature. This way the image can be fitted by a Bose-Einstein distribution of the momenta of the atoms, without a condensate spoiling the central part.
As the TOF are not long enough to remove all initial size effects, we computed the expected profiles for different temperatures and fugacities with all the atoms initially confined in a disk of radius 20 µm as in the experiment. We then compare the experimental profile to all the computed profiles and find the closest one. An example is shown figure 2.14 (a). The problem is that the two parameters of the fit T and z are very coupled, as can be seen in figure 2.14 (b). They form a valley of low χ^2 in the μ, T plane and this is not enough to find the correct temperature. We thus coupled these measurements to an in situ measurement of the atom number[a]. This way, one can find along the line corresponding of the measured atom number the lowest χ^2. We use the equation of state of an ideal gas, in red in figure 2.14 (b). This gives plausible temperatures for different heights of in-plane confinement powers. But the method is not so easy to implement as the repumped fraction must remain small so that the measurement does not perturb too much the system.

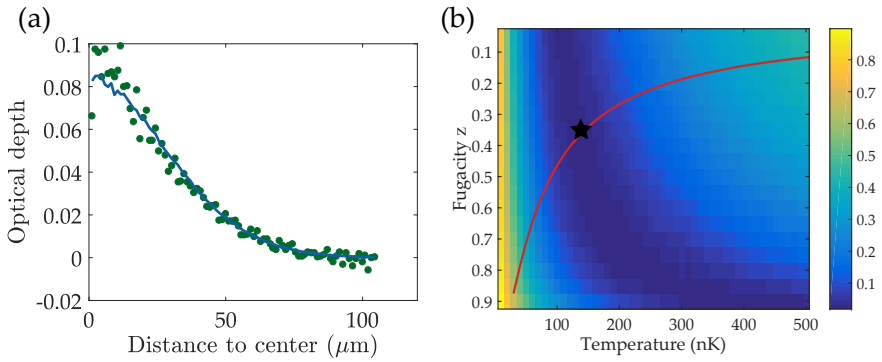

Figure 2.14 *– An example of result of the thermometry. 10 images are required for this thermometry. The profile in (a) is an azimuthal average of the data after a TOF of 8.7 ms, together with its best fitted profile. In (b) is shown the distance of the fit to the data (a.u.). The red line corresponds to the measured atom number in the z, T plane. The small black star shows the best fit along this line, giving the fugacity and temperature of the thermometer.*

[a]The atom number was here measured with the cross section $\sigma_{\text{eff}} = \frac{7}{15}\sigma_0$.

II Light scattering

3

About light scattering by atomic clouds

3.1 Introduction

The interaction of light with matter is a very broad subject, whose description should be able to explain the colour of the sky as well as the amplification of light in a laser, or the behaviour of an atom strongly coupled to photons [136, 137, 138]. Its current understanding allows to create materials and devices with tailored properties, from quantum information systems such as memories [139] and nanophotonic optical isolators [140] to solar cells combining highly absorptive materials with transparent electrodes [141].

Different descriptions, considering the wave or particle nature of light, and the matter as a homogeneous medium or constituted of randomly positioned scatterers have been developed. In the view of point scatterers, the "multiple scattering" regime corresponds to a regime in which a photon scatters on several particles. All effects arising because of multiple scattering of photons in a sample are grouped in the term of "collective effects". But some are more trivial than other, and more vocabulary is needed to separate them.

The color of the sky is for example explained by the dependence with the light wavelength of elastic scattering of photons by small particles [142]. Considering the electric and magnetic fields, light propagation through an homogeneous medium can be well described by the generalized Maxwell equations, considering an effective refractive index in the medium. However some phenomena need a more complex description of light-matter interaction to be understood.

Among such fascinating phenomena are superradiance, corresponding to the emission of light by a collection of scatterers faster than for a single scatterer, which has been observed in very different kind of materials such as HF gas [143], Rydberg atoms [144], Fe nuclei [145] and dilute clouds of cold atoms [146, 147, 148] and its counterpart subradiance which has been observed in [149] and [150]. A prediction of these phenomena in the case of a sample smaller than the light wavelength was done by Dicke in his seminal paper [151].

Another interesting effect is the coherent backscattering (CBS), a robust interference effect arising when coherent light is shone on a sample. It consists in a peak of scattered light in the reversed direction of the exciting beam, due to interfering paths of photons. This effect has been observed in a variety of media, such as powder suspensions [152, 153], biological tissues [154] as well as with laser-cooled atomic gases [155, 156].

In the point of view of electro-magnetic fields, and if their intensity is low compared

to the saturation intensity of the atoms, the field emitted by an isolated atom is proportional to the exciting field, and takes the form of a dipolar radiation[a]. Light scattering then arises due to the response field of each dipole to the driving field, but also due to dipole-dipole interactions that arise from the exchange of virtual photons between dipoles. The dipole-dipole interaction term has a dispersive (real) part, which is responsible for collective level shifts, and a radiative (imaginary part) giving rise to line broadening and collective superradiant emission [157]. We note that even for an isolated single atom, virtual photons due to vacuum fluctuations modify the energy levels of the atom, which is known as the *Lamb shift* [158]. When several atoms are put close enough together, some virtual photons might be exchanged between the atoms, leading to a *cooperative Lamb shift* [159], observed for example in [160, 161, 145]. The link between this shift and superradiance has also been verified experimentally in [145]. This motivates spectroscopic studies to search for "non-trivial" collective effects in light scattering. We note that these interactions are also responsible for the Rydberg blockade [162, 163, 164, 165].
In this part of the thesis, the transmission of light through a slab of ultracold atoms is experimentally studied (chapter 4), as well as the propagation of photons inside the slab (chapter 5). The slab is uniform, sub-wavelength thick and has an aspect ratio of more than 1:100. The atomic density is typically 10^{14} cm^{-3}, which makes it a dense sample even if much less dense than condensed matter systems. However in condensed matter systems, all the incident light is not scattered. A fraction is absorbed by the sample, which complicates the interpretation of results. For systems of molecules as well, some energy might be transferred to excitation of rotational levels which cannot occur for atoms. We now focus only on non-absorptive materials, for which all photons have to be re-emitted at a wavelength close to the incident one, as is the case for atomic clouds in vacuum.
The aim of this introductory chapter is to discuss briefly some results of theory of light scattering to understand better the important challenges of the domain, and explain where our experiments sit compared to other groups.

3.2 Modelling light scattering

Before describing different modellings, it is useful to detail the difference between the coherent and incoherent part of the scattered light. We will then describe three often used models.

3.2.1 Response of a single dipole

The response of a single atom to an electromagnetic field is well known [166]. If the intensity of the incoming beam is low compared to the saturation intensity, an atom i at $\boldsymbol{r}_i$ in an electric field $\mathbf{E}_0$ radiates a field whose value at $\boldsymbol{r}$ is given by

$$\mathbf{E}_i(\boldsymbol{r}) = \alpha[\mathbf{G}(\boldsymbol{r} - \boldsymbol{r}_i)] \cdot \mathbf{E}_0(\boldsymbol{r}_i), \tag{3.1}$$

where α is the atom polarizability defined as

[a] We consider here a $J_g = 0 \rightarrow J_e = 1$ transition.

$$\alpha = 6\pi \mathrm{i} k^{-3}/(1 - 2\mathrm{i}\delta/\Gamma), \tag{3.2}$$

where k is the light wavelength, δ is the detuning of the light and Γ the linewidth of the transition. The $[\mathbf{G}]$ term corresponds to the Green's function[a] of an oscillating dipole for polarized light. It is a 3×3 tensor, of value

$$\mathbf{G}_{\alpha\beta}(\boldsymbol{r}) = -\frac{1}{3}\delta(\boldsymbol{r})\delta_{\alpha\beta} - \frac{k^3}{4\pi}\frac{\mathrm{e}^{\mathrm{i}kr}}{kr}\left[\left(1 + \frac{3\mathrm{i}}{kr} - \frac{3}{(kr)^2}\right)\frac{r_\alpha r_\beta}{r^2} - \left(1 + \frac{\mathrm{i}}{kr} - \frac{1}{(kr)^2}\right)\delta_{\alpha\beta}\right], \tag{3.3}$$

where α and β are the indices. The terms in $1/r^2$ and $1/r^3$ correspond to near-field terms and the one in $1/r$ to a far-field term.
We now look at the resulting field when several dipoles are put together, and define from this microscopical approach a coherent and incoherent part.

3.2.2 Coherent and incoherent parts

From point scatterers: microscopic approach

Before describing the main possible modelisations of light scattering, we do a small calculation following the lines of [167] which is instructive to understand the difference between coherent and incoherent scattering.
We consider N dipoles placed at the positions $\{\boldsymbol{r}_i\}_{i=1,\dots,N}$, in an incoming field $\mathbf{E}_0(\boldsymbol{r})$. We assume that each of these dipoles independently radiates the field $\mathbf{E}_i(\boldsymbol{r})$ given in Eq. (3.1). This corresponds to a case where each photon is scattered by an atom at most once, and constitutes the *single-scattering approximation*.
The total field at a point $\boldsymbol{r}$ is then

$$\mathbf{E}_\mathrm{S}(\boldsymbol{r}) = \sum_i \mathbf{E}_i(\boldsymbol{r}), \tag{3.4}$$

where $\mathbf{E}_i(\boldsymbol{r})$ is given in equation (3.1). The Poynting vector can be calculated from

$$\mathbf{S}_\mathrm{S}(\boldsymbol{r}) \propto \mathbf{E}_\mathrm{S}(\boldsymbol{r}) \cdot \mathbf{E}_\mathrm{S}^*(\boldsymbol{r}). \tag{3.5}$$

This must then be averaged over many samples of the gas[b]. Terms of the form $\exp(\mathrm{i}(\boldsymbol{k}_\mathrm{init} - \boldsymbol{k}_\mathrm{final}) \cdot \boldsymbol{r}_j)$ for photons incoming with the wave vector $\boldsymbol{k}_\mathrm{init}$ and leaving with $\boldsymbol{k}_\mathrm{final}$ on the atom at $\boldsymbol{r}_j$ average to zero over disorder. This leads to

$$8\pi\overline{\mathbf{S}_\mathrm{S}(\boldsymbol{r})} \propto N(N-1)|\overline{\mathbf{E}_i(\boldsymbol{r})}|^2 + N\overline{\mathbf{E}_i(\boldsymbol{r}) \cdot \mathbf{E}_i^*(\boldsymbol{r})}. \tag{3.6}$$

The first term corresponds to coherent scattering. It results from adding the fields of different scatterers and is thus proportional to N^2. It is principally emitted in the forward direction, and the bigger the sample the narrower the cone of emission. Due to these properties, it is sometimes called coherent forward scattering. In absorption

[a] impulse response of the Maxwell equations.
[b] The overline denotes averaging over disorder, or over many realizations of the sample.

imaging, it is this part which interferes destructively with the probe beam, resulting in the "shadow" of the cloud[a]. The second term corresponds to incoherent scattering, for which the intensities radiated by the atoms are summed. It is thus proportional to N.

From Maxwell equations: macroscopic approach

This separation between a coherent and incoherent part is also visible from a macroscopic point of view. Consider the propagation of an electromagnetic wave in a random medium characterized by a fluctuating dielectric constant. We split the field into a mean field $\overline{\mathbf{E}}$ and a fluctuating component $\delta\mathbf{E}$

$$\mathbf{E} = \overline{\mathbf{E}} + \delta\mathbf{E}, \tag{3.7}$$

with $\overline{\delta\mathbf{E}} = 0$. If the random medium is statistically homogeneous, the mean field satisfies a propagation equation in a homogeneous effective medium with an effective refractive index n_{eff} [170]

$$\nabla^2\overline{\mathbf{E}} - n_{\text{eff}}^2 k^2 \overline{\mathbf{E}} = 0, \tag{3.8}$$

where k is the wave-vector of light in vacuum. In this case the mean field behaves as a wave in a homogeneous medium, which is why it is called the coherent component. This corresponds to the framework of macroscopic electromagnetism [171]. Computing the intensity of the field from equation (3.7), one gets

$$I = \overline{\mathbf{E}\mathbf{E}^*} = |\overline{\mathbf{E}}|^2 + \overline{|\delta\mathbf{E}|^2} = I_{\text{coh}} + I_{\text{incoh}}. \tag{3.9}$$

The first term corresponds to the mean field, thus to the coherent intensity. The second term corresponds to the energy of the fluctuations of the field, and thus to the incoherent intensity.
It is worth noting that the two parts also have very different attenuations for light propagating in an homogeneous medium. The coherent field is attenuated following the Beer-Lambert law, *ie* in $\exp(-z/\ell_{\text{sc}})$ where ℓ_{sc} is the scattering mean free path of a photon in the medium. The incoherent field however is radiated over the whole space, the power must thus decrease as $1/z^2$ and the field decreases as $1/z$.

3.2.3 Modelling of the coherent part: dielectric approach

In the macroscopic electromagnetism framework, the response of the medium to an electric field is characterized by its polarization $\mathbf{P}$, that expresses the density of induced electric dipole moments in a dielectric material. It is assumed to be linear in the electric field, with a dimensionless proportionality constant χ called the susceptibility of the medium:

$$\mathbf{P} = \varepsilon_0 \chi \mathbf{E}. \tag{3.10}$$

[a]This has been shown experimentally in [168, 169]. The authors managed to separate the driving field from the field emitted by the atoms by switching off quickly the driving field. The used transition has a narrow linewidth making the observation of the field radiated by the atoms possible. It appeared as flashs of light when the driving field was switched off.

If the system is dilute enough, its susceptibility χ is related to the atomic polarizability α and the atomic density ρ through

$$\chi(\omega) = \rho\alpha(\omega). \tag{3.11}$$

This does not take into account any effect from the rest of the sample, and for dense samples a first mean field correction has to be introduced. The question is how do all the other atoms in the medium affect the local response in a part of the medium. An elegant way to derive this mean field correction can be found in [172], chapter 11. The idea is to isolate by thought a sphere in a dielectric sample driven by an electric field. The field in the sample can be decomposed as $\mathbf{E}_{\text{tot}} = \mathbf{E}_{\text{hole}} + \mathbf{E}_{\text{sphere}}$. The field of a uniformly polarized sphere is $\mathbf{E}_{\text{sphere}} = -\mathbf{P}/3\varepsilon_0$, leading to $\mathbf{E}_{\text{hole}} = \mathbf{E}_{\text{tot}} + \mathbf{P}/3\epsilon_0$. The effective field felt by an atom in the sample is then $\mathbf{E}_{\text{hole}}$. This leads to a mean field correction of the susceptibility

$$\chi(\omega) = \frac{\rho\alpha(\omega)}{1 - \rho\alpha(\omega)/3}, \tag{3.12}$$

known as *Clausius-Mosotti* or *Lorentz-Lorenz equation*. The corresponding refractive index $n_{\text{eff}} = (1+\chi)^{1/2}$ is the quantity entering in equation (3.8). One sees from this equation that the real part of χ induces a modification of the phase of the incident field in the forward direction, whereas its imaginary part corresponds to the damping of the intensity, describing the diffuse scattering of light. In this representation, the incoherent scattering is thus just treated as absorption, making this model unable to describe fluorescence light (for example observed perpendicularly to the incoming beam).

To describe the propagation of light one has to solve Maxwell equations in and out the sample using the refractive index. A pioneering work has been done by Mie [173], but it is rare that analytical solutions can be found. One then requires finite elements methods to simulate any geometry. One could think that the approximation of a continuous medium is only valid for dense systems. It can in fact sometimes be better for dilute samples, as they do not suffer from decoherences induced for example by Van der Walls interactions between close dipoles [174].

It is possible from this model to extract a frequency shift of the resonance line compared to the single-atom case. The predicted shift is the so-called *Lorentz-Lorenz shift* and is to the red:

$$\Delta_{\text{LL}} = -2\pi\frac{\rho\Gamma}{2k^3}. \tag{3.13}$$

The consistency of this approach to study light scattering in the forward direction can be shown by comparing the result of this model to the one of an assembly of point-like dipoles. The authors of [167] computed analytically the field radiated by an assembly of atoms whose positions are governed by a gaussian probability density function, and without interactions between dipoles (thus corresponding to equation 3.4). They computed the average outward energy flux (average over many samples of the gas) similarly as equation (3.6). They showed that this flux in the forward direction is exactly the same as the one computed for a continuous material of similar gaussian shape and of polarization $\mathbf{P}(\boldsymbol{r}) = \varepsilon_0\alpha\rho(\boldsymbol{r})\mathbf{E}(\boldsymbol{r})$.

3.2.4 Modelling of the incoherent part: random walk approach

As shown in 3.6, the incoherent part corresponds to the sum of intensities radiated by the atoms. It can then be modelled by a random walk (RW) of incoherent photons which jump between scatterers. It is important to distinguish between the two notions of *multiple scattering* and *recurrent scattering*. The *multiple scattering* regime is reached as soon as photons scatter in average on several atoms, but as shown figure 3.1, one can consider only paths for which the photon cannot jump back to the atoms it comes from. On the opposite, for *recurrent scattering* one can allow this back and forth. This definition is important as non-trivial effects are expected in the recurrent scattering regime.

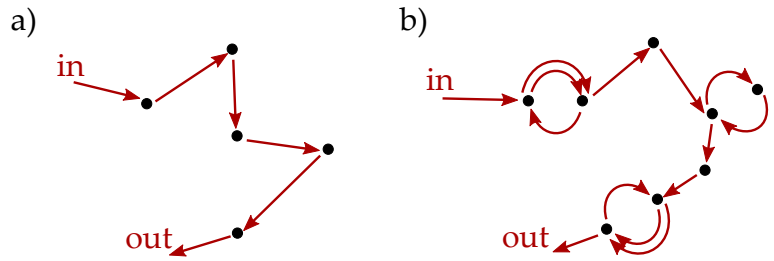

Figure 3.1 *– Schematic drawing of paths of photons. In a) the photon scatters between atoms but never goes back on the same atom. In b) the photon sometimes goes back on the same atom, which constitutes the recurrent scattering regime.*

Numerical simulations can be done directly with random walks of photons [175, 157, 176]. An example extracted from [175] is shown figure 3.2 and will be compared to another model.
Alternatively, the incoherent part can be modelled as a radiative transfer [177, 178], in which the photons obey a diffusion equation of diffusion constant

$$D_0 = \ell_{\mathrm{sc}}^2/3\tau_{\mathrm{tr}}, \tag{3.14}$$

where ℓ_{sc} is the scattering mean free path of a photon and τ_{tr} is the transport time, corresponding to the average time delay between two successive scattering events[a].

3.2.5 "Full" Modelling: coupled dipoles approach

A widely used approach to describe the radiation of an assembly of dipoles is the so-called coupled dipole simulations (CD). It corresponds to an exact solution of the steady-state field radiated by $\mathrm{J_g} = 0 \rightarrow \mathrm{J_e} = 1$ (4 levels) dipoles in the low intensity limit[b]. Practically, one has to set the position of the dipoles, and solve a $3N \times 3N$ linear system to get the radiated field, where N is the number of considered dipoles.

[a] We note that this model can be improved to include weak localisation effects [179], but this is beyond the scope of this chapter.

[b] A model including all energy levels of ^{87}Rb D2 line atoms has also been developped in [180], but is limited to smaller atom numbers.

The equations are derived in more details in [181, 157], but very briefly, using equation 3.1, the total field $\mathbf{E}_{\text{tot}}(\boldsymbol{r}_i)$ at the position of dipole i has to satisfy the self consistent equation

$$\mathbf{E}_{\text{tot}}(\boldsymbol{r}_i) = \mathbf{E}_0(\boldsymbol{r}_i) + \alpha \sum_{j \neq i} [\mathbf{G}(\boldsymbol{r}_i - \boldsymbol{r}_j)] \cdot \mathbf{E}_{\text{tot}}(\boldsymbol{r}_j). \tag{3.15}$$

This leads to a set of $3N \times 3N$ equations for the $3N$ unknown quantities $\mathbf{E}_{\text{tot}}(\boldsymbol{r}_i)$, that can be solved numerically for each set of positions of the dipoles. The total field can then be computed at any position as

$$\mathbf{E}_{\text{tot}}(\boldsymbol{r}) = \mathbf{E}_0(\boldsymbol{r}) + \alpha \sum_{j} [\mathbf{G}(\boldsymbol{r} - \boldsymbol{r}_j)] \cdot \mathbf{E}_{\text{tot}}(\boldsymbol{r}_j). \tag{3.16}$$

Averaging over a big enough set of positions of the dipoles, one can extract the coherent and incoherent scattered intensities.
The advantage of this model is that it takes interactions between dipoles at all orders into account, thus including recurrent scattering. One can even introduce the motion of the atoms in it as done by [182, 157]. However, due to the size of the matrix which has to be inverted, it is limited to at most 10^4 atoms. One often must then perform finite size-scaling to compare to experimental results [182, 157, 148], which will be discussed in section 3.3.3. This advantage might also be a drawback as this model does not explain the origin of the seen effects.
One thus has to compare the results of different models to extract the physical causes. The figure 3.2 extracted from [175] shows the comparison between the computed radial photon scattering from an incoherent random walk (RW) and from a coupled dipole (CD) simulations in the same conditions. The two models agree well except on a forward lobe at $\theta = 0$ and on the narrow cone in the backward direction. The forward lobe is explained by the coherent term of equation 3.6, also called forward scattering. The backward narrow cone however, corresponding to coherent back scattering (CBS), cannot be recovered neither with the incoherent RW nor with the dielectric approach, and requires a more sophisticated model.

Expansion in scattering orders

Equation (3.15) can be written in a matricial form [183] as

$$(I - \mathcal{G})\underline{\mathbf{E}_{\text{tot}}} = \underline{\mathbf{E}_0}, \quad \text{with} \quad \mathcal{G} = \alpha \sum_{j \neq i} [\mathbf{G}(\boldsymbol{r}_i - \boldsymbol{r}_j)], \tag{3.17}$$

and $\underline{\mathbf{E}_{\text{tot}}}$ and $\underline{\mathbf{E}_0}$ big vectors containing the $3N$ components of the effective electric field acting on the j^{th} atom.
Developing the inverse of the matrix of equation 3.17 corresponds to a development in scattering orders:

$$\mathbf{E}_{\text{tot}}(\boldsymbol{r}) = (I + \mathcal{G} + \mathcal{G}^2 + ...)\mathbf{E}_0(\boldsymbol{r}), \tag{3.18}$$

or writing explicitly the propagators

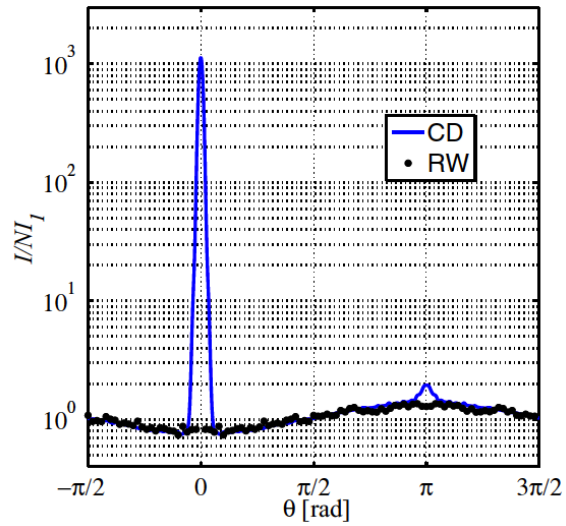

Figure 3.2 – *Comparison between the computed radial photon scattering from an incoherent random walk (RW) and from a coupled dipole (CD) simulations of a gaussian cloud. The angle $\theta = 0$ corresponds to the forward direction and $\theta = \pi$ to the backward direction. Figure extracted from [175].*

$$\begin{aligned}\mathbf{E}_{\text{tot}}(\boldsymbol{r}_j) =& \mathbf{E}_0(\boldsymbol{r}_j) + \alpha \sum_{m\neq j} [\mathbf{G}(\boldsymbol{r}_j - \boldsymbol{r}_m)]\mathbf{E}_0(\boldsymbol{r}_m) \\ &+ \alpha^2 \sum_{m\neq j} [\mathbf{G}(\boldsymbol{r}_j - \boldsymbol{r}_m)] \sum_{\ell\neq m} [\mathbf{G}(\boldsymbol{r}_m - \boldsymbol{r}_\ell)]\mathbf{E}_0(\boldsymbol{r}_\ell) + ...\end{aligned} \tag{3.19}$$

This constitutes another method for solving (3.15) when the series converge. This development is used for example in [181, 183]. The authors of [183] also showed that by taking the second scattering order, they recover the coherent back scattering, which was not present taking only into account the first order.
It is also possible to select only terms of the series including two atoms as:

$$\begin{aligned}\mathbf{E}_{\text{tot}}(\boldsymbol{r}_j) =& \mathbf{E}_0(\boldsymbol{r}_j) + \alpha \sum_{m\neq j} [\mathbf{G}(\boldsymbol{r}_j - \boldsymbol{r}_m)]\mathbf{E}_0(\boldsymbol{r}_m) \\ &+ \alpha^2 \sum_{m\neq j} [\mathbf{G}(\boldsymbol{r}_j - \boldsymbol{r}_m)][\mathbf{G}(\boldsymbol{r}_m - \boldsymbol{r}_j)]\mathbf{E}_0(\boldsymbol{r}_j) \\ &+ \alpha^3 \sum_{m\neq j} [\mathbf{G}(\boldsymbol{r}_j - \boldsymbol{r}_m)][\mathbf{G}(\boldsymbol{r}_m - \boldsymbol{r}_j)][\mathbf{G}(\boldsymbol{r}_j - \boldsymbol{r}_m)]\mathbf{E}_0(\boldsymbol{r}_m) + ...\end{aligned} \tag{3.20}$$

which allows to compute two geometrical series as

$$\begin{aligned}\mathbf{E}_{\text{tot}}(\boldsymbol{r}_j) = \mathbf{E}_0(\boldsymbol{r}_j) + \sum_{m\neq j} \Bigg\{ &\left[\frac{\alpha^2\mathbf{G}^2}{1-\mathbf{G}^2}\right](\boldsymbol{r}_m - \boldsymbol{r}_j)\mathbf{E}_0(\boldsymbol{r}_j) \\ &+ \left[\frac{\alpha\mathbf{G}}{1-\mathbf{G}^2}\right](\boldsymbol{r}_j - \boldsymbol{r}_m)\mathbf{E}_0(\boldsymbol{r}_m)\Bigg\} + ...\end{aligned} \tag{3.21}$$

All recurrent scattering terms between two atoms are thus taken into account, but only scattering processes including up to two atoms are considered. This constitutes a perturbative approach in second order in density. This is what is done analytically for continuous atomic distributions in [184] and in section 4.2.1.

3.2.6 Definition of "cooperative effects"

We claim in the two next chapters that induced dipole-dipole interactions have a significant effect in our samples. The terminology of "collective" and "cooperative effects" is not very well established, and might even be different between areas where light diffusion is studied. Two recent papers [167, 185] propose to make a difference between the two. The authors of [167] want to qualify as cooperative only the effects which cannot be recovered by "the mean field approach of traditional optics".
We describe here one simple case for which one could have thought seeing cooperative effects, whereas it is explained by traditional optics. This illustrates as they write, that "the limit between independent-atom response, mean field, and cooperative behaviour is not easy to draw, even in theory".
Going back to equation (3.6), one notes that the light scattered in the forward direction is enhanced as N^2 with N the number of atoms. This could be reminiscent of the Dicke cooperative regime, and one could think that this enhancement is a cooperative effect. But this is obviously not the case because we just added the fields from independent radiators. Here this enhancement is simply due to a phase matching between scatterers, fully predicted by a mean field dielectric approach.
The authors of [167, 185] thus emphasize the importance of performing RW and dielectric approaches in the same geometry to compare to the experimental results, and then check if the seen effects can be called cooperative or not.

3.3 Experimental investigations and interpretations

We now turn to some experimental investigations on atomic clouds in various groups and their agreement or disagreement with different models, to put in perspective the studies made in our group in the next two chapters.

3.3.1 Different experimental investigations

Light scattering experiments are conducted by sending a beam of light onto a sample of atoms. The main observables are then the fluorescence of the cloud and the transmission of the probe beam through the cloud. Looking at the fluorescence corresponds to probing the incoherent part of the scattered light. In our first article (Chapter 4 and [186]), we looked at the absorption of the probe, thus looking mainly at the coherent part. In our second article (Chapter 5 and [187]), we focus on the incoherent part.
The measurements usually consist of scans of the frequency of the probe. The resulting profile is then fitted by a Lorentzian function from which one can extract a maximum, a width and a shift of the resonance.

Several cold atom experiments study light scattering, allowing for comparisons of rather close systems but in a wide range of densities, optical depths, geometries and temperatures. For light scattering studies, the temperature has to be compared to the linewidth of the transition. More precisely, if the Doppler broadening, $k\bar{v}$ where k is the wave vector of the transition and $\bar{v}$ the rms velocity of the atoms is smaller than the linewidth transition Γ, the sample is said homogeneously broadened, whereas if $k\bar{v} > \Gamma$, it is inhomogeneously broadened and a loss of coherence is expected. We give some numbers for the different regimes studied.

- For atomic clouds, the highest densities are reached in hot atomic vapours as in the group of of Charles Adams in Durham [160]. The densities are very large (up to 10^{16} cm^{-3}) and using very thin cells one can keep a low optical depth (OD). The samples are inhomogeneously broadened.
- The opposite regime is the one of atoms trapped in a MOT as in the group of Robin Kaiser in Nice [150, 147]. There the atoms are cold and at very low density (10^{11} cm^{-3}) and very large OD (up to 30). The samples are homogeneously broadened.
- Higher densities, still for cold atoms are found in the groups of Mark Havey [188, 148] and Jun Ye [182], reaching 10^{12} cm^{-3}.
- Finally, homogeneously broadened samples at quite high densities (10^{14} cm^{-3}) are found in the group of Antoine Browaeys [189, 190, 180] for samples smaller than the light wavelength or in thin slabs of typically $20 \times 20 \times 0.3\,\mu$m in our group.

As stated earlier, only the coherent part of the beam can be modelled by a dielectric approach. We note that rather close effects are seen on fluorescence or absorption experiments [189, 180], and we will in the following consider mainly modelling of the coherent part.

3.3.2 About the shifts of the resonance

The cooperative Lamb shift (CLS) is a cooperative optical effect that is intimately connected with the phenomenon of superradiance [145]. A very convincing measurement of it has been reported in [160]. The CLS originates from the exchange of virtual photons between atoms and contrary to the Lorentz-Lorenz shift, it depends on the geometry of the sample. It has been computed for the case of a thin slab in [159]:

$$\Delta_{\mathrm{CLS}} = -|\Delta_{\mathrm{LL}}| + \frac{3}{4}|\Delta_{\mathrm{LL}}|\left(1 - \frac{\sin 2k\ell}{2k\ell}\right), \tag{3.22}$$

where Δ_{LL} is Lorentz-Lorenz red shift of equation (3.13) and ℓ is the width of the slab. Coupled dipoles simulations have been performed in [191] for the geometry of the experiment of [160], and the numerical result was in disagreement with 3.22 and with the experimental results. The reason for this disagreement is that some correlations present in the simulations are washed out in the experiment of [160] because the sample is inhomogeneously Doppler broadened due to the high temperature of the atoms. Taking into account this inhomogeneous broadening in the simulations by shifting the resonance frequency of each atom by a Gaussian random variable, one

can recover the CLS.
The role of Doppler broadening has been tested experimentally in [182]. Using two different transition lines of their cloud of ^{88}Sr atoms, the authors show that even simple interference effects such as forward scattering are washed out by inhomogeneous broadening.
We note that recently, in [167], the CLS was recovered theoretically but this time using a mean field theory. The authors then interpret this as an "etalon effect", making this shift not anymore a "cooperative effect" according to their definition.

Recovering the blue shift theoretically for a slab

It is possible to compute the susceptibility of the gas one order further in density than section 3.2.3. This corresponds to including all the recurrent scattering terms between two atoms of the development (3.19) using the computation of series of (3.21). It is done analytically for a homogeneous distribution in [184], and leads in general to

$$\chi(\omega) = \frac{\rho\alpha(\omega)}{1 - \rho\alpha(\omega)/3 + \beta(\omega)}, \tag{3.23}$$

where $\beta(\omega)$ is the contribution of recurrent scattering and might be challenging to compute for some geometries [180]. This term will be computed numerically in section 4.2.1 for the slab geometry, and has strong effects in our range of densities. In particular, even if it still corresponds to a mean field theory as it is a modification of the refractive index, it predicts a blue shift, compatible with the coupled dipoles prediction for low enough densities.

3.3.3 Finite-size scaling for coupled dipoles

The authors of [157] computed analytically with averaging over disorder the field emitted by a dilute spherical sample up to the third term of equation 3.19 (thus including up to two scattering events for a photon), neglecting the polarization. They found that the resonance profile should be Lorentzian, with the line broadening being a function of ρR, R being the size of the sample, and the frequency shift a function of ρ. This is the starting point for the finite-size scaling that they use for their coupled dipoles simulations, ρR being proportional to the OD and ρ being the density.
The multiple scattering increases when the size of the medium is increased, whereas the recurrent scattering does not. The latter increases only when the density is increased. As just stated, it seems that some effects depend on the OD (such as the line broadening) whereas other ones depend on the density (such as the shift of the resonance frequency). Some effects are thus more linked to first-order multiple scattering, whereas other rely on the occurrence of recurrent scattering.
The relevant parameters for the different effects are important for the finite-size scaling required to compare coupled dipoles simulations to experiments. The scalings are done in [182] the following way. As the OD scales as $N/(kR)^2$ whereas the density scales as N/R^3, they rescale their results as $N^{1/2}$ if the OD is kept constant or as $N^{1/3}$ if the density is kept constant [157].

For the thin slab geometry, as is the case for us, the density and the OD have the same scaling in $N^{1/2}$. This explains the linear behaviour in $N^{-1/2}$ found empirically in section 4.2.2.
Coupled dipoles simulations with the appropriate finite-size scaling seem to fit the experimental data for the groups of Mark Havey [148] and Jun Ye [182]. They do not match however for the group of Antoine Browaeys [180] and our group (see section 4.3). The problem might however be different for [180] as due to their low atom number they can simulate the whole system with the CD. It is then the 12-levels modelisation (which corresponds to the hyperfine structure of ^{87}Rb) they use which might not capture all the physics here. Switching to two-levels atoms by using a strong magnetic field as they did however seems to lead to a better agreement between experiment and CD simulations [192].

3.3.4 About "cooperative effects" in MOTs

Before concluding this introductory section to light scattering in atomic clouds, we will briefly discuss the interesting case of experiments realized in MOTs in the group of Robin Kaiser.
It is not obvious that one could observe super or subradiance in such low-density systems as MOTs. If one considers simply two dipoles for example, super or subradiant behaviours are expected only if the separation between the two is on the order of the light wavelength.
For quantities which can be defined in steady state in a bulk medium, it is clear that the relevant parameter is the atomic density. For transient phenomena involving light escaping however, one can understand that the size of the sample should play a role. It turns out in this case that the relevant parameter becomes the OD. One can even get some understanding of why some atoms have to radiate together in certain conditions for dilute samples. We follow here the argument of [185]. Consider a sample of finite size R radiating in free space. The diffraction limit restricts the divergence of modes efficiently coupled to the sample to be bigger than $\theta \approx 1/(kR)$ or to a solid angle bigger than $1/(kR)^2$. This limits the number of modes in which the system emits efficiently to be of the order of $M \approx (kR)^2$. If the number of atoms N in the sample exceeds M, some atoms have to radiate in the same mode, which corresponds to some cooperativity. Note that the parameter N/M corresponds to the OD for a 3D system.

3.4 Conclusion

The interaction of light with matter is a complicated problem, but recent experimental and theoretical developments for clouds of atoms allow precise comparisons between theoretical models and experiments. From the theory side it is however still not clear what should be called cooperative or not, and further discussions between different communities are still needed.
The experiments we describe in the two next chapters are probing a new regime, obtained using a dense, homogeneously broadened, uniform sample in a slab geometry

with a 1:100 aspect ratio. The high quantum efficiency and the low noise of the camera allow us to measure very low photon numbers and to track the propagation of photons in the slab.
One problem of our experiments however is that due to the high density, atoms feel important Van der Walls forces as soon as they are excited. It is possible to give an estimate of theses forces using a two atoms model. The separation in energy between the two new eigenstates of the system of one atom excited in the direction orthogonal to r and one in the ground state is of the order of

$$\Delta E_{\pm} \propto \mp \frac{\hbar\Gamma}{(kr)^3}. \tag{3.24}$$

The corresponding force between the two atoms while one is in the excited state is then

$$|\mathbf{F}| \sim -3\frac{\hbar\Gamma}{r(kr)^3}. \tag{3.25}$$

The atoms spend an average time on the order of Γ^{-1} in the excited state. The velocity acquired during this time is

$$v \sim \frac{|\mathbf{F}|\Gamma^{-1}}{m} \sim 3\frac{v_{\text{recoil}}}{(kr)^4}, \tag{3.26}$$

with v_{recoil} the speed acquired by an atom when it absorbs a photon, which is of 6 mm/s for ^{87}Rb. Pictures of this effect with velocities up to 10 cm/s (corresponding to about 150 atoms/µm^2) can be found in [117], chapter 5. This leads to non-negligeable motion of the atoms during the time of probing which is on the order of 10 µs. One could of course think of reducing this probe time, but it was needed to have a good enough signal to noise ratio. Similar problems might be encountered for the experiments of [182] for which the times of probing are between 50 and 100 µs. The experiments of [180] circumvent this issue by using very short pulses of 300 ns. It would be interesting to explore this track and switch to shorter pulses (and thus another method of detection) if further investigation of this topic had to be performed on our setup.

4

Study of light transmission

The study of dipole-dipole interactions described in the previous chapter requires large densities of scatterers. Achieving these densities is concomitant with a vanishingly small transmission $\mathcal{T}$ of the light through the sample. It is therefore desirable to switch to a 2D or thin slab geometry as we are able to prepare in order to investigate the physical consequences of these resonant interaction effects at the macroscopic level.
In this chapter, we study the transmission of nearly resonant light through uniform slabs of atoms. We report experiments realized on a dense layer of atoms with a tunable density and thickness. For dense clouds, the transmission is strongly enhanced compared to the one expected from the single-atom response. We also observe a broadening and a blue shift of the resonance line on the order of the natural linewidth. This blue shift contrasts with the mean-field Lorentz-Lorenz red shift and is a signature of the strongly-correlated regime reached in our system because of dipole-dipole interactions [191]. To our knowledge, it is the first time that a blue shift is reported. In addition, we observe deviations of the resonance lineshape from the single-atom Lorentzian behavior, especially in the wings where the transmission decays more slowly. We model this system with coupled dipole simulations complemented by a perturbative approach which qualitatively supports our observations. After describing our experimental system in Sec. 4.1, we investigate theoretically light scattering for the geometry explored in the experiment in Sec. 4.2. In Sec. 4.3 we present our experimental results and compare them with theory. We conclude in Sec. 4.4.

4.1 Experimental methods

The sections of this chapter were initially published in [186], and are reproduced without modifications.

4.1.1 Cloud preparation

We prepare a cloud of ^{87}Rb atoms with typically $N = 1.3(2) \times 10^5$ atoms in the $|F = 1, m_F = -1\rangle$ state. The atoms are confined in an all-optical trap, described in more detail in [116], with a strong harmonic confinement in the vertical direction z with frequency $\omega_z/2\pi = 2.3(2)$ kHz leading to a gaussian density profile along this direction. The transverse confinement along the $x-$ and $y-$ directions is produced

by a flat-bottom disk-shaped potential of diameter $2R = 40\,\mu$m. For our initial cloud temperature $\simeq 300\,$nK, there is no extended phase coherence in the cloud[a]. Taking into account this finite temperature, we compute for an ideal Bose gas an r.m.s. thickness $\Delta z = 0.25(1)\,\mu$m, or equivalently $k\Delta z = 2.0(1)$. This situation corresponds to $nk^{-2} \approx 1.5$, where $n = N/(\pi R^2)$ is the surface density and to a maximum density $\rho k^{-3} \approx 0.3$ at the trap center along z where ρ is the volume density. We tune the number of atoms that interact with light by partially transferring them to the $|F = 2, m_F = -2\rangle$ state using a resonant microwave transition. Atoms in this state are sensitive to the probe excitation, contrary to the ones in the $|F = 1, m_F = -1\rangle$ state. In this temperature range the Doppler broadening is about 3 orders of magnitude smaller than the natural linewidth of the atomic transition.

The cloud thickness is varied in a controlled way using mainly two techniques: (i) Varying the vertical harmonic confinement by modifying the laser power in the blue-detuned lattice that traps the atoms, thus changing its frequency from $\omega_z/2\pi = 1.1(2)\,$kHz to $\omega_z/2\pi = 2.3(2)\,$kHz. Using the ideal Bose gas statistics in the tight harmonic trap, for a gas of $N = 1.3(2) \times 10^5$ atoms at a temperature of $T \simeq 300\,$nK, this corresponds to r.m.s. thicknesses between $0.3\,\mu$m and $0.6\,\mu$m. (ii) Allowing the atoms to expand for a short time after all traps have been switched off. The extent of the gas in the xy–direction does not vary significantly during the time of flight (ToF) (duration between 0.7 ms and 4.7 ms). In that case, the r.m.s. thickness varies between $3\,\mu$m and $25\,\mu$m. For the densest clouds, the thickness is also influenced by the measurement itself. Indeed, the light-induced dipole-dipole forces between atoms lead to an increase of the size of the cloud during the probing. In the densest case, we estimate from measurements of the velocity distribution after an excitation with a duration of $\tau = 10\,\mu$s that the thickness averaged over the pulse duration is increased by $\sim 20\,\%$. In some experiments, in which the signal is large enough, we limit this effect by reducing the probe duration τ to $3\,\mu$s.

4.1.2 Transmission measurement

We probe the response of the cloud by measuring the transmission of a laser beam propagating along the $z-$direction. The light is linearly polarized along the $x-$axis and tuned close to the $|F = 2\rangle \rightarrow |F' = 3\rangle$ D_2 transition. The duration of the light pulse is fixed to $10\,\mu$s for most experiments and we limit the imaging intensity I to the weakly saturating regime with $0.075 < I/I_{\rm sat} < 0.2$, where $I_{\rm sat} \simeq 1.67\,$mW/cm^2 is the resonant saturation intensity. We define $\Delta\nu$ as the detuning of the laser beam with respect to the single-atom resonance. The cloud intensity transmission $|\mathcal{T}|^2$ is extracted by comparing images with and without atoms and we compute the optical depth $\mathrm{D} = -\ln|\mathcal{T}|^2$ (see Sec. 4.1.3). The numerical aperture of the optical system is limited on purpose to minimize the collection of fluorescence light from directions different from the propagation direction of the light beam.

[a]The 2D phase-space density of the cloud is below the transverse condensation threshold as defined in [193].

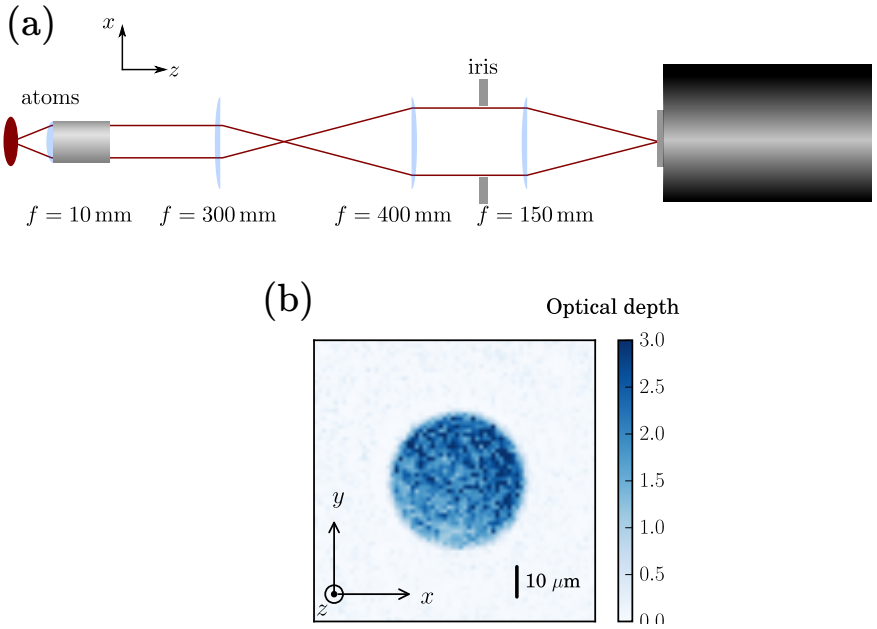

Figure 4.1 *– (a) Schematic representation of the imaging setup. The atoms are confined by a single, disk-shaped potential which is imaged using a microscope objective onto a back-illuminated CCD camera. The numerical aperture of the system is limited to* ≈ 0.2 *using an iris in the Fourier plane of the atoms to limit the collected fluorescence light. (b) Typical in-situ image obtained on a back illuminated CCD camera of the in-plane density distribution averaged over three individual measurements. For this example, the atom surface density is* $n = 25\,\mu m^{-2}$*. We extract a region of interest with uniform density for our analysis with a typical area of* $200\,\mu m^2$*.*

4.1.3 Computation of the optical depth

We extract the optical depth (D) of the clouds by comparing pictures with and without atoms. The read-out noise on the count number N_{count} is $\mathrm{d}N_{\text{count}} \sim 5$ per pixel. We subtract from these images equivalent pictures without any imaging pulse to remove the background counts and obtain two pictures M_{with} and M_{without}. The typical noise on the count number per pixel is thus $\mathrm{d}N = \sqrt{2}\,\mathrm{d}N_{\text{count}} \sim 7$.
The magnification of the optical system is 11.25, leading to an effective pixel size in the plane of the atoms of $1.16\,\mu$m. The typical mean number of counts per pixel accumulated during the $10\,\mu$s imaging pulse is 80 on the picture without atoms. We optimize the signal-to-noise ratio by summing all the pixels in the region of interest for M_{with} and M_{without}. This yields a total count number in the picture with atoms N_{with} and without atoms N_{without} from which we compute the optical depth: $\mathrm{D} = -\ln(N_{\text{with}}/N_{\text{without}})$. The region of interest varies with the time-of-flight of the cloud. This region is a disk that ensures that we consider a part of the cloud with approximately constant density (with 15% rms fluctuations), comprising typically 200 pixels. With these imaging parameters we can reliably measure optical depths up to 4 but we conservatively fit only data for which $\mathrm{D} < 3$. At low densities, the

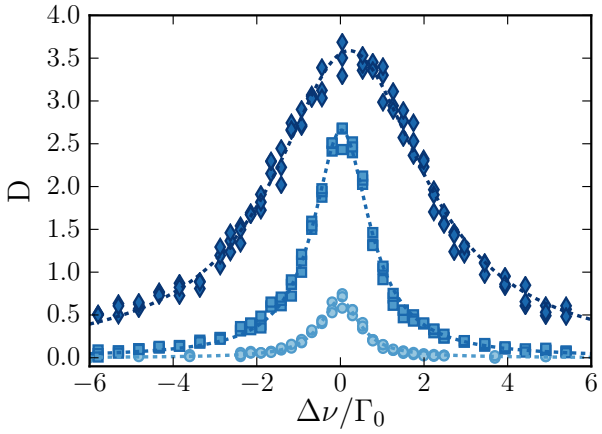

Figure 4.2 *– Example of resonance curves. Symbols represent the experimental data, and the corresponding dashed lines are Lorentzian fits. All curves are taken with the cloud thickness* $k\Delta z = 2.4(6)$ *and for surface densities of* $nk^{-2} = 0.06(1)$ *(circles),* $0.38(6)$ *(squares) and* $1.5(2)$ *(diamonds). The errors on the fitted parameters are determined using a basic bootstrap analysis, repeating the fitting procedure 100 times on a set of random points drawn from the original set of data, of the same length as this original set.*

statistical error on D due to the read-out noise is about 0.01. At $\mathrm{D} \sim 3$, it reaches 0.12.

4.1.4 Atom number calibration

As demonstrated in this article, dipole-dipole interactions strongly modify the response of the atomic cloud to resonant light and make an atom number calibration difficult. In this work, we measure the atom number with absorption imaging for different amounts of atoms transferred by a coherent microwave field from the $|F = 1, m_F = -1\rangle$ "dark" state to the $|F = 2, m_F = -2\rangle$ state in which the atoms are resonant with the linearly polarized probe light. We perform resonant Rabi oscillations for this coherent transfer and fit the measured atom number as a function of time by a sinus square function. We select points with an optical depth below 1, to limit the influence of dipole-dipole interactions. This corresponds to small microwave pulse area or to an area close to a 2π pulse, to make the fit more robust. From the measured optical depth D, we extract $nk^{-2} = (15/7)\,\mathrm{D}/(6\pi)$. The factor 7/15 corresponds to the average of equally-weighted squared Clebsch-Gordan coefficients for linearly polarized light resonant with the $F = 2$ to $F' = 3$ transition. This model does not take into account possible optical pumping effects that could lead to an unequal contribution from the different transitions and hence a systematic error on the determination of the atom number.

4.1.5 Experimental protocol

Our basic transmission measurements consist in scanning the detuning $\Delta\nu$ close to the $F = 2$ to $F' = 3$ resonance ($|\Delta\nu| < 30\,\mathrm{MHz}$) and in measuring the optical depth at a fixed density. The other hyperfine levels $F' = 2, 1, 0$ of the excited $5P_{3/2}$ level play a negligible role for this detuning range. The position of the single-atom resonance is independently calibrated using a dilute cloud. The precision on this calibration is of $0.03\,\Gamma_0$, where $\Gamma_0/2\pi = 6.1$ MHz is the atomic linewidth. The measured resonance curves are fitted with a Lorentzian function:

$$\Delta\nu \mapsto \mathrm{D}_{\max}/[1 + 4\,(\Delta\nu - \nu_0)^2\,/\Gamma^2]. \tag{4.1}$$

This function captures well the central shape of the curve for thin gases, as seen in the examples of Fig. 4.2. When increasing the atomic density we observe a broadening of the line $\Gamma > \Gamma_0$, a non-linear increase of the maximal optical depth $\mathrm{D}_{\max}$ and a blue shift $\nu_0 > 0$. In Sec. 4.3 we present the evolution of these fitted parameters for different densities and thicknesses. Note that in our analysis all points with values of D above 3 are discarded to avoid potential systematic errors. Whereas this threshold has little influence for thin clouds (as shown in Fig. 4.2) for which the maximal optical depths are not large compared to the threshold, for thick gases this typically removes the measurements at detunings smaller than $1.5\,\Gamma_0$. Hence, in this case, we consider the amplitude and the width of the fits to be not reliable and we use the position of the maximum of the resonance ν_0 with caution.
We investigate the dependence of the fit parameters $\mathrm{D}_{\max}$, Γ and ν_0 for different atomic clouds in Sec 4.3. These results are compared to the prediction from a theoretical model that we describe in the following Section.

4.2 Theoretical description

Light scattering by a dense sample of emitters is a complex many-body problem and it is quite challenging to describe. The slab geometry is a textbook situation which has been largely explored. A recent detailed study of the slab geometry can be found in Ref. [167]. We focus in this section first on a perturbative approach which is valid for low enough densities. We then report coupled dipole simulations following the method presented in [181] but extended with a finite-size scaling approach to address the situation of large slabs. We also discuss the regime of validity for these two approaches.

4.2.1 Perturbative approach

We describe here a semi-analytical model accounting for the multiple scattering of light by a dilute atom sample, inspired from reference [184]. By taking into account multiple scattering processes between atom pairs, it provides the first correction to the Beer-Lambert law when decreasing the mean distance l between nearest neighbors towards k^{-3}.

Index of refraction of a homogeneous system

In reference [184], the index of refraction of a homogeneous dilute atomic gas was calculated, taking into account the first non-linear effects occurring when increasing the volume atom density. The small parameter governing the perturbative expansion is ρk^{-3}, where ρ is the atom density. At second order in ρk^{-3} two physical effects contribute to the refraction index, namely the effect of the quantum statistics of atoms on their position distribution, and the dipole-dipole interactions occurring between nearby atoms after one photon absorption. Here we expect the effect of quantum statistics to remain small, and thus neglect it hereafter (see Ref. [194] for a recent measurement of this effect). Including the effect of multiple scattering processes between atom pairs, one obtains the following expression for the refractive index:

$$n_r = 1 + \frac{\alpha\rho}{1 - \alpha\rho/3 + \beta\rho} \tag{4.2}$$

$$\beta = -\int \mathrm{d}\boldsymbol{r} \left[\frac{\alpha^2\mathbf{G}'^2 + \alpha^3\mathbf{G}'^3\mathrm{e}^{-ikz}}{1 - \alpha^2\mathbf{G}'^2}\right]_{xx}(\boldsymbol{r}) \tag{4.3}$$

where we introduced the atom polarisability $\alpha = 6\pi i k^{-3}/(1 - 2i\delta/\Gamma)$ and the Green function $[\mathbf{G}]$ of an oscillating dipole

$$\begin{aligned}
\mathbf{G}_{\alpha\beta}(\boldsymbol{r}) &= -\frac{1}{3}\delta(\boldsymbol{r})\delta_{\alpha\beta} + \mathbf{G}'_{\alpha\beta}(\boldsymbol{r}), \\
\mathbf{G}'_{\alpha\beta}(\boldsymbol{r}) &= -\frac{k^3}{4\pi}\frac{e^{ikr}}{kr}\left[\left(1 + \frac{3i}{kr} - \frac{3}{(kr)^2}\right)\frac{r_\alpha r_\beta}{r^2}\right. \\
&\qquad \left. - \left(1 + \frac{i}{kr} - \frac{1}{(kr)^2}\right)\delta_{\alpha\beta}\right],
\end{aligned} \tag{4.4}$$

in which retardation effects are neglected [195]. Note that for a thermal atomic sample of Doppler width larger than Γ, we expect an averaging of the coherent term β to zero due to the random Doppler shifts. When setting $\beta = 0$ in Eq. (4.2) we recover the common Lorentz-Lorenz shift of the atomic resonance [196]. We plot in Fig. 4.3 the imaginary part of the index of refraction as a function of the detuning δ, for a typical atom density used in the experiment (solid line) and compare with the single-atom response with (dotted line) and without (dashed line) Lorentz-Lorenz correction. The resonance line is modified by dipole-dipole interactions and we observe a blue shift of the position of the maximum of the resonance [179].

Transmission through an infinite slab with a gaussian density profile

In order to account more precisely for the light absorption occurring in the experiment, we extend the perturbative analysis of light scattering to inhomogeneous atom distributions, for which the notion of index of refraction may not be well-defined. The atom distribution is modeled by an average density distribution $\rho(z)$ of infinite extent along x and y, and depending on z only, as $\rho(z) = \rho_0 \exp[-z^2/(2\Delta z^2)]$. We describe the propagation of light along z in the atomic sample. The incoming electric field is denoted as $E_0 e^{i(kz-\omega t)}\mathbf{e_x}$. The total electric field, written as $\mathbf{E}(z)e^{-i\omega t}$, is

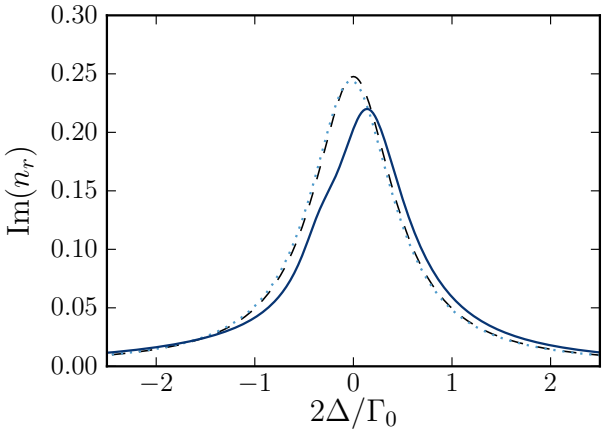

Figure 4.3 – *Imaginary part of the index of refraction of an homogeneous atomic sample of density $\rho k^{-3} \simeq 0.026$. The three curves corresponds to the absorption of independent atoms (dashed black line), to the resonance line taking into account the Lorentz-Lorenz correction (dotted blue line), and to the perturbative analysis discussed in the text (solid black line), which takes into account multiple scattering of photons between pairs of atoms [184].*

given by the sum of the incoming field and the field radiated by the excited atomic dipoles:

$$\mathbf{E}(z) = E_0 e^{ikz}\mathbf{e_x} + \int \mathrm{d}^3\boldsymbol{r}'\,\rho(z')\frac{[\mathbf{G}(\boldsymbol{r}-\boldsymbol{r}')]}{\epsilon_0}\mathbf{d}(z'), \tag{4.5}$$

where $\mathbf{d}(z)$ is the dipole amplitude of an atom located at z and ϵ_0 is the vacuum permittivity. The integral over x and y can be performed analytically, leading to the expression

$$\mathbf{E}(z) = E_0 e^{ikz}\mathbf{e_x} + \frac{ik}{2\epsilon_0}\int \mathrm{d}z'\,\rho(z')e^{ik|z-z'|}\mathbf{d}_\perp(z'), \tag{4.6}$$

where $\mathbf{d}_\perp(z)$ is the dipole amplitude projected in the x, y plane.
The dipole amplitude can be calculated from the atom polarisability α and the electric field at the atom position. Taking into account multiple light scattering between atom pairs, we obtain a self-consistent expression for the dipole amplitude, valid up to first order in atom density, as $\mathbf{d}(z) = d(z)\mathbf{e_x}$, with

$$\begin{aligned} d(z) = {} & \alpha\epsilon_0 E_0 e^{ikz} \\ & + \int \mathrm{d}\boldsymbol{r}'\,\rho(z')\Bigg\{\left[\frac{\alpha\mathbf{G}}{1-\alpha^2\mathbf{G}^2}\right]_{xx}(\boldsymbol{r}-\boldsymbol{r}')d(z') \\ & \qquad + \left[\frac{\alpha^2\mathbf{G}^2}{1-\alpha^2\mathbf{G}^2}\right]_{xx}(\boldsymbol{r}-\boldsymbol{r}')d(z)\Bigg\}. \end{aligned} \tag{4.7}$$

Note that the dipole amplitude also features a component along z, but it would appear in the perturbative expansion in the atom density at higher orders.
The electric field and dipole amplitude are numerically computed by solving the linear system (4.6)-(4.7). The optical depth is then calculated as $\mathrm{D} = -\log(|E(z)|^2/|E_0|^2)$

for $z \gg \Delta z$. The results of this approach will be displayed and quantitatively compared to coupled dipole simulations in the next subsection.

4.2.2 Coupled dipole simulations

Methods

Our second approach to simulate the experiments follows the description in Ref. [181] and uses a coupled dipole model. We consider atoms with a $J = 0$ to $J = 1$ transition. For a given surface density n and thickness Δz we draw the positions of the N atoms with a uniform distribution in the xy plane and a Gaussian distribution along the z direction. The number of atoms and hence the disk radius is varied to perform finite-size scaling. For a given detuning and a linear polarization along x of the incoming field, we compute the steady-state value of each dipole $\boldsymbol{d}_j$ which is induced by the sum of the contributions from the laser field and from all the other dipoles in the system. The second contribution is obtained thanks to the tensor Green function $\mathbf{G}$ giving the field radiated at position $\mathbf{r}$ by a dipole located at origin. Practically, the values of the N dipoles are obtained by numerically solving a set of $3N$ linear equations, which limits the atom number to a few thousands, a much lower value than in the experiment (where we have up to 10^5 atoms). From the values of the dipoles we obtain the transmission $\mathcal{T}$ of the sample:

$$\mathcal{T} = 1 - \frac{i}{2}\sigma\frac{nk^{-2}}{N}\sum_j \frac{k^3}{6\pi\epsilon_0 E_L} d_{j,x} e^{-ikz_j} \tag{4.8}$$

where z_j is the vertical coordinate of the j-th atom, E_L the incoming electric field, and $d_{j,x}$ is the x component of the dipole of the j-th atom. From the transmission, we compute the optical depth $\mathrm{D} = -\ln|\mathcal{T}|^2$ and fit the resonance line with a Lorentzian line shape to extract, as for the experimental results, the maximum, the position and the width of the line.

As the number of atoms used in the simulations is limited, it is important to verify the result of the simulations is independent of the atom number. In this work, we are mostly interested in the response of an infinitely large system in the $xy-$plane. It is indeed the situation considered in the perturbative approach and in the experimental system for which the diameter is larger than $300\,k^{-1}$ and where finite-size effects should be small. The atom number in the simulations is typically two order of magnitudes lower than in the experiment and finite-size effects could become important. For instance, some diffraction effects due to the sharp edge of the disk could play a role [167]. Consequently, we varied the atom number in the simulations and observed, for simulated clouds with small radii, a significant dependence of the simulation results on the atom number. We have developed a finite-size scaling approach to circumvent this limitation. We focus in the following on transmission measurements as in the experiment.

We show two examples of this finite-size scaling approach for $k\Delta z = 1.6$ in Fig. 4.4 and $k\Delta z = 80$ in Fig. 4.5. For low enough surface densities, the results of the simulations (maximal optical depth, width, shift,...) for different atom numbers in the simulation are aligned, when plotted as a function of $1/\sqrt{N_{\mathrm{sim}}}$, and allow for the

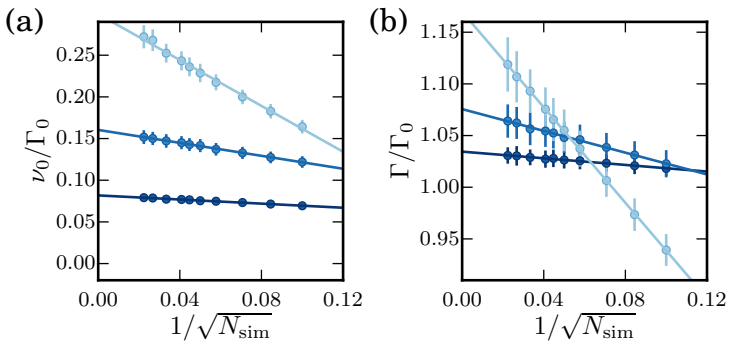

Figure 4.4 *– Example of finite-size scaling to determine the position of the maximum of the resonance ν_0. Here $k\Delta z = 1.6$ and (from bottom to top) $nk^{-2} = 0.05$, 0.11 and 0.21. Simulations are repeated for different atom number N_{sim}. The number of averages ranges from 75 (left points, $N_{\mathrm{sim}} = 2000$) to 25 000 (right points, $N_{\mathrm{sim}} = 100$). When plotting the shift as a function of $1/\sqrt{N_{\mathrm{sim}}} \propto 1/R$, and for low enough densities, data points are aligned and allow for a finite-size scaling. Vertical error bars represent the standard error obtained when averaging the results over many random atomic distributions.*

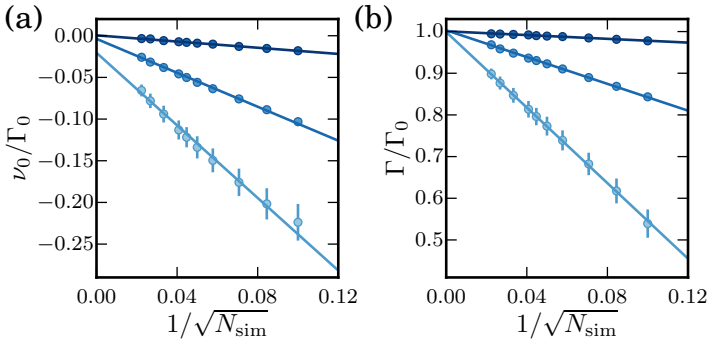

Figure 4.5 *– Example of finite-size scaling to determine (a) the position of the maximum of the resonance ν_0 and (b) the width Γ of the resonance. Here, $k\Delta z = 80$ and (from top to bottom) $nk^{-2} = 0.027$, 0.08 and 0.13. Simulations are repeated for different atom number N_{sim}. The number of averages ranges from 75 (left points, $N_{\mathrm{sim}} = 2000$) to 25 000 (right points, $N_{\mathrm{sim}} = 100$). Vertical error bars represent the standard error obtained when averaging the result over many random atomic distributions.*

desired finite-size scaling. All the results presented in this section and in Sec. 4.3[a] are obtained by taking the extrapolation to an infinite system size, which corresponds to the offset of the linear fit in Figs. 4.4 and 4.5.

Interestingly, we observe in Fig. 4.4 for a thin cloud that considering a finite-size system only leads to a small underestimate of the blue shift of the resonance. However, for thicker slabs, such as in Fig. 4.5, we get, for finite systems, a small red shift and a

[a] except for Fig. 4.9(b) for which simulations are performed for a fixed atom number of 2000.

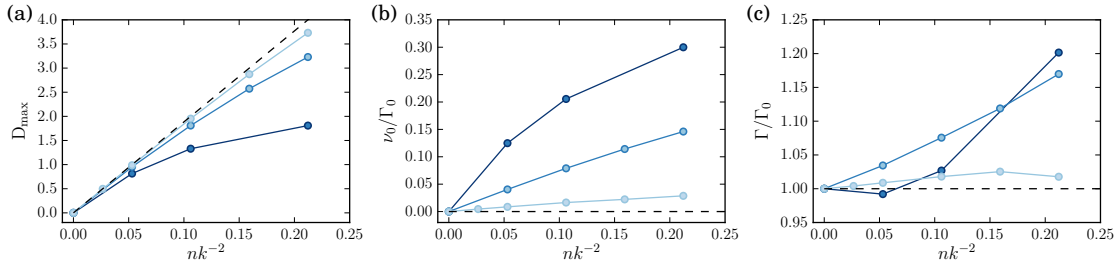

Figure 4.6 *– Coupled dipole simulations for different thicknesses. (a) Maximal optical depth, (b) Position of the maximum of the line, (c) Width of the resonance line. We report results for $k\Delta z$ =0, 1.6 and 8, the darkest lines corresponding to the smallest thicknesses. The black dashed lines correspond to the single-atom response.*

narrowing of the line. Considering our experimental system, we have $1/\sqrt{N} \approx 0.003$, leading to a small correction according to the fits in Fig. 4.5. However, for such thick systems we are able to simulate only systems with low nk^{-2}, typically 0.1, whereas we can reach densities 15 times larger in the experiment, which could enhance finite-size effects. Simulation of thick and optically dense slabs is thus challenging and the crossover between the thin slab situation explored in this article and the thick regime is an interesting perspective of this work.

Role of the thickness and density of the cloud

We now investigate the results of coupled dipole simulations for different densities and thicknesses of the atomic cloud. We limit the study to low densities, for which the finite-size scaling approach works. It is important to note that the computed line shapes deviate significantly from a Lorentzian shape and become asymmetric. Consequently there is not a unique definition for the center of the line and for its width. In our analysis, we fit the resonance lines around their maximum with a typical range of $\pm 0.5\,\Gamma$. The shift thus corresponds to a variation of the position of the maximum of the line and the "width" characterizes the curvature of the line around its maximum. The results of these fits are reported in Fig. 4.6 as a function of surface density for different thicknesses. In these plots, we observe the same features as qualitatively described in Sec. 4.1: A decrease of the maximal optical depth with respect to the single-atom response (Fig. 4.6(a)), a blue shift of the position of the maximum (Fig. 4.6(b)) and a broadening of the line (Fig. 4.6(c)). For a fixed thickness, these effects increase with surface density and for a fixed surface density they are more pronounced for lower thicknesses. Note that we only explore here surface densities lower than 0.25 which is quite lower than the maximum experimental value (~ 1.5). Whereas our finite-size scaling approach can be well-extended for very thin systems ($k\Delta z < 1$) it fails for thick and optically dense systems[a].

[a]We guess that this is due to the limited atom number used in the simulation which prevents from investigating a regime where the geometry of the simulated cloud has an aspect ratio similar to the experimental one.

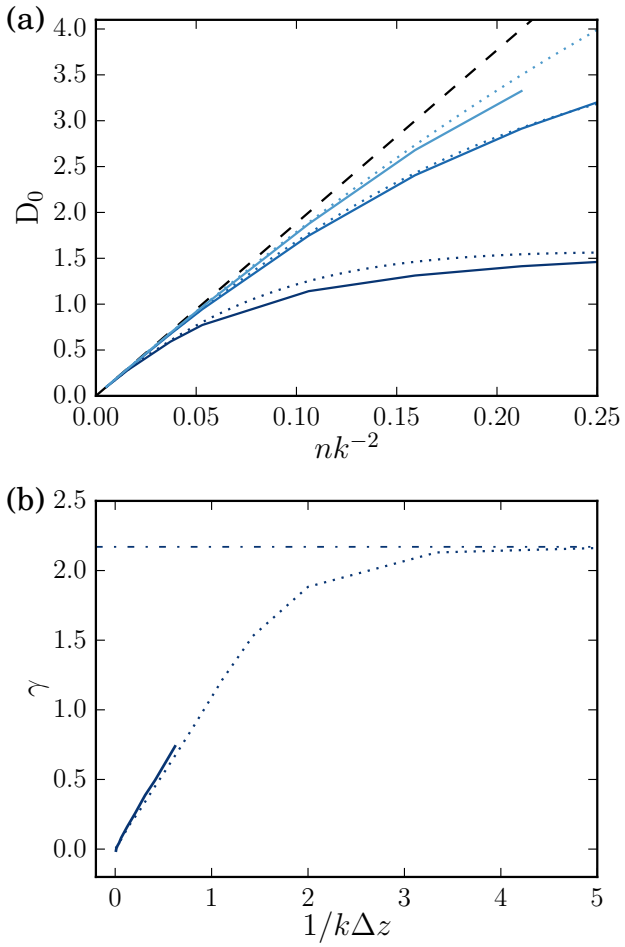

Figure 4.7 *– Comparison between the coupled dipole simulations and the perturbative model. (a) Behavior of the optical depth at the single-atom resonance $\mathcal{D}_0$ with surface density for different thicknesses ($k\Delta z$ =0, 1.6 and 3.2, from bottom to top). Coupled dipole simulations are shown as solid lines, perturbative approach as dotted lines and the dashed line is the Beer-Lambert prediction. (b) Slope β of the blue shift $\nu_0 = \beta n k^{-2}$ as a function of the inverse thickness $1/k\Delta z$. The solid line is the result of the coupled dipole model, the dash-dotted line is the zero-thickness coupled dipole result ($1/k\Delta z \to \infty$), the dotted line is the perturbative model.*

Comparison with the perturbative model

The perturbative approach is limited to low densities $\rho k^{-3} \ll 1$ but it gives the response of an infinitely expanded cloud in the transverse direction. Coupled dipole simulations can in principle address arbitrarily large densities but the number of atoms considered in a simulation is limited, and thus for a given density the size of the system is limited. Coupled dipole simulations are thus more relevant for thin and dense sample and the perturbative approach more suited for non-zero thickness samples.

In Fig. 4.7 we choose two illustrative examples to confirm, in the regime where both

models could be used, that these two approaches are in quantitative agreement. In Fig. 4.7(a) we compare the maximum optical depth as a function of surface density for three different thicknesses. The perturbative approach is typically valid, for this set of thicknesses, up to $nk^{-2} \sim 0.1$. We investigate the shift of the position of the maximum in Fig. 4.7(b). We report, as a function of the inverse thickness $(1/k\Delta z)$, the slope γ of the shift with density, $\nu_0 = \gamma n k^{-2}$, computed for surface densities below 0.1. The dotted line is the result from the perturbative approach, the solid line corresponds to coupled dipole simulations and the dash-dotted line to the result for zero thickness. The perturbative approach approximates well coupled dipole simulations. This result also confirms that the finite-size scaling approach provides a good determination of the response of an infinite system in the $xy-$direction.
We have identified in this Section the specific features of the transmission of light trough a dense slab of atoms. We focus here on the transmission coefficient to show that we observe the same features in the experiment and we will make a quantitative comparison between our experimental findings and the results obtained with coupled dipole simulations. Our theoretical analysis is complemented by a study of the reflection coefficient of a strictly 2D gas detailed in in section 4.5.

4.3 Experimental results

We show in Fig. 4.8 the results of the experiments introduced in Sec. 4.1. The fitted $\mathrm{D_{max}}$ for different surface densities is shown in Fig. 4.8(a). We compare these results to the Beer-Lambert prediction (narrow dashes) $\mathrm{D_{BL}} = n\sigma_0$ and to the same prediction corrected by a factor 7/15 (large dashes). This factor is the average of the Clebsch-Gordan coefficients relevant for π-polarized light tuned close to the $|F = 2\rangle \rightarrow |F' = 3\rangle$ transition and, as discussed previously, it is included in the calibration of the atom number. At large surface densities, we observe an important deviation from this corrected Beer-Lambert prediction: we measure that $\mathrm{D_{max}}$ seems to saturate around $\mathrm{D_{max}} \approx 3.5$ whereas $\mathrm{D_{BL}} \approx 13$[a]. We also show the prediction of the coupled dipole model, as a solid line for the full range of surface densities at $k\Delta z = 0$ and as a dotted line for the numerically accessible range of surface densities at $k\Delta z = 2.4$. The coupled dipole simulation at $k\Delta z = 0$ shows the same trend as in the experiment but with $\mathrm{D_{max}}$ now bounded by 2. A reason could be the non-zero thickness of the atomic slab. In order to test this hypothesis, we investigated the influence of probing duration for the largest density. For such a density we could decrease the pulse duration while keeping a good enough signal to noise ratio (see inset in Fig. 2(b)). For a shorter probing duration, hence for a smaller expansion of the cloud, $\mathrm{D_{max}}$ decreases, in qualitative agreement with the expected effect of the finite thickness.
The saturation of the optical depth with density is a counterintuitive feature. It shows that increasing the surface density of an atomic layer does not lead to an increase of its optical depth. Coupled dipole simulations at $k\Delta z = 0$ even show that the system becomes slightly more transparent as the surface density is increased.

[a]The observed saturation is not due to our detection procedure. In the fitting procedure, we only select points with a measured optical depth below 3 to avoid any bias.

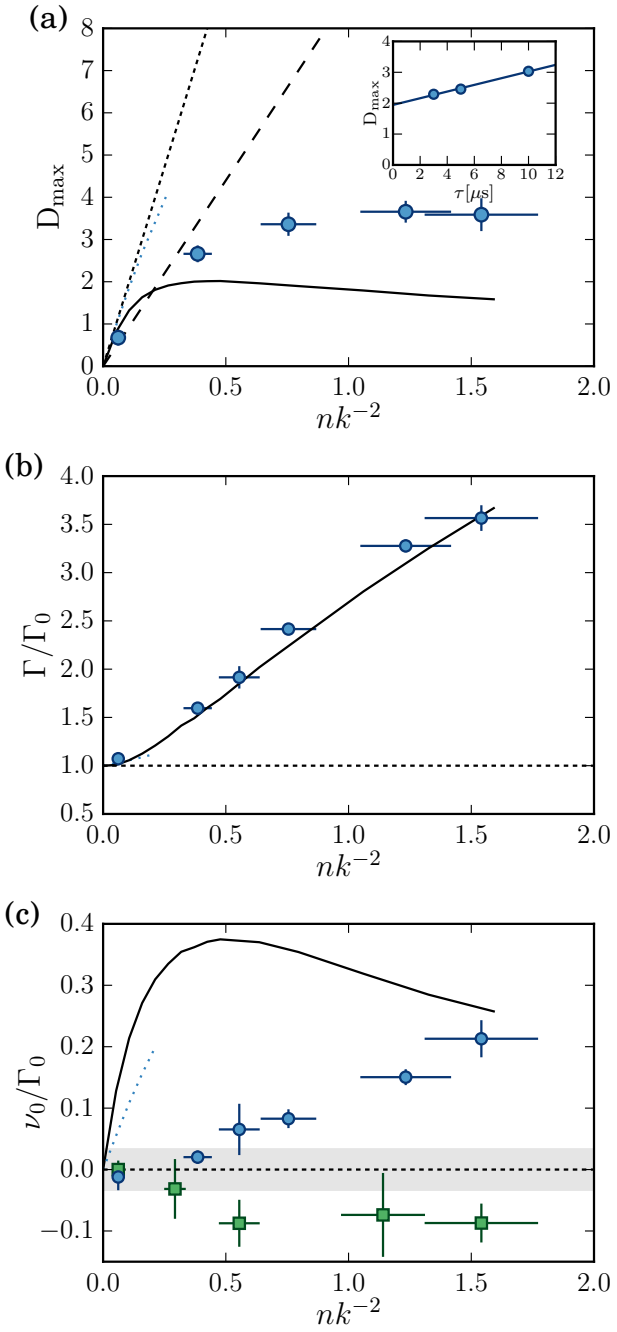

Figure 4.8 – *Maximum optical depth (a), broadening (b) and frequency shift (c) of the resonance line for our thinnest samples with $k\Delta z = 2.4(6)$ (circles) and for thicker samples with $k\Delta z = 30(8)$ (squares). In (a) the shaded area represents the uncertainty in the frequency calibration of the single-atom resonance. In (a) and (b), the dark black solid (resp. light blue dotted) line is the prediction of the coupled dipole model for $k\Delta z = 0$ (resp. $k\Delta z = 2.4$) in its accessible range of densities. The dashed lines represent the single-atom response.*

These behavior may be explained qualitatively by the broadening of the distribution of resonance frequencies of the eigenmodes of this many-body system. A dense system scatters light for a large range of detunings but the cross section at a given detuning saturates or becomes lower as the surface density is increased.
We display in Fig. 4.8(b) the width Γ of the Lorentzian fits for $k\Delta z = 2.4(6)$ along with coupled dipole simulation results[a]. We observe a broadening of the resonance line up to more than $3\,\Gamma_0$. This broadening is confirmed by the simulation results for $k\Delta z = 0$ (solid line). Note that the exact agreement with the experimental data should be considered as coincidental. The range on which we can compute the broadening for $k\Delta z = 2.4$ (light dotted line) is too small to discuss a possible agreement.
We show in Fig. 4.8(c) the evolution of ν_0 with density. A blue shift, reaching $0.2\,\Gamma_0$ for the largest density, is observed. At the largest density, an even larger shift is observed when decreasing the pulse duration ($\approx 0.4\,\Gamma_0$, not shown here). We also display the result of the coupled dipole model for the cases $k\Delta z = 2.4$ and $k\Delta z = 0$. Both simulations confirm the blue shift but predict a different behavior and a larger effect. In addition, we show the variation of ν_0 for a thick cloud with $k\Delta z = 30(8)$. In that case we observe a marginally significant red shift[b].
The experimental observation of a blue shift has never been reported experimentally to our knowledge. It is in stark contrast, both in amplitude and in sign, with the mean-field prediction of the Lorentz-Lorenz red shift $\nu_0^{\mathrm{MF}}/\Gamma_0 = -\pi\rho k^{-3} = -\sqrt{\pi/2}\,nk^{-2}/(k\Delta z)$, written here at the center of the cloud along z. The failure of the Lorentz-Lorenz prediction for cold atom systems has already been observed and discussed for instance in Refs [191, 182, 180]. As discussed with the perturbative approach in Sec. 4.2, the Lorentz-Lorenz contribution is still present but it is (over)compensated by multiple scattering effects for a set of fixed scatterers. In hot vapors, where the Doppler effect is large, the contribution of multiple scattering vanishes and thus the Lorentz-Lorenz contribution alone is observed. The related Cooperative Lamb shift has been recently demonstrated in hot vapor of atoms confined in a thin slab in Ref. [160]. In the cold regime where scatterers are fixed, such effects are not expected [167]. However, in these recent studies with dense and cold samples a small red shift is still observed [191, 182, 180]. This difference on the sign of the frequency shift with respect to the results obtained in this work may be explained by residual inhomogeneous broadening induced by the finite temperature or the diluteness of the sample in Ref. [182] and by the specific geometry in Ref. [180], where the size of the atomic cloud is comparable to λ and where diffraction effects may play an important role. As discussed in Sec. 4.2, our observation of a blue shift is a general result which applies to the infinite slab. It is robust to a wide range of thicknesses and density, and while we computed it theoretically for a

[a] We guess that this is due to the limited atom number used in the simulation which prevents from investigating a regime where the geometry of the simulated cloud has an aspect ratio similar to the experimental one.

[b] For thick clouds the expected optical depth of the cloud becomes larger than the maximal value we can detect. We then only fit the points with a measured optical depth below 3. From this fit we cannot estimate reliably the value of the maximum and width of the resonance line, but we can get an estimate of the "center" of the line which may deviate from the position of the maximum of the resonance for an asymmetric lineshape.

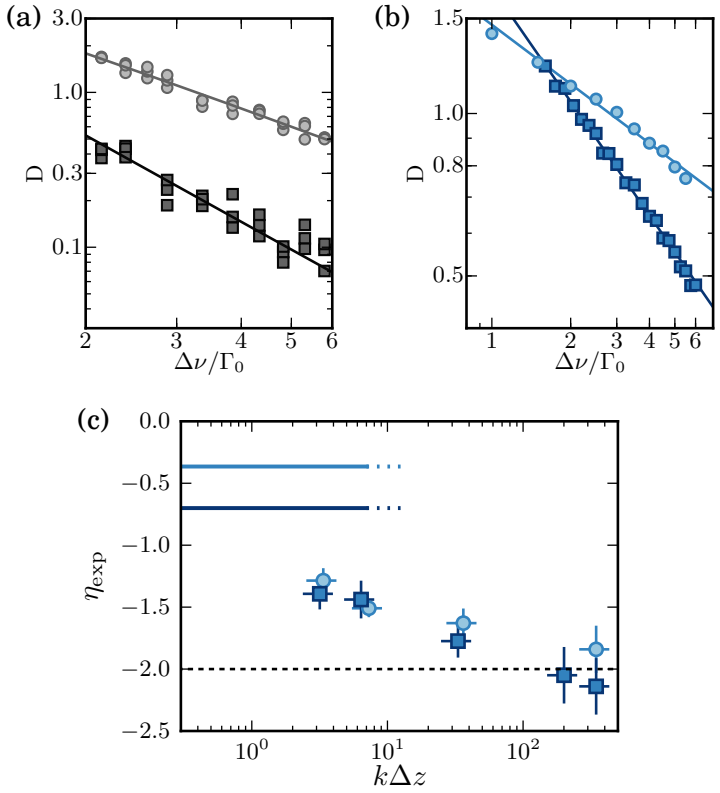

Figure 4.9 *– Non-Lorentzian wings of the resonance line. (a) Two examples of the scaling of optical depth with $\Delta\nu$ (blue side), in log-log scale, for $k\Delta z = 2.4(6)$ (circles) and for $k\Delta z = 350(90)$ (squares) and their power-law fit. (b) Coupled dipole simulations at zero thickness and for $nk^{-2} = 1.5(2)$. The optical depth is plotted as a function of detuning (resp. minus the detuning) from the resonance line, for the blue (circles) (resp. red (squares)) side. The solid lines are power-law fits. (c) Experimental results for $nk^{-2} = 1.5(2)$. Circles (resp. squares) represent the fitted exponents η_{r} (resp. η_{b}) to the far-detuned regions of the resonance line on the red and blue side, respectively. The fit function is $\Delta\nu \mapsto \mathrm{D}(\Delta\nu) = A\,(\Delta\nu - \nu_0)^{\eta}$. The error on the fitted exponents is also determined using a bootstrap analysis. The horizontal dashed black line ($\eta = -2$) emphasizes the expected asymptotic value for low densities for a Lorentzian line (at large detunings).*

two-level system, it also shows up experimentally in a more complex atomic level structure. It was also predicted in Ref. [167] but for a uniform distribution along the z axis instead of the Gaussian profile considered in this work, and also discussed in [179]. Consequently, we believe that it is an important and generic feature of light scattering in a extended cloud of fixed randomly distributed scatterers.

Finally, we compare the lineshape of the resonance with the Lorentzian shape expected for a single atom. We measure for $nk^{-2} = 1.5(2)$, the optical depth at large detunings, and for various cloud thicknesses. We fit it with a power law on

the red-detuned (resp. blue-detuned) frequency interval with exponent η_r (resp. η_b) as shown, for two examples, in Fig. 4.9(a). If the behavior were indeed Lorentzian, the exponents should be -2 in the limit of large detuning. As seen in Fig. 4.4(c), for the thinnest gases, the fitted exponents are significantly different from the expected value and can reach values up to -1.3, showing the strong influence of dipole-dipole interactions in our system. We show the result of coupled dipole simulations for $k\Delta z = 0$ in Fig. 4.4(b) along with their power-law fit. We extract the exponents $\eta_\mathrm{r} = -0.36(1)$ and $\eta_\mathrm{b} = -0.70(1)$ that are report as solid lines in Fig. 4.4(c). Our experimental results interpolate between the single-atom case and the simulated 2D situation.

4.4 Conclusion

In summary we have studied the transmission of a macroscopic dense slab of atoms with uniform in-plane density and a transverse gaussian density distribution. We observed a strong reduction of the maximum optical density and a broadening of the resonance line. More surprisingly, we showed the presence of a large blue shift of the resonance line and a deviation from Lorentzian behavior in the wings of the resonance line. These results are qualitatively confirmed by coupled dipole simulations and a perturbative approach of this scattering problem. We also confirm the difficulty already observed to obtain a quantitative agreement between coupled dipole simulations and experimental results in the dense regime [189, 180]. Possible explanations for this discrepancy are (i) residual motion of the atoms during the probing due to the strong light-induced dipole-dipole interactions, (ii) a too large intensity used in the experiment which goes beyond the validity of the coupled dipole approach, (iii) the influence of the complex atomic level structure. We were careful in this work to limit the influence of the two first explanations and the last possibility is likely to be the main limitation. The complex level structure leads to optical pumping effects during the probing and thus the scattering cross-section of the sample is not well-defined. A simple way to take into account the level structure is, as discussed in Sec. 4.3, to renormalize the scattering cross section by the average of the Clebsch-Gordan coefficients involved in the process. For ^{87}Rb atoms this amounts for the factor 7/15 already discussed earlier. However this is a crude approximation which neglects optical pumping effects during scattering and whose validity in the dense regime is not clear. Two approaches can be considered to remove this limitation. First, one can use another atomic species such as strontium or ytterbium bosonic isotopes which have a spin singlet ground state and in which almost exact two-level systems are available for some optical transitions. Scattering experiments on strontium clouds have been reported [197, 169, 182] but they did not explore the dense regime tackled in this work. The comparison with theory thus relies on modeling their inhomogeneous density distribution accurately. Second, an effective two-level system can be created in the widely used alkali atoms by imposing a strong magnetic field which could separate the different transitions by several times the natural linewidth as demonstrated in some recent experiments on three-level systems [198, 199]. This method could be in principle applied on

our setup to create an effective two-level system and could help to understand the aforementioned discrepancies.
Finally, we note that this article focuses on the steady-state transmission of a cloud illuminated by a uniform monochromatic beam. The slab geometry that we have developed here is of great interest for comparison between theory and experiments and our work opens interesting perspectives for extending this study to time-resolved experiments, to fluorescence measurements or to spatially resolved propagation of light studies.

4.5 Additional remark: reflection coefficient of a 2D gas

Thanks to their large scattering cross section at resonance, arrays of atoms can be used to emit light with a controlled spatial pattern [200]. A single-atom mirror has been demonstrated [201] and, more generally, regular two-dimensional arrays of atoms have been considered for realizing controllable light absorbers [202] or mirrors [203] with atomic-sized thicknesses. For the disordered atomic samples considered in this article the strong decrease of the transmission because of dipole-dipole interactions could lead to a large reflection coefficient. For a strictly two-dimensional gas we show as a solid line in Fig. 4.10 the result of the coupled dipole model for the intensity reflection coefficient $|\mathcal{R}|^2$ at resonance and at normal incidence as a function of density. This intensity reflection coefficient has a behavior with density similar to the optical depth D (dotted line). The relation between these two quantities depends on the relative phase between the incoming and the reflected field. For a transmitted field in phase with the incident field we find, using the boundary condition $\mathcal{R}+\mathcal{T}=1$, a lower bound for this reflection coefficient, $|\mathcal{R}|^2 \geq (1-|\mathcal{T}|)^2$, shown as a dashed line in Fig. 4.10. The intensity reflection coefficient is close to this lower bound in the regime explored in this work. The maximum computed value for the reflection coefficient is close to 40 % which shows that a single disordered layer of individual atoms can significantly reflect an incoming light beam[a]. Note that for a non-2D sample light can be diffused at any angle. For our experimental thickness and the relevant densities the reflection coefficient is in practice much lower than the above prediction.

[a] We have investigated here only the behavior at normal incidence. A full characterization of such a atomic mirror is beyond the scope of this work

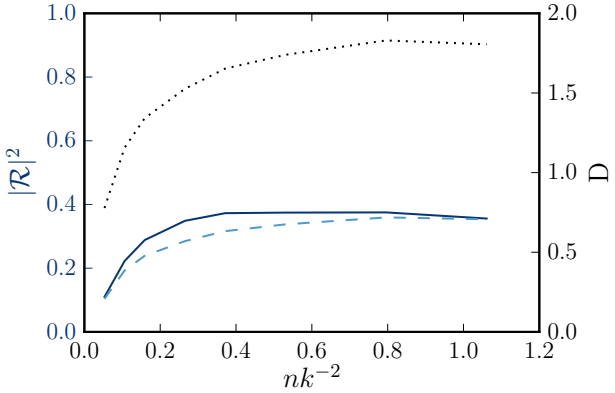

Figure 4.10 – *Intensity reflection coefficient as a function of surface density for $k\Delta z = 0$ (solid line). For comparison we show the corresponding optical depth* D *(dotted line, right axis) and the lower bound for the reflection coefficient deduced from this optical depth (dashed line).*

5

Study of light diffusion

The tunability of our experimental setup and the high resolution of our imaging system makes a spatially resolved study of light diffusion possible. In this chapter, we explore light propagation in a dense cloud of atoms by fluorescence measurements. We are thus probing the incoherent part of the scattered light, whereas in the previous chapter we were mainly probing the coherent part.
Atoms are confined in a layer geometry in the focal plane of a high resolution imaging system, which allows us to inject light in a region with sharp boundaries and monitor its spreading away from this region (see Fig. 5.1(a)). We observed that the fluorescence intensity, which measures the local photon escape rate, decays exponentially with the distance from the excitation zone. We show that this behaviour is compatible with a two-dimensional (2D) diffusive model. For resonant light, we measured the decay length of the fluorescence signal as a function of the atomic density. We found that it saturates in the regime of high density, where photons undergo a few tens of scattering events before leaving the sample. For detuned light, the photon escape rate is significantly modified, in a way that suggests a light-guiding mechanism reminiscent of a graded-index planar waveguide. We also observed these phenomena in numerical simulations based on a model of coupled dipoles, and explained them by an analytical model of light guiding in an open, disordered 2D slab.

5.1 Results

The sections of this chapter are now published in [187], and are reproduced almost without modifications. Only titles have been added and some phrases changed to be consistent with the rest of the thesis.

5.1.1 Light spreading in a dense atomic cloud

Here we explore the phenomenon of multiple scattering of light in a dense and large cloud of atoms. In our ultracold sample the motion of the atoms is negligible on the timescale of the experiment, so they act as a gas of fixed, randomly distributed point scatterers. Atoms are confined in a layer geometry in the focal plane of a high resolution imaging system, which allows us to inject light in a region with sharp boundaries and monitor its spreading away from this region (see Fig. 5.1(a)). We observed that the fluorescence intensity, which measures the local photon escape rate, decays exponentially with the distance from the excitation zone. We show

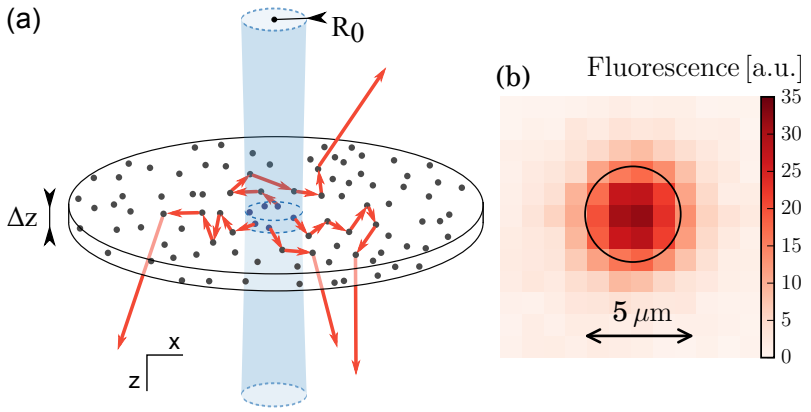

Figure 5.1 *– Experimental setup. A layer of atoms is illuminated at its center with a resonant light beam of radius R_0. Photons initially emitted in the excitation region can be scattered several times in the atomic layer before exiting the system and being collected and imaged. (b) Typical fluorescence image at resonance and maximum density. The black circle, of diameter of $2R_0 = 5\,\mu m$, delineates the excitation region. Intensity is not uniform inside the excitation region partially because of finite optical resolution but also and more importantly, because of the light diffusion process itself, as described in the text.*

that this behavior is compatible with a two-dimensional (2D) diffusive model. For resonant light, we measured the decay length of the fluorescence signal as a function of the atomic density. We found that it saturates in the regime of high density, where photons undergo a few tens of scattering events before leaving the sample. For detuned light, the photon escape rate is significantly modified, in a way that suggests a light-guiding mechanism reminiscent of a graded-index planar waveguide. We also observed these phenomena in numerical simulations based on a model of coupled dipoles, and explained them in a semi-quantitative way by an analytical model of light guiding in an open, disordered 2D slab.

We use a dense layer of ^{87}Rb atoms as previously described in Refs. [116, 186] and in the methods section. In the xy plane, we produce a uniform disk-shaped atomic layer with a controllable surface density up to $\rho_{2D} = 135(15)\,\mu m^{-2}$. Atoms are strongly confined along the vertical z direction with an approximately gaussian density distribution of r.m.s. thickness $\Delta z \approx 0.3\,\mu m < \lambda_0$, with $\lambda_0 = 2\pi/k = 0.78\,\mu m$ the resonant wavelength for the $|F = 2\rangle$ to $|F' = 3\rangle$ D2 transition of rubidium atoms. This corresponds to a maximum density at the center of the gaussian profile of $\rho_{3D}k^{-3} = 0.35(5)$ where $\rho_{3D} = \rho_{2D}/(\sqrt{2\pi}\Delta z)$.

The atomic cloud is locally excited by light at a wavelength λ_0, propagating perpendicular to the atomic plane along the z axis, as illustrated in Fig. 5.1(a), and linearly polarized along x. In the illuminated region, the intensity of the beam is on the order of $7\,I_{sat}$, where $I_{sat} = 1.6\,mW\,cm^{-2}$ is the saturation intensity for this transition (with a linewidth $\Gamma = 2\pi \times 6\,MHz$) [a]. The light beam profile on the

[a] The intensity we used is large enough to ensure that, even if our samples have large optical depths, the cloud is well-excited for all positions along the z direction.

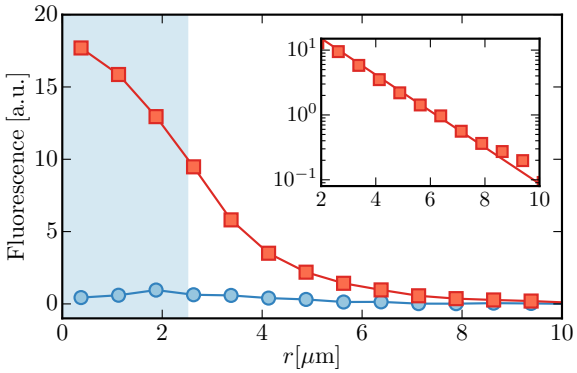

Figure 5.2 – *Fluorescence decay. Binned and azimuthally averaged profile for the measured atomic fluorescence (squares). Circles show the small background signal observed without atoms. The shaded area represents the excitation region. Statistical errors bars due to photon counting are smaller than the size of the points. The inset shows the same data outside the excitation region in a semilog plot to emphasize the exponential decay of the fluorescence signal. Data are averaged over 100 measurements.*

atomic cloud is given by the image of a pinhole whose diameter on the atomic cloud is $2R_0 = 5\,\mu\text{m}$. The excitation duration is $\tau = 10\,\mu\text{s}$. The atomic fluorescence is collected, spatially filtered and imaged on a CCD camera. We detect only photons with a linear polarization perpendicular to the excitation polarization and block the residual transmitted light in the spatial mode of the incident beam. The optical resolution of our system ($\sim 1\,\mu\text{m}$) is characterized in section 5.3.2. Atoms outside the illuminated region are only excited by scattered light and feel a much lower intensity than in the illuminated region. Taking into account our collection and detection efficiencies, assuming that the scatterers are independent and that polarization is randomized for photons emitted from outside the excitation region, we obtain a rough estimate for the intensity seen by atoms at $1\,\mu\text{m}$ from the edge of the illuminated region of approximately $0.1\,I_{\text{sat}}$. It is important to operate in this low saturation regime to enable comparison with the simulations described below.

We show in Fig. 5.1(b) a typical measurement of the atomic fluorescence signal integrated over the full duration of the excitation. The circle indicates the illuminated region. Photons are detected up to several micrometers away from this region. We show in Fig. 5.2 a binned and azimuthally averaged profile of the fluorescence image. There is a large ratio between the atomic signal and residual stray light over the explored experimental range. Outside the illuminated region we observe an exponential decay with distance of the atomic fluorescence over almost two decades (see inset in Fig. 5.2). The decay lengths investigated in this work typically range from 1 to $2\,\mu\text{m}$.

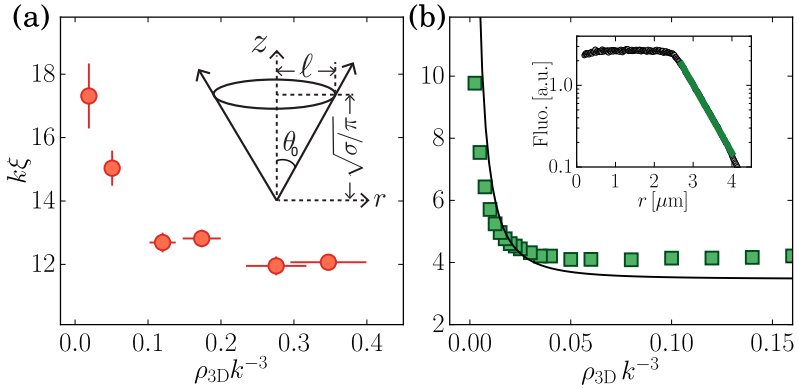

Figure 5.3 *– (a) Measured decay length ξ for different densities at resonance ($\Delta = 0$). Vertical error bars correspond to the standard deviation of the results of exponential fits to the data obtained with a bootstrap approach. Each data set is obtained from the average of 100 measurements. Horizontal error bars represent the statistical uncertainty on the atom number. The inset shows the relevant parameters of the simple model described in section 5.1.3. (b) Decay length ξ obtained from the analytical result of Eq. (5.3) (solid line) and numerical simulations of a model of classical coupled dipoles (squares) as a function of density. Statistical error bars on ξ obtained from the fitting procedure of the coupled dipole simulations are smaller than the size of the points. The inset shows the fluorescence signal computed with coupled dipole simulations for $\rho_{3D}k^{-3} = 0.12$ and averaged over > 1000 atomic distributions. The solid line is the exponential fit outside the illuminated region.*

5.1.2 Diffusion model

We could explain the spatial shape of the fluorescence signal by a diffusion model of light transport. In this framework and in the steady-state regime, the light energy density $I(\mathbf{r})$ at a point $\mathbf{r}$ in the sample obeys a diffusion equation with losses:

$$-D_0\nabla^2 I(\mathbf{r}) = -\gamma I(\mathbf{r}) + S(\mathbf{r}), \tag{5.1}$$

where D_0 is the diffusion constant, γ the escape rate of photons and $S(\mathbf{r})$ the source term describing the laser excitation. We consider the situation where the source term is $S(\mathbf{r}) = S_0$ for $r < R_0$ and 0 otherwise. The solution of this equation in two dimensions is given by

$$I(\mathbf{r}) = \frac{S_0}{2\pi D_0}\iint_{|\mathbf{r}'|<R_0} K_0\left(\frac{|\mathbf{r}-\mathbf{r}'|}{\xi}\right) d^2r' \underset{r\gg R_0+\xi}{\propto} \frac{e^{-r/\xi}}{\sqrt{r}}, \tag{5.2}$$

where K_0 is the modified Bessel function of the second kind of order zero and $\xi = \sqrt{D_0/\gamma}$. Outside the illuminated region, at large r, the function $I(r)$ decays almost exponentially [a] in agreement with our measurements. These results allow us

[a] We neglect the $\sqrt{r}$ dependence which has almost no influence on the shape of the signal in the range of distance we explore in this work.

to relate the measured photon decay length ξ to the diffusion constant D_0 and to the escape rate γ that we cannot measure individually in a direct way.

5.1.3 Variation of the decay length with density at resonance

We first focus on a resonant excitation. For different densities, we fit the experimental fluorescence signal by $Ae^{-r/\xi}$ and obtain the decay length as a function of density (see Fig. 5.3(a)). The low density regime (lower values of $\rho_{3D}k^{-3}$) corresponds to the case where a photon is typically leaving the sample after the first scattering event outside the illuminated region. This scattering event occurs at a distance from the edge of the illuminated region given by the mean free path $\ell = 1/(\rho_{3D}\sigma)$, where σ is the light cross section (note that the validity of this expression of ℓ becomes dubious for ℓ smaller than the interparticle distance). In this dilute regime we expect $\xi \sim \ell$ to decrease when the density increases, as observed in Fig. 5.3(a). In the opposite regime of large densities, we observe a saturation of the decay length. It remains around $k\xi \approx 12$ while varying the density by a factor of about 3. We checked that this saturation is not due to the finite resolution of our imaging system which allows us to measure decay lengths below 1 µm ($k\xi \lesssim 8$).
We have developed a simple geometrical model to explain the main features of the curve in Fig. 5.3(a). For resonant light, the typical time between two scattering events is Γ^{-1}, so that $D_0 \sim \Gamma\ell^2$. The photon loss rate $\gamma \sim \Gamma p$ is related to the probability p of escaping the cloud after a scattering event, leading to $\xi = \sqrt{D_0/\gamma} \sim \ell/\sqrt{p}$. The saturation of ξ with increasing density thus stems from the compensation of two antagonistic effects: (i) the decrease of mean free path, which tends to make the decay length smaller and (ii) the decrease of the escape probability of scattered photons. To be more quantitative, we estimate p by a geometric argument (inset in Fig. 5.3(a)): an atom in a 2D gas emitting a photon can be considered as being placed at the center of a vertical cylinder of radius ℓ, corresponding to the typical distance to the next scatterer. The photon will escape the cloud if its emission angle θ_0 is small enough so that it would meet the next scatterer at a height larger than $\sqrt{\sigma/\pi}$. Emitted photons that escape the medium are then effectively contained within a cone of half-angle θ_0. This gives a probability $p \sim 2 \times 2\pi(1 - \cos\theta_0)/(4\pi)$ with $\tan\theta_0 = \ell/\sqrt{\sigma/\pi}$, and in turn:

$$k\xi = \frac{k\ell}{\sqrt{1 - (1 + \ell^2\pi/\sigma)^{-1/2}}}\,. \tag{5.3}$$

We display Eq. (5.3) computed for the resonant scattering cross section $3\lambda_0^2/(2\pi)$ in Fig. 5.3(b) (solid line). At low densities, $\xi \sim \ell$ decays rapidly with increasing density, as observed in the experiment. At larger densities, $p \sim \ell^2\pi/(2\sigma)$ so that ξ becomes independent of the density and much larger than the mean free path.
Using a random walk picture and this estimate of p, we find that the typical number of scattering events before a photon leaves the sample is $N_{\text{scatt}} = 1/p = 2\sigma/(\pi\ell^2)$. Considering an atomic density of $\rho_{3D}k^{-3} = 0.07$, in the "plateau" of Fig 5.3(b) but not too large so that ℓ could still be interpreted with the classical picture of a mean

free path, we get a typical value of about 20 scattering events. This value justifies the diffusion model and confirms that we investigate experimentally a steady-state situation (the total duration of a photon random walk, $\approx N_{\mathrm{scatt}}\Gamma^{-1}$, is much shorter than the duration τ of the illumination pulse).

As shown in Fig. 5.3(b), the variation of decay length with density is also reproduced by numerical simulations based on the method of coupled dipoles. For these simulations, we model our atomic system by a random ensemble of classical coupled dipoles (with transition $J = 0$ to $J = 1$) and compute the exact radiated field from these dipoles for a given excitation field taking into account simultaneously all effects related to dipole-dipole interactions and interferences. We assume that the dipoles are randomly positioned in a layer geometry with the same thickness as in the experiment and that they stay fixed during the excitation (see section 5.3.3).

The two models that we have developed are in good agreement with each other. But although these predictions qualitatively reproduce the measurements in Fig. 5.3a, note the difference by a factor ≈ 3 between the scales of the two graphs. Possible reasons for this difference are discussed below.

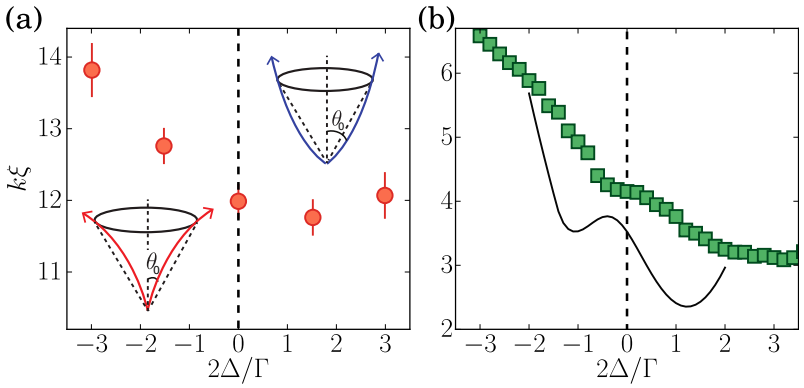

Figure 5.4 *– Decay length versus detuning. (a) Experimental results obtained for a dense cloud with $\rho_{3D}k^{-3} \simeq 0.35$. The insets show the bending of the trajectories which depends on the sign of the detuning. The dashed lines in the insets correspond to the maximal emission angle a photon leaving the sample could have without considering the bending effect. Taking into account the bending effect, this maximal angle is smaller for negative detuning and larger for positive detunings. Each point is the average result of 100 measurements. (b) Decay length computed from a numerical model of coupled dipoles (squares), decay length $\xi = \ell/\sqrt{1-\cos\theta}$ obtained by solving Eq. (5.4) for θ (solid line). All theory curves are computed for the largest density we are able to handle $\rho_{3D}k^{-3} = 0.1$. Complementary data for other densities are presented in section 5.3.3. Statistical error bars obtained from the fitting procedure for the coupled dipole simulations are smaller than the size of the points.*

5.1.4 A graded-index waveguide

An interesting feature of atomic systems is the possibility to change dramatically the response of the system by varying the detuning Δ of the excitation light with respect to the resonance. We report in Fig. 5.4(a) the influence of the detuning on the experimental decay length ξ for the cloud of highest density. We observe a clear asymmetry around $\Delta = 0$: the decay length is larger for negative than for positive detunings, which indicates that photons are escaping more easily the sample when $\Delta > 0$. Clearly, the results of Fig. 5.4(a) cannot be explained by the dependence of Eq. (5.3) on Δ, which originates only from the photon scattering cross section by a single atom and is thus symmetric with respect to $\Delta = 0$.
We attribute the asymmetry mainly to a refractive-index gradient effect and we developed a simple model to describe this effect. We approximate the atomic slab by a continuous medium with a spatially-varying index of refraction $n(z)$ along the vertical direction and use the low-density expression for this index: $n(z) = 1 - [6\pi\rho_{3\mathrm{D}}(z)\Delta/\Gamma]/[k^3(1 + 4\Delta^2/\Gamma^2)]$. It is thus either larger than one below the resonance ($\Delta < 0$), or lower than one above the resonance ($\Delta > 0$). In our system, the density distribution $\rho_{3\mathrm{D}}(z)$ has an approximately gaussian shape with a maximum at $z = 0$ leading to a gradient of the index of refraction. For negative detuning, $n(z)$ decreases with $|z|$ from the center of the cloud. This gives rise to a phenomenon of light guiding close to the one encountered in optical waveguides, explaining qualitatively why the decay length gets larger. For $\Delta > 0$, the opposite effect is expected, with a decrease of the decay length.
More quantitatively, the effect of the refractive-index gradient on ξ can be estimated by modifying the geometrical picture of the inset in Fig. 5.3(a) to account for the *bending* of photon trajectories that escape the layer, as illustrated in the insets of Fig. 5.4(a) for $\Delta > 0$ and $\Delta < 0$. For negative detunings, this bending leads to a decrease of the maximum value of the emission angle θ_0 for which a photon leaves the cloud. Similarly, it leads to an increase of θ_0 for positive detunings. In section 5.3.4, we compute the equation for the trajectory $z(r)$ of a photon emitted in $z = 0$, $r = 0$ and determine the emission angle θ_0 that fulfills the "escape condition"

$$z(\ell) = \sqrt{\sigma/\pi}. \tag{5.4}$$

where $\sigma = 3\lambda_0^2/(2\pi)/(1 + 4\Delta^2/\Gamma^2)$. To find $z(r)$, we use the low-density expression of $n(z)$ given above, and approximate the density profile $\rho_{3\mathrm{D}}(z)$ of the atomic layer by an inverted parabola. The decay length obtained from this model is displayed in Fig. 5.4(b) as a function of Δ and shows a significant asymmetric behavior with detuning.
A similar asymmetry is also visible in our numerical simulations of coupled dipoles (see Fig. 5.4(b)). Complementary data presented in section 5.3.3 suggests that the asymmetry becomes more pronounced at higher densities (which cannot be explored with this simple analytic model). Note that differences show up between the numerical simulations and our geometrical model. In particular, the simulations display a weaker variation with Δ than the one predicted by Eq. (5.4). This effect could be attributed to light-induced dipole-dipole interactions between atoms. These interactions are known to give rise to a broadening and a blue shift of the line [186],

present in the simulations but not taken into account in Eq. (5.4). More generally, cooperative effects could be taken into account by modifying also the mean free path and the cross section, which are fundamental parameters of our model. Calculation of these parameters in the dense regime is however a difficult task that we leave for future work.

5.2 Discussion

Since the measured decay lengths are on the order of the optical wavelength, their measurement is rather challenging. We discuss two possible experimental limitations for this measurement. First, the finite resolution of the imaging system leads to an overestimate of the decay length, but our setup benefits from a good spatial resolution, and we estimate that this correction should be at most on the order of 10%. Second, light-induced forces caused by dipole-dipole interactions are strong when operating in the dense regime. We have thus chosen the duration of the excitation short enough to limit the atomic motion, while being long enough to probe the steady-state regime. With these parameters dipole-dipole interactions still lead to a small increase of the cloud size along the vertical axis. This increase of the cloud thickness (only in the illuminated region where the scattering rate is large) could favor the propagation of photons to a larger distance. For a pulse duration twice longer [a] we observed an increase of the decay length ξ by about 20 %.
Both the coupled dipole simulations and the geometrical model predict a variation of ξ with density and detuning qualitatively similar to the experimental results, but with a factor ~ 3 difference in the absolute value for ξ. A possible explanation for this discrepancy is the complex level structure of the rubidium atom. For instance, the averaging of the Clebsch-Gordan coefficients over all possible π transitions relevant for our incident linearly polarized light should at least lead to a correction of the effective single-atom scattering cross section which is not taken into account in our expression of the mean free path ℓ[b]. Taking into account this level structure on the determination of ξ requires complex simulations beyond the scope of this article [190].
An alternative approach would be to reproduce this study with atomic species like ytterbium and strontium which present well-isolated $J = 0$ to $J = 1$ transitions. One could also couple our method for producing thin slabs with the method to isolate an effective two-level system in a multilevel atom discussed in Refs [204, 198, 199] and based on the large Zeeman effect produced by an external magnetic field.
In summary, we have explored the diffusion of light in a dense and extended sample of fixed scatterers. Experiments with cold atomic systems are usually limited to lower densities. Still, the dense regime was explored in [205, 180, 190] but with a microscopic sample where light propagation cannot be investigated, and also in [160] but with a hot and thus Doppler-broadened cloud. Complementary studies on light

[a] The amplitude of the signal becomes too low for shorter pulses

[b] An average with equal weights on all the transition gives a cross section decreased by a factor 7/15, but it neglects any optical pumping effects during the excitation. The scattering cross section should also be modified to take into account the spectrum of the photons emitted by the illuminated region. Indeed, as the Rabi frequency of our excitation beam is on the order of Γ, we expect a modification of the fluorescence spectrum.

transport in photonic planar waveguides have also been reported, for instance, in Ref.[206]. However, our system reveals a unique combination of multiple scattering, high densities and guiding effects which can be tuned rather easily. Our experiment paves the way to a deeper understanding of the propagation of light in dense samples and possibly on the role of interference-induced (localization) effects in this geometry [207, 208]. Indeed, while the observation of photon localization is still elusive [207], presumably due to the vector nature of light detrimental to interference [208], the problem could be circumvented in a 2D system illuminated by a light field linearly polarized perpendicular to the disordered plane. Our atomic system could constitute a good candidate for that objective, using the decay length – directly controlled by the diffusion coefficient – as a probe for localization [209].

5.3 Methods

5.3.1 Preparation of the atomic cloud

We confine ^{87}Rb atoms in a combination of blue-detuned optical dipole traps. Atoms are strongly confined along the vertical z direction with a confinement frequency $\omega_z/2\pi = 1.9(1)\,\mathrm{kHz}$, leading to an approximately gaussian density distribution along z. In the xy plane, we use a flat-bottom potential, which produces a uniform disk-shaped atomic layer of radius $R = 20\,\mu\mathrm{m}$. The layer typically contains $1.7(2) \times 10^5$ atoms at a temperature of $T_0 = 270(10)\,\mathrm{nK}$. This corresponds to an r.m.s. thickness of the density distribution of $\Delta z = 0.26(1)\,\mu\mathrm{m}$.
We tune this density by varying the number of atoms in the $|F = 2, m_F = -2\rangle$ hyperfine ground state, which is sensitive to our light probe. The population in this state is controlled thanks to partial transfer from the $|F = 1, m_F = -1\rangle$ state in which the atoms are initially spin-polarized. As discussed in Ref. [186], dipole-dipole interactions play a dominant role at the densities achieved in our setup. Because of these interactions, the thickness of the cloud could increase, depending on its density, during the light excitation. We estimate that the effective cloud thickness, in the illuminated region, could reach at the end of the excitation the maximum value of $0.4\,\mu\mathrm{m}$.

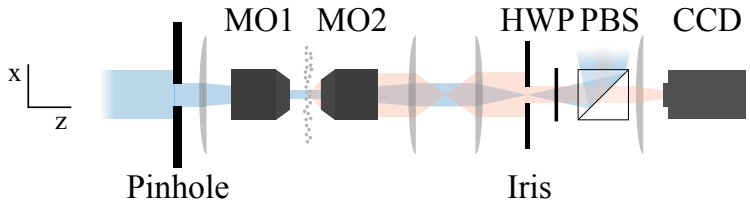

Figure 5.5 *– Schematics of the imaging system. A pinhole is imaged on the atomic cloud thanks to a microscope objective (MO1). The atomic fluorescence is imaged on a camera (CCD) thanks to a second and identical objective (MO2) and a set of lenses. Fluorescence is spatially filtered thanks to an iris and the detected polarization is chosen by adjusting a combination of a half-wave plate (HWP) and a polarization beam splitter (PBS).*

5.3.2 Imaging system

Our imaging system is depicted in Fig. 5.5. The fluorescence light emitted by the atomic cloud is collected using a microscope objective with a numerical aperture of 0.4. Using the full aperture of this objective leads to a deterioration of the sharpness of the decay signals we measure. We attribute this effect to residual optical aberrations which are important for photons propagating at large angle with respect to the optical axis. These aberrations can be due to the optics we used or to an imperfect alignment of these optics. To limit the effective aperture we use an iris (see Fig. 5.1). We have empirically adjusted its opening to get the sharpest decay while not decreasing too much the detected signal. We report in Fig. 5.6 the decay length and the signal measured for the atomic fluorescence and for the excitation light beam as a function of the opening of this iris. The atomic fluorescence signal is obtained for the densest cloud excited on resonance.

First, we consider the profile of the excitation light beam on the camera. This is still done by detecting the polarization perpendicular to the excitation light beam polarization but with unblocking the residual transmitted light, which originates from the non-perfect polarization components. Because of the finite optical resolution, the edges of the beam profile are not perfectly sharp. We apply the same procedure as for the fluorescence signal to determine an effective decay length from an exponential fit. We observe that the decay length and the signal amplitude are almost independent of this opening, as expected for a collimated beam impinging on the atoms which is thus not affected by the spatial filtering. It also shows that our optical system allows to measure decay lengths below $1\,\mu$m. Second, we consider the atomic fluorescence. The decay length which increases for large opening is almost constant for small openings ($4 < D_{\text{iris}} < 7\,\text{mm}$). The number of collected photons increases monotonically with the iris diameter. We have chosen for the data presented in section 5.1 an opening of $D_{\text{iris}} = 6.5\,\text{mm}$, inside the region where ξ is rather constant but maximizing the measured signal.

5.3.3 Coupled dipole simulations.

These simulations are performed following Ref. [181]. We consider a set of atoms with a $J = 0 \rightarrow J = 1$ transition. We draw randomly their position close to the experimental density distribution: atoms are confined in a disk and have a gaussian distribution along the z-direction with an r.m.s width of $0.3\,\mu$m. We compute the amplitude of the dipoles with an excitation localized inside a disk of diameter $5\,\mu$m. To obtain a quantity proportional to the fluorescence signal at a given position on the camera we compute the modulus square of each dipole. The decay lengths reported in Figs 5.3(b) and 5.4(b) are obtained by an exponential fit to the fluorescence signal in the range $r_1 = 2.7\,\mu$m to $r_2 = 4\,\mu$m, where r is the distance from the center. For each density we adapt the atom number in the simulations (from 100 up to 4000) and the number of repetitions on which the result of the simulations are averaged (from 20 to more than 10^5).

We show in Fig. 5.7 the results of these coupled dipole simulations for additional

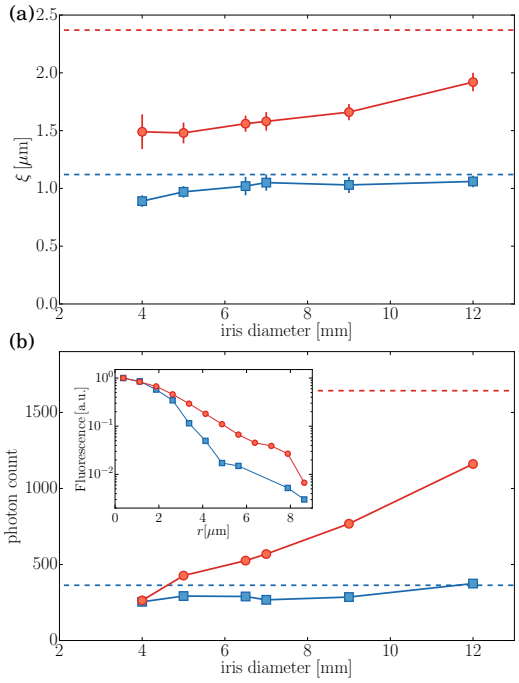

Figure 5.6 *– Influence of the filtering iris. Measured decay length (a) and total number of photons detected on the CCD camera (b) for the light excitation beam alone (squares) and for the atomic fluorescence (disks). For both graphs, the dashed lines are the corresponding results without the iris. Vertical error bars correspond to the standard deviation of the results of exponential fits to the data obtained with a bootstrap approach. Each data set is obtained from the average of 50 measurements. The inset in (b) shows the fluorescence and excitation light beam signals (both normalized to unity) for* $D_{\mathrm{iris}} = 6.5\,mm$.

values of the atomic density and a constant thickness. For all densities we observe a similar asymmetry as in Fig. 5.4. When increasing density, the resonance peak gets broader, as observed in transmission experiments [186]. Note that the density $\rho k^{-3} = 0.1$ is the highest value we could reach in our simulations and remains lower than the achieved experimental densities.

5.3.4 Semi-analytical model of light guiding

We recall that at any detuning, the decay length is given by

$$k\xi = \frac{k\ell}{\sqrt{1-\cos\theta_0}}, \tag{5.5}$$

where the variation of the maximum emission angle θ_0 with Δ is depicted in the insets of Fig. 5.4. When $\Delta = 0$, we have $\tan\theta_0 = \ell/\sqrt{\sigma/\pi}$, which straightforwardly leads to Eq. 5.3. When $\Delta \neq 0$, the geometry of the cone is modified by the changes of ℓ and σ with detuning, which are symmetric with respect to $\Delta = 0$. But, in addition, the photon trajectories are bent and θ_0 has to be determined by taking into account the curvatures of these trajectories.

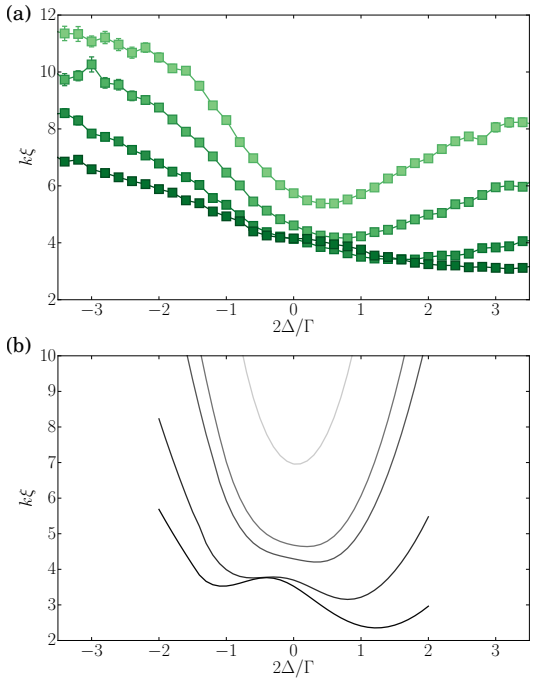

Figure 5.7 – *Role of the detuning. (a) Results from the coupled dipole model with $\rho_{3D}k^{-3}$=0.01, 0.02, 0.05, and 0.1 (from top to bottom) and with, for all curves, $k\Delta z = 0.3$. Error bars, which are mostly smaller than the size of the points, represent the statistical error obtained from the fitting procedure. (b) Results from the analytical model with $\rho_{3D}k^{-3}$=0.01, 0.02, 0.025, 0.05 and 0.1 (from top to bottom).*

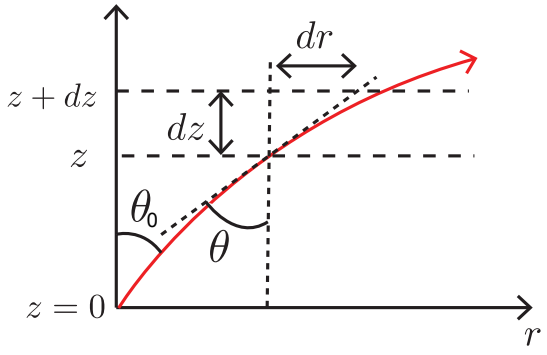

Figure 5.8 – *Parametrization of a photon trajectory.*

To estimate it, we use the parametrization shown in Fig. 5.8 (here displayed for $\Delta < 0$). The z axis is normal to the atomic layer, with $z = 0$ corresponding to the center of the layer where the density is maximum. From the figure we have $\sin\theta = dr/\sqrt{dr^2 + dz^2} = 1/\sqrt{1 + (dz/dr)^2}$. Using that $\sin\theta = \sin\theta_0\, n(z=0)/n(z)$ (Snell's law), we infer

$$\left(\frac{dz}{dr}\right)^2 = \left[\frac{n(z)}{n_0 \sin\theta_0}\right]^2 - 1, \tag{5.6}$$

where $n_0 = n(z = 0)$. To solve Eq. (5.6), we use a low-density approximation for the

refractive-index profile of the layer:

$$n(z) \simeq 1 - \frac{3\pi\rho_{3\mathrm{D}}(z)}{k^3}\frac{\delta}{1+\delta^2}, \tag{5.7}$$

where $\delta = 2\Delta/\Gamma$ and $\rho_{3\mathrm{D}}(z)$ is the density profile of the cloud. Note that the change of the index of refraction is maximal for $\delta = 1$ and this formula thus holds for $\rho_{3\mathrm{D}}k^{-3} < 2/(3\pi)$. To make the calculation analytical, we approximate the density profile by a parabolic one such that $n(z=0) = n_0 = 1 - (3\pi\rho_{3\mathrm{D}}\delta)/[k^3(1+\delta^2)]$ and $n(z = \sqrt{\sigma/\pi}) = 1$:

$$n(z) \simeq n_0 - \frac{n_0 - 1}{\sigma/\pi}z^2. \tag{5.8}$$

Inserting this profile into Eq. (5.6), we find the differential equation for the photon trajectory:

$$\frac{d^2z}{dr^2} + \frac{2(n_0-1)z}{n_0(\sigma/\pi)\sin^2\theta_0} - \left(\frac{n_0-1}{n_0}\right)^2 \frac{2z^3}{(\sigma/\pi)^2\sin^4\theta_0} = 0, \tag{5.9}$$

whose solution is given by

$$\begin{aligned} z(r) \;=\; & \frac{\sqrt{\sigma/\pi}\cos^2\theta_0}{\sqrt{n_0-1}}\frac{1}{1-\mathrm{sg}(\Delta)\sin\theta_0}\frac{1}{\sqrt{1+\mathrm{sg}(\Delta)\sin\theta_0}} \\ & \times \mathrm{sn}\left[\frac{r\sqrt{n_0-1}}{\sqrt{\sigma/\pi}\sin\theta_0}\sqrt{1-\mathrm{sg}(\Delta)\sin\theta_0}, \frac{1+\mathrm{sg}(\Delta)\sin\theta_0}{1-\mathrm{sg}(\Delta)\sin\theta_0}\right], \end{aligned} \tag{5.10}$$

where sn is the sinus Jacobi elliptic function, sg the sign function and $n_0 = n(z = 0) = 1-(3\pi\rho_{3\mathrm{D}}\delta)/[k^3(1+4\Delta^2/\Gamma^2)]$. The angle θ_0 is finally obtained from the implicit equation

$$z(r=\ell) = \sqrt{\sigma/\pi}. \tag{5.11}$$

For positive detuning, Eq. (5.11) always has a solution for θ. At large detuning, this solution approaches $\pi/2$, a regime where $k\xi(\delta \gg 1) \simeq k\ell$ (note that this asymptotic result coincides with the prediction of Eq. 5.3 at large detuning). For negative detuning on the other hand, Eq. (5.11) has no solution when δ is smaller than a certain δ_c, which is due to the phenomenon of total reflection. When $\delta < \delta_c$, the escape probability p is no longer limited by the presence of the surrounding scatterers but by the bending of trajectories. In this regime, the radius of the escape cylinder is thus no longer given by ℓ, but by the length ℓ_c where $dz/dr(r=\ell_c) = 0$ (ℓ_c coinciding with ℓ exactly at $\delta = \delta_c$). Consequently, when $\delta < \delta_c$ the angle θ is a solution of the implicit equation

$$z(\ell_c) = \sqrt{\sigma/\pi} \;\text{ with }\; \frac{dz}{dr}(r=\ell_c) = 0. \tag{5.12}$$

The curves shown in Figs 5.3, 5.4 and 5.7(b) are obtained by numerically solving Eq. (5.11) (for $\delta > \delta_c$) and Eq. (5.12) (for $\delta < \delta_c$) for θ_0, then computing $k\xi$ using Eq. (5.5). The asymmetry of the decay length with detuning is more pronounced at low densities for the coupled dipole model than for the guiding model. This indicates

that our simple guiding model gives a good qualitative picture but, in addition, cooperative effects plays a substantial role in our experiments. One could take into account, at first order, these cooperative effects by a suitable modification of the cross section and linewidth appearing in Eq. (5.5).

III Out-of-equilibrium and superfluid studies

6

Merging of N independent condensates

6.1 Motivation for this work

6.1.1 Kibble-Zurek mechanism and its study in bulk systems

The Kibble-Zurek theory made a breakthrough in the domain of out-of-equilibrium physics by describing the emergence of an ordered phase after a quench through a second order phase transition. In particular it quantitatively predicts the related formation of topological defects.
Phase transitions are usually described by an order parameter, such as the magnetization in the case of ferromagnetic system, or the macroscopic wave function for Bose-Einstein condensation. Consider a system in equilibrium, described by a coherence length ξ. A second order phase transition can be characterized by several critical exponents. We will use the static critical exponent ν, linked to the divergence of ξ when the temperature approaches the critical temperature T_c, as

$$\xi \propto |T - T_c|^{\nu}, \tag{6.1}$$

and the dynamical critical exponent z, characterizing the relaxation time τ needed to establish these diverging correlations,

$$\tau \propto \xi^{z}. \tag{6.2}$$

As ξ diverges when the temperature of the system decreases towards T_c, τ diverges as well, making the establishment of equilibrium harder and harder. This leads during the cooling process to a "freeze-out" period, starting when the relaxation time τ becomes larger than the remaining time before reaching the transition. The correlation length is then assumed to remain fixed at a value $\hat{\xi}$. In the case of BEC, this results in the formation of phase domains of typical size $\hat{\xi}$ that have random independent values of the order parameter.
In most systems, one cannot access the phase domains, but only the result after some time evolution[a]. During this coarsening dynamics, the different domains merge and might nucleate topological defects. These defects are long-lived and their average number might be predicted. In his seminal paper [210], Zurek proposed to test this mechanism with ^{4}He. He proposed a thin ring geometry, with the width of the ring smaller than the average size of a domain, to relate simply the number of domains

[a]The freezing hypothesis has nevertheless been verified in the group of Zoran Hadzibabic [91], measuring the coherence length (and thus the average domain size) at short times after the quench.

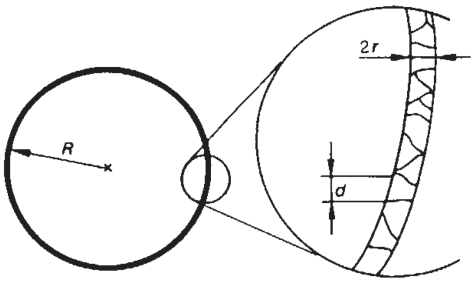

Figure 6.1 *– Geometry proposed by Zurek for ^{4}He. For a ring of circumference $C = 2\pi R$, there will be about C/d domains, which would lead after coarsening dynamics and repeating the experiment in a distribution of supercurrents of width $\approx \sqrt{C/d}$. Figure extracted from [210].*

.

to the probability of formation of topological defects. In figure 6.1, the different expected domains in the ring geometry can be seen.
To determine the probability of nucleating a topological defect, he assumed a linear ramp of temperature $T(t)$, with $T(0) > T_c$, and T_c reached at time t_c:

$$T(t)/T_c = 1 + (t_c - t)/\tau_Q, \tag{6.3}$$

where τ_Q is the characteristic quench time. He then obtained a power-law scaling of the typical domain size with the quench time

$$\hat{\xi} \propto \tau_Q^{\nu/(1+\nu z)}. \tag{6.4}$$

It is then possible, using the geodesic rule[a], to compute the probability to nucleate a topological defect, which for the case of BEC are vortices[b]. This will be done rigorously in section 6.2.2, and leads for the ring geometry to a width of the distribution of quantized supercurrents proportional to the square root of the number of domains. This experiment has never been realized with ^{4}He to our knowledge, but has been done with long symmetric Josephson tunnel junctions in [213] and with cold atoms previously in our group in [214].
Other studies focussing on the detection of topological defects in the bulk include for example works on ^{3}He [215, 216], ^{4}He [217], liquid crystals [218], trapped ions [219, 220, 221], ferroelectric materials [222], bulk superconductors [223] and cold atoms (at the MOT stage) in [224]. For ultracold atoms, the first studies were made in harmonic traps [225, 226, 227], and then in uniform traps [214, 91, 193], which have been reviewed in [228]. These experiments rely on the detection of topological defects, and an assumption has to be made to link the size of the domains to the average number of defects, using the geodesic rule. It is thus important to verify that the coarsening dynamics happens as predicted by the KZM, which is the object of this chapter.

[a] This rule expresses the fact that the system tends to minimize the absolute value of the relative phase between neighboring domains due to energetic reasons [211, 212].

[b] or quantized supercurrents for the ring geometry.

6.1.2 Disentangling the Kibble-Zurek mechanism: study of coarsening dynamics

The possibility to tune dynamically the potential imprinted on the atoms allows us to test the second part of the KZM, *ie* the coarsening dynamics, and thus the relevance of the geodesic rule for our system. This study extends earlier works on the merging of two [229] and three [230] condensates in a harmonic trap and on the dynamics of a large number of condensates in a two-dimensional (2D) optical lattice [231].
This has also been investigated in a ring geometry using Josephson junctions in [232]. The authors measured the flux randomly generated in a $YBa_2Cu_3O_{7-\delta}$ (YBCO) loop interrupted by 214 grain-boundary Josephson junctions in series. The YBCO becomes a superconductor at $T_c = 90$ K. In their experimental protocol, they cool the sample from 100 to 77 K. At 90 K, segments of the film separating the junctions become superconducting, but the junctions themselves are still normal and the superconducting segments are effectively separated. The coupling energy of the junction is indeed much smaller than $k_B T$. But when the temperature decreases further, the critical currents of the junctions increase, and the whole loop becomes coherent. A comparison of timescales shows that all junctions close in a time much shorter than the time needed for the coherence in the whole loop to establish, validating the analogy with the KZM. The result of their paper is the width of the gaussian distribution of fluxes measured inside the loop, obtained by repeating the cooling of the system a sufficient number of times. This width is about two times larger than what is expected from the geodesic rule. They however recover a theoretical value closer to their experimental one by taking the true energy dependence of a Josephson junction into account, which is not proportional to the gradient of the phase squared as is assumed in the geodesic rule.
More generally, the thermalization of isolated quantum systems still contains open questions today. Investigating phase relaxation as is done in the following work might help to understand better these dynamics.

6.2 Study of the relaxation dynamics in the merging of N independent condensates

The following sections of this chapter were initially published in [233], and are reproduced almost without modifications. Only titles have been added and some phrases changed to be consistent with the rest of the thesis.

In this chapter we investigate the relaxation dynamics of up to $N = 12$ uncorrelated Bose-Einstein condensates (BECs) after merging them in a ring-shaped optical trap. We measure the statistical distribution of metastable supercurrents and relate their emergence to the evolution of the phase defects generated at the boundaries of the BECs. The experimental protocol is depicted in Fig. 6.2(a). Initially the condensates are characterized by random phase differences $\delta\phi_i$ $(i = 1, ..., N)$ between condensates i and $i + 1$, that can lead to a net phase accumulation around the ring after merging

[Fig. 6.2(b)]. Due to the single-valuedness of the wavefunction, the phase winding around the ring has to be equal to $2\pi\nu$, with winding number $\nu \in \mathbb{Z}$. This correponds to the formation of supercurrents with quantized velocities, which we detect through matter-wave interference [Fig. 6.2(c)] with an additional ring-shaped condensate with uniform phase [234, 214]. Our results show that the magnitude of the supercurrent scales in quantitative agreement with the geodesic rule.
Additionally we explore the underlying dynamics by merging pairs of neighboring condensates. First, we study it globally by monitoring the evolution of the winding-number distribution as a function of time. Secondly, we detect local phase defects and study their dynamics in a time-resolved manner. The observed relaxation timescales are compatible with the evolution of soliton-like phase defects.

6.2.1 Experimental protocol

The experiment started by loading a cold cloud of $1.4(2) \times 10^5$ ^{87}Rb atoms in the $|F = 1, m_F = 0\rangle$ state into a pancake-type dipole trap with tight harmonic confinement along the vertical direction, $\omega_z = 2\pi \times 1.58(1)\,\mathrm{kHz}$, and negligible confinement in the xy-plane [116]. The in-plane trap was shaped using a digital micromirror device (DMD) in direct imaging with an optical resolution of $\sim 1\,\mu$m to create a uniform double-ring trap as illustrated in Fig. 6.2(b). All experimental studies were performed in the outer ring, which was partitioned into several segments, while the inner ring served as a uniform phase reference for detection [234, 214]. The distance between the segments as well as between the two rings was $2.5(2)\,\mu$m, defined as the full width at half maximum of the density dip in the measured in-situ distributions [Fig. 6.2(b)]. This separation is large enough to enable the formation of uncorrelated condensates, as shown in section 6.3.3.
After 2 s evaporative cooling, we reached a final temperature of $T < 20\,\mathrm{nK}$, thereby entering the quasi-2D regime $k_B T < \hbar\omega_z$, with k_B the Boltzmann constant and $\hbar$ the reduced Planck constant. The upper temperature limit of 20 nK is the smallest detectable temperature using our calibration method. This corresponds to 2D phase-space densities $\mathcal{D} = \lambda_T^2 n > 80$ deeply in the superfluid regime[a]; here $n = 36(4)/\mu\mathrm{m}^2$ is the 2D atomic density, $\lambda_T = \hbar\sqrt{2\pi/(mk_BT)}$ the thermal wavelength and m the mass of one atom.
Subsequently, we merged the BECs in the outer ring within 10 ms by decreasing the width of the potential barriers [Fig. 6.2(b)] using our dynamically configurable DMD. The velocity at which the barriers were closed was chosen small compared to the speed of sound c_0 in order to prevent the formation of shock waves and high-energy excitations [235, 236]. For our experimental parameters $c_0 = \sqrt{ng_{2\mathrm{D}}/m} \approx 1.4(1)\,\mathrm{mm/s}$, where $g_{2\mathrm{D}} = g_{3\mathrm{D}}/(\sqrt{2\pi}l_z)$ is the 2D interaction parameter, $g_{3\mathrm{D}} = 4\pi\hbar^2 a/m$, $a = 5.3\,\mathrm{nm}$ the scattering length and $l_z = \sqrt{\hbar/(m\omega_z)} = 0.27\,\mu$m the harmonic oscillator length.
After a typical relaxation time of 0.5 s, we detected the phase winding after 2D

[a] According to the Mermin-Wagner theorem there is no true long-range order in low-dimensional systems, however, for our experimental parameters the characteristic correlation length exceeds the size of the condensate by several orders of magnitude, which enables the formation of a Bose-Einstein condensate.

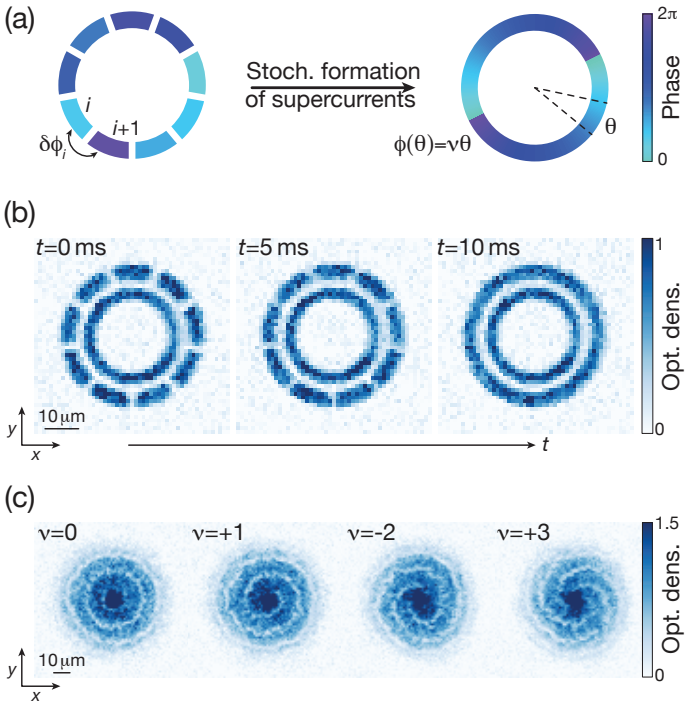

Figure 6.2 – *Experimental protocol. (a) Illustration of the experimental sequence. An annular trap is partitioned into N segments of equal length. Uncorrelated BECs are prepared in these segments with random phase differences $\delta\phi_i$, $i = 1, ..., N$, between adjacent condensates. After merging into a single annular condensate, supercurrents with winding number $\nu \in \mathbb{Z}$ are formed. (b) In-situ density distribution in the ring trap for $N = 9$ at different times t during the merging. The outer ring has a mean radius of $19.5\,\mu m$ and a width of $5\,\mu m$. The inner ring serves as a phase reference for the detection. It has a mean radius of $13\,\mu m$ and a width of $4\,\mu m$. Each image is an average over 5 or 6 experimental realizations. (c) Matter-wave interference after a 2D time-of-flight (TOF) of 6 ms. The chirality of the pattern and the number of spiral arms reveal the winding number ν of the supercurrent in the outer ring.*

time-of-flight by releasing the in-plane confinement abruptly while keeping the vertical one. We recorded the resulting interference pattern after 6 ms using standard absorption imaging along the z-direction [Fig. 6.2(c)]. The chirality of the pattern and the number of spiral arms are a direct measure of the winding number ν of the supercurrent that was formed in the outer ring [234, 214]. In an independent calibration measurement (see section 6.3.2), we found that the probability of creating a supercurrent in the inner ring was $\lesssim 0.6\%$.

6.2.2 Principle of the measurements

Each repetition of the experiment results in a different set of random phase differences $\delta\phi_i$ that leads to the formation of a supercurrent with winding number $\nu = \sum_{i=1}^{N} \delta\phi_i/(2\pi)$, where $-\pi < \delta\phi_i \leq \pi$. The interval for the phase differences $\delta\phi_i$ is

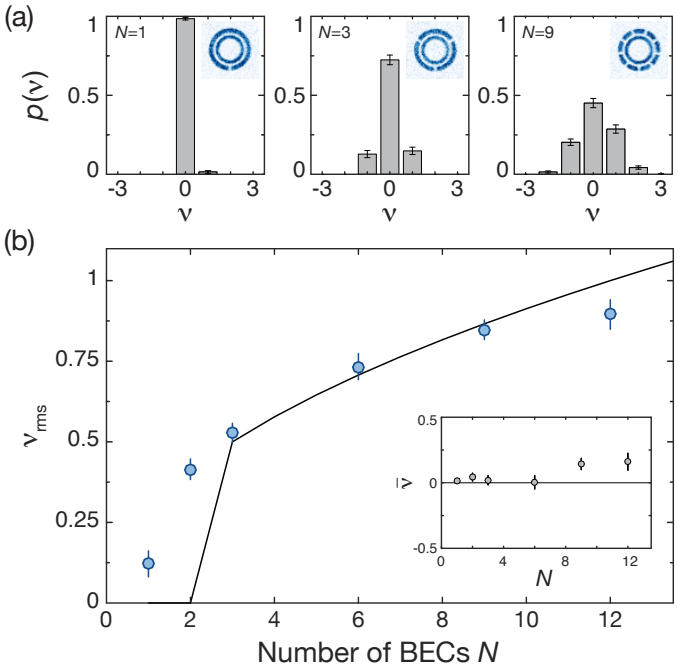

Figure 6.3 *– Formation of supercurrents as a function of the number of BECs N. (a) Probability distributions $p(\nu)$ for $N = 1$, 3 and 9 obtained from $\mathcal{M} = 202, 238$ and 388 measurements respectively. The insets display in-situ images before the merging averaged over 4-6 realizations. (b) Measured rms-width ν_{rms} of the probability distributions as a function of N. Each data point consists of $\mathcal{M} > 200$ independent measurements. The corresponding mean values $\bar{\nu}$ are displayed in the inset. The solid line is the predicted scaling given in Eq. (6.5). All error bars display the combined uncertainty from the experimental determination of the winding number and the statistical error due to a finite number of measurements $\mathcal{M}$, which was evaluated using a bootstrapping approach.*

chosen according to the geodesic rule, which expresses the fact that the system tends to minimize the absolute value of the relative phase between neighboring condensates due to energetic reasons [211, 212]. By repeating the measurement $\mathcal{M}$ times we extracted the corresponding probability distributions $p(\nu)$ as illustrated in Fig. 6.3(a). We observe an increase of the probability for non-zero winding numbers with N resulting in a broadening of the distribution. The measured center $\bar{\nu} = \sum_\nu p(\nu)\nu$ and rms-width $\nu_{\mathrm{rms}} = \sqrt{\mathcal{M}/(\mathcal{M}-1)\sum_\nu p(\nu)(\nu-\bar{\nu})^2}$ of the individual distributions are depicted in Fig. 6.3(b).

Ideally the smallest number of domains that allows for the formation of topological defects is three. In this case the probabilities $p_{\mathrm{th}}(\nu)$ can be computed following simple arguments [237, 230]. There are three possible cases: if $\delta\phi_1 + \delta\phi_2 > \pi$, the total sum of all phase differences has to amount to 2π, if $\delta\phi_1 + \delta\phi_2 < -\pi$ the total sum amounts to -2π and for all other cases it vanishes. The resulting probabilities are $p_{\mathrm{th}}(+1) = p_{\mathrm{th}}(-1) = 1/8$, which is compatible with our experimental results $p(+1) = 0.15(2)$ and $p(-1) = 0.13(2)$ displayed in Fig. 6.3(a). In general the probability distribution is determined by the Euler-Frobenius distribution [238] and

we obtain

$$\nu_{\mathrm{rms}}(N) = \begin{cases} 0\ , & \text{if } N < 3 \\ \dfrac{1}{2\sqrt{3}}\sqrt{N}\ , & \text{if } N \geq 3\ . \end{cases} \tag{6.5}$$

The distribution is symmetric around $\nu = 0$, with $\bar{\nu} = 0$, which is in agreement with our experimental data obtained for small N [Fig. 6.3(b)]. For $N \geq 9$ there seems to be a small systematic shift to positive values.

6.2.3 Results for the number of segments

Our experimental results shown in Fig. 6.3(b) are in agreement with the predicted scaling for $N \geq 3$. There is a discrepancy for $N = 1$, where we measure a non-zero probability for the formation of supercurrents $p(\nu \neq 0) = 1.5(8)\%$. We attribute this to phase fluctuations of the condensate due to finite temperature effects, which are enhanced for larger systems. We tested that reducing the radius of the condensate by one third significantly reduces the probability for non-zero winding numbers. For $N \geq 3$ thermal fluctuations are not expected to have a large influence because the length of the condensates is smaller. Regarding the case of $N = 2$ we found that this particular configuration was very sensitive to the alignment of our trap. Small trap inhomogeneities had a significant impact on the obtained distributions.
For the largest number of condensates $N = 12$ we measure slightly smaller values than expected, most likely due to an increased sensitivity to experimental imperfections and overlapping timescales. If the merging of the BECs is performed too slowly, there are two main effects that can lead to a reduction of ν_{rms}. If supercurrents are already formed during the merging, their lifetime could be reduced substantially due to the presence of residual weak potential barriers [56]. At the same time an asynchronous merging of the barriers could effectively reduce the total number of initial condensates, if the phase of neighboring condensates homogenizes before the merging is complete. We have investigated this in more detail for $N = 9$ and found a significant reduction of the winding numbers for merging times larger than 50 ms (see section 6.3.4). Both effects are expected to be more critical for increasing N.
We typically wait 0.5 s after merging the condensates before detecting the supercurrents. This waiting time is short compared to the lifetime of the supercurrents in our trap (see section 6.3.5). Indeed we observe no significant decay of the supercurrents for waiting times on the order of 10 s. On the other hand it is long enough to let the system relax to a steady state with a smoothened phase profile, without a significant number of defects in the interference pattern.

6.2.4 Results on time evolution

In order to gain a deeper insight into the underlying relaxation dynamics, we performed two separate experiments. First, we probed the evolution of the winding number distribution by merging the BECs on the ring in two successive steps. The sequence started by merging pairs of neighboring condensates within 10 ms to reduce the number of condensates by a factor of two, then we let the system relax for a

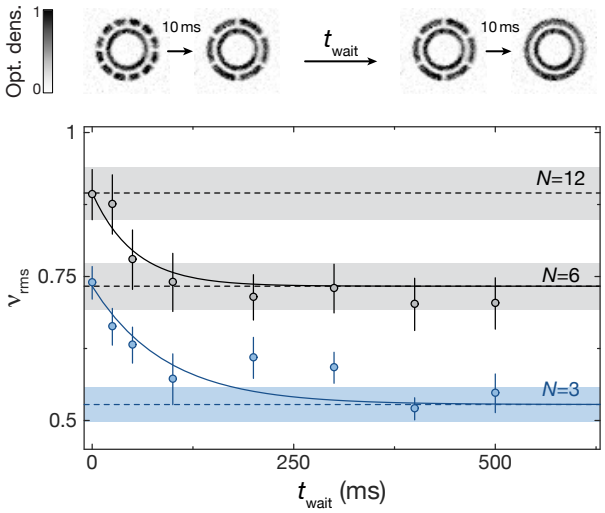

Figure 6.4 *– Relaxation dynamics from N to $N/2$ condensates, when merging them in two successive steps. The in-situ images above the main graph illustrate the experimental sequence for $N = 12$. Each image is an average over 5 individual measurements. The main graph depicts our experimental results for $N = 12$ (black) and $N = 6$ (blue). Each data point consists of $\mathcal{M} > 200$ measurements. The corresponding mean values $\bar{\nu}$ are shown in section 6.3.6. The error bars depict the uncertainty obtained from our finite number of measurements $\mathcal{M}$ and the experimental uncertainty in the determination of the winding numbers. The dashed lines indicate the measured values shown in Fig. 6.3(b) and the shaded areas illustrate the corresponding error bars. The solid lines are fits of exponential functions $f_j(t_{wait}) = A_j e^{-t_{wait}/\tau_j} + B_j$, $j = \{6, 12\}$, to our data, where τ_j is the only free fit parameter and the other variables are determined by the dashed lines extracted from Fig. 6.3(b).*

variable time t_{wait} and subsequently merged the remaining $N/2$ condensates in 10 ms into a single annular BEC (Fig. 6.4). After an additional evolution time of 0.5 s we detected the probability distributions $p(\nu)$ using the detection method explained above.

We identify two limiting cases for the data shown in Fig. 6.4. If there is no additional wait time ($t_{\mathrm{wait}} = 0$) between the two merging steps, the system has not enough time to relax and the probability distribution resembles the one discussed in Fig. 6.3, where all condensates were merged in a single step. On the other hand, if t_{wait} is longer than the relaxation time, the phase of neighboring condensates homogenizes after the first step, so that we effectively reduce the number of initial phase domains to $N/2$ and the distribution approaches the one for $N/2$ initial BECs merged in a single step. The measurements were performed for $N = 12$ and $N = 6$ and the dashed lines indicate the limiting cases explained above. In order to extract a timescale for the relaxation, we fit an exponential decay to each of the two datasets. The amplitude and offset of the fitting function are determined by the data points displayed in Fig. 6.3(b). One can infer two different timescales $\tau_{12} = 52(17)$ ms and $\tau_6 = 90(30)$ ms associated with the relaxation dynamics, which most likely depend

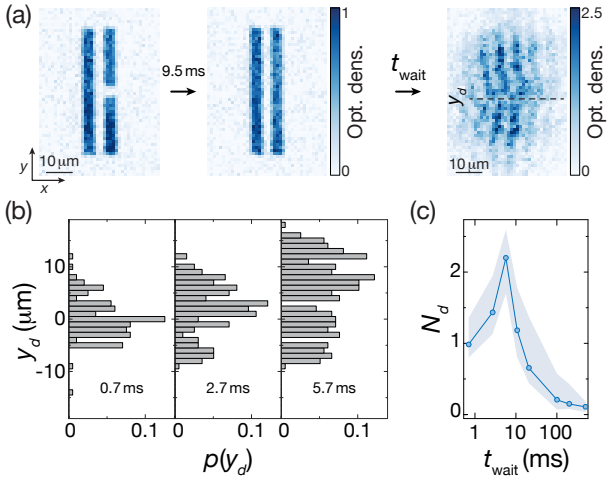

Figure 6.5 – *Defect dynamics. (a) In-situ density distribution of two line-shaped condensates (first two images) with dimensions* $50\,\mu m \times 5\,\mu m$ *before and after the merging (averaged over 4 individual realizations). The condensates are separated by* $3\,\mu m$*. After merging the condensates in* $9.5\,ms$ *the system evolves for a variable time* t_{wait}*. Phase defects are detected by matter-wave interference after TOF (image on the right). A typical image for* $t_{wait} = 0.7\,ms$ *is depicted on the right. The phase defect at position* y_d *is highlighted by the dashed line. (b) Position distribution* $p(y_d)$ *of the phase defects as a function of the waiting time* t_{wait} *evaluated from 200 individual measurements. The histograms are normalized by the total number of measurements. Phase dislocations are detected, if the phase difference between neighboring pixels (corresponds to* $1.16\,\mu m$ *in the atomic plane) is larger than* 0.3π *(see section 6.3.7). (c) Mean number of phase defects* N_d *as a function of time. The data was evaluated using a threshold of* 0.3π*. The shaded area illustrates the sensitivity due to this analysis (upper bound:* 0.16π*, lower bound:* 0.43π*).*

on the spatial extent of the condensates, that differ by almost a factor of two for the two datasets.

In a second set of measurements we focus on the microscopic relaxation dynamics via the time-resolved detection of local phase defects. We merged two condensates and probed the evolution of the phase profile through interference with a reference condensate (Fig. 6.5a). The length of each condensate is comparable to the length of one segment studied in the relaxation dynamics discussed above for $N = 6$. At short times ($\sim 1\,ms$), we observe a phase defect in the center of the fringes, at the original position of the potential barrier (Fig. 6.5b). With increasing time more phase defects appear and also start to propagate. After 5 ms the number of defects decays and we find an almost uniform distribution of their positions[a]. At long times ($> 100\,ms$) almost all defects have disappeared in agreement with the results displayed in Fig. 6.4.

We interpret the observed dynamics by the formation of dark solitons at the position

[a]The asymmetry in the position distribution of the phase defects (third panel of Fig. 6.5b) is due to a bias in the contrast of the interference fringes.

of the potential barrier, whereby their shape depends on the random phase differences between neighboring condensates [239, 240, 241]. Subsequently, the generated excitations propagate, interact with each other and eventually decay [242, 241] to form a steady state with a smoothened phase profile (Fig. 6.4b,c). Note, that the lifetime of solitonic excitations is typically short for 3D systems, but can be strongly enhanced in low-dimensional geometries [243, 226, 227]. The propagation speed of dark solitons depends on their depth and is at maximum equal to the speed of sound c_0, which is compatible with the observed relaxation timescales. The round-trip time at c_0 in the ring trap is about 90 ms for the configuration studied in Fig. 6.3.

6.2.5 Conclusion

In conclusion, we have reported the first quantitative study of the $\sqrt{N}$-scaling as predicted by the geodesic rule and show that the underlying relaxation dynamics is consistent with the formation of soliton-like defects. Future experiments could benefit from phase-imprinting techniques [239, 240, 241] to study the dynamics in a fully deterministic manner. In particular, it would be interesting to study the dynamics as a function of temperature and geometry.

6.3 Supplementary information

6.3.1 About the experimental sequence

The experimental sequence started by loading a cold cloud (> 500 nK) of ^{87}Rb atoms into a blue-detuned optical potential at wavelength $\lambda = 532$ nm. In the vertical direction the atoms were confined by an optical accordion with an initial lattice spacing of 11 μm. The in-plane confinement was provided by an additional laser beam that was shaped with a digital micromirror device (DMD) to engineer almost arbitrary in-plane trapping geometries. A detailed description of the experimental setup can be found in Ref. [116].
In order to optimize the final atom number in the double-ring trap, displayed in Fig. 6.2(b), we loaded the atoms into a disk-shaped trap with a radius of about 30 μm. Using the dynamical mode of our DMD we then displayed a movie that successively changed the trap from the disk to the final double-ring configuration. The movie consisted of 20 images and had a duration of 0.2 s. The last image of this movie abruptly introduced the potential barriers to partition the outer ring into N individual segments. At the same time we compressed the optical accordion to a final lattice spacing of 5.6 μm [116]. This has the advantage that we can lower the power of the accordion beams, which reduces the strength of defects in the optical potential, while keeping a strong harmonic confinement along the z-direction.
As a next step we implemented a protocol to generate a reliable uniform phase in the inner ring, which is important for our interference-based detection technique [234, 214]. In order to achieve that, we introduced an additional barrier in the inner ring simultaneously with the ones in the outer ring. This prevents the formation of random supercurrents in the inner ring during evaporation [56]. We cooled the

atoms within 2 s by lowering the power of the dipole trap. Using an independent temperature calibration we extracted a final temperature of $T < 20\,\mathrm{nK}$. This value corresponds to the lowest detectable temperature using our calibration method.
Subsequently, we slowly removed the barrier of the inner ring by displaying a movie of 19 images with our DMD that decreased the width of the barrier gradually in 1.9 s from 2.5(2) μm to zero. This procedure ensures that we have a probability for creating a supercurrent in the inner ring that is $\lesssim 0.6\%$. This value was evaluated from an independent calibration measurement explained in the following section.
Subsequently we merged the segments in the outer ring within 10 ms by displaying a movie that consisted of 20 images on the DMD with decreasing barrier widths. We then let the system evolve for 500 ms and performed a 2D time-of-flight (TOF). For that we suddenly switched off the in-plane trap while keeping a slightly increased vertical confinement with frequency $\omega_z = 2\pi \times 2\,\mathrm{kHz}$. After an expansion time of 6 ms we recorded the interference pattern along the z-direction using standard absorption imaging.
All in-situ images presented in this chapter were taken with partial imaging. The displayed densities correspond to 15% of the total density and the imaging intensity was about $I/I_{\mathrm{sat}} = 0.2$, where $I_{\mathrm{sat}} = 1.67\,\mathrm{mW/cm^2}$. To obtain a better contrast for the time-of-flight images we imaged the total atomic density at higher imaging intensity $I/I_{\mathrm{sat}} = 0.6$.

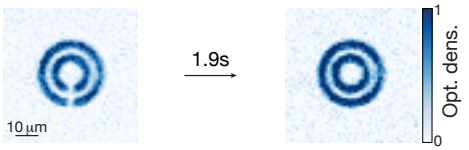

Figure 6.6 *– Calibration measurement for the inner ring depicted in Fig. 6.2(b) which serves as a uniform phase reference in our detection scheme. In-situ images of the atoms in the double-ring trap averaged over 6 and 10 individual images respectively. Initially there is a* 2.5(2) μ*m-wide barrier in each ring (image on the left). The image on the right shows the atomic density distribution after removing the barriers in* 1.9 *s.*

6.3.2 Phase reference of the inner ring

To investigate the formation of supercurrents in the inner ring using the protocol described in the previous section, we loaded the atoms into a double-ring trap with slightly smaller dimensions (Fig. 6.6). The outer ring has the same dimensions as the inner ring depicted in Fig. 6.2(b), with an inner radius of 11 μm and an outer one of 15 μm. The second ring is smaller with an inner radius of 5 μm and an outer one of 9 μm. The experimental sequence started by loading the atoms into this double ring potential, where we have introduced a 2.5(2) μm-wide barrier in both rings (Fig. 6.6). Using the detection method described above, we took $\mathcal{M} = 159$ measurements without observing any non-zero phase winding. In order to estimate the probability for non-zero phase windings in the ring we compute an upper bound according to the maximum likelihood estimation. According to this, the true probability $p(\nu \neq 1)$

is likely to be smaller than $1/159 = 0.6\%$ [244].

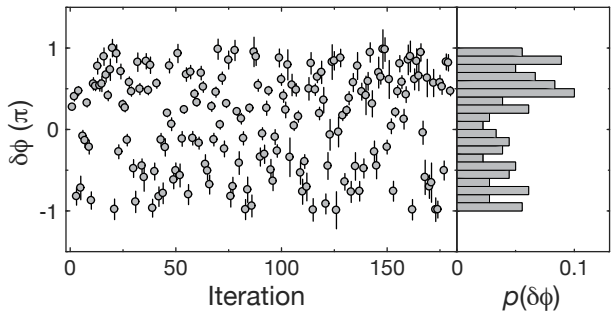

Figure 6.7 *– Relative phase between the two ring-shaped condensates. The relative phases $\delta\phi$ were evaluated using the data displayed in Fig. 6.3(a) for $N = 1$ and restricting the analysis to images with $\nu = 0$. The results are shown in the left panel. The corresponding histogram displaying the binned probabilities $p(\delta\phi)$ is depicted in the right panel.*

6.3.3 Independence of BECs

A crucial ingredient of our experimental protocol is the ability to form uncorrelated condensates in our trap via the introduction of additional potential barriers. The height of the potential is determined by the total depth of the optical potential and the width of $2.5(2)\,\mu$m is the full width at half maximum of the density dip in the in-situ distribution. In order to test the independence of the individual condensates we evaluated the relative phase $\delta\phi$ between two ring-shaped condensates with uniform phases separated by $2.5(2)\,\mu$m. For the analysis we took the data displayed in Fig. 6.3(a) for $N = 1$ and removed all images with non-zero phase winding. For each image we computed the radial average and subtracted the background obtained by the total average of all images. The resulting density modulation was fitted with a sinusoidal function $f(r) = A\sin(kr + \delta\phi)$ to determine the phase of the interference pattern $\delta\phi$ (Fig. 6.7). The period k was set to the mean period obtained from the individual fit results and the amplitude A and the phase offset $\delta\phi$ were free fit parameters. In total we have evaluated $\mathcal{M} = 180$ images, where we have excluded those, where the fit error of $\delta\phi$ exceeded 0.25π. The obtained distribution (Fig. 6.7) is characterized by the mean values: $\langle\cos(\delta\varphi)\rangle = 0.11(5)$ and $\langle\sin(\delta\varphi)\rangle = -0.16(5)$. Ideally these values would vanish for a perfectly random distribution. We attribute the residual deviations to a systematic error in our fitting protocol, which is mainly caused by the non-uniform shape of the overall time-of-flight distribution. The assumption of initially uncorrelated BECs is further supported by additional experimental tests, where we have measured the probability distribution for $N = 9$ for different thicknesses of the potential barriers and did not observe any significant change when varying the width by $\sim \pm 20\,\%$.

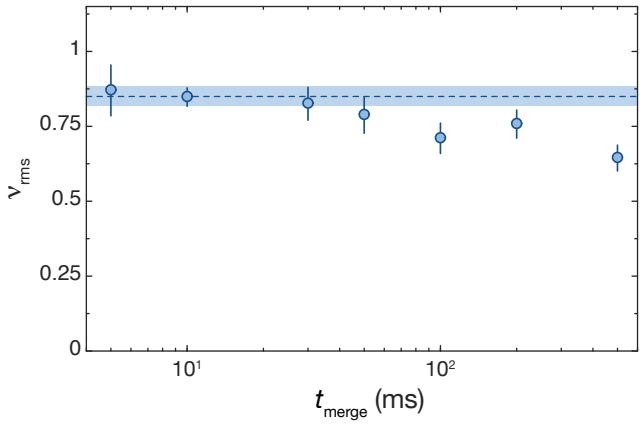

Figure 6.8 *– Width of the distribution for $N = 9$ as a function of the merging time t_{merge}. Each data point was obtained from a set of 50-100 individual measurements. The data point at 10 ms corresponds to the merging time we used for the data presented in section 6.2 and consists of $\mathcal{M} = 388$ measurements. The vertical error bars denote the statistical uncertainty due to a finite number of measurements $\mathcal{M}$ and the uncertainty in the determination of the winding numbers.*

6.3.4 Width of the distribution for different merging times

For the measurements presented in section 6.2 we merged the condensates within 10 ms. This time was chosen between two limiting regimes. If the condensates are merged too fast, we may create shock waves and high-energy excitations [235, 236] as opposed to the quasi-adiabatic generation of supercurrents we want to probe in the experiment. On the other hand if the merging is performed too slowly, the formation of supercurrents with non-zero phase winding might be reduced due to an asynchronous closing of the individual barriers since the phase between neighboring condensates may homogenize before the merging is complete. Moreover, the lifetime of the supercurrents may be reduced in the presence of weak potential barriers around the ring when the supercurrents are formed during the merging [56]. Experimentally we investigated these effects for $N = 9$ initial condensates. We found that varying the merging time by about one order of magnitude between 5 ms and 50 ms did not significantly influence our experimental results (Fig. 6.8). When the barriers were removed abruptly instead we observed a significant increase in the width of the distribution ν_{rms} and the interference pattern exhibited many phase defects.

6.3.5 Lifetime of supercurrents

For the measurements reported in section 6.2 we typically wait 0.5 s after merging the condensates. We have studied the lifetime of the supercurrents using the same experimental sequence and increasing the waiting time before detection. The results are displayed in Fig. 6.9. We observed no significant decay of the supercurrents for waiting times that are on the order of the atomic lifetime (inset Fig. 6.9). This timescale is large compared to timescale of a typical experimental sequence.

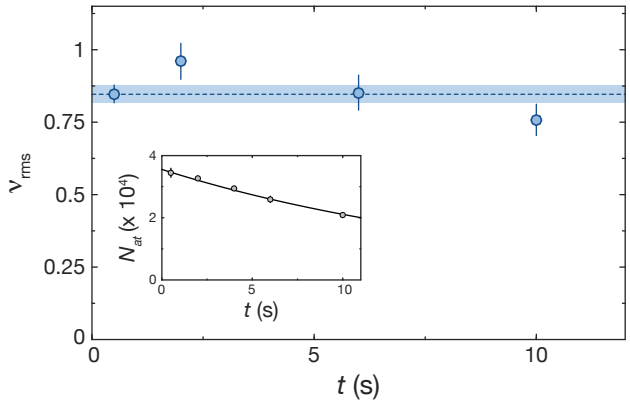

Figure 6.9 *– Lifetime of supercurrents and atoms for $N = 9$ segments. The data points show the measured rms-width ν_{rms} as a function of time t after merging the condensates. Each data point was evaluated from $\mathcal{M} > 100$ images. The data point at $t = 0.5\,s$ corresponds to the typical experimental sequence with $\mathcal{M} = 388$ [Fig. 6.3(a)]. It is further highlighted by the dashed line, the shaded area represents its uncertainty. All error bars display the combined error of statistical uncertainties and uncertainties in the analysis of the interference patterns. The inset displays the corresponding atom numbers. For each data point we evaluated between 2 and 13 measurements and the vertical error bars depict the standard deviation. The solid line is the fit of an exponential function $f(t) = Ae^{-t/\tau}$ to our data, resulting in $\tau = 19(1)\,s$.*

6.3.6 Center values for the relaxation measurements

In Fig. 6.10 we display the mean values $\bar{\nu}$ of the distributions corresponding to the data displayed in Fig. 6.4, where we have studied the relaxation from N to $N/2$ condensates, when merging them in two successive steps. For $N = 6$ initial segments we observe consistently larger asymmetries in the distributions and they seemed to be reproducible over the course of several days. In the case of $N = 12$ the observed asymmetries are consistent with statistical fluctuations.

6.3.7 Experimental sequence and data analysis for the merging of two condensates

The experimental sequence for the study of the dynamics of the defects was as follows: We loaded a rectangle of size $50 \times 30\,\mu$m with thermal atoms and dynamically reduced its width to $13\,\mu$m within 0.2 s. A separation of width $3\,\mu$m was abruptly introduced in the middle of the rectangle to create two lines of dimensions $50 \times 5\,\mu$m. One of the lines was further cut into two lines of length $23.5\,\mu$m. The other line serves as a phase reference for the detection. The system was then cooled down within 2 s to the same temperature as in section 6.2. After an equilibration time of 1 s the separation between the two $23\,\mu$m-long lines was removed within 9.5 ms, following the same procedure as discussed in the previous sections. We then let the system relax for a variable time t_{wait} and subsequently detected the interference pattern by performing

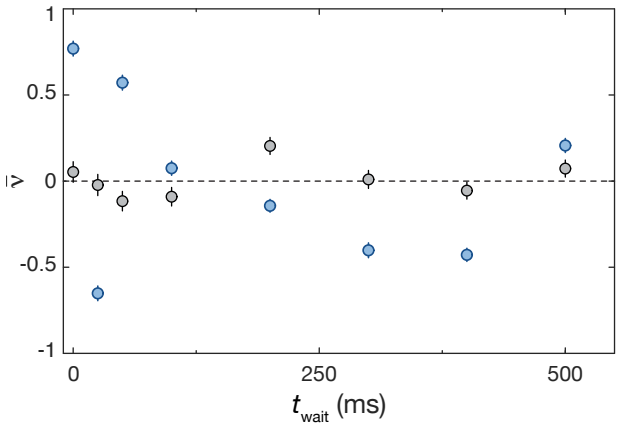

Figure 6.10 *– Center values $\bar{\nu}$ of the distributions corresponding to the widths ν_{rms} shown in Fig. 6.4 for $N = 12$ (black) and $N = 6$ (blue) respectively. Each data point consists of $\mathcal{M} > 200$ measurements. The vertical error bars depict the standard deviation obtained from statistical uncertainties and the experimental uncertainty in the determination of the winding numbers.*

a 2D-TOF of 3 ms (as introduced in section 6.3.1) followed by a 3D-TOF of 3 ms during which we removed all confining potentials.

Phase defects in the interference pattern were analyzed in the following way: We chose a region-of-interest in the center of the cloud in the x-direction, which represents two periods of the fringes (Fig. 6.11a) and performed a sliding average of the image along y to smoothen the profile. The wavevector of the fringes along x was determined via Fourier transform. For each position in the y-direction, the modulus of this Fourier coefficient gives us the visibility of the fringes and its phase is the local relative phase of the two lines at this position. The dislocations can be found at the positions where both the visibility drops and the phase jumps. More precisely we were looking for coincidences of minima of the visibility and maxima of the absolute value of the phase gradient along the y-direction. We removed an overall smooth gradient of the phase across the whole cloud to avoid any systematic bias between positive and negative phase jumps. We evaluated the data for different threshold values φ_c between neighboring pixels (this corresponds to an effective pixel size of 1.16 μm in the atomic plane), where a phase dislocation is detected above this threshold. All phase dislocations below this value are discarded. This threshold is needed in order to avoid the detection of false dislocations. The extracted positions y_d of the detected phase dislocations are shown in the histograms (Fig. 6.11b), which are normalized by the total number of individual measurements.

In order to evaluate the total number of defects N_d (Fig. 6.5c) as a function of time we assume that phase jumps occur with an equal probability in the interval $(-\pi, \pi]$. The threshold value φ_c will artificially reduce the number of detected defects by a factor $(1 - \varphi_c/\pi)$. Therefore we use this as a correction factor and rescale our data accordingly. This is certainly true for short times but it is not necessarily the case for long times because the relaxation dynamics most likely depend on the initial phase difference between the two condensates. Nonetheless it helps us to estimate

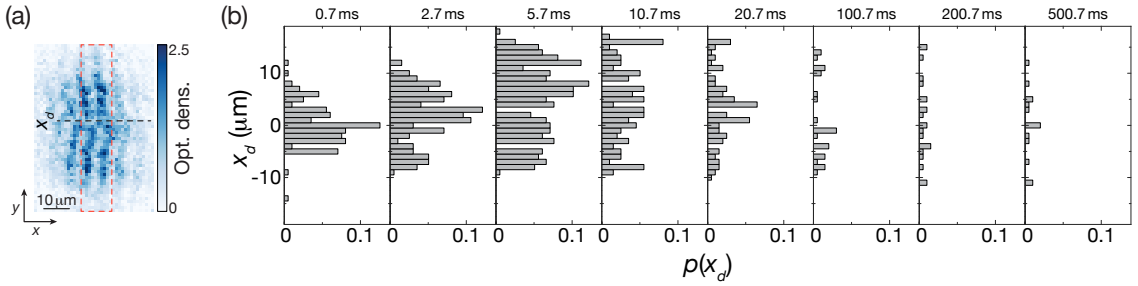

Figure 6.11 *– (a) Interference pattern after an evolution time $t_{wait} =$ 0.7 ms detected after a 2D-TOF of 3 ms plus a 3D-TOF of 3 ms. The red-dashed lines mark the region-of-interest for the data analysis. The phase dislocation at x_d his highlighted by a black dashed line. (b) Position distributions $p(y_d)$ of the phase dislocations for various evolution times t_{wait}. The histograms are normalized by the total number of images. For each time t_{wait} we have taken about 200 individual measurements. For this data the threshold for the analysis described in the text is $\varphi_c = 0.3\pi$.*

the error we make in the data analysis due to the finite threshold value φ_c. In Fig. 6.5c we display the results for different threshold values between 0.16π and 0.43π.

7

Further characterization of the setup

The project of the next chapter requires precise calibrations of the magnification of the camera and of the effective cross-section σ of an atom with light in our experimental conditions. We present here the methods that we used for these calibrations.

7.1 Calibration of the magnifications

A micromirror of the DMD has an effective size $M_2 \times M_1 \times d_{DMD}$ on the vertical imaging camera, where M_1 is the magnification between the DMD plane and the atomic plane, M_2 the magnification between the atomic plane and the camera plane and $d_{DMD} = 13.68\,\mu m$ is the real size of a mirror of the DMD.
Measuring the product $M_1 \times M_2$ is easy and is done section 7.1.1. However one would like to determine M_1 and M_2 individually as one wants to know exactly the distances in the atomic plane. This is possible by also measuring the ratio M_2/M_1 thanks to Bragg diffraction, as is done section 7.1.2.
The following analysis has been carried out by Raphaël Saint-Jalm while I was writing this thesis.

7.1.1 Lattice in situ: measure of $M_1 \times M_2$

We trap the atoms in lattices with different spacings. Each lattice consists in stripes of equal sizes of mirrors switched ON and OFF on the DMD. The lattice on the atoms has a period of $M_1 n_{DMD} d_{DMD}$, where n_{DMD} is the period on the DMD expressed in number of mirrors. On the camera it represents a period of

$$n_{Cam} = \frac{(M_1 \times M_2) n_{DMD} d_{DMD}}{d_{Cam}}, \tag{7.1}$$

where n_{Cam} is expressed in number of pixels of the vertical imaging camera and d_{cam} is the real size of one pixel of the camera ($13.0\,\mu m$).
For each lattice period we take several images (typically 7) that we average. Figure 7.1a shows an example of the measurements with the image of the atoms taken with the Princeton camera for $n_{DMD} = 24$. We compute the profile of the atomic signal along the direction of the lattice and fit its central part with a sinus function (see Fig. 7.1b), from which we get a period expressed in units of pixels of the camera.
We then plot the period on the camera as a function of the period on the DMD and deduce the slope β_1 of this linear law: $n_{Cam} = \beta_1 \times n_{DMD}$. Figure 7.2 displays the

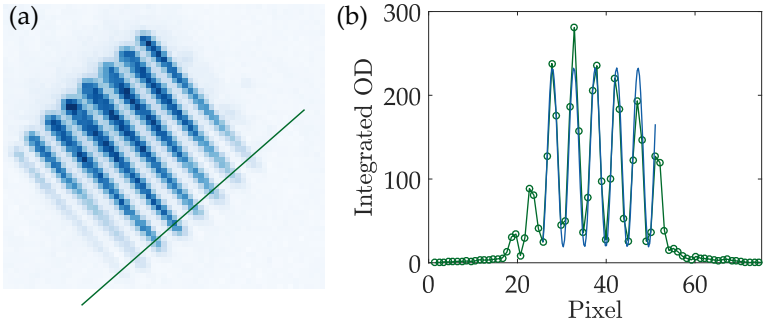

Figure 7.1 *– Example of an in situ lattice experiment for* $\mathrm{n_{DMD}} = 24$*. (a) Image of the atoms taken with the Princeton camera. (b) Fitted profile of the image of the atoms. The profile is obtained by integrating a part of the image along the line perpendicular to the green line on (a).*

determination of this slope: we get $\beta_1 = 0.1715$, meaning according to equation 7.1 that:

$$\frac{(\mathrm{M_1} \times \mathrm{M_2})\mathrm{d_{DMD}}}{\mathrm{d_{Cam}}} = 0.1715. \tag{7.2}$$

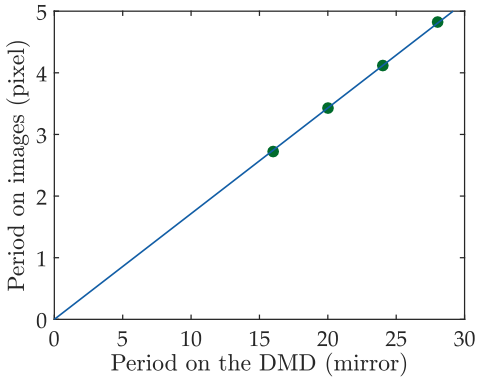

Figure 7.2 *– Determination of the factor* β_1*. We get* $\beta_1 = 0.1715$*, with a precision of* 0.5%*.*

7.1.2 Bragg diffraction through a lattice: measure of $\mathrm{M_2/M_1}$

This experiment is conducted in the following way. We stop the usual experimental sequence at the evaporated red-detuned crossed dipole trap. The cloud is small and degenerate. We flash a lattice displayed on the DMD during a short duration (typically 20 µs). The atomic velocity distribution then exhibits equally spaced peaks separated by

$$v_{\mathrm{recoil}} = \frac{\hbar k_{\mathrm{recoil}}}{m_{\mathrm{Rb}}}, \tag{7.3}$$

where $\mathrm{m_{Rb}}$ is the mass of one atom of Rubidium and k_{recoil} is the recoil momentum corresponding to the lattice on the DMD. This can thus be rewritten

$$v_{\mathrm{recoil}} = \frac{h}{m_{\mathrm{Rb}}\mathrm{M_1 n_{DMD} d_{DMD}}}. \tag{7.4}$$

Several diffraction peaks can be distinguished after time of flight, allowing us to measure v_{recoil}. The atoms however fall during the TOF and gravity has to be compensated to make a precise measurement. We thus made the experiment with the atoms in the $|F = 1, m_F = -1\rangle$ state and with the quadrupole trap compensating gravity. The effect of the residual harmonic confinement in the plane during TOF (as described in section 2.5.3) has to be taken into account. The position y_ℓ of the peak number ℓ (ℓ is a positive or negative integer) will be given by:

$$y_\ell(t_{\mathrm{TOF}}) = y_0(t_{\mathrm{TOF}}) + \frac{\ell h}{m_{\mathrm{Rb}}\mathrm{M_1 n_{DMD} d_{DMD}}} \sin(2\pi f_\perp t_{\mathrm{TOF}}), \tag{7.5}$$

where $f_\perp$ is the residual frequency of the magnetic trap in the xy-plane, and $y_0(t_{\mathrm{TOF}})$ is the position of the central peak.
We want to measure the distance between two neighbouring peaks as a function of the time of flight and get the initial velocity v_{recoil}. For each lattice period we vary the time of flight between 8 and 20 ms and average a few images (typically 3). For each image we find the center of each peak (there are usually between five and ten peaks). We then plot the average distance between neighbouring peaks as a function of the time of flight duration and fit the result with a sine curve with fixed origin and free amplitude and frequency. The product of the amplitude and the pulsation gives us the initial velocity ℓv_{recoil}. Figure 7.3 displays an example of the fitting procedure.

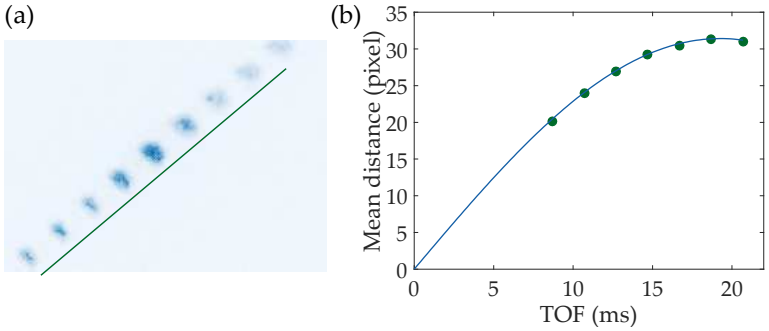

Figure 7.3 *– Example of a Bragg diffraction experiment for* $\mathrm{n_{DMD}} = 8$ *pixels. (a) Image of diffraction after a time of flight of 12 ms. The profile is then integrated along the line perpendicular to the green line to determine the position of each peak. (b) Distance between neighbouring peaks and fit with a sine function (the residual frequency of the magnetic trap is found to be* $f_\perp = 12.9$ *Hz).*

We plot the initial velocity of the atoms as a function of the inverse of the period of the lattice on the DMD $\mathrm{n_{DMD}}$, and determine the slope β_2 of the law: $v_{\mathrm{recoil}}/\mathrm{d_{Cam}} = \beta_2 \times 1/\mathrm{n_{DMD}}$. Figure 7.4 shows the determination of this slope: we get $\beta_2 = 20.39\,\mathrm{ms}^{-1}$, which means, according to equation 7.4,

$$\frac{h\mathrm{M}_2}{m_{\mathrm{Rb}}\mathrm{M}_1\mathrm{d}_{\mathrm{DMD}}\mathrm{d}_{\mathrm{Cam}}} = 20.39\,\mathrm{ms}^{-1}. \tag{7.6}$$

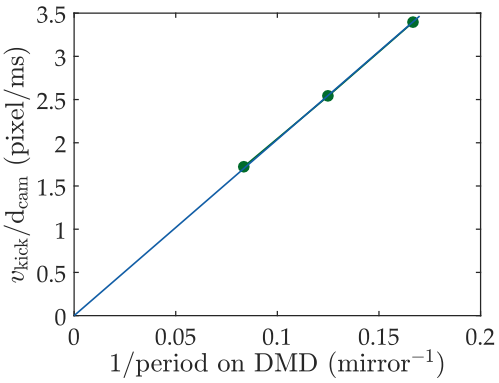

Figure 7.4 *– Determination of the factor β_2. We get $\beta_2 = 20.39\,\mathrm{ms}^{-1}$, with a precision of $\approx 1\%$.*

7.1.3 Conclusion of the calibration

M_1 and M_2 are then obtained combining equations 7.2 and 7.6:

$$\mathrm{M}_2 = \sqrt{\frac{\mathrm{d}_{\mathrm{Cam}}^2 m_{\mathrm{Rb}}\beta_1\beta_2}{h}} = 11.37, \tag{7.7}$$

and

$$\mathrm{M}_1 = \sqrt{\frac{h\beta_1}{\mathrm{d}_{\mathrm{DMD}}^2 m_{\mathrm{Rb}}\beta_2}} = 1.434 \times 10^{-2}. \tag{7.8}$$

Commonly used quantities in the lab are rather effective sizes in the atomic plane, which give an effective pixel size of the camera of 1.144 µm and an effective size of one mirror of the DMD of 0.1962 µm in the atomic plane.
We note that a period on the DMD of 6 pixels still leads to a good Bragg diffraction signal. This corresponds for a trapping of the atoms in this lattice to a distance between two neighbouring sites of 1.2 µm, which offers interesting perspectives for our system. The expected tunnelling rates between sites were discussed in section 2.3.3.

7.2 Calibration of the effective atomic cross-section with light σ

The precise calibration of the atom number from absorption imaging is usually not an easy task for cold atom experiments. We remind from chapter 2 that the atomic density can be inferred as

$$n^{(2D)} = -\frac{1}{\sigma}\ln\left(\frac{I_{\text{out}}}{I_{\text{in}}}\right), \tag{7.9}$$

where $I_{\text{in/out}}$ correspond to the incoming/outgoing numbers of photons, and σ is the effective cross-section of an atom with light, which might depend on its internal state, on the polarization of the light and of the ambient magnetic field. We define the "fudge factor" F as

$$F = \frac{\sigma_0}{\sigma}, \quad \text{where} \quad \sigma_0 = \frac{7}{15}\frac{3\lambda^2}{2\pi}. \tag{7.10}$$

This factor is usually determined using the Bose-Einstein condensation threshold in a 3D dipole trap, where the critical atom number N_c and temperature T_c in the ideal gas limit are linked by

$$T_c = \frac{\hbar\bar{\omega}}{k_{\text{B}}} 1.202^{1/3} N_c^{1/3}, \tag{7.11}$$

where $\bar{\omega}/2\pi$ is the geometrical average of the trapping frequencies in the three directions. This method thus requires a good measure of the three trapping frequencies, and a precise thermometry. Furthermore, due to the 1/3 power of the atom number in the threshold, this determination is not very precise. We preferred to implement a method which could be realized directly in the final trap of our experiment and thus did this calibration another way, inspired by the group of Philipp Treutlein [245, 119].

7.2.1 Principle of the calibration

Consider atoms in a superposition of states, usually called a coherent spin state of the form

$$|\Psi\rangle = \left(c_1 |1\rangle + c_2 |2\rangle\right)^{\otimes N}, \tag{7.12}$$

where N is the total atom number and c_1, c_2 are complex coefficients with $|c_1|^2+|c_2|^2 = 1$. For this state the atoms are uncorrelated and after measurement each atom will have a probability $p_1 = |c_1|^2$ to be in state $|1\rangle$ and $p_2 = |c_2|^2$ to be in state $|2\rangle$.
We now consider the variables N_1 and N_2 corresponding to the measured atom numbers in $|1\rangle$ and $|2\rangle$, respectively. N_1 and N_2 follow a binomial distribution of mean and variance:

$$\overline{N_1} = p_1 N, \quad \text{Var}(N_1) = N p_1 (1-p_1), \tag{7.13}$$

$$\overline{N_2} = p_2 N, \quad \text{Var}(N_2) = N p_2 (1-p_2). \tag{7.14}$$

The variance of these variables will be maximized for $p_1 = p_2 = 1/2$ which is the case that we consider from now on. The idea of our calibration is that there is a relation between the mean atom number in one state and its fluctuations: the standard deviation of the measured atom number in one state is the square root of one fourth of the mean atom number in this state.

This however assumes that the total atom number N is perfectly reproducible from one shot to the other, which is not the case in the experiment. To circumvent this, we rather measure $N_1 - N_2$ for which the mean and variance are

$$\overline{N_1 - N_2} = 0, \quad \mathrm{Var}(N_1 - N_2) = \mathrm{Var}(N_1) + \mathrm{Var}(N_2) - 2\,\mathrm{Cov}(N_1, N_2). \tag{7.15}$$

The computation of the covariance gives

$$\begin{aligned} \mathrm{Cov}(N_1, N_2) &= \mathrm{E}[(N_1 - \mathrm{E}[N_1])(N_2 - \mathrm{E}[N_2])] \\ &= \mathrm{E}[N_1 N_2] - \mathrm{E}[N_1]\mathrm{E}[N_2] - \mathrm{E}[N_2]\mathrm{E}[N_1] + \mathrm{E}[N_1]\mathrm{E}[N_2] \\ &= \mathrm{E}[N_1(N - N_1)] - N^2/4 \\ &= -N/4. \end{aligned} \tag{7.16}$$

We then have

$$\mathrm{Var}(N_1 - N_2) = N. \tag{7.17}$$

A calculation treating the N atoms as a combined quantum system using the second quantification leads to the same result [119, 246].
We can see that it is better to look at $N_1 - N_2$ rather than at N_1 and N_2 individually with a simple numerical simulation. Let's assume that we have 10 000 atoms and that we pick N_1 atoms along a binomial distribution of parameter $p = 0.5$ on 100 000 experiments. If the total atom number is exactly 10 000 for the 100 000 experiments then the variances of N_1 and N_2 are close to 2 500 and the variance of $N_1 - N_2$ is close to 10 000 as expected from the calculations above. If we now pick atom numbers with a gaussian noise of 5%, we get about 18 000 for the variances of N_1 and N_2 whereas the variance of $N_1 - N_2$ is still close to 10 000. Using $N_1 - N_2$ instead of N_1 and N_2 individually thus removes additional noise due to total atom number fluctuations.

7.2.2 Experimental sequence

Measuring both the atom numbers N_1 and N_2 for each experimental sequence implies to change a bit the way we image the atoms. Compared to the usual absorption imaging, we send 3 imaging pulses instead of 2 and use another image without imaging beam to remove the background. For our vertical imaging path, the frame-transfer mode of the camera allows us to have a time of the order of 1 ms between the two imaging pulses. We thus first image the atoms in the $|F = 2\rangle$ state, then repump the $|F = 1\rangle$ atoms with a microwave (MW) pulse and image them. In the following, the two images with atoms are labelled as "subimage 1" and "subimage 2", and the image without atom as "subimage 0".
We choose to perform this method with the atoms in the final trap, because the depth of field of the microscope objectives is short and thus the vertical expansion of the atoms should be small. We also use imaging pulses of 30 μs instead of 10 μs usually as we want to increase the number of scattered photons per atom. The experimental protocol is shown figure 7.5.

We use data with a total optical depth below 1 to avoid effects observed at higher densities, where much less atoms are seen in the second pulse than in the first one. This effect is still present for low densities but is reduced. We attribute it to collisions between atoms leaving the trap and those who remain.

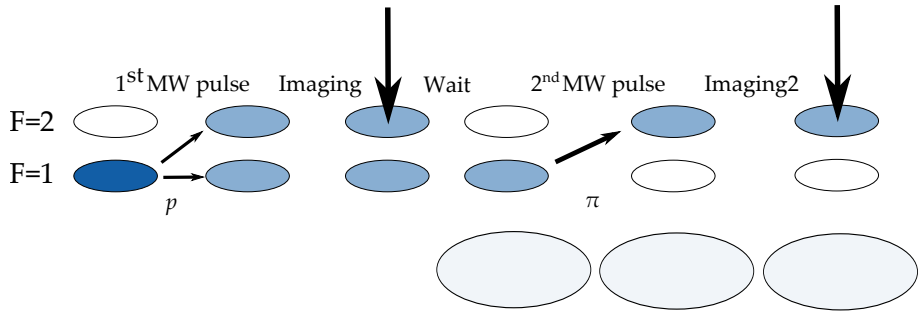

Figure 7.5 *– Experimental sequence starting when the atoms are in the final trap. A first MW pulse is applied. During the first imaging pulse, a fraction p of the atoms is imaged. The vertical black arrows denote the imaging beams. They should act only on the $|F = 2\rangle$ atoms. The remaining $|F = 1\rangle$ atoms must then be transfered to $|F = 2\rangle$ by a MW π-pulse, before being imaged. The big pale clouds correspond to the imaged atoms which are leaving the field of view of the camera after being imaged. We checked that they do not have a significant contribution during the second imaging pulse.*

7.2.3 Taking shot noise and read-out noise into account for one image

From equation 7.17, it is in principle possible to extract the wanted fudge factor F by measuring the variance of $N_1 - N_2$ for different total atom numbers. To measure the correct variance, all other additional noises have to be well estimated. In particular, the photonic shot noise of $I_{\text{in/out}}$ has to be well understood. We propose here a method based on a linearisation of the fluctuations to estimate their effect.

- The number of photons detected in one pixel follows a Poisson distribution, of variance equal to the mean value. We thus describe the photonic shot noise with a random variable $\epsilon_{p,0}(\boldsymbol{q}, i)$, where p stands for photons, 0 is the number of the subimage, $\boldsymbol{q}$ is the index of the pixel and i the index of the image. This random variable is of mean 0 and variance 1, and is multiplied by the square root of the mean photon number to match the variance of the Poisson distribution.
- The read-out noise of the camera also has to be taken into account. It is described by the random variable $\zeta_{p,0}(\boldsymbol{q}, i)$, which is also of mean 0 and variance 1, and will be multiplied by 5.0[a].

[a]The value $5.0 = \sqrt{50.5/2}$ was determined by a precise calibration of the read-out noise and gain of the camera by taking pictures with light at different intensities (and no atoms). Considering single pixels, a linear fit for the difference between two images gives

$$\text{Var}(N_{p,1} - N_{p,2}) = 50.5 + 1.0217\,(\bar{N}_{p,1} + \bar{N}_{p,2}). \tag{7.18}$$

The number of photons $N_{p,0}(\boldsymbol{q}, i)$ detected in subimage 0, in pixel $\boldsymbol{q}$, for the image i can be written

$$N_{p,0}(\boldsymbol{q}, i) = \bar{N}_{p,0}(\boldsymbol{q}) + \epsilon_{p,0}(\boldsymbol{q}, i)\sqrt{\bar{N}_{p,0}(\boldsymbol{q})} + 5.0\ \zeta_{p,0}(\boldsymbol{q}, i), \tag{7.19}$$

where $\bar{N}_{p,0}(\boldsymbol{q})$ is the average for this pixel over all the images.
For the images with atoms, the same formula applies. The mean photon number depends on the number of atoms which will absorb light, following the Beer-Lambert law. This traduces for the mean number of photons as

$$\bar{N}_{p,1}(\boldsymbol{q}, i) = \bar{N}_{p,0}(\boldsymbol{q})\ \mathrm{e}^{-\sigma \bar{N}_{a,1}(\boldsymbol{q},i)/A_{\boldsymbol{q}}}, \tag{7.20}$$

where $\bar{N}_{a,1}(\boldsymbol{q}, i)$ is the mean number of atoms in pixel $(\boldsymbol{q}, i)$ and $A_{\boldsymbol{q}}$ the area of one pixel. Taking into account the noises as above, we get

$$N_{p,1}(\boldsymbol{q}, i) = \bar{N}_{p,0}(\boldsymbol{q})\ \mathrm{e}^{-\sigma N_{a,1}(\boldsymbol{q},i)/A_{\boldsymbol{q}}} + \epsilon_{p,1}(\boldsymbol{q}, i)\sqrt{\bar{N}_{p,0}(\boldsymbol{q})\ \mathrm{e}^{-\sigma N_{a,1}(\boldsymbol{q},i)/A_{\boldsymbol{q}}}} + 5.0\ \zeta_{p,1}(\boldsymbol{q}, i), \tag{7.21}$$

with again $\bar{\epsilon}_{p,1}(\boldsymbol{q}) = \bar{\zeta}_{p,1}(\boldsymbol{q}) = 0$ and $\mathrm{Var}[\epsilon_{p,1}(\boldsymbol{q})] = \mathrm{Var}[\zeta_{p,1}(\boldsymbol{q})] = 1$. For each pixel $\boldsymbol{q}$ and each image i, we can calculate the optical density $d_1(\boldsymbol{q}, i)$:

$$d_1(\boldsymbol{q}, i) = \ln\left(\frac{N_{p,0}(\boldsymbol{q}, i)}{N_{p,1}(\boldsymbol{q}, i)}\right). \tag{7.22}$$

Both detected photon numbers are large compared to 1, so that we can perform an expansion in powers of $1/\sqrt{N_{p,0/1}}$ and obtain at second order:

$$\begin{aligned} d_1(\boldsymbol{q}, i) \approx \frac{\sigma}{A_{\boldsymbol{q}}} N_{a,1}(\boldsymbol{q}, i) \ &+ \frac{\epsilon_{p,0}(\boldsymbol{q}, i)}{\sqrt{\bar{N}_{p,0}(\boldsymbol{q}, i))}} - \frac{\epsilon_{p,1}(\boldsymbol{q}, i)}{\sqrt{\bar{N}_{p,1}(\boldsymbol{q}, i))}} \\ &+ 5.0\frac{\zeta_{p,0}(\boldsymbol{q}, i)}{\bar{N}_{p,0}(\boldsymbol{q}, i))} - 5.0\frac{\zeta_{p,1}(\boldsymbol{q}, i)}{\bar{N}_{p,1}(\boldsymbol{q}, i))} \\ &+ \frac{\epsilon^2_{p,1}(\boldsymbol{q}, i)}{2\bar{N}_{p,1}(\boldsymbol{q}, i))} + \frac{\epsilon_{p,0}(\boldsymbol{q}, i)\epsilon_{p,1}(\boldsymbol{q}, i)}{\sqrt{\bar{N}_{p,0}(\boldsymbol{q}, i))}\sqrt{\bar{N}_{p,1}(\boldsymbol{q}, i))}} \\ &+ o\left(\frac{1}{\bar{N}_{p,0/1}(\boldsymbol{q}, i))}\right). \end{aligned} \tag{7.23}$$

The first line corresponds to the mean value plus the photonic shot noises of each picture, the second line to read-out noises, and the third line to terms arising from cross-products, which are negligible for our parameters and will be forgotten in the following. The average of this quantity over the N images is

$$\bar{d_1}(\boldsymbol{q}) \equiv \langle d_1(\boldsymbol{q}, i)\rangle_i \approx \frac{\sigma}{A_{\boldsymbol{q}}}\bar{N}_{a,1}(\boldsymbol{q}), \tag{7.24}$$

whereas its variance is

$$\mathrm{Var}[d_1(\boldsymbol{q})] \approx \frac{\sigma^2}{A^2_{\boldsymbol{q}}}\mathrm{Var}[N_{a,1}(\boldsymbol{q})] + \frac{1}{\bar{N}_{p,0}(\boldsymbol{q})} + \frac{1}{\bar{N}_{p,1}(\boldsymbol{q})} + \frac{25.0}{\bar{N}^2_{p,0}(\boldsymbol{q})} + \frac{25.0}{\bar{N}^2_{p,1}(\boldsymbol{q})}. \tag{7.25}$$

There is no significant quadratic contribution at the single pixel level, but there starts to be when packing 8×8 pixels in a macropixel.

Note that we made here a further simplification to evaluate the variance of the third term of Eq. (7.23)[a].

7.2.4 Taking shot noise and read-out noise into account for the difference of two images

The calibration requires to consider the two atom numbers $N_{a,1}$ and $N_{a,2}$ as explained earlier. In the following we are thus interested in the sum $S(\boldsymbol{q}, i)$ and the difference $D(\boldsymbol{q}, i)$ of the two optical densities d_1 and d_2. For the sum, we only need the average and we treat the various fluctuations at order zero:

$$\bar{S}(\boldsymbol{q}) = \frac{\sigma}{A_{\boldsymbol{q}}} \bar{N}_a(\boldsymbol{q}), \tag{7.28}$$

with $N_a = N_{a,1} + N_{a,2}$ the total atom number. For the difference, as

$$D(\boldsymbol{q}, i) = d_1(\boldsymbol{q}, i) - d_2(\boldsymbol{q}, i) = \ln\left(\frac{N_{p,2}(\boldsymbol{q}, i)}{N_{p,1}(\boldsymbol{q}, i)}\right), \tag{7.29}$$

the same result as 7.23 applies, just replacing the index 0 by 2.
Assuming as in (7.27) that we can neglect the fluctuations of $N_{a,1}$ and $N_{a,2}$ for the terms $1/\sqrt{\bar{N}_{p,1}}$ and $1/\sqrt{\bar{N}_{p,2}}$, we deduce the mean and the variance of D:

$$\bar{D}(\boldsymbol{q}) = 0, \tag{7.30}$$

$$\mathrm{Var}[D(\boldsymbol{q})] = \frac{\sigma^2}{A_{\boldsymbol{q}}^2} \bar{N}_a(\boldsymbol{q}) + \frac{1}{\bar{N}_{p,1}(\boldsymbol{q})} + \frac{1}{\bar{N}_{p,2}(\boldsymbol{q})} + \frac{25.0}{\bar{N}_{p,1}^2(\boldsymbol{q})} + \frac{25.0}{\bar{N}_{p,2}^2(\boldsymbol{q})}. \tag{7.31}$$

To summarize, one should consider the two quantities $\bar{S}(\boldsymbol{q})$ and

$$\tilde{V}(\boldsymbol{q}) = \mathrm{Var}[D(\boldsymbol{q})] - \left(\frac{1}{\bar{N}_{p,1}(\boldsymbol{q})} + \frac{1}{\bar{N}_{p,2}(\boldsymbol{q})}\right) - 25.0\left(\frac{1}{\bar{N}_{p,1}^2(\boldsymbol{q})} + \frac{1}{\bar{N}_{p,2}^2(\boldsymbol{q})}\right), \tag{7.32}$$

which satisfy the set of two equations:

$$\sigma \bar{N}_a(\boldsymbol{q}) = A_{\boldsymbol{q}}\, \bar{S}(\boldsymbol{q}), \tag{7.33}$$

$$\sigma^2 \bar{N}_a(\boldsymbol{q}) = A_{\boldsymbol{q}}^2 \tilde{V}(\boldsymbol{q}). \tag{7.34}$$

The effect of removal of the shot noise and read-out noise pixel by pixel can be seen in figure 7.6.

[a] The calculation of the variance of the 3rd term of (7.23) actually requires a bit more care, since $N_{a,1}(\boldsymbol{q}, i)$ is itself a random variable. Setting as above

$$N_{a,1}(\boldsymbol{q}, i) = \bar{N}_{a,1}(\boldsymbol{q}) + \epsilon_a(\boldsymbol{q}, i)\, \sqrt{\bar{N}_{a,1}(\boldsymbol{q})} \tag{7.26}$$

and assuming that $\sigma\sqrt{\bar{N}_{a,1}(\boldsymbol{q})}/A_{\boldsymbol{q}} \ll 1$ (*ie* the fluctuations of the OD are small compared to 1, even if the OD itself can be of order 1), we have for this 3rd term:

$$\frac{\epsilon_{p,1}(\boldsymbol{q}, i)}{\sqrt{\bar{N}_{p,0}(\boldsymbol{q})\, \mathrm{e}^{-\sigma N_{a,1}(\boldsymbol{q},i)/A_{\boldsymbol{q}}}}} \approx \frac{\epsilon_{p,1}(\boldsymbol{q}, i)}{\sqrt{\bar{N}_{p,1}(\boldsymbol{q})}} + \frac{\epsilon_{p,1}(\boldsymbol{q}, i)\epsilon_a(\boldsymbol{q}, i)}{2\sqrt{\bar{N}_{p,1}(\boldsymbol{q})}} \frac{\sigma\sqrt{\bar{N}_{a,1}(\boldsymbol{q})}}{A_{\boldsymbol{q}}} \approx \frac{\epsilon_{p,1}(\boldsymbol{q}, i)}{\sqrt{\bar{N}_{p,1}(\boldsymbol{q})}}. \tag{7.27}$$

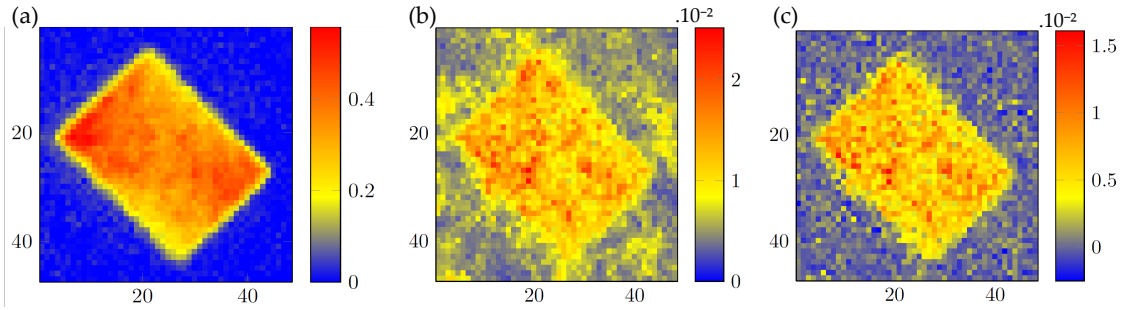

Figure 7.6 *– Effect of removal of the shot noise and read-out noise pixel by pixel, using 91 images. (a)* $\bar{S}(\boldsymbol{q})$*, (b)* $\mathrm{Var}[D(\boldsymbol{q})]$ *and (c)* $\tilde{V}(\boldsymbol{q})$*.*

7.2.5 A first method of calibration

Before turning to a more sophisticated method to determine the atom number in a selected zone, we present a treatment based on a Monte Carlo simulation to check the validity of the linearisation of the fluctuations used before. We also show the result of this method when varying the size of the considered zone, and thus the atom number.

Selection of images

A careful processing of the images is required to extract the correct atom number fluctuations. First an electronic background, obtained by averaging ≈ 30 images[a] without atoms and without probe light, is subtracted to each subimage. We also filter the images keeping only those with no "anomalous" deviation. For each value of i_{sub} (between 0 and 2) and each pixel $\boldsymbol{q}$, we calculate the average $\bar{N}_{\mathrm{count}}(i_{\mathrm{sub}}, \boldsymbol{q})$ and the standard deviation $\bar{s}(i_{\mathrm{sub}}, \boldsymbol{q})$ of the number of counts (average taken over all images for the same parameters). We then eliminate the images which have at least one pixel $\boldsymbol{q}$ that deviates from $\bar{N}_{\mathrm{count}}$ by more than $\eta\, \bar{s}$ for one value of i_{sub}. The threshold factor η is set at $\eta = 4.26$, which should lead to the elimination of less than 1% of the images if the statistics were gaussian. This procedure is repeated until no image is removed. In practice we eliminate by this way between 5 and 15 images out of 100. We then consider a zone of 8×8 pixels, optimized such that the variations of the sum of $\bar{S}(\boldsymbol{q})$ on the zone are minimal over the images.

Check of validity of linearisation: comparison with an ab-initio simulation

The treatment described above is based on a linearisation of the various sources of fluctuation, and the validity of this approximation could be questioned. In addition the treatment does not take into account the losses of atoms between the first and second images, which we found experimentally. Although they are relatively small, this could create a significant bias of the results.
In order to address these points, we have developed a simulation which models as closely as possible the detection process. In practice, each photon count on a given pixel is randomly drawn using a Poisson distribution with the appropriate mean value.

[a] They should be taken the same day as the background value drifts from day to day.

N_{pix}	$\bar{N}_{p,0}$	$\bar{N}_{p,1}$	$\bar{N}_{p,2}$	F_{linear}	$\bar{N}_{a,linear}$	F_{sim}	$\bar{N}_{a,sim}$
1^2	449	371	375	5.73	20.86	5.59	20.51
2^2	1794	1482	1499	2.74	9.90	2.69	9.89
3^2	4006	3303	3345	2.20	7.95	2.13	7.84
4^2	7176	5927	5996	1.98	7.11	1.92	7.10
5^2	10849	8944	9056	1.73	6.23	1.69	6.27
6^2	16023	13213	13381	1.61	5.79	1.59	5.88
7^2	21897	18096	18327	1.66	5.88	1.54	5.67
8^2	28705	23706	23983	1.62	5.78	1.60	5.87

Table 7.1 *– Average quantities over an optimized* 8×8 *window.* $\bar{N}_{p,i_{sub}}$ *are the average number of photons detected in a square region of* N_{pix} *pixels. It is visible from these numbers that less atoms are present in the second image than in the first one, as less photons are absorbed.* F_{linear} *and the corresponding* $\bar{N}_{a,linear}$ *are obtained with the shot noise and read-out noise removed as described section 7.2.3.* F_{sim} *and* $\bar{N}_{a,sim}$ *are obtained with the ab-initio simulation.The mean optical depths for this run are* $\bar{d}_1 = 0.195$ *and* $\bar{d}_2 = 0.183$.

The effect of the $\pi/2$ pulse is described by using a random draw from the binomial distribution and the results of the simulations are processed as the experimental ones. The details of the simulations are described in appendix in section D.1. Note that this simulation explicitly uses the gain of the camera, 1.025, determined from the analysis of images without atoms.
The results for different macropixels (*ie* pixels binned together in squares of 1×1 to 8×8 pixels), shown in table 7.1, lead to two conclusions:

- The simulations are in excellent agreement with the linearised analysis of the statistics of the measured optical depths. This validates the linearisation of fluctuations used above, at least in this regime of relatively low optical densities.
- It also confirms that the analysis based on single pixels is not satisfying. The fudge factor is indeed extremely high (about 6) for single pixels whereas it drops to about 1.6 for zones bigger than 5×5 pixels. We attribute this effect to the spreading of the response of individual atoms on several pixels due to the finite resolution of the imaging system.

There are two ways to circumvent this. The first one is to focus on macro-pixels and look for convergence when the size of the macro-pixel is increased. This is what is done in table 7.1 and in section 7.2.5. The problem with this approach is that if one is dealing with slightly non-homogeneous samples, it may add extra noise in a way that is difficult to control. The other way is to try to include in the modelling the smoothening of the optical response at the single pixel level. This is done in section 7.3.

Results varying the size of interest, removing linearized noise

This analysis can equivalently be done in a way closer to the one of [245, 119], in which the number of atoms is varied. The authors of [245, 119] used several

experimental sequences to prepare samples with different the atom number, but as our sample has a uniform atomic density, the atom number inside a macropixel can be tuned by changing the number of pixels N_{pix} considered. To solve the set of two equations 7.33 and 7.34, we plot in figure 7.7 $(A_{\boldsymbol{q}}/\sigma_0)^2\,\tilde{V}(\boldsymbol{q})$ corresponding to $\mathrm{Var}(N_1+N_2)$ versus $A_{\boldsymbol{q}}/\sigma_0\,\bar{S}(\boldsymbol{q})$ which corresponds to $\overline{N_1+N_2}$ for different atom numbers[a]. The fitted slope is then the inverse of the wanted fudge factor. The run considered in figure 7.7 had a quite low optical depth $\bar{S}=0.38$ and led to a fudge factor of 1.68.
However, another run with higher optical depths ($\bar{S}=0.77$) led to a fudge factor of about 2.3 with this method. This discrepancy of results between the two runs is less important with the more sophisticated method that we present now.

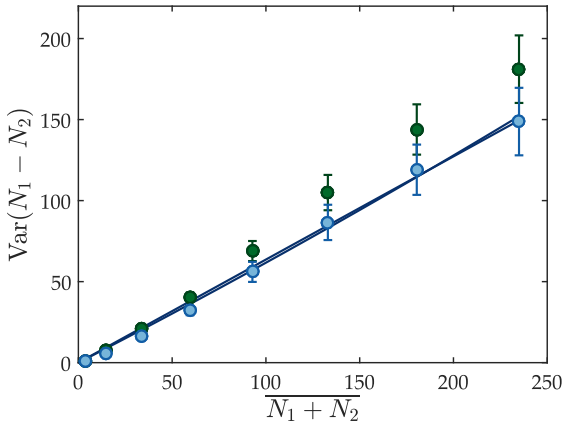

Figure 7.7 *– Result of the analysis on a zone of 8×8 pixels, considering squares of 1×1 to 8×8 pixels. The green points are the results without removing the shot noise and read-out noise and the blue ones with this removing. The fit of the blue points by a function $y=ax^2+bx$ gives $a=0.594$ and $b=0.0002$ and is thus very close to a linear fit. Confidence intervals for the points are determined by a bootstrapping method. The determined fudge factor $1/a$ is 1.68 for this low density run.*

7.3 Calibration by modeling the optical response

The projection of the atoms onto the two different states produces well-controlled binomial noise with zero correlation length. However, due to the finite resolution of the imaging system, an atom might affect several pixels, which leads to a wrong atom number determination for small zones in table 7.1. This spreading of the effect of one atom on several pixels has been studied and characterized for example in [70], so that the authors extract the density fluctuations of the 2D Bose gas. We propose here an alternative method, looking this time at the source of fluctuations that comes from the projection of the atoms onto the two different states. This gives

[a] N_1 and N_2 correspond to the inferred atom numbers according to absorption imaging with the cross section σ_0.

us the response function of our imaging system together with the atomic density $\bar{N}_a$ in the considered zone.

7.3.1 A coarse-grain approximation

We suppose that the light intensity in a point $\boldsymbol{r}$ on the camera can be written

$$I(\boldsymbol{r}) = I_0(\boldsymbol{r}) \ \exp\left(-\int \alpha(\boldsymbol{r}-\boldsymbol{r}') \ \rho_a(\boldsymbol{r}') \ \mathrm{d}^2 r'\right), \tag{7.35}$$

with $\rho_a(\boldsymbol{r}')$ the atomic density at $\boldsymbol{r}'$. Suppose also that the response function $\alpha(\boldsymbol{r}-\boldsymbol{r}')$ varies relatively smoothly on the scale of a pixel. This relation can then be written in a discrete way:

$$I(\boldsymbol{q}) = I_0(\boldsymbol{q}) \ \exp\left(-\frac{1}{A_q}\sum_{\boldsymbol{q}'} \sigma(\boldsymbol{q}-\boldsymbol{q}') \ N_a(\boldsymbol{q}')\right), \tag{7.36}$$

so that the OD at a pixel $\boldsymbol{q}$ is now (to be compared with Eq. (7.23)):

$$d(\boldsymbol{q}, i) \approx \frac{1}{A_q}\sum_{\boldsymbol{q}'} \sigma(\boldsymbol{q}-\boldsymbol{q}') \ N_a(\boldsymbol{q}', i) \ + \ \text{photon noise } (\boldsymbol{q}, i), \tag{7.37}$$

The photon noises[a] between two different pixels $\boldsymbol{q}_A$ and $\boldsymbol{q}_B$ are not correlated. However as we show below, there can be some correlations between the fluctuations of the ODs in $\boldsymbol{q}_A$ and $\boldsymbol{q}_B$ if there exists an atom in pixel $\boldsymbol{q}$ that contributes significantly to the pixels $\boldsymbol{q}_A$ and $\boldsymbol{q}_B$ via the sum over the $\sigma(\boldsymbol{q}_{A/B} - \boldsymbol{q})$.
We will use the covariances between pixels and their link to the σ matrix that we just described to reconstruct the σ_i and find the atom number on the selected zone.

7.3.2 Extracting the σ matrix using correlations

To deconvolve the effect of the finite resolution of the imaging system, we compute the different $\mathrm{Cov}[D(\boldsymbol{q}_A), D(\boldsymbol{q}_B)]$, where D is the difference of ODs between the two images on the same pixel. It is shown in appendix in section D.2 that for $\boldsymbol{q}_A \neq \boldsymbol{q}_B$, the covariances for our experimental protocol correspond to:

$$\mathrm{Cov}[D(\boldsymbol{q}_A), D(\boldsymbol{q}_B)] = \frac{1}{A_q^2}\sum_{\boldsymbol{q}} \sigma(\boldsymbol{q}_A - \boldsymbol{q}) \ \sigma(\boldsymbol{q}_B - \boldsymbol{q}) \ \bar{N}_a(\boldsymbol{q}), \tag{7.38}$$

and to

$$\tilde{V}(\boldsymbol{q}_A) = \frac{1}{A_q^2}\sum_{\boldsymbol{q}} \sigma^2(\boldsymbol{q}_A - \boldsymbol{q}) \ \bar{N}_a(\boldsymbol{q}), \tag{7.39}$$

where $\tilde{V}$ is obtained from $\mathrm{Var}[D]$ by subtracting photon shot noise and read-out noise as in (7.32). Also the sum of the two ODs reads

$$\bar{S}(\boldsymbol{q}_A) = \frac{1}{A_q}\sum_{\boldsymbol{q}} \sigma(\boldsymbol{q}_A - \boldsymbol{q}) \ \bar{N}_a(\boldsymbol{q}). \tag{7.40}$$

[a] We include here the read-out noise in the photon noise to reduce the amount of notation.

The set of equations (7.38-7.39-7.40) allows one to reconstruct the imaging transfer function $\sigma(\boldsymbol{q}-\boldsymbol{q}')$ as well as the pixel contents $N_a(\boldsymbol{q})$ from the measured covariances. The link is however quite complicated to describe and is also done in appendix, in section D.2.
To obtain a better signal to noise ratio, we average the covariances for all $\boldsymbol{Q} = \boldsymbol{q}_B - \boldsymbol{q}_A$ on a selected zone. This is shown in figure 7.8a for $\boldsymbol{Q}$ ranging from (-3,-3) to (3,3). The Cov[D]($\boldsymbol{Q}$) matrix is symmetric along the x and y axes. We chose to take advantage of these symmetries, and take the corresponding averages for the covariances, which are named $C_0, ..., C_5$ as shown in figure 7.8b.
It is then possible to extract the σ_i of the σ matrix, as explained in section D.2. We chose to model the response function of the imaging system with 5 coefficients $\sigma_0, ..., \sigma_4$ as shown in figure 7.8c. We obtain together with these coefficients the atomic density in the selected zone.

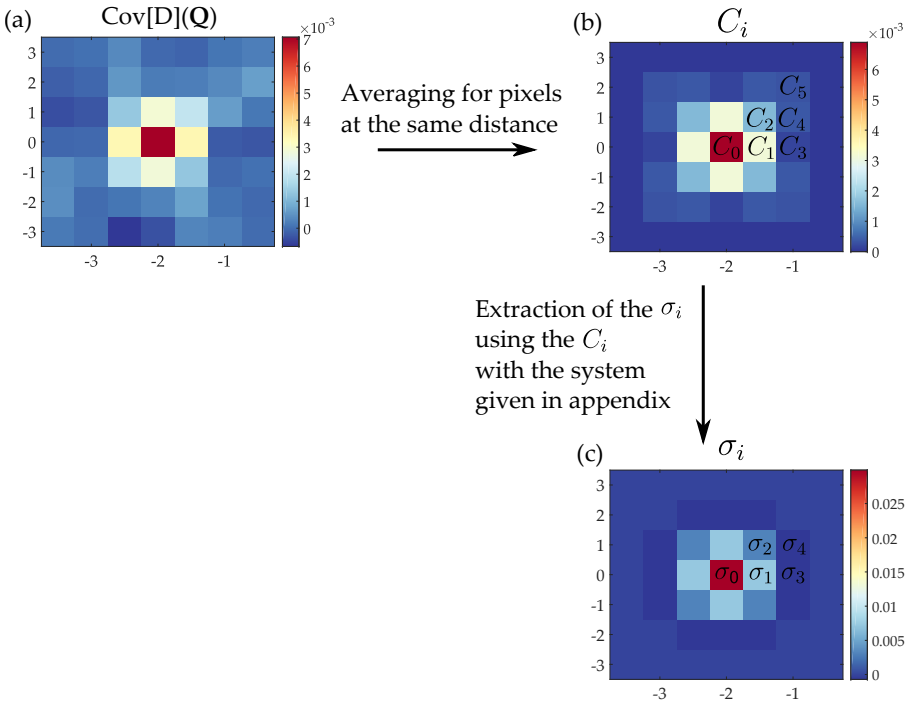

Figure 7.8 *– Method that we used for extracting the σ_i coefficients from the measured covariances between pixels. (a) Cov[D]($\boldsymbol{Q}$) corresponding to the averaged covariances for all $\boldsymbol{Q} = \boldsymbol{q}_B - \boldsymbol{q}_A$ on a selected zone. (b) C_i coefficients obtained by averaging the Cov[D]($\boldsymbol{Q}$) corresponding to the same $I\boldsymbol{Q}I$. (c) σ_i coefficients obtained by solving the system given in appendix, in section D.2.*

7.3.3 Robustness using subsets of images

In order to check the robustness of the results, which depends on the stability of the experiment when the various runs were taken, one can perform the same analysis for only a subset of images in each run. We have chosen the following selection criterion:

Table 7.2 *– Value of the fudge factor depending on a subset of images for three different runs. The average value of the optical depths for subimages 1 and 2 are also indicated. The run used as an example in this chapter is run 2.*

	$\bar{d}_1$	$\bar{d}_2$	1	2	3	4	5
Run 1	0.354	0.309	1.37	2.04	1.42	1.34	1.32
Run 2	0.195	0.183	1.66	1.69	1.68	1.66	1.56
Run 3	0.410	0.360	1.80	1.81	1.71	1.67	1.80

- choice 1: all images (about 100) provided they pass the stability test indicated in section 7.2.5
- choice 2: only images between 51 and 100
- choice 3: only images between 1 and 50
- choice 4: only even images
- choice 5: only odd images

The results are given in table 7.2. Clearly the runs 2 and 3 are more stable than Run 1. This is also visible on the analysis of section 7.2.5 where a much stronger quadratic contribution is seen compared to the two other runs (but not shown here for this run). The fudge factor of 1.6 is confirmed for run 2, but the result $F = 2.3$ of section 7.2.5 for run 3 is now only 1.8. It is this result which should be kept as the finite optical resolution of the imaging system is taken into account in this analysis[a].

[a]We note that the found fudge factor could be modified for our usual imaging due to the fact that for the analysis of this chapter the imaging lasts 30 µs versus 10 µs for the usual one. We checked that this has almost no effect by comparing different runs. For run 2 the OD is not modified and for run 3 it goes from 0.77 to 0.80 for the usual imaging.

8

Study of Sound propagation

8.1 Motivation for this project

Propagation of sound waves is at the heart of the study and understanding of quantum fluids. In liquid helium, the two-fluid model introduced by Laszlo Tisza was confirmed by the observation of first and second sound modes [247]. In this system the first sound corresponds to a density wave for which the normal and superfluid fractions oscillate in phase, whereas second sound is a temperature wave for which the two components oscillate out of phase.

Sound wave propagation is also central to the study of dilute quantum gases. The existence of first and second sound modes within an hydrodynamic two-fluid model was predicted for weakly interacting Bose-Einstein condensates (BEC) [248] and propagation of sound in an elongated BEC was observed in Refs. [249, 250]. Sound velocity measurements were also exploited, for instance, in one-dimensional systems to determine their Luttinger parameter [251]. Weakly interacting Bose gases are compressible systems (compared to liquid helium) and the nature of first and second sound is strongly modified. In this case, second sound is mainly an oscillation of the superfluid part alone and is a direct continuation of the Bogoliubov excitations at low temperatures. Sound waves were also predicted [252] and observed [253, 254] in ultracold strongly interacting Fermi gases, whose behavior is closer to the case of liquid helium.

Propagation of sound in weakly interacting two-dimensional (2D) Bose gases was recently discussed in Ref. [75]. Similarly to the 3D case, the existences of first and second sound modes were predicted within a two-fluid hydrodynamic approach. However, in 2D, as described earlier in this thesis, the velocity of second sound exhibits a jump when crossing from the normal to the superfluid state the Berezinskii-Kosterlitz-Thouless (BKT) critical point. This discontinuity is a signature of the jump of the superfluid density at the transition point. Indeed, in the limit of very dilute Bose gases the speed of sound is directly proportional to the square root of the superfluid fraction [255]. Experimentally, 2D Bose fluids were first realized with liquid helium films adsorbed on a substrate [256]; in this case the presence of the substrate blocks the motion of the normal component and thus prevents the investigation of such phenomena.

8.1.1 Hydrodynamics and two-fluid model

The two-fluid model forms the basic framework for understanding the occurence of first and second sound in superfluid systems. We follow here the lines of [257] to derive the quartic equation whose solutions are the two speeds of sound. The two-fluid model assumes that the system can be described as composed of two parts: a normal and a superfluid one. The mass density $\rho = nm$ and the mass current are then:

$$\rho = \rho_s + \rho_n, \tag{8.1}$$
$$m\boldsymbol{j} = \rho_s \boldsymbol{v_s} + \rho_n \boldsymbol{v_n}. \tag{8.2}$$

The continuity equations of the fluid read (Eq. (8.4) reflects the fact that the entropy is carried only by the normal part):

$$\frac{\partial \rho}{\partial t} + \nabla \cdot m\boldsymbol{j} = 0, \tag{8.3}$$
$$\frac{\partial s}{\partial t} + \nabla \cdot s\boldsymbol{v_n} = 0. \tag{8.4}$$

In addition, hydrodynamic equations at equilibrium give

$$m\frac{\partial \boldsymbol{j}}{\partial t} + \nabla p = 0, \tag{8.5}$$
$$m\frac{\partial \boldsymbol{v_s}}{\partial t} + \nabla \mu = 0. \tag{8.6}$$

All these equations combined with the usual thermodynamic relation

$$\rho \mathrm{d}\mu = -ms\mathrm{d}T + \mathrm{d}p, \tag{8.7}$$

lead to the two coupled equations, with $\tilde{s} = s/\rho$:

$$\frac{\partial^2 \rho}{\partial t^2} = \nabla^2 p, \tag{8.8}$$
$$\frac{\partial^2 \tilde{s}}{\partial t^2} = \frac{\rho_s \tilde{s}^2}{\rho_n} \nabla^2 T. \tag{8.9}$$

We describe the propagation of a sound wave of velocity c by linearizing these equations around equilibrium. Writing the perturbations as

$$\rho = \rho + \rho_{\mathrm{osc}} \mathrm{e}^{i(kx-\omega t)}, \tag{8.10}$$
$$p = p + p_{\mathrm{osc}} \mathrm{e}^{i(kx-\omega t)}, \tag{8.11}$$
$$\tilde{s} = \tilde{s} + \tilde{s}_{\mathrm{osc}} \mathrm{e}^{i(kx-\omega t)}, \tag{8.12}$$
$$T = T + T_{\mathrm{osc}} \mathrm{e}^{i(kx-\omega t)}, \tag{8.13}$$

and using the relationships

$$\delta\rho = \frac{\partial\rho}{\partial p}\delta p + \frac{\partial\rho}{\partial T}\delta T, \quad \delta\tilde{s} = \frac{\partial\tilde{s}}{\partial p}\delta p + \frac{\partial\tilde{s}}{\partial T}\delta T, \tag{8.14}$$

we get the quartic equation whose positive solutions are the two speeds of sound:

$$\left[\frac{\partial\tilde{s}}{\partial T}\frac{\partial\rho}{\partial p} - \frac{\partial\tilde{s}}{\partial p}\frac{\partial\rho}{\partial T}\right]c^4 + \left[\frac{\partial\tilde{s}}{\partial T} + \frac{\rho_s\tilde{s}^2}{\rho_n}\frac{\partial\rho}{\partial p}\right]c^2 + \frac{\rho_s\tilde{s}^2}{\rho_n} = 0, \tag{8.15}$$

where the derivatives with respect to T are taken at constant pressure and vice-versa. The quantities involved in this formula are however not very convenient to compute. We first rewrite this equation in terms of other thermodynamic variables that we define now.

8.1.2 Reminder of thermodynamics

In addition to the phase-space-density $\mathcal{D}$ which has been described in chapter 1, we introduce other thermodynamic variables such as the pressure P, the entropy per particle S and specific heat per particle C_v. We use their dimensionless counterparts:

$$\mathcal{P} = \frac{\lambda_\mathrm{T}^2}{k_\mathrm{B}T}P, \quad \mathcal{S} = S/k_\mathrm{B}, \quad \text{and} \quad \mathcal{C}_\mathrm{v} = C_\mathrm{v}/k_\mathrm{B}. \tag{8.16}$$

The reduced pressure $\mathcal{P}$ was theoretically [258] and experimentally [66, 64] determined. All these quantities are related, using $X = \mu/k_\mathrm{B}T$, by

$$\mathcal{D} = \mathrm{d}\mathcal{P}/\mathrm{d}X, \quad \mathcal{S} = 2\mathcal{P}/\mathcal{D} - X, \quad \mathcal{C}_\mathrm{v} = 2\mathcal{P}/\mathcal{D} - \mathcal{D}/(\mathrm{d}\mathcal{D}/\mathrm{d}X). \tag{8.17}$$

8.1.3 Prediction

Using once again thermodynamic relations, equation (8.15) can be rewritten, with $\bar{c} = c/c_\mathrm{B}$ the speed of sound normalized to the Bogoliubov speed of sound:

$$\left(\frac{\tilde{g}\mathcal{D}}{2\pi}\right)^2\bar{c}^4 - \frac{\tilde{g}}{2\pi}\left(2\mathcal{P} + \frac{\mathcal{D}\mathcal{S}^2}{\mathcal{C}_\mathrm{v}}\frac{f_\mathrm{s}}{1-f_\mathrm{s}}\right)\bar{c}^2 + \frac{\mathcal{D}\mathcal{S}^2}{\mathcal{C}_\mathrm{v}(\mathrm{d}\mathcal{D}/\mathrm{d}X)}\frac{f_\mathrm{s}}{1-f_\mathrm{s}} = 0, \tag{8.18}$$

which corresponds to the result of [75]. Knowing all needed thermodynamic quantities, the two solutions $\bar{c}_1$ and $\bar{c}_2$ of the equation can be found. Using an interpolating function on the results of Prokof'ev and Svitsunov [259] to get the thermodynamic variables, one can plot the two solutions, as done in figure 8.1.

8.2 Experimental study

The following sections of this chapter were initially published in [260], and are reproduced almost without modifications. Only titles have been added and some phrases changed to be consistent with the rest of the thesis.

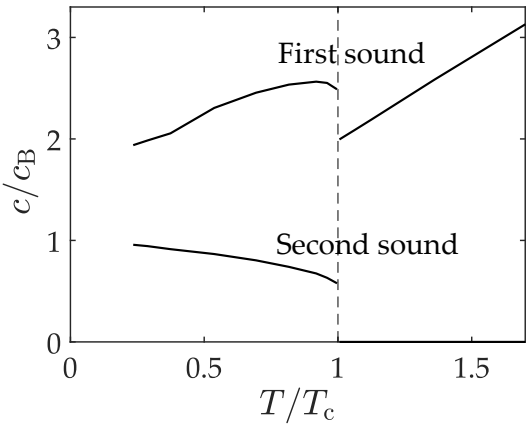

Figure 8.1 *– Expected normalized speeds of sound for different degeneracies. An interpolation of the results of Prokof'ev and Svitsunov [259] is used to get the thermodynamic variables required to solve the quartic equation (8.18).*

In this chapter, we report on the first observation of sound propagation in a 2D Bose fluid. We observe a single density sound mode both in the superfluid and normal regimes. Deep in the superfluid regime, the measured sound speed agrees well with the Bogoliubov prediction. We measure a weak damping rate compatible with Landau damping, a fundamental mechanism for the understanding of collective modes of superfluids at finite temperature [261]. For higher temperatures, we observe a decrease of the sound velocity consistent with the second sound speed variation predicted in Ref. [75] from two-fluid hydrodynamics. The damping of sound increases with temperature and, above the critical point, we still observe strongly damped density waves with no discernable discontinuity at the critical point. The discrepancy with the two-fluid model predictions could be due to a departure from hydrodynamic behavior.

8.2.1 Protocol for travelling waves

Our experimental setup has been described in Refs [116, 233] and more details can be found in section 8.3. Briefly, we confine ^{87}Rb atoms in the $|F = 1, m = 0\rangle$ ground state into a 2D rectangular box potential of size $L_x \times L_y = 30(1) \times 38(1)$ µm (see Fig. 8.2a). The confinement along the vertical z direction can be approximated by a harmonic potential of frequency $\omega_z/(2\pi) = 4.59(4)$ kHz. We always operate in the quasi-2D regime where interaction and thermal energies are smaller than $\hbar\omega_z$. The gas is characterized by the effective coupling constant $g = \hbar^2\tilde{g}/m = (\hbar^2/m)\sqrt{8\pi}\, a_s/\ell_z$, where a_s is the s-wave scattering length, $\ell_z = \sqrt{\hbar/(m\omega_z)}$ and m the atomic mass [76]. We operate here in the weakly-interacting regime: $\tilde{g} = 0.16(1)$. In the quasi-2D regime and for a given $\tilde{g}$, the equilibrium state of the cloud is only characterized by a dimensionless combination of T and n_{2D}, thanks to an approximate scale-invariance [76]. In the following we use the ratio T/T_c, where $T_c = 2\pi n_{2D}\hbar^2/[mk_B \ln(380/\tilde{g})]$ is the calculated critical temperature for the BKT phase transition [102]. In this work,

we study Bose gases from the highly degenerate regime ($T/T_c \approx 0.2$) to the normal regime ($T/T_c \approx 1.4$).
We first investigate propagating waves which we excite by a density perturbation. Prior to evaporative cooling in the box potential, we apply to the cloud a repulsive potential, which creates a density dip on one side of the rectangle (see Fig. 8.2a). The extension of this dip is about 1/4 of the length of the box and its amplitude is chosen so that the density in this region is decreased by a factor of 1/3. After equilibration, we abruptly remove the additional potential and monitor the propagation of this density dip. We show in Fig. 8.2b a typical time evolution of the density profile integrated along the transverse direction to the perturbation for a strongly degenerate gas. In this regime, the density perturbation propagates at constant speed and bounces several times off the walls of the box. Using the calibrated size of the box, we extract a speed $c = 1.49(3)\,\mathrm{mm/s}$. This value is slightly lower than the Bogoliubov sound speed $c_B = \sqrt{g n_{2D}/m} = 1.6(1)\,\mathrm{mm/s}$ expected at zero temperature for the measured density $n_{2D} = 29(3)\ \mu\mathrm{m}^{-2}$. The measured speed is also close to the second sound mode velocity $c_{HD}^{(2)} = 1.4(1)\,\mathrm{mm/s}$, estimated from two-fluid hydrodynamics at our experimental value of $T/T_c = 0.37(12)$ [75]. The first sound, expected to propagate at a much higher speed $c_{HD}^{(1)} = 3.3(3)\,\mathrm{mm/s}$ [75], does not appear in our measurements that feature a single wavefront only. The absence of first sound in our experiments can be explained by its very small coupling to isothermal density excitations in a weakly interacting gas [75].

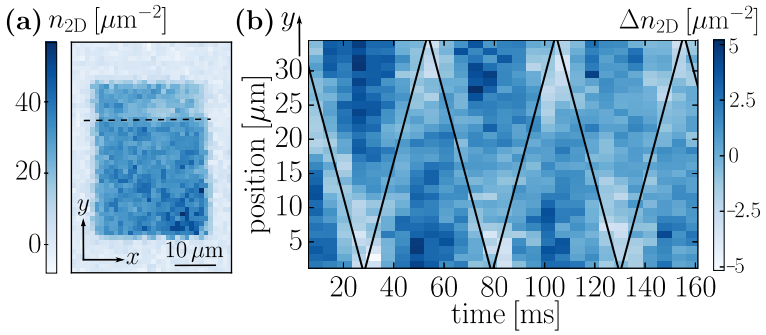

Figure 8.2 *– Experimental protocol and observation of propagating waves. (a) Absorption image of the cloud perturbed by a local additional potential. The excitation is delimited by the horizontal dashed line and depletes the atomic density by a factor around 1/3. (b) Example of time evolution of the variation of the density profile n_{2D} with respect to its spatial mean value (integrated along x) obtained after abruptly removing the additional potential. For this example $T/T_c = 0.37(12)$ and $n_{2D} = 29(3)\ \mu\mathrm{m}^{-2}$. The position of the dip is fitted by a triangle function (black solid line) which gives, $c = 1.49(3)$ mm/s.*

8.2.2 Analysis of the data of travelling waves

In order to probe the role of the cloud degeneracy on the sound wave propagation, we vary both n_{2D} and T. For each configuration, we excite the cloud with the protocol

described above, while adjusting the intensity of the depleting laser beam to keep the density dip around 1/3 of non-perturbed density. At lower degeneracies, sound waves are strongly damped and the aforementioned measurements of the density dip position become inadequate. We thus focus on the time evolution of the lowest-energy mode [262]. We decompose the density profiles integrated along x as

$$n(y,t) = \bar{n} + \sum_{j=1}^{\infty} A_j(t)\ \cos(j\pi y/L_y), \tag{8.19}$$

where $\bar{n}$ is the average density along y and the A_j are the amplitudes of the modes. The choice of the cosine basis ensures the cancellation of the velocity field on the edges of the box. Our excitation protocol mainly couples to the lowest energy modes. We keep the excitation to a low value to be in the linear regime while still observing a clear signal for the lowest-energy mode, which in return provides a too weak signal for a quantitative analysis of higher modes [a]. For each duration of the evolution, we compute the overlap of the atomic density profile with the lowest-energy mode. Examples of the time evolution of the normalized amplitude $\tilde{A}_1(t) = A_1(t)/A_1(0)$ for different degrees of degeneracy are shown in Fig. 5.3. We observe damped oscillations with a damping rate increasing with T/T_c. We fit the experimental data by an exponentially damped sinusoidal curve $e^{-\Gamma t/2}[\Gamma/2\omega \sin(\omega t) + \cos(\omega t)]$ to determine the energy damping rate Γ and the frequency ω [b]. We then determine the speed of sound $c = L_y\omega/\pi$ and the quality factor of this mode $Q = 2\omega/\Gamma$.

8.2.3 Results

We consolidate all our measurements of speed of sound and quality factors in Fig. 8.4. To facilitate comparison with theory, we show in Fig. 8.4a the values of c normalized to c_B. The non-normalized results are reported in section 8.5 for completeness. In the temperature range $T \lesssim 0.9\,T_c$, we measure weakly damped density oscillations, corresponding to a well-defined sound mode ($Q \gtrsim 10$). In this regime, we observe a significant decrease by about $\approx 25\%$ of the sound velocity for increasing values of T/T_c . The measured velocities agree well with the prediction from two-fluid hydrodynamics [75] combined with the equation of state of the 2D Bose gas [263]. According to the analysis of [75] for weakly interacting gases, the change of speed of sound is mainly due to the variation of the superfluid fraction f_s from ≈ 1 at $T = 0$ to ≈ 0.5 close to $T = T_c$ with the approximate scaling $c_{HD}^{(2)} \propto f_s^{1/2}$ [264]. We note the absence of a discernable discontinuity of sound velocity at T_c, in disagreement with the two-fluid hydrodynamic approach.

In order to explain this disagreement, we first note that collective excitations in ultracold Bose gases can be of different nature depending on the relative amplitude

[a] The study of the second spatial mode gives oscillation frequencies that are in good approximation twice larger than the lowest-energy mode and thus results in very similar speeds of sounds. However, the damping rate of this mode is also larger (see Fig. 8.5) and we cannot robustly estimate its lifetime for our deliberately weak excitation protocol.

[b] The choice of this oscillating function ensures a null derivative of the amplitude of the mode at $t = 0$, when the potential creating the density dip is removed. This behavior is expected from the continuity of the wavefunction and of its derivative describing the state of the gas at $t = 0$.

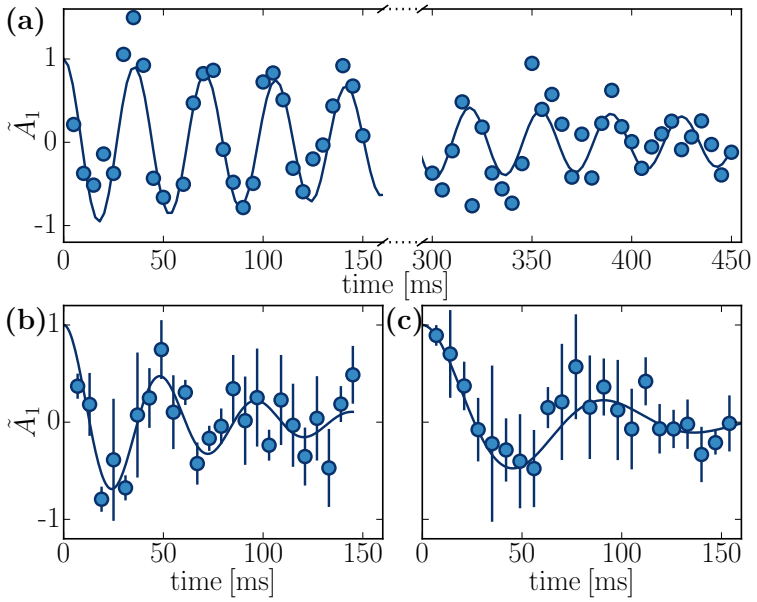

Figure 8.3 *– Time evolution of the normalized amplitude of the lowest-energy mode for (a) $T/T_c = 0.21(11)$, (b) $T/T_c = 0.95(5)$, (c) $T/T_c = 1.38(18)$. The solid line is a fit of an exponentially damped sinusoidal oscillation. For (b) and (c) graphs, each data point is the average of three measurements and the error bars represent the associated standard deviation. In (a) each point corresponds to a single measurement.*

of mean-field effects and collisions between particles [266, 267, 268]. In the very degenerate regime $T \ll T_c$, the system is naturally described within quantum hydrodynamics [269], where interactions between particles occur via a mean-field energy E_{int}. This is valid for $\omega \ll E_{int}/\hbar$, which is satisfied for our setup. In this regime we expect sound waves propagating at c_B, as observed in the experiment. For larger temperatures, but still below T_c, the normal fraction becomes significant. In order to use an hydrodynamic two-fluid model in that case, the local equilibrium condition also requires $\omega \ll \Gamma_{coll}$, where $\Gamma_{coll} = \hbar\tilde{g}^2 n/(2m)$ is the collision rate [96]. The same condition holds for the single fluid case above T_c. The opposite "collisionless" regime has been recently studied in Refs. [270, 271]. It also leads to the existence of a sound mode, originating solely from mean-field interactions described for example by a Landau-Vlasov kinetic equation. For $T \gtrsim T_c$ this collisionless sound mode has a velocity notably smaller than the hydrodynamic result and close to the prediction of Ref. [75] for the second sound velocity at T_c. For our data above T_c we estimate Γ_{coll}/ω to be in the range $1.6 - 3.4$, which indicates that we are in a crossover between these limiting hydrodynamic and collisionless regimes.

The distinction between the quantum hydrodynamics regime and the crossover regime ($\Gamma_{coll} \sim \omega$) is supported by the study of the measured quality factors (see Fig. 8.4b). For $T \ll T_c$, damping can be described at first order by the decay of low-lying collective excitations via scattering on thermal excitations [261, 272], the so-called Landau damping mechanism. It predicts an increase of the quality factor when decreasing temperature due to the reduction of the number of thermal excitations

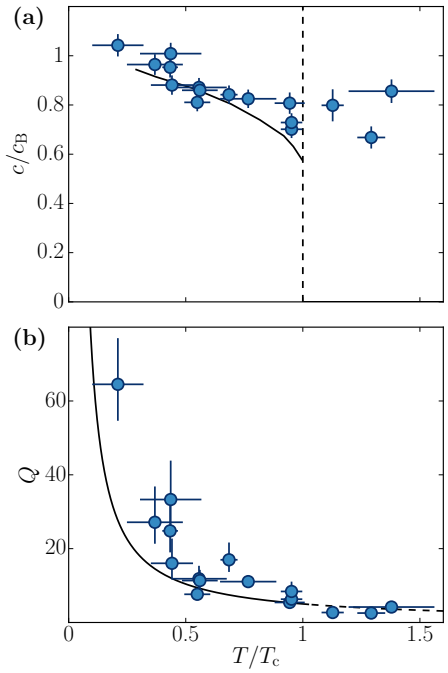

Figure 8.4 *– Speed of sound and quality factor. (a) Measured speed of sound c normalized to c_B. The vertical dashed line shows the position of the critical point. The solid line shows the result from the two-fluid hydrodynamic model applied to the 2D Bose gas [75]. A fit to the data points below T_c by this hydrodynamic model with a free multiplicative factor shows that the measurements are globally 3% above the theoretical prediction. This could correspond to a 6% systematic error in the calibration of n_{2D} used to determine $c_B \propto n_{2D}^{1/2}$. Our estimated uncertainty on n_{2D} is on the order of 11% (see section 8.4.3) and our measurements are thus compatible with the predicted value of the speed of second sound $c_{HD}^{(2)}$. (b) Quality factor $Q = 2\omega/\Gamma$ of the lowest-energy mode. The solid line is the prediction for Landau damping [265] (continued as a dashed line for $T > T_c$). For both graphs, the error bars represent the statistical uncertainty extracted from the fitting procedures used to determine c, Γ and T/T_c.*

available for scattering with the sound mode [a]. This perturbative approach is meaningful for large enough quality factors and does not take into account interactions between phonon modes. The solid line in Fig. 8.4b corresponds to Landau prediction for a 2D system [265]. It shows an overall good agreement with our data, even close to T_c where it gradually looses its validity. Finally, above T_c, we measured low quality factors, showing that the observed sound mode is strongly damped, in agreement with the predictions of the collisionless sound mode [270].

[a]Note that Beliaev damping, another mechanism for the decay of low-lying excitations, is absent for the first spatial mode of the box. Indeed, it corresponds to a decay of a low-lying excitation into two excitations with lower energies and thus does not exist for the lowest energy mode.

8.2.4 Standing waves

In the highly degenerate regime, the low damping rate allows us to observe standing waves. To study them, we modulate sinusoidally the amplitude of the potential creating the dip of density on one edge of the box [273]. After ≈1 s we extract, for each frequency ν of the excitation, the amplitude of the (time-dependent) density modulation induced on the cloud (see section 8.4.1 for details). We show in Fig. 8.5 the contribution of the three lowest-energy modes to the amplitude of the modulation as a function of the excitation frequency. For each mode j we observe a clear resonance peak centered at a frequency ν_j. We display in the insets the resonance frequencies and width of the modes. The ν_j's are equally spaced, as confirmed by the linear fit. In addition, the right inset shows the widths of the peaks. They also increase approximately linearly with j [a], meaning that the quality factor associated to these peaks is almost the same, as expected for Landau damping.

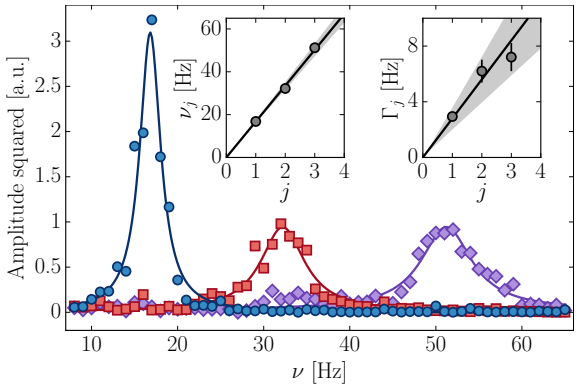

Figure 8.5 *– Observation of standing waves in the box potential. Contribution of the three lowest-energy modes to the amplitude of the density modulation: $j = 1$ (circles), $j = 2$ (squares), $j = 3$ (diamonds). The solid lines are Lorentzian fits. The two insets show the resonance frequencies ν_j and the full widths at half maximum Γ_j resulting from these fits. The solid lines in the insets are linear fit to the data and the shaded areas represent the uncertainty on the fitted slope. From the slope $c/(2L_y)$ of the fit to the resonance frequencies, we find $c = 1.90(9)$ mm/s. For this specific experiment, the length of the cloud is $L_y = 57(1)$ µm and the degree of degeneracy is $T/T_c = 0.41(7)$.*

8.2.5 Conclusion

We focus in this work on a weakly interacting Bose gas which features a large compressibility compared to liquid helium or strongly interacting Fermi gases. A natural extension of this work would thus be to investigate second sound propagation for increasing interactions [264]. It would also be interesting to investigate first sound, e.g. by applying a localized temperature excitation [254]. During the completion of

[a] Because of the finite duration of the excitation (1 s), the width of the peaks is Fourier limited at a typical width of 1 Hz, which should be taken into account for a more quantitative analysis.

this work we were informed that a related study with a homogeneous 3D Fermi gas was currently performed at MIT [a].

8.3 Supplementary information

8.4 Experimental setup

We confine ^{87}Rb atoms in the $|F = 1, m = 0\rangle$ ground state into a 2D rectangular box potential of size $L_x \times L_y = 30(1) \times 38(1)$ µm. The trapping potential is made by a combination of far-detuned repulsive optical dipole traps [116, 233]. The confinement along the vertical z direction can be approximated by a harmonic potential of frequency $\omega_z/(2\pi) = 4.59(4)$ kHz corresponding to a dimensionless interaction parameter $\tilde{g} = 0.16(1)$. The value of $\tilde{g}$ is slightly modified by the effect of interactions. We estimate that $\tilde{g}$ varies by about 10% for the range of surface densities explored in this work. We control the temperature T thanks to evaporative cooling by varying the height of the potential barrier providing the in-plane confinement. The surface density n_{2D} of the cloud is varied from 10 to 80 µm^{-2} by removing a controlled fraction of the atoms from our densest configuration. This removal is realized by a partial transfer of the atoms to the $|F = 2, m = 0\rangle$ state with a microwave resonant field and a subsequent blasting of the transferred fraction with a resonant laser beam. We determine the ratio T/T_c by a method inspired from Ref. [274] and based on a measurement of the equation of state of the system that we detail below.

8.4.1 Protocol for characterizing standing waves

We consider a cloud in a rectangular box of size $L_x \times L_y$. We create an excitation of density at frequency ω at one end of the rectangle and we choose this excitation to be invariant along the x-direction. We decompose this excitation on density modes whose gradient vanishes on the edges of the box and which are invariant along the x-direction. We define these spatial modes by $S_j(x, y) = \sqrt{2/(L_x L_y)}\ \cos(k_j y/2)$, where $k_j = 2j\pi/L_y$ and $j \in \mathbb{N}^*$.
In the linear regime, the response of the system is expected to occur at the same frequency ω, and each mode S_j will be excited with an amplitude $B_j(\omega)$ and a phase shift $\varphi_j(\omega)$ with respect to the excitation. Therefore, the density profile at time t will be given by

$$n_{2D}(\omega, t, x, y) = \bar{n}_{2D} + \sum_j B_j(\omega)\sqrt{\frac{2}{L_x L_y}}\cos\left(\frac{k_j y}{2}\right)\cos[\omega t + \varphi_j(\omega)], \quad (8.20)$$

where $\bar{n}_{2D}$ is the mean density. Our aim is to determine the amplitudes $B_j(\omega)$. However, measuring the full time evolution of n_{2D} for all frequencies would correspond

[a] M. Zwierlein, talk at the BEC 2017 Frontiers in Quantum Gases, Sant Feliu de Guixols

to a large amount of data acquisition. Instead, even without any prior knowledge of $\varphi_j(\omega)$, the amplitudes can be extracted using the following strategy: We measure the density profile at four different times t_i, $i \in \{1, 2, 3, 4\}$, and we choose these times so that we explore one oscillation: $\omega t_i = \omega t_1 + (i-1)\pi/2$. We get four density profiles $\rho_i(\omega, y)$, and we compute two quantities q_1 and q_2:

$$q_1(\omega, y) = \rho_3(\omega, y) - \rho_1(\omega, y) \tag{8.21}$$

$$= -2 \sum_j B_j(\omega) \sqrt{\frac{2}{L_x L_y}} \cos\left(\frac{k_j y}{2}\right) \cos[\omega t_1 + \varphi_j(\omega)], \tag{8.22}$$

and

$$q_2(\omega, y) = \rho_4(\omega, y) - \rho_2(\omega, y) \tag{8.23}$$

$$= 2 \sum_j B_j(\omega) \sqrt{\frac{2}{L_x L_y}} \cos\left(\frac{k_j y}{2}\right) \sin[\omega t_1 + \varphi_j(\omega)]. \tag{8.24}$$

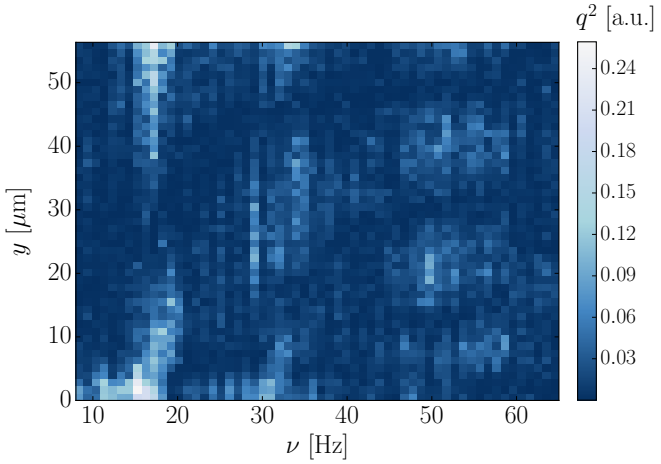

Figure 8.6 *– ntegrated spatial profile of the density modulation as a function of the modulation frequency. Each column shows q^2 which is the squared amplitude of the density modulation integrated along the x direction, determined from four pictures at different times and averaged over two runs. For this specific experiment, the length of the cloud is $L_y = 57(1)\,\mu\text{m}$ and the degree of degeneracy is $T/T_c = 0.41(7)$.*

We separate the contribution of the different modes by projecting $q_1(\omega, y)$ and $q_2(\omega, y)$ on the eigenmodes of the box:

$$c_l^{(j)}(\omega) = \sqrt{\frac{2}{L_x L_y}} \int_0^{L_x} \int_0^{L_y} q_l(\omega, y) \cos\left(\frac{k_j y}{2}\right) \mathrm{d}x\, \mathrm{d}y \tag{8.25}$$

$$= -2B_j(\omega) \cos\left[\omega t_1 + (l-1)\pi/2 + \varphi_j(\omega)\right], \tag{8.26}$$

for $l = 1$ or 2. The contribution of the j-th mode is then given by

$$[B_j(\omega)]^2 = \frac{1}{4}\left(\left[c_1^{(j)}\right]^2 + \left[c_2^{(j)}\right]^2\right). \tag{8.27}$$

We display in Fig. 8.5 a quantity proportional to $B_j^2(\omega)$ for the three first modes. In addition we also compute the quantity

$$q^2(\omega, y) \quad = q_1^2(\omega, y) + q_2^2(\omega, y), \tag{8.28}$$

which is displayed in Fig. 8.6. If the different modes are well separated, the excitation frequency ω is resonant with at maximum one spatial mode and the sum in Eq. (8.20) contains only one term. Therefore, we have

$$q^2(\omega, y) \approx 8B_{j_\omega}^2(\omega)/L_y \cos^2(k_{j_\omega} y/2), \tag{8.29}$$

where j_ω is the number of the mode that is excited at frequency ω. In this case, $q^2(\omega, y)$ has a simple interpretation: It is proportional to the squared amplitude of the mode and it reveals the spatial dependence of the mode with y.

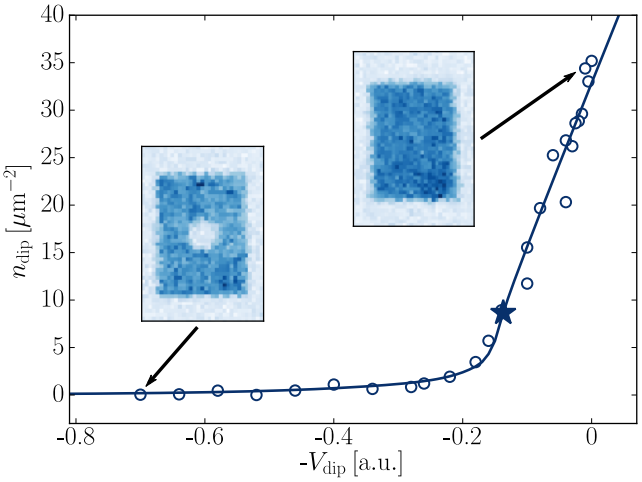

Figure 8.7 *– Surface density in the dip as a function of the applied potential V_{dip} along with the fit with the equation of state. The two insets are the average of absorption images for two example values of the potential in the dip. The star shows the expected position of the BKT phase transition. The value of the fit to $V_{\mathrm{dip}} = 0$ gives the degree of degeneracy of the cloud. For this cloud we get $T/T_{\mathrm{c}} = 0.21(11)$, where the uncertainty is given by the 95% confidence interval from the fitting procedure. Each data point is the average of three measurements.*

8.4.2 Determination of the cloud's degeneracy

The state of a weakly-interacting two-dimensional Bose gas at equilibrium and for a given $\tilde{g}$ can be characterized by a single dimensionless parameter, for instance T/T_{c} or equivalently its phase-space density $\mathcal{D} = n_{2\mathrm{D}}\lambda_T^2$, where $\lambda_T^2 = 2\pi\hbar^2/(mk_BT)$. Taking advantage of this scale invariance, we use here a method inspired from [274] to determine directly the phase-space density of the cloud without independent measurements of the atomic density and the temperature, and hence without accumulating errors in these two calibrations.

The principle of the measurement is to use an additional potential V_{dip} in a small region of the cloud (dip zone). Atoms inside this zone are in thermal equilibrium with the rest of the cloud but they experience an effective local chemical potential μ_{dip} shifted from the overall chemical potential μ: $\mu_{\mathrm{dip}} = \mu - V_{\mathrm{dip}}$. By measuring the surface density in the dip as a function of V_{dip} and using the known equation of state (EoS) of the gas, we determine the degree of degeneracy of the cloud.

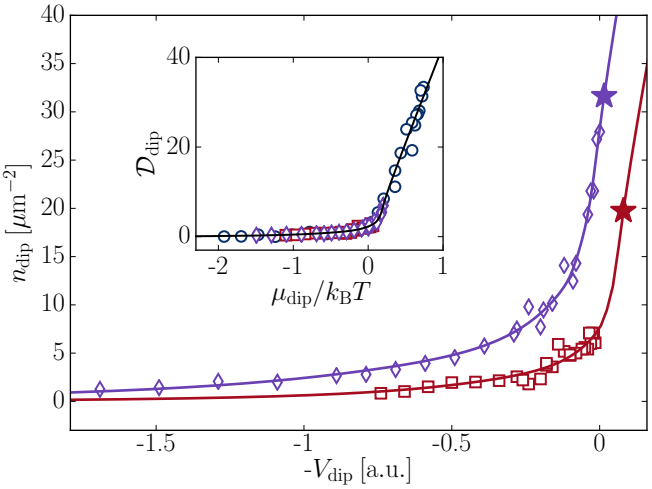

Figure 8.8 *– Two additional examples of the determination of the degree of degeneracy for different parameters (violet diamonds: $T/T_{\mathrm{c}} = 0.95(5)$, red squares: $T/T_{\mathrm{c}} = 1.86(19)$. Each data point is the average of three measurements. The stars correspond to the positions of the BKT phase transition. In the inset we show that all points of Fig. 8.7 and this figure, when properly rescaled in terms of phase-space density and chemical potential, collapse on the EoS of the 2D Bose gas (black solid line).*

In more detail, we shine on the cloud confined in the usual box potential an additional disk-shaped repulsive laser beam, as shown in the insets of Fig. 8.7. The disk-shaped region has to be small enough so that the change of potential in this part does not influence the rest of the gas: We use here a disk of radius 5 µm in a rectangle of 30 µm × 38 µm which corresponds to approximately 7 % of the total area of the box. We now write the equation of state of the gas with phase-space density $\mathcal{D}$ and in the dip zone with phase-space density $\mathcal{D}_{\mathrm{dip}}$,

$$\mathcal{D} = f\left(\frac{\mu}{k_{\mathrm{B}}T}\right) \quad \text{and} \quad \mathcal{D}_{\mathrm{dip}} = f\left(\frac{\mu_{\mathrm{dip}}}{k_{\mathrm{B}}T}\right), \tag{8.30}$$

where we have assumed equal temperatures for the two regions and where $\mu_{\mathrm{dip}} = \mu - V_{\mathrm{dip}}$. The function f describes the equation of state of the 2D Bose gas. Introducing the surface densities n and n_{dip} in the main region and in the dip of the cloud we get

$$n = \frac{1}{\lambda_T^2} f\left(\frac{\mu}{k_{\mathrm{B}}T}\right) \quad \text{and} \quad n_{\mathrm{dip}} = \frac{1}{\lambda_T^2} f\left(\frac{\mu - V_{\mathrm{dip}}}{k_{\mathrm{B}}T}\right). \tag{8.31}$$

A typical measurement of the surface density n_{dip} as a function of the applied potential V_{dip} is shown in Fig. 8.7. For a large value of the potential V_{dip} the density

tends to zero in the dip (see left inset). In the limit of no additional potential we recover a uniform density distribution (see right inset). Note that the range of measured n_{dip} being large we use a partial imaging method [127] to adjust the density of cloud probed with our absorption imaging beam. It is indeed crucial that the measured optical depth scales linearly with the atomic density and it is known that it is not the case for optically dense samples [186].
The data points are then fitted with a rescaled EoS:

$$n_{\mathrm{dip}} = p_1 f\left(\frac{p_2 - V}{p_3}\right), \tag{8.32}$$

where p_1, p_2 and p_3 are three fitting parameters. The phase-space density $\mathcal{D}_{\mathrm{dip}}$ then simply reads

$$\mathcal{D}_{\mathrm{dip}} = \frac{n_{\mathrm{dip}}}{p_1}. \tag{8.33}$$

The same fitting parameter p_1 is used to extract the phase-space density $\mathcal{D} = n/p_1$ of the unperturbed gas. The results of this procedure for different clouds are shown in Fig. 8.8 along with their determined degree of degeneracy.

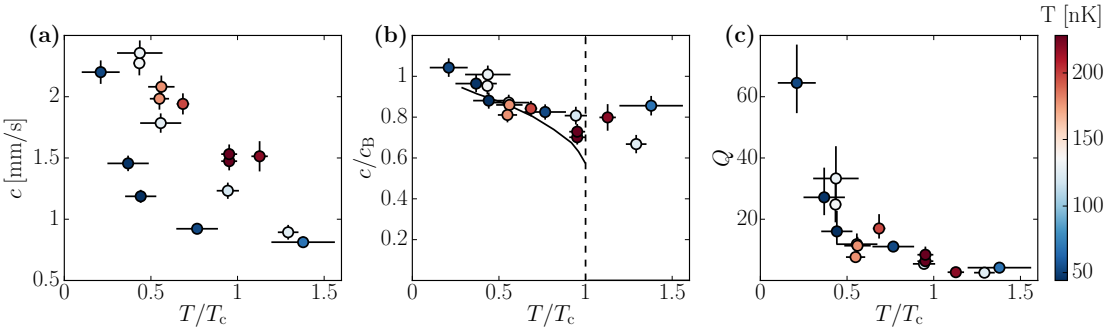

Figure 8.9 *– Speed of sound and damping. (a) Speed of sound (not normalized to Bogoliubov speed of sound). The color code gives the temperature for each point. The variation of c from 0.8 to 2.5 mm/s is mainly due to the change of density of the cloud. (b) Measured speed of sound normalized to the Bogoliubov speed of sound c_{B} with the same color code as in (a) (c) Quality factor $Q = \omega/\Gamma$ of the first mode determined for the experimental points with the same color code as in (a).*

8.4.3 Density calibration

Atom number calibration is a difficult task in our system because of the important role of dipole-dipole interactions in standard absorption imaging techniques [186] and the complex atomic level structure of the Rb atom. In this work we use the method inspired from Ref. [275]. Starting from a dilute cloud trapped in the optical box potential and in the $|F = 1, m = 0\rangle$ state, we use a $\pi/2$ microwave pulse to create a coherent superposition of this initial state with the $|F = 2, m = 0\rangle$ state. We measure independently the population $N_1 \approx N/2$ and $N_2 \approx N/2$ in these two

states for each experimental run, where N is the total atom number in the region of interest. We extract from typical sets of a hundred measurements the variance of the population difference $\mathrm{Var}(N_2 - N_1)$, which for a pure projection measurement, equals to N and then allows one to determine the atom number. For more details about the influence of laser intensity noise and finite imaging resolution, see chapter 7.

From this calibration we deduce that the cross-section for our absorption imaging is decreased by a factor 1.8(0.2) with respect to the two-level case with an infinitely narrow line: $\sigma_0 = (7/15) \times 3\lambda^2/(2\pi)$, where λ is the resonant wavelength. The factor 7/15 originates from the average of the Clebsch-Gordan coefficients for $\pi-$polarized light resonant with the $|F = 2\rangle$ to $|F = 3\rangle$ D_2 transition, as used in our experiment. This projection noise calibration is done with clouds with a typical optical depth of 0.4. The measurements of the cloud's density for determining the Bogoliubov speed of sound were done with a larger optical depth around 1. Using the results from Ref. [186], we then add another correction of 15% to take into account the decrease of the cross-section because of light-induced dipole-dipole interactions for an optical depth of 1 compared to 0.4. In conclusion, we correct our bare measurements of optical depth by $\eta = 2.07(0.23)$. Note that this correction is only used for the scaling of the vertical axis of Fig. 8.4a, and that all the measurements reported in section 8.2 are independent of the correction factor thanks to the direct determination of degeneracy of the cloud described above.

8.5 Summary of the measurements

We report in Table 8.1 the direct results from the measurements and the determination of the quantities plotted in Fig. 8.4. The determination of T/T_c and n_{2D} is described in the previous sections of this Supplemental Material. From these two parameters and using the formula $T_c = 2\pi n_{2D}\hbar^2/[mk_B \ln(380/\tilde{g})]$ we determine the temperature T. From the fit of the time evolution of the density profile we determine Γ and $\omega = \pi c/L_y$ and hence c/c_B and $Q = 2\omega/\Gamma$, where $c_B = \sqrt{gn_{2D}/m}$. The data shown in Fig. 8.3(a-c) correspond to measurements I, N and H, respectively.

8.5.1 Complementary results

The degeneracy of the gas is scanned by varying both the sample's temperature and density. The bare results for the speed of sound, without dividing by c_B, are shown in Fig. 8.9a. The temperature of the sample can be extracted from the measurement of the degeneracy of the cloud and of its density, as $\mathcal{D} \propto n_{2D}/T$. The resulting temperatures are shown by the color of the points in Fig. 8.9.

The density is varied by a factor 7 and the temperature by a factor 4. Figs. 8.9b and 8.9c show the same results as in section 8.2 but giving the temperature for each data point. The collapsing of all the points of Fig. 8.9 on a single curve in Fig. 8.9b is expected for the propagation of sound in the hydrodynamic regime in weakly-interacting 2D Bose gases, due to their scale-invariant behavior.

#	T/T_c	n_{2D} [μm^{-2}]	T [nK]	c [mm/s]	Γ [s^{-1}]	c/c_B	Q
A	0.43	67	132	2.27	15.3	0.95	24.8
B	0.94	28	118	1.23	38.6	0.80	5.4
C	1.29	21	124	0.89	60.1	0.66	2.6
D	0.37	27	45	1.46	8.90	0.96	27.2
E	0.44	65	127	2.36	11.6	1.00	33.3
F	0.44	22	43	1.19	12.4	0.88	16.0
G	0.77	15	51	0.92	14.0	0.82	11.1
H	1.38	11	66	0.81	32.7	0.85	4.2
I	0.21	53	50	2.20	5.50	1.04	64.5
J	0.56	50	125	1.79	25.3	0.87	11.9
K	0.56	69	175	2.08	31.0	0.85	11.4
L	1.13	43	217	1.51	94.7	0.79	2.7
M	0.95	52	225	1.47	39.6	0.70	6.3
N	0.95	52	225	1.53	31.0	0.72	11.1
O	0.69	63	195	1.94	19.3	0.84	17.0
P	0.55	71	176	1.98	44.1	0.81	7.6

Table 8.1 *– Summary of all the measurements reported in this chapter*

8.5.2 Landau damping

Landau damping mechanism describe the decay of phonons due to interaction with thermal excitations. Landau damping rate Γ for two-dimensional systems has been computed in Refs. [265, 276]. The damping of a given sound mode can be characterized by a dimensionless quality factor $Q = \omega/\Gamma$, where ω is the mode frequency. This quality factor is independent of the mode and only depends in 2D on the dimensionless ratio T/T_c. Its explicit expression, which is plotted in Fig. 8.4b is

$$1/Q(\tau) = \frac{\tilde{g}}{16\pi\tau} \times \int_0^\infty dx \left(\frac{2}{\sqrt{1+x^2}} + \frac{1}{1+x^2} \right)^{3/2} (\sqrt{1+x^2} - 1)\ \mathrm{Csch}^2[x/(2\tau)], \tag{8.34}$$

where

$$\mathrm{Csch} = 1/\sinh \quad \text{and} \quad \tau = \frac{2\pi}{\tilde{g}\ln(380/\tilde{g})}\frac{T}{T_c}. \tag{8.35}$$

In the regime $T/T_c \gg \tilde{g}/(2\pi)$ relevant in our experiments, the integral can be approximated by its asymptotic expression for $\tau \gg 1$, leading to the simplified expression

$$Q \simeq \frac{2}{\pi}\ln(380/\tilde{g})\frac{T_c}{T}.$$

In the opposite regime of very low temperatures $T/T_c \ll \tilde{g}/(2\pi)$, we find the asymptotic behavior

$$Q \simeq \frac{2}{\sqrt{3}\pi^3}\tilde{g}\ln(380/\tilde{g})^2 \left(\frac{T_c}{T}\right)^2.$$

We remind that for bosonic superfluids in 3D, including liquid ^{4}He, the Landau damping rate scales as T^4 in the low-temperature regime, i.e. $Q \propto 1/T^4$ [277].

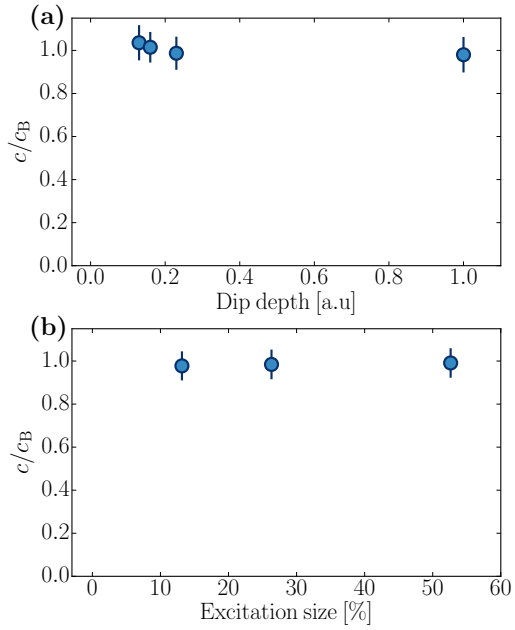

Figure 8.10 *– Normalized speed of sound for a gas in the degenerate regime ($T/T_c \approx 0.25$) for different excitation protocols. (a) Influence of depth of the excitation dip. The data in section 8.2 were taken for a dip depth of 0.16 a.u.. The value of 1 corresponds to an almost fully depleted dip. (b) Influence of the size of the excitation region. For the data presented in section 8.2, we used an excitation size of 25%.*

8.5.3 Influence of the excitation

We checked that our measurements of speed of sound are independent of the details of the excitation protocol. We show in Fig. 8.10a the influence of the amplitude of the excitation dip (where the density is about 2/3 of the total density in section 8.2) and observe no important variation of the speed of sound even for an almost full depletion in the dip region. We report in Fig. 8.10b the influence of the size of the excitation region (25% of the box length in section 8.2) and also observe no strong influence of this parameter.

9

Conclusion and perspectives

9.1 Conclusion of the thesis

In this work, the theory of the uniform 2D Bose gas has been discussed, and a uniform 2D Bose gas has been realized. The experimental setup benefits from several improvements thanks to the previous generations of experiments built in the team. The vertical confinement ("optical accordion") is in particular made as a proposed in [121], allowing for the compression of the atomic cloud along the transverse direction. This enables us to load a significant number of atoms in a single plane and then to compress the cloud to reach vertical confinement frequencies of up to 10 kHz. Such a high frequency places the gas far in the quasi-2D regime for the range of temperatures and densities used. The tunability of the setup allows furthermore to change the interaction strength $\tilde{g}$ dynamically. During this thesis, the setup has proven to be very stable and robust. The high tunability of the in-plane confinement of the atoms has also been widely used.

The interaction of the cloud with near resonant light has been studied, first probing mainly the coherent part of the scattered light through absorption imaging. This led in particular to the first observation of a blue shift of the resonance, which was expected for homogeneously-broadened dense uniform slabs of atoms. Non-Lorentzian behaviour of the resonance curves far from resonance was also demonstrated. Perspectives for this work could be to measure the shift for a sample of very small size, and check if the redshift seen for example in [180] is also recovered. Properties of a mirror made of a single layer of atoms were also discussed in section 4.5. This is an interesting topic as such an object is surely one of the lightest mirror which could be realized.

The setup also provides a new platform to study propagation of light in a spatially resolved way. The characteristic length on which photons propagate was studied and a detuning-dependent guiding effect in the slab was shown. A model was proposed for this effect in collaboration with Nicolas Cherroret and Dominique Delande (from Laboratoire Kastler Brossel). This type of experiment is to our knowledge quite new in the field. There is however room for improvement for the two works on light scattering presented here. A quite long probing times (10 µs) was for example required, during which the atomic repartition might change, as the dipole-dipole induced interactions correspond to strong forces between atoms at our densities.

Out-of-equilibrium physics of the gas was then studied. The expected distribution of supercurrents from the merging of uncorrelated BECs in a ring geometry was recovered and a timescale for this return to equilibrium was measured for different

lengths of the system. The propagation of defects was also observed, with a speed compatible with the expected speed of sound in the system.
Finally, the speed of sound was measured in our uniform Bose gas for different degeneracies. In the degenerate regime the measured sound is the second sound, and the measurements match nicely the predictions of [75]. Above the BKT transition however, the proposal [75] predicts a single sound mode whose speed should be more than two times larger than the one of second sound below the BKT threshold. We still observe a sound above T_{BKT}, but its speed is very close to the values measured in the degenerate regime, in contrast to the predictions. This behaviour might be explained by the non-hydrodynamicity of the gas above the transition [278]. This study might be extended to a gas with stronger interactions, which could also lead to an observation of the first sound predicted in [75].

9.2 Remaining experimental challenges of the 2D Bose gas

The two main challenges remaining for the experimental study of the 2D Bose gas are a precise measurement of the decay of the first order correlation function and a determination of the superfluid fraction for different degeneracies[a].
In the case of a uniform and infinite system, the first order correlation function should jump from an exponential to an algebraic decay of power 1/4 at the BKT transition. Density and phase fluctuation scalings within the critical region have been investigated via the measure of the power spectrum after different times of flight [71, 72], but these measurements did not allow yet to characterize properly the decay of the first order correlation function with distance. The analysis of the contrast in the interference patterns of atoms emerging from two traps as a function of the spatial range done in [34] led to the observation of a decrease in the degree of phase order close to the transition. The results below the BKT transition are compatible with an algebraic decay of power 1/4, but the authors pointed out that this might be partly fortuitous. Indeed, even though they concentrated on the quasi-uniform part of the images, geometrical effects due to the trapping might still be important. The change of behaviour from exponential to algebraic has been seen in [73] in the case of fermionic atoms in the bosonic regime, but the measured coefficients of algebraic decay are far from the theoretical value. This might be explained by the harmonic trapping as discussed in [74]. It is thus favorable to measure it in our setup with a uniform cloud, as described in the perspectives.
Concerning the second challenge, a direct observation of superfluidity in terms of frictionless flow has been made by rotating a moving obstacle formed by a micron-sized laser beam in a harmonically trapped gas in [279]. The authors did not observe a significant heating of the gas below a critical velocity when the obstacle was moved in a region of the trap where the system is superfluid, whereas a heating was reported when probing the normal part. Another observation of superfluidity in this system was reported with the measurements of frequency of so-called scissor modes in [280] via a local correlation analysis. However, these measurements did not provide

[a] Independent measurements are desirable even if there is an intimate link between the algebraic decay exponent η and the superfluid density n_{s} with the thermal wavelength λ_{T} as $\eta = 1/n_{\mathrm{s}}\lambda_{\mathrm{T}}^2$.

a quantitative determination of the superfluid fraction for different degeneracies. Proposals have been made to measure this quantity [281, 282, 283], but require the implementation of an artificial gauge field. We rather implemented another proposal [75], by measuring the speed of sound in the gas from the thermal to the degenerate regime. It is an interesting quantity as it is related to the superfluid fraction. The link is however not so clear as the hydrodynamic criterion required in the proposal [75] might not be valid for all degeneracies in our system. More theoretical work is required to be able to link this measurement of sound speed to the superfluid fraction.

9.3 Perspectives

We now have at our disposal a robust and tunable setup, which allows us to study a wide range of subjects. I briefly describe here a series of experimental projects which have either already been started in the lab or could be implemented in the future, before discussing briefly broader perspectives on the setup.

9.3.1 First-order correlation function measurements

As discussed in the previous section, one of the remaining challenges on the 2D Bose gas is a better observation of the decay of the first order correlation function with the distance. The momentum distribution measurement using the method of condensate focussing described in section 2.5.3 could be a way to achieve this goal. For an infinite system, the Fourier transform of the momentum distribution is indeed the first order correlation function. This technique is used in [73], but we hope to make a cleaner measurement thanks to the uniformity of our sample.
However in our case the long vertical expansion (of the order of 50 µm) and the short depth of field of the microscope objective (about 5 µm) lead to a degradation of the signal. We plan to overcome this limitation by imaging only a selected slab of the cloud.

9.3.2 Demixing experiments

Demixing experiments between a binary mixture of Bose-Einstein condensates have been performed quite soon after the first realizations of BECs [284]. It has been observed with different species [285], and the influence of an external magnetic field on the pattern formation between different spin states has been studied [286]. this has been studied in harmonic but not yet in box-like potentials to our knowledge.
We noticed that after transferring part of the atoms from one hyperfine state to another and letting them evolve, reproducible spatial patterns could be observed for each species. More precisely, starting from a degenerate sample, half of the atoms are transferred from the $|F = 1, m_F = 0\rangle$ to the $|F = 2, m_F = 0\rangle$ and the system is then let free to evolve. Pictures are then taken at different times as shown in figure 9.1. We checked that the other species corresponds to the complementary image. The two species thus seem to demix. The transfer between two states could be done

in a spatially resolved way by using Raman beams combined with the projection technique used to create the box potentials.

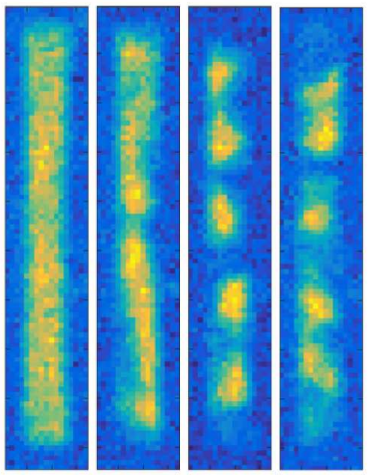

Figure 9.1 *– In-situ images of the atoms in $|F = 2, m_F = 0\rangle$ at different times after the MW pulse. The images are taken at 0, 50, 100 and 150 ms.*

9.3.3 Broader perspectives

In addition of the two remaining challenges on the 2D Bose gas that I discussed above, our experimental setup allows us to study other areas of physics. Light scattering, which has been explored in a part of this thesis constitutes a first example. The agreement between the models and the obtained results remains partial, and further investigation would be welcome. This could be addressed from an experimental point of view by better filtering the observed spatial modes of the light, for example by coupling it into an optical fiber. It might also enable a time-resolved measurement of the transmission. The complex level structure of ^{87}Rb atoms might explain some of the differences, and experiments with "two-level" atoms, like those reported recently in [192] would be very helpful.
Another topic of broad interest which can be studied is out-of-equilibrium physics. The thermalization of isolated quantum systems, and its fundamental link to statistical mechanics is still an open question today. Cold atoms offer an interesting platform to study these mechanisms because they are naturally a quantum many-body system, very isolated from the environment. Important studies on this topic have been performed for example in the group of Jörg Schmiedmayer (see among others [287, 288]).
A long-term goal of our setup is to investigate transport of atoms in a narrow channel. This has been studied with fermions in Zurich for two reservoirs linked by a 2D [58, 289, 59] or 1D channel [60], but experiments with bosons remain sparse[a] [61].

[a]Some of the experiments with fermions in Zurich were done on the BEC side of the BEC-BCS crossover, but in this case the gas is strongly interacting, contrary to the case that we would investigate.

Transport is usually induced by a temperature difference and/or a chemical potential imbalance between two connected reservoirs, which can be created in our setup. The connection between the two reservoirs can be made in many different ways (single or multimode channel, channel with a periodic lattice or a disordered medium inside...) and the regime of the gas in the reservoirs can be varied from thermal to superfluid leading to many possible interesting situations. The dynamics of the fluid at the edges of the channel where vortices are expected to form is also an interesting problem [290]. Moreover, adding disorder in the channel by projecting a laser speckle pattern might lead to the realization of a superleak, letting the superfluid pass through the channel but not the thermal part [291].
Finally, the implementation of gauge fields is possible on the setup, via the idea of optical flux lattices [292, 293]. Artificial gauge fields have been implemented with success on cold atoms, using different techniques [18, 19, 294, 295, 53, 296, 297, 298]. They however have their individual challenges in the view of reaching strongly correlated regimes and optical flux lattices may turn out to exhibit an improved performance in this regard.

IV Appendices

A

Implementation of Monte Carlo simulations

We present here in more details the simulations briefly described in section 1.5.1.

A.1 Modelisation

We consider a square of side L filled with N_a atoms at a temperature T. We describe this gas by a classical field $\psi(x, y)$ normalized as

$$\int |\psi(\boldsymbol{r})|^2 \, \mathrm{d}^2 r = N_\mathrm{a}, \tag{A.1}$$

and with the Dirichlet boundary conditions

$$\psi(0, y) = \psi(L, y) = \psi(x, 0) = \psi(x, L) = 0. \tag{A.2}$$

The field can be expanded in modes adapted to this geometry:

$$\psi(\boldsymbol{r}) = \frac{2}{L} \sum_{q_x, q_y} \sin\left(\frac{\pi x q_x}{L}\right) \sin\left(\frac{\pi y q_y}{L}\right) \phi(\boldsymbol{q}), \quad q_x, q_y \in \mathbb{N}^* \tag{A.3}$$

which can be inverted in

$$\phi(\boldsymbol{q}) = \frac{2}{L} \int \sin\left(\frac{\pi x q_x}{L}\right) \sin\left(\frac{\pi y q_y}{L}\right) \psi(\boldsymbol{r}) \, \mathrm{d}^2 r. \tag{A.4}$$

A.2 Space discretization

For the numerical calculation we will evaluate the fields ψ and ϕ on sites of a lattice. For convenience we will take a square of $(N_\mathrm{s} + 1)^2$ sites. We will now use the index j_x and j_y such that:

$$x_{j_x} = \frac{L}{N_\mathrm{s}} j_x, \quad y_{j_y} = \frac{L}{N_\mathrm{s}} j_y, \quad 0 \leq j_x, j_y \leq N_\mathrm{s}. \tag{A.5}$$

According to our boundary conditions, only $(N_\mathrm{s} - 1)^2$ sites can have a non-zero value. For the classical field simulations, as discussed in section 1.5.1 we must now implement an ultraviolet cutoff.

A.2.1 Implementation of the ultraviolet cutoff

The implementation of a cutoff on the $\boldsymbol{q}$ is very natural when one does simulations on a grid. As $\psi(\boldsymbol{r})$ is defined on a $N_\mathrm{s} \times N_\mathrm{s}$ grid, $\phi(\boldsymbol{q})$ is defined on a grid of the same size. This cutoff must match the one defined in equation (1.74):

$$\frac{\hbar^2\pi^2 q_\mathrm{cut}^2}{2mL^2} = k_\mathrm{B}T \quad \rightarrow \quad q_{cut} = \frac{2}{\sqrt{\pi}}\frac{L}{\lambda_T}. \tag{A.6}$$

The vectors $\boldsymbol{q}$ we have to take into account are thus in the first quarter of a disk of radius q_cut, or in an area $q_\mathrm{cut}^2\pi/4 = (L/\lambda_T)^2$. As we work on a square grid both for ψ and ϕ, we take a square of the same area, so for the discretized components of $\boldsymbol{q}$:

$$1 \leq q_x, q_y \leq \frac{L}{\lambda_T}. \tag{A.7}$$

As we have N_s sites on the side of the grid, we thus have $N_\mathrm{s} = L/\lambda_T$, meaning that the step of our grid is $\ell = L/N_\mathrm{s} = \lambda_T$.
As the phase space density $\mathcal{D} = \lambda_T^2 N_\mathrm{a}/L^2 = N_a/N_\mathrm{s}^2$, we see that changing $\mathcal{D}$ in our simulations keeping the grid constant corresponds to changing the atom number. For the classical field approximation, we assumed that we have at least one atom per mode, which means that for a given grid of size $N_\mathrm{s} \times N_\mathrm{s}$, we must keep $N_\mathrm{a} > N_\mathrm{s}^2 \Rightarrow \mathcal{D} > 1$. The temperature is a bit more hidden in our simulations. We will discuss it more in section A.4 when all variables will have been defined.

A.2.2 Normalization of the fields

We normalize the discretized field such that it has a modulus of one on each site:

$$\Psi(\boldsymbol{j}) = \sqrt{\frac{L^2}{N_\mathrm{a}}}\psi(\boldsymbol{r_j}). \tag{A.8}$$

Because of the chosen boundary conditions, we have to use the sine Fourier transform instead of the usual Fourier transform. The two discrete sine Fourier transforms linking the discretized fields $\Psi(\boldsymbol{j} = (j_x, j_y))$ and $\Phi(\boldsymbol{q} = (q_x, q_y))$ are

$$\Phi(\boldsymbol{q}) = \frac{2}{N_\mathrm{s}}\sum_{\boldsymbol{j}} \sin\!\left(\frac{\pi j_x q_x}{N_\mathrm{s}}\right)\sin\!\left(\frac{\pi j_y q_y}{N_\mathrm{s}}\right)\Psi(\boldsymbol{j}), \tag{A.9}$$

and

$$\Psi(\boldsymbol{j}) = \frac{2}{N_\mathrm{s}}\sum_{\boldsymbol{q}} \sin\!\left(\frac{\pi j_x q_x}{N_\mathrm{s}}\right)\sin\!\left(\frac{\pi j_y q_y}{N_\mathrm{s}}\right)\Phi(\boldsymbol{q}). \tag{A.10}$$

The chosen normalization of $\Psi(\boldsymbol{j})$ leads to a relation between $\Phi(\boldsymbol{q})$ and $\phi(\boldsymbol{q})$. One has indeed, starting from (A.4):

$$\phi(\boldsymbol{q}) = \frac{2}{L}\frac{L^2}{N_\mathrm{s}^2}\sum_{\boldsymbol{j}}\sin\Big(\frac{\pi x q_x}{L}\Big)\sin\Big(\frac{\pi y q_y}{L}\Big)\psi(\boldsymbol{r_j}) \tag{A.11}$$

$$= \frac{2}{L}\frac{L^2}{N_\mathrm{s}^2}\sqrt{\frac{N_\mathrm{a}}{L^2}}\sum_{\boldsymbol{j}}\sin\Big(\frac{\pi x q_x}{L}\Big)\sin\Big(\frac{\pi y q_y}{L}\Big)\Psi(\boldsymbol{j}) \tag{A.12}$$

$$= \frac{2}{L}\frac{L^2}{N_\mathrm{s}^2}\sqrt{\frac{N_\mathrm{a}}{L^2}}\frac{N_\mathrm{s}}{2}\Phi(\boldsymbol{q}) \tag{A.13}$$

$$= \sqrt{\mathcal{D}}\,\Phi(\boldsymbol{q}). \tag{A.14}$$

A.3 Field evolution

The energy of the gas is the sum of the kinetic energy (energies of the modes of the box)

$$E_\mathrm{kin} = \frac{\hbar^2}{2m}\int|\nabla\psi|^2\mathrm{d}^2r = \frac{\hbar^2\pi^2}{2mL^2}\sum_{\boldsymbol{q}}(q_x^2+q_y^2)|\phi(\boldsymbol{q})|^2, \tag{A.15}$$

and the interaction energy

$$E_\mathrm{int} = \frac{\hbar^2}{2m}\tilde{g}\int|\psi|^4\mathrm{d}^2r. \tag{A.16}$$

For the field evolution we compute these energies, in terms of the discretized fields, and per atom per unit of $k_\mathrm{B}T$. We get

$$\frac{1}{N_\mathrm{a}}\frac{E_\mathrm{kin}}{k_\mathrm{B}T} = \frac{1}{N_\mathrm{a}k_\mathrm{B}T}\frac{\hbar^2\pi^2}{2mL^2}\;D\;\sum_{\boldsymbol{q}}q^2\;|\Phi(\boldsymbol{q})|^2 \tag{A.17}$$

$$= \frac{\pi}{4}\frac{1}{N_\mathrm{s}^4}\sum_{\boldsymbol{q}}\;q^2\;|\Phi(\boldsymbol{q})|^2, \tag{A.18}$$

and

$$\frac{1}{N_\mathrm{a}}\frac{E_\mathrm{int}}{k_\mathrm{B}T} = \frac{1}{N_\mathrm{a}k_\mathrm{B}T}\frac{\hbar^2}{2m}\;\tilde{g}\;\frac{L^2}{N_\mathrm{s}^2}\sum_{\boldsymbol{j}}|\psi(\boldsymbol{r_j})|^4 \tag{A.19}$$

$$= \frac{1}{N_\mathrm{a}k_\mathrm{B}T}\frac{\hbar^2}{2m}\;\tilde{g}\;\frac{N_\mathrm{a}^2}{N_\mathrm{s}^2L^2}\sum_{\boldsymbol{j}}|\Psi(\boldsymbol{r_j})|^4 \tag{A.20}$$

$$= \frac{\tilde{g}\mathcal{D}}{4\pi}\frac{1}{N_\mathrm{s}^2}\sum_{\boldsymbol{j}}|\Psi(\boldsymbol{r_j})|^4. \tag{A.21}$$

Starting from a certain field, we compute its evolution using the splitting method, alternating the evolution linked to kinetic and interaction energy. We use as time step the one associated to the lattice:

$$t_0 = \frac{m\ell^2}{\hbar} = \frac{2\pi\hbar}{k_B T}. \tag{A.22}$$

The evolution linked to kinetic energy is expressed in the momentum space, using $\tau = t/t_0$:

$$i\frac{\partial \Phi}{\partial \tau} = \frac{Q^2}{2}\Phi(\boldsymbol{q}), \quad \text{with } \boldsymbol{Q} = \pi\frac{\boldsymbol{q}}{N_\mathrm{s}}, \tag{A.23}$$

and the evolution linked to the interaction energy

$$i\frac{\partial \Psi}{\partial \tau} = G|\Psi(\boldsymbol{j})|^2\Psi(\boldsymbol{j}), \quad \text{with } G = \tilde{g}\mathcal{D}. \tag{A.24}$$

A.3.1 Algorithm used

The starting point is a state $\Psi(\boldsymbol{j})$ with white noise. We let this state evolve by the splitting method according to the equations above for a certain number of iterations so that it thermalizes thanks to the non-linearity in the interaction energy evolution. We then compute the phase-space density $\mathcal{D}$ looking at the variance of the population of the modes of high q, for which the interaction energy is negligible compared to the kinetic energy. Indeed:

$$\langle|\phi(\boldsymbol{q})|^2\rangle \approx \frac{k_\mathrm{B}T}{\epsilon_q - \mu}, \tag{A.25}$$

which gives for the variance of the discretized field, and using $\mu \ll \epsilon_q$

$$\langle|\Phi(\boldsymbol{q})|^2\rangle \approx \frac{1}{\mathcal{D}}\frac{1}{\pi q^2/4N_\mathrm{s}^2}. \tag{A.26}$$

We then get $\mathcal{D}$:

$$\mathcal{D} \approx \frac{4}{\pi\langle|\Phi(\boldsymbol{q})|^2 q^2/N_\mathrm{s}^2\rangle}. \tag{A.27}$$

The found microscopical states are then post selected so that the $\mathcal{D}$ found after evolution is compatible with the initial $\mathcal{D}$ used for the evolution with a relative error of less than 10%. An example of result after thermalization is shown figure A.1. It is also possible to look at vortices in these simulations directly looking at the phase, as is done for example in [299].

A.4 Useful variables of the model

We specify only three variables in the simulations to describe the system: N_s, G and $\mathcal{D}$. They are linked to the usual parameters used to describe the gas, N_a, L, $\tilde{g}$ and λ_T by:

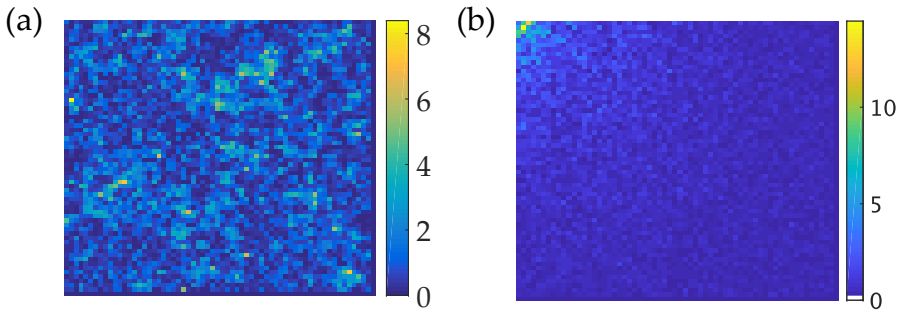

Figure A.1 *– Plots of $|\psi|^2$ in (a) and $|\phi|$ in (b) of one microscopical state for $\mathcal{D} = 6$ on a 64×64 grid.*

$$N_{\mathrm{s}} = \frac{L}{\lambda_T} \tag{A.28}$$

$$G = \tilde{g} N_{\mathrm{a}} \left(\frac{\lambda_T}{L} \right)^2 \tag{A.29}$$

$$\mathcal{D} = N_{\mathrm{a}} \left(\frac{\lambda_T}{L} \right)^2 \tag{A.30}$$

It is thus clear that the temperature is only defined through the combination of variables λ_T/L. Two systems with different sizes and different temperatures but same N_{a}, $\tilde{g}$ and ratio λ_T/L will then lead to the same simulation.
As shown in section 1.5.2, these simulations are good enough to recover the transition from an exponential to algebraic decay of the correlation function even in a finite-size system. We also used them to compare the speeds of sound to the ones found in the experiments of chapter 8 of this thesis.

B

PHYSICAL REVIEW A 95, 013632 (2017)

Loading and compression of a single two-dimensional Bose gas in an optical accordion

J. L. Ville,[1] T. Bienaimé,[2] R. Saint-Jalm,[1] L. Corman,[3] M. Aidelsburger,[1] L. Chomaz,[4] K. Kleinlein,[1] D. Perconte,[5] S. Nascimbène,[1] J. Dalibard,[1] and J. Beugnon[1,*]

[1]*Laboratoire Kastler Brossel, Collège de France, CNRS, ENS-PSL Research University, UPMC-Sorbonne Universités, 11 place Marcelin-Berthelot, 75005 Paris, France*

[2]*INO-CNR BEC Center and Dipartimento di Fisica, Università di Trento, 38123 Povo, Italy*

[3]*Institute for Quantum Electronics, ETH Zurich, 8093 Zurich, Switzerland*

[4]*Institut für Experimentalphysik, Universität Innsbruck, Technikerstraße 25, 6020 Innsbruck, Austria*

[5]*Unité Mixte de Physique, CNRS, Thales, Université Paris-Sud, Université Paris-Saclay, 91767 Palaiseau, France*

(Received 23 November 2016; published 27 January 2017)

The experimental realization of two-dimensional (2D) Bose gases with a tunable interaction strength is an important challenge for the study of ultracold quantum matter. Here we report on the realization of an optical accordion creating a lattice potential with a spacing that can be dynamically tuned between 11 and 2 μm. We show that we can load ultracold ^{87}Rb atoms into a single node of this optical lattice in the large spacing configuration and then decrease nearly adiabatically the spacing to reach a strong harmonic confinement with frequencies larger than $\omega_z/2\pi = 10$ kHz. Atoms are trapped in an additional flat-bottom in-plane potential that is shaped with a high resolution. By combining these tools we create custom-shaped uniform 2D Bose gases with tunable confinement along the transverse direction and hence with a tunable interaction strength.

DOI: 10.1103/PhysRevA.95.013632

I. INTRODUCTION

Thanks to their high degree of isolation from the environment and the rich toolbox developed from atomic physics, quantum gases are ideal platforms to study strongly correlated systems [1] or to develop new metrology devices [2]. A key ingredient is the development of custom-shaped optical potentials allowing one to confine atoms in tunable geometries. Atoms are routinely trapped in low-dimensional setups, optical lattices, or, as recently demonstrated, flat-bottom potentials for three-dimensional (3D) [3] and two-dimensional (2D) [4,5] gases.

Low-dimensional systems are of particular interest for several reasons. The role of thermal and quantum fluctuations is enhanced compared to 3D and leads to rich physics such as the existence of the Berezinskii-Kosterlitz-Thouless superfluid phase in two dimensions [6,7]. When placed in (artificial) magnetic fields, they can give rise to topological phases of matter similar to those appearing in the quantum Hall effect [8]. From a more technical point of view, 2D systems, now routinely used in "atomic microscope" experiments [9,10], are well suited to implement high-resolution imaging or trap shaping with a resolution typically better than 1 μm, without being limited by a short focal depth or line-of-sight integration.

In 2D cold atomic clouds the interparticle interactions are characterized by a dimensionless parameter $\tilde{g} = \sqrt{8\pi}a/\ell_z$, where a is the s-wave scattering length and ℓ_z is the harmonic oscillator length along the strongly confining direction [11]. Varying the confinement (hence ℓ_z) thus opens the possibility of controlling the interaction strength for a fixed value of a and eventually entering the strongly interacting regime for large values of $\tilde{g}$ [12,13].

One of the challenges of realizing 2D systems is to load a large fraction of an initial (3D) Bose-Einstein condensate (BEC) in a single highly anisotropic trap with relatively weak confinement in the xy plane and a strong one along the third (z) direction. A possible approach consists of making a single potential minimum using either phase plates, creating a node of intensity of blue-detuned light [14], or a tightly focused red-detuned single beam [15]. Another approach consists of making an optical lattice by crossing two interfering beams at a fixed angle. In that case, the lattice spacing and hence the achievable strength of the confinement along the z axis are limited by the requirement of a single node loading [16,17]. Yet another possibility is to use a small-spacing lattice, load several planes, and then remove atoms in all the planes but one [18]. This procedure may lead to an important atom loss that is detrimental for exploring large systems. Single-plane 2D Bose gases have also been demonstrated in radio-frequency-dressed magnetic traps with a moderate transverse confinement [19] or in more complex setups involving an evanescent optical field close to a dielectric surface [20].

In this paper we create a single 2D cloud with a large number of atoms and a tunable confinement using a so-called "optical accordion." It consists of loading atoms in a single node of a large-spacing lattice and then increasing the angle between the two interfering beams to make the confinement stronger. This technique has been demonstrated optically, but not implemented on an atomic cloud, in Refs. [21,22] and used to increase the spacing of a lattice trapping ultracold atoms [23]. Compression of quantum gases has been reported in Ref. [24] using a different technique involving a reflexion on a dielectric surface. It has also recently been mentioned in Ref. [25], without any technical detail or study of the compression process. In this work we demonstrate single-plane loading and a fivefold increase of the trapping frequency of a Bose gas in an optical accordion and study the adiabaticity of the compression stage. With far-detuned light and moderate power we obtain clouds of 10^5 ^{87}Rb atoms confined with frequencies $\omega_z/2\pi$ higher than 10 kHz. We show that this compression can be realized in about 100 ms with a small

*beugnon@lkb.ens.fr

amount of additional heating compared to the ideal adiabatic evolution. These experiments are carried out with a flat-bottom in-plane potential.

II. ACCORDION OPTICAL SETUP

The design of our accordion lattice is inspired from [22] and depicted in Fig. 1(a). A single laser beam of wavelength $\lambda = 532$ nm is split by a pair of polarizing beam splitters (PBSs) into two parallel beams propagating along the y axis. These two beams cross in the focal plane of a lens, and their interference forms a one-dimensional (1D) optical lattice. The position of the incoming beam on the PBSs is moved thanks to a motorized translation stage. This position controls the distance between the two beams reflected by the PBSs, hence the angle between the beams in the focal plane and the fringe spacing. The relative phase between the two beams, which determines the absolute position of the fringes, is controlled by a piezoelectric stack glued on the mirror reflecting the top beam. The two beams are transmitted through a common polarizing beam-splitter cube positioned just before the lens [not shown in Fig. 1(a)] to ensure that they have identical polarization. In this work we use an elliptical beam with measured waists at atom positions of $w_x = 88(2)\,\mu$m and $w_z = 38(6)\,\mu$m in the horizontal and vertical directions, respectively. The uncertainty corresponds to the standard deviation of the measurement for the different lattice spacings studied here. The choice of these values for the waists results from the compromise between getting the highest intensity with the available power and having a large enough horizontal waist to get a uniform confinement over the sample size (see next section) and a large enough vertical one to ensure a robust overlap between the two beams when changing the lattice spacing, as discussed below.

In our setup we change the full angle θ between the two interfering beams from 3° to 15°. The maximum angle is limited by the available numerical aperture on this axis, and the minimum angle is constrained by the finite size of the beams, which should not be clipped by the edges of the PBSs. We measure the lattice period i resulting from the interference of the two beams by imaging the intensity pattern in the atom plane on a camera, and we obtain the results shown in Fig. 1(b). By translating the initial beam by 11.5 mm, we vary i from 11.0(1) to 1.9(1) μm. The data points are fitted by

$$i = \frac{\lambda}{2}\sqrt{1 + [f/(d + d_0)]^2}, \tag{1}$$

where d is the displacement of the stage from the position giving our largest lattice period. Here, d_0 is an arbitrary offset, and f is the focal length of the lens.

The main challenge for realizing the accordion lattice is to avoid displacements of the beams in the focal plane when changing their angle. A large displacement of the two beams decreases their overlap and leads to a lower lattice depth and hence to a reduction of the trapping frequency or even to atom loss. In our setup, the main limitation is the imperfect quality of the lens. For instance, spherical aberrations and surface irregularities induce variations of the beam positions. We have tested standard achromatic doublets and an aspherical lens (Asphericon A50-100) and have found that the displacement

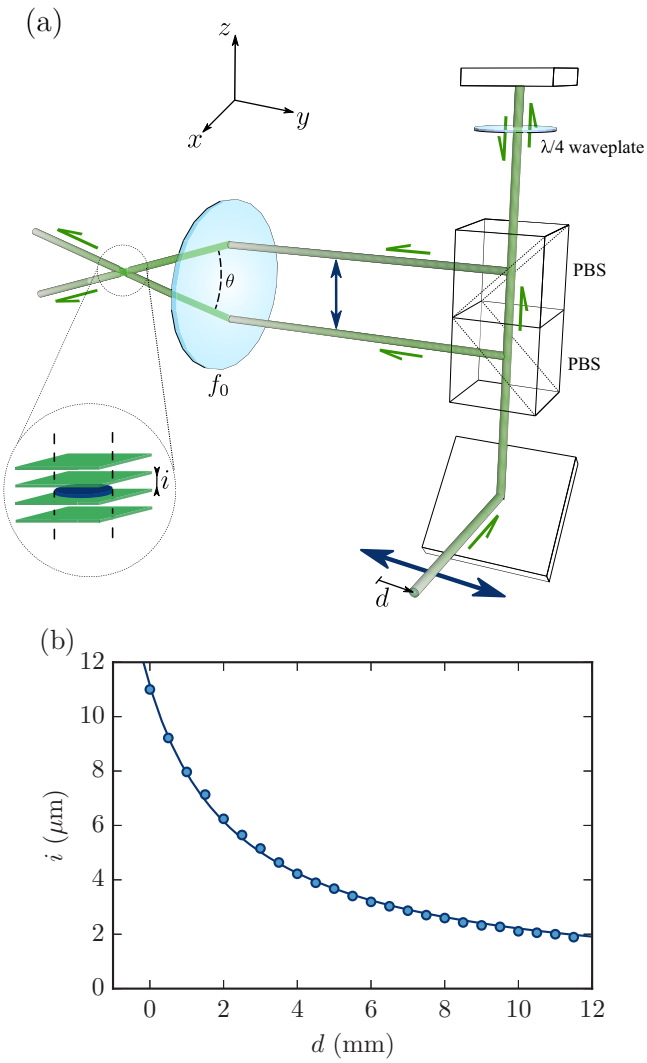

FIG. 1. (a) Sketch of the optical design allowing one to change the angle between the two interfering beams as proposed in [22]. The initial beam is moved (bottom arrow) by a distance d with a motorized translation stage (model LS-110 from PI miCos) that changes the distance between the two beams reflected by the polarizing beam splitters (PBS) of 25 mm size. These two beams are then focused on the atomic cloud by an aspherical 2-inch-diameter lens of focal length $f_0 = 100$ mm. The top beam is reflected on a mirror glued on a piezoelectric stack and goes twice through a quarter-wave plate. (b) Measured lattice spacing i of the vertical lattice at the atom position for different positions d of the translation stage. The data points are fitted by Eq. (1) with f and d_0 as free parameters. We obtain $f = 103(1)$ mm and $d_0 = 2.46(3)$ mm. The one-standard-deviation errors obtained from the fit on the measured lattice spacing are smaller than the size of the points.

is much smaller for the aspherical lens [26]. We show in Fig. 2 the positions of the centers of both beams in the z direction. The beams move by typically less than 20 μm in both directions, justifying our choice of $w_z = 39$ μm. We measure a displacement with a similar amplitude along the horizontal axis. We note that this motion of relatively small amplitude of the beams could induce irregular variations of the

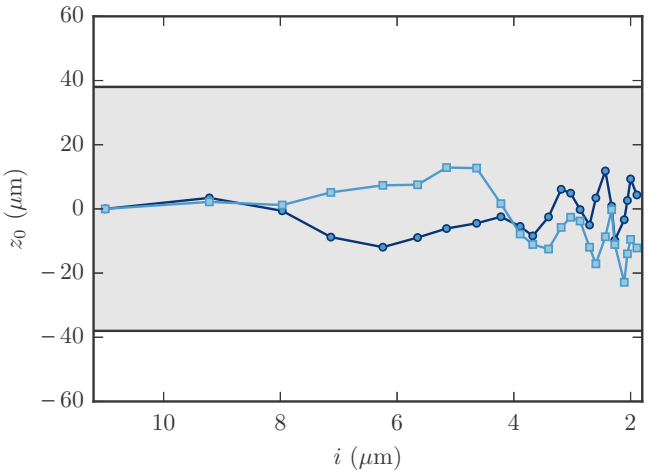

FIG. 2. Variation of the vertical positions z_0 with respect to their initial positions of the two interfering beams for different values of the lattice spacing i. Squares (circles) correspond to the bottom (top) beam. The shaded area corresponds to $\pm w_z$, where w_z is the averaged measured vertical waist over all the lattice spacings.

trap depth and center that may induce heating when changing the lattice spacing as discussed in Sec. IV.

III. MAKING A UNIFORM 2D BOSE GAS

We now describe the experimental system and the procedure used to realize 2D uniform gases. A sketch of the setup is shown in Fig. 3. We use two identical microscope objectives (numerical aperture of 0.45) above and below a glass cell. The bottom objective is used for absorption imaging of the cloud on a CCD camera with a typical resolution of 1 μm. The top objective allows us to image, with a similar resolution and a magnification of 1/70, a trapping potential programmed on a digital micromirror device (DMD). This spatial light modulator is an array of 1024×784 square mirrors of size 13.8 μm. The orientation of each of these mirrors can be chosen between two states. In this work, all the mirrors are set in a state reflecting light towards the atomic cloud except the ones from a central disk-shaped area whose image in the atomic plane has a radius of 20 μm. The DMD reflects a blue-detuned beam at a wavelength of 532 nm with a maximum power of about 300 mW and a waist of 45 μm at the atom position. These parameters correspond to a maximum potential height at the edge of the disk of $k_B \times 4$ μK. In all the experiments described in the following, atoms are confined in the optical potential created by the combination of this box-potential beam and the accordion beams described in the previous section. The cloud is imaged using standard absorption imaging techniques either along the vertical axis or along the horizontal axis common with the accordion beams.

To load the 2D box potential we first prepare a 3D BEC using standard methods. We start from a 3D magneto-optical trap of ^{87}Rb atoms which contains 10^9 atoms. After cooling, compression, and optical pumping into the $F = 1$ manifold we load the atoms in the $F = 1$, $m_F = -1$ state in a magnetic quadrupole trap realized by a pair of conical coils along the vertical axis. After compression we proceed to

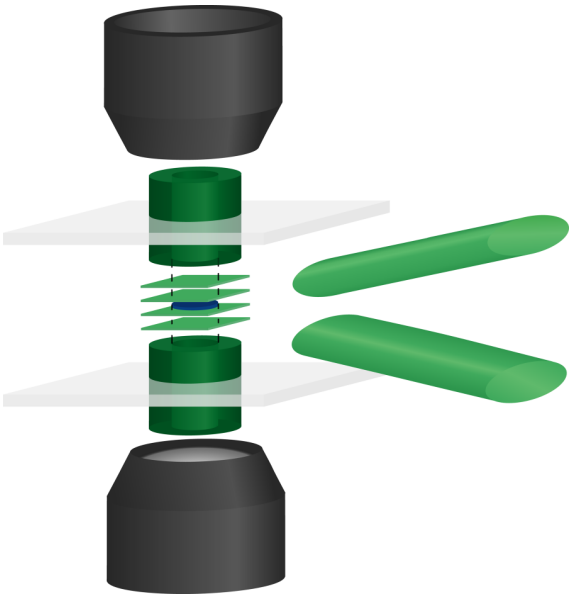

FIG. 3. Sketch of the experimental setup. The vacuum cell, simply depicted here as two horizontal glass plates, is surrounded by a pair of identical microscope objectives with a numerical aperture of 0.45. Atoms (in blue in the center) are trapped in the combination of blue-detuned dipole traps. Confinement along the vertical direction is realized by the interference of two beams at an angle (on the right) that create the accordion lattice. In-plane confinement is ensured by imaging the surface of a DMD on the atomic plane thanks to the top microscope objective. Here we created a disk-shaped uniform potential. This trap is loaded from a 3D BEC.

forced evaporative cooling using a radio-frequency field ramp. Afterward, we decompress the magnetic trap to load atoms in an optical dipole trap consisting of two beams operating at a wavelength around 1064 nm and crossing at a right angle in the horizontal plane. Their vertical and horizontal waists are, respectively, 30 and 90 μm, and the depth potential is calculated to be around 70 μK. We then lower the trap depth to realize forced evaporative cooling, and we get almost pure BECs with typically 3×10^5 atoms.

We now detail the loading of the 3D BEC in the box potential. We first ramp the box potential beam to full power in 300 ms. We then compress the BEC vertically to obtain a robust single-plane loading by increasing the power of one of the red-detuned dipole trap beams back to its maximum initial value in 125 ms while decreasing the other dipole trap power to zero. We then ramp the power of the accordion beams to their maximal value of 325 mW per beam in 25 ms with a maximum spacing of the accordion lattice of 11 μm. Finally, we ramp off the crossed dipole trap beams. The global spatial phase of the accordion lattice is adjusted thanks to the piezoelectric stack to get a dark fringe centered on the initial position of the atomic cloud. The optical alignment of the accordion beams is optimized so as to load the atoms in a fringe which is not moving when compressing the accordion lattice. We can then reliably load the atoms in a single plane [see Fig. 4(a)] [27]. Further evaporative cooling can be performed by lowering the power of the box potential beam and/or of the accordion beam to reach the 2D regime for which the thermal energy and the

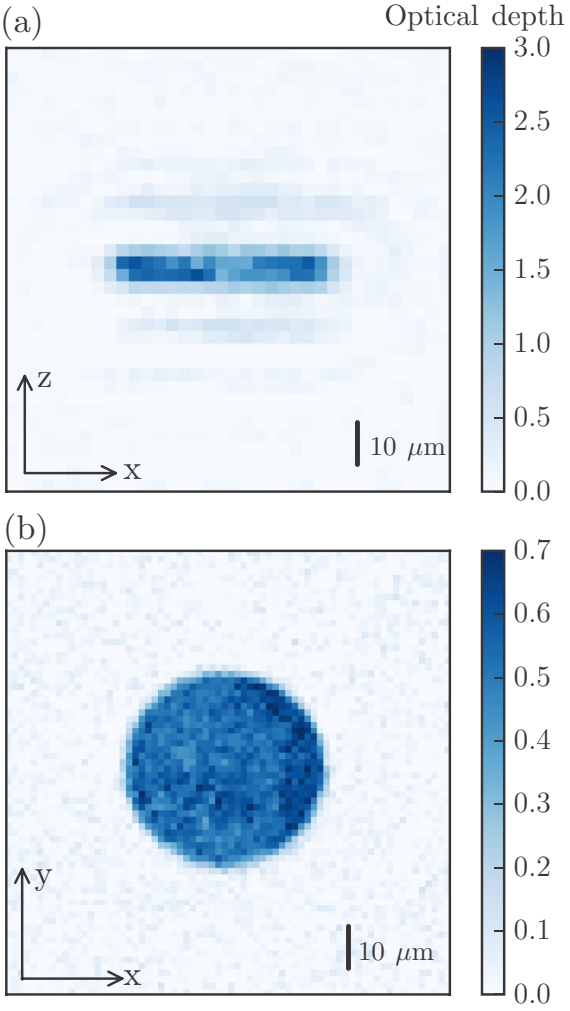

FIG. 4. *In situ* absorption images of the trapped cloud before compression with $\omega_z/2\pi = 2.1$ kHz and $T = 800$ nK. The cloud diameter is 40 μm. To avoid saturation of the absorption signal, we transfer, using a microwave field, only a small fraction of the 10^5 atoms from the $F = 1$ state to the $F = 2$ state before imaging atoms in $F = 2$. (a) Side view (transferred fraction: 100%, average of five pictures). The weak signals above and below the main cloud are fringes due to the propagation of light through our dense sample. We have checked that their position is independent of the lattice spacing of the accordion lattice. (b) Top view (transferred fraction: 2.4%, average of 35 pictures).

interaction energy are smaller than $\hbar\omega_z$. A typical picture of the cloud taken along the vertical axis is presented in Fig. 4(b).

IV. COMPRESSION IN THE ACCORDION

The main feature of this setup is the possibility to compress the gas along the z direction once the atoms are loaded in a single node of the lattice. In this section we describe our characterization of the compression process starting from atoms loaded in the largest-spacing configuration. First, we measure the oscillation frequency of the cloud in the vertical direction for different lattice spacings at maximum power. This frequency is determined as follows. We excite the center-of-mass motion of the cloud along the z direction by suddenly changing the power in the accordion beams, we let the cloud oscillate, and, finally, we measure the vertical position of the atomic cloud after a short free expansion. The trapping frequency is given by a sinusoidal fit of the data. The results are shown in Fig. 5. By compressing the lattice spacing from 11 to 2 μm we observe an increase of the oscillation frequency from 2.15(5) to 11.2(3) kHz. We also plot in Fig. 5 the expected frequency calculated with the measured power, waists, and lattice spacing. Our measurements are consistently below this calculation. We attribute this effect to the inaccurate calibration of the beam waists and powers and the imperfect overlap of the beams.

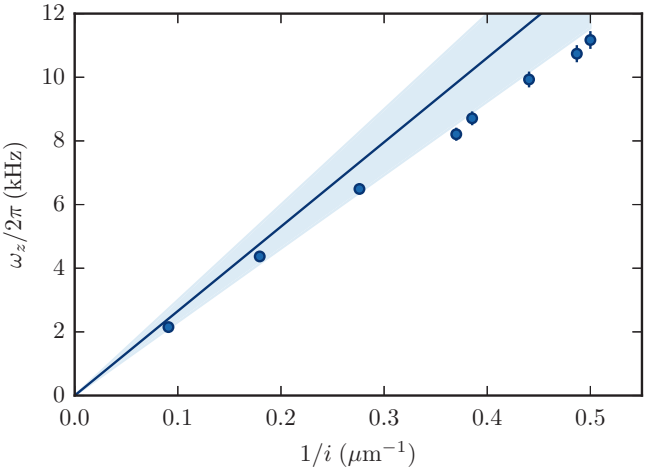

FIG. 5. Measured oscillation frequency along the vertical direction for different lattice spacings. The solid line is the calculated frequency with the independently measured parameters of the beams, and the shaded area corresponds to the uncertainty on the calibration of the beam parameters. The error bars represent the standard deviation given by the fit algorithm on the measured frequency and are close to the size of the data points and not visible for the low frequencies.

We now discuss the effect of compression on the cloud's temperature T, which is measured with a method detailed in Appendix A. In order to avoid evaporation of atoms during this compression, we first proceed to a cooling stage. It consists of lowering the power of the in-plane confining laser to evaporate the cloud and then setting it back to its initial value. After this evaporation cooling, we typically obtain $N = 3 \times 10^4$ atoms in the large-spacing lattice at a temperature of $T_0 = 180$ nK. With these parameters, the total 2D phase-space density, defined as $\mathcal{D} = N\lambda_T^2/A$, with A being the disk area and λ_T being the thermal de Broglie wavelength, is $\mathcal{D} = 4.8$, which corresponds to a noncondensed gas [5]. We then compress the cloud to various final vertical confinements at a constant velocity of the translation stage (90 mm/s) within 0.13 s while keeping the overall sequence duration constant. We show in Fig. 6(a) the measured final temperature (blue circles) for various final trapping frequencies. We observe a significant increase in the cloud's temperature by a factor of about 2 for the largest final frequency. The atom number is unchanged during this compression, and thus it rules out any evaporation process.

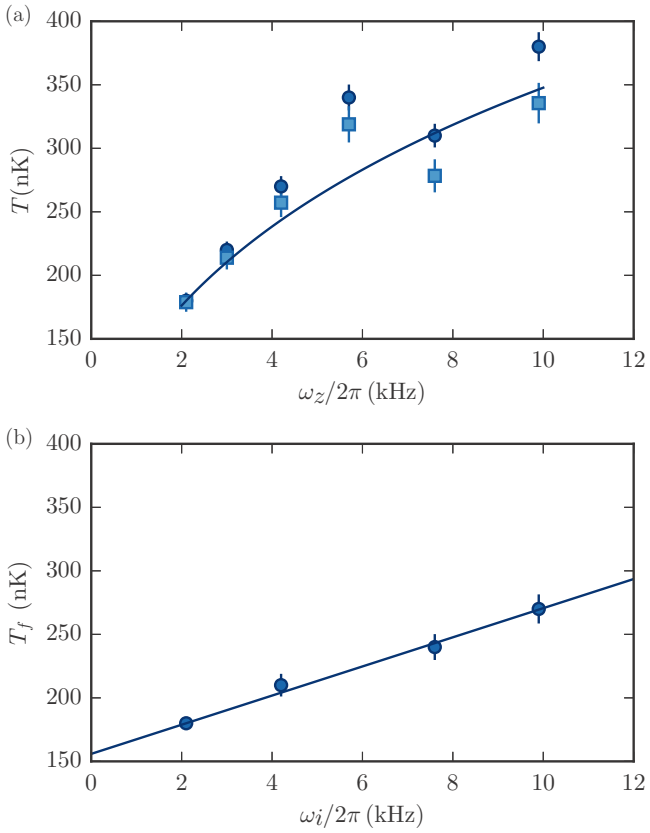

FIG. 6. Compression in the optical accordion. (a) Temperature measured after compression to a final frequency ω_z (circles) and corrected by the fit of the measured heating displayed in (b) (squares). The solid line is a calculation for an adiabatic compression of an ideal Bose gas with our trap geometry (see Appendix B). (b) Temperature T_f measured after a compression to the intermediate frequency ω_i and decompression to the initial frequency. The solid line is a linear fit to the data. The measured heating is divided by 2 before subtraction to the data in (a), considering that the heating for a full cycle is two times larger than the heating for the single compression.

The measured increase of temperature during the compression process could have two origins. (i) It could simply result from the change in density of states in a purely adiabatic process [solid line in Fig. 6(a)]. (ii) There may be an additional heating process due to imperfections in the trap compression as discussed in Sec. II. In order to test the adiabaticity of the process we realize a compression up to a given intermediate frequency ω_i followed by a decompression to the initial frequency. The measured final temperatures T_f are reported in Fig. 6(b). For a purely adiabatic compression-decompression cycle we expect no increase in temperature. We observe a deviation from adiabaticity which can reach 90 nK for a full compression-decompression sequence or, assuming the same amount of additional heating for compression and decompression, 45 nK for the compression stage. This heating remains small compared to the 150 nK increase in temperature expected for a purely adiabatic process as described in the next paragraph. This heating varies approximately linearly with the target frequency ω_i. We have measured a similar heating for lower velocities of the translation stage.

To further explore the origin of the temperature increase observed here, we compare our results to the prediction for adiabatic compression of an ideal Bose gas confined in our trap geometry. The result of this calculation, detailed in Appendix B and applied to the measured initial temperature and frequency, is shown in Fig. 6(a) as a solid line. We also show the measured temperatures corrected by half the heating measured for the compression-decompression cycle [Fig. 6(b)] as squares. They are in good agreement with the calculated temperature. We conclude that the deviation from adiabaticity in our experimental setup leads to an additional heating that remains small compared to the increase of temperature expected in the adiabatic case.

V. OUTLOOK: AN ADJUSTABLE INTERACTION STRENGTH

We have realized a 2D uniform Bose gas with a tunable confinement. As discussed in the Introduction, in such gases the role of interactions is described, up to logarithmic corrections [11], by the dimensionless parameter $\tilde{g} = \sqrt{8\pi}a/\ell_z$, where $\ell_z = \sqrt{\hbar/(m\omega_z)}$ is the harmonic oscillator ground-state length for a particle of mass m in the harmonic potential of frequency ω_z. Tuning the confinement thus allows one to control the strength of interaction in such systems without tuning the scattering length via a Feshbach resonance [13] or adding an in-plane lattice potential to control the effective mass of the atoms [12]. In our setup, by varying $\omega_z/2\pi$ between 1 and 11 kHz by tuning the lattice spacing or the laser power, we can adjust $\tilde{g}$ between 0.08 and 0.26. Obtaining such comparatively large values of $\tilde{g}$ is of great interest for realizing strongly correlated states for which the gap between the ground state and the excited states usually scales linearly with $\tilde{g}$ [28]. The demonstration of such an optical accordion is thus a significant step in this direction.

Our system is compatible with the realization of flat-bottom potentials with a shape that can be changed, potentially in a dynamic way, thanks to the use of DMDs. Our system is thus an ideal platform to study in- and out-of-equilibrium many-body physics in two-dimensional systems. Another asset of this geometry is the possibility to realize evaporative cooling with this accordion lattice. In the usual evaporation schemes a particle is evaporated when it has a high enough energy and when it reaches a position in the trap where it could be lost (like the edge of the box potential in the work described here). In this situation temperature gradients might be created in the sample. Lowering the depth of the accordion lattice by decreasing its intensity or by adding a magnetic field gradient allows for an evaporation independent of the atom position and could lead to more efficient evaporative cooling. This feature is particularly interesting when studying quench cooling of 2D quantum gases [5].

ACKNOWLEDGMENTS

We thank Z. Hadzibabic for fruitful discussions. This work is supported by DIM NanoK, ANR (ANR-12-BLANAGAFON), and ERC (Synergy UQUAM). L.C. acknowledges the support from DGA. M.A. is supported

within the Marie Curie Project BosQuanTran of the European Commission.

J.L.V. and T.B. contributed equally to this work.

APPENDIX A: TEMPERATURE MEASUREMENT

The temperatures reported in the main text were measured using the following procedure. Immediately after loading the atoms in the optical box potential, we send a short pulse of a microwave field that transfers a small fraction of about 10% of the atoms from the $|1\rangle = |F = 1, m = -1\rangle$ state to the $|2\rangle = |F = 2, m = -2\rangle$ state. We then proceed to forced evaporation by lowering the power of the box potential beam and realize the experimental sequences discussed in the main text. We assume that the atoms in state $|2\rangle$ thermalize with the main cloud of atoms in $|1\rangle$. By choosing the fraction of atoms in state $|2\rangle$ to be small enough we always prevent the formation of a Bose-Einstein condensate in this state. To extract the temperature of the sample we release the atoms from the trap and image the density distribution of atoms in state $|2\rangle$ integrated along the vertical direction and after a time-of-flight of 8.7 ms. For each point we average typically 10 images with the same experimental conditions.

We compare the radially averaged profile of these distributions to a numerically computed profile considering an ideal gas with an initial velocity distribution given by the Bose distribution and an initial uniform position in the box potential and assuming an expansion without any interparticle interaction. The theoretical profile has two free parameters, the temperature T and the fugacity z, which we optimize to obtain the best fit to the experimental data points. With our signal-to-noise ratio, there is a continuous set of (z,T) that fits almost equally well a given experimental profile, making a robust estimate of the temperature difficult. We circumvent this issue by using the independently measured atom number as an additional input parameter to compute $z(T)$, leaving T as the only free parameter.

From the distribution of temperature measurements for a fixed experimental sequence, we estimate that the one-standard-deviation statistical error bars on the temperature measurement are around $\pm 3\%$ of the measured temperature. The main source of uncertainty is given by the uncertainty on the atom number that we use to estimate the temperature. In our range of parameters, the estimated uncertainty of 25% in the atom number calibration leads to an uncertainty of about 15% in the temperature. In the main text, we display error bars corresponding to only the $\pm 3\%$ statistical uncertainty.

APPENDIX B: ADIABATIC COMPRESSION

We consider a gas of noncondensed bosons of mass m confined in the xy plane in a box potential of surface A and along the vertical direction in a harmonic potential of frequency ω_z. We set $\rho_0 = mA/(2\pi\hbar^2)$ for the in-plane density of states and $z_j = z\exp(-j\beta\hbar\omega_z)$, where z is the gas fugacity, $\beta = 1/k_B T$, and j is the integer labeling the jth state of the vertical harmonic oscillator. The average occupation number $\bar{n}_{j,k}$ of a given energy state with an in-plane wave number k is

$$\bar{n}_{j,k} = \left\{ z^{-1} \exp\left[\beta\left(j\hbar\omega_z + \frac{\hbar^2 k^2}{2m} \right) - 1 \right] \right\}^{-1}. \quad \text{(B1)}$$

Introducing the polylogarithm function $g_\alpha(z) = \sum_{k=1}^{\infty} z^k/k^\alpha$, we compute N_j, J_j, and S_J, which are, respectively, the atom number, the grand-canonical potential, and the entropy of state j.

$$\begin{aligned} N_j &= \rho_0 k_B T g_1(z_j), \\ J_j &= -\rho_0 (k_B T)^2 g_2(z_j), \\ S_j &= -\left.\frac{\partial J_j}{\partial T}\right|_{\mu,\omega_z} = \rho_0 k_B T [2g_2(z_j) - g_1(z_j)\ln(z_j)]. \end{aligned} \quad \text{(B2)}$$

We compute the temperature evolution for an adiabatic compression by evaluating, for each value of the final compression frequency ω_z, the temperature and the fugacity, keeping $S = \sum_j S_j$ and $N = \sum_j N_j$ constant. The result of this calculation is shown in the main text in Fig. 6 and is reproduced in Fig. 7.

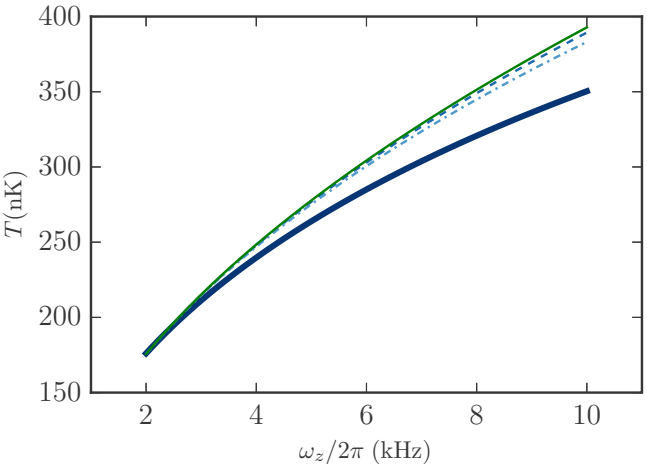

FIG. 7. Adiabatic compression. We show, for an initial temperature of 180 nK and an initial frequency of 2.1 kHz, the temperature increase during compression calculated numerically for different models. The thick solid line corresponds to the bosonic case. The green solid line is given by an analytical result obtained in the classical case with a weak confinement along z and scales as $\omega_z^{1/2}$. The dashed line and the dot-dashed line are associated with the fermionic and the Maxwell-Boltzmann statistics cases, respectively.

The previous calculation can be straightforwardly extended to fermionic statistics and to the classical Maxwell-Boltzmann statistics by replacing $g_\alpha(z)$ by $f_\alpha(z) = -g_\alpha(-z)$ and by z, respectively. The results for these cases are also represented in Fig. 7 as a dotted line and a dot-dashed line respectively, and show that, in all cases, the increase in temperature during adiabatic compression is larger than for the bosonic case. Indeed, Bose statistics leads to a larger population of the low-lying states of the vertical harmonic oscillator than the classical distribution and thus to a smaller increase of temperature when increasing the confinement frequency.

Finally, we also plot in Fig. 7 an analytical result obtained for the classical Maxwell-Boltzmann statistics but assuming a weak confinement along the vertical direction ($\beta\hbar\omega_z \ll 1$). In this case the 3D density of states is given by $\rho(\varepsilon) = \rho_0/(\hbar\omega_z)\,\varepsilon$, and the entropy reads

$$S/(Nk_B) = 3 + \ln[\rho_0(k_BT)^2/(N\hbar\omega_z)]. \quad \text{(B3)}$$

An adiabatic compression thus leads to an increase in temperature as $T \propto \sqrt{\omega_z}$, which corresponds to the green solid line shown in Fig. 7 and which is very close to the numerical calculation for the Maxwell-Boltzmann statistics. We note that in the experiments presented here the fugacity is close to 1 and the Maxwell-Boltzmann approximation is clearly not valid.

[1] I. Bloch, J. Dalibard, and W. Zwerger, Rev. Mod. Phys. **80**, 885 (2008).

[2] A. Cronin, J. Schmiedmayer, and D. Pritchard, Rev. Mod. Phys. **81**, 1051 (2009).

[3] A. L. Gaunt, T. F. Schmidutz, I. Gotlibovych, R. P. Smith, and Z. Hadzibabic, Phys. Rev. Lett. **110**, 200406 (2013).

[4] L. Corman, L. Chomaz, T. Bienaimé, R. Desbuquois, C. Weitenberg, S. Nascimbène, J. Dalibard, and J. Beugnon, Phys. Rev. Lett. **113**, 135302 (2014).

[5] L. Chomaz, L. Corman, T. Bienaimé, R. Desbuquois, C. Weitenberg, S. Nascimbène, J. Beugnon, and J. Dalibard, Nat. Commun. **6**, 6162 (2015).

[6] V. L. Berezinskii, Sov. Phys. JETP **34**, 610 (1972).

[7] J. Kostlerlitz and D. Thouless, J. Phys. C **6**, 1181 (1973).

[8] J. Dalibard, F. Gerbier, G. Juzeliūnas, and P. Öhberg, Rev. Mod. Phys. **83**, 1523 (2011).

[9] W. Bakr, J. Gillen, A. Peng, S. Fölling, and M. Greiner, Nature (London) **462**, 74 (2009).

[10] J. F. Sherson, C. Weitenberg, M. Endres, M. Cheneau, I. Bloch, and S. Kuhr, Nature (London) **467**, 68 (2010).

[11] Z. Hadzibabic and J. Dalibard, Riv. Nuovo Cimento **34**, 389 (2011).

[12] L.-C. Ha, C.-L. Hung, X. Zhang, U. Eismann, S.-K. Tung, and C. Chin, Phys. Rev. Lett. **110**, 145302 (2013).

[13] P. A. Murthy, I. Boettcher, L. Bayha, M. Holzmann, D. Kedar, M. Neidig, M. G. Ries, A. N. Wenz, G. Zürn, and S. Jochim, Phys. Rev. Lett. **115**, 010401 (2015).

[14] S. P. Rath, T. Yefsah, K. J. Günter, M. Cheneau, R. Desbuquois, M. Holzmann, W. Krauth, and J. Dalibard, Phys. Rev. A **82**, 013609 (2010).

[15] P. Cladé, C. Ryu, A. Ramanathan, K. Helmerson, and W. D. Phillips, Phys. Rev. Lett. **102**, 170401 (2009).

[16] N. Gemelke, X. Zhang, C.-L. Hung, and C. Chin, Nature (London) **460**, 995 (2009).

[17] M. G. Ries, A. N. Wenz, G. Zürn, L. Bayha, I. Boettcher, D. Kedar, P. A. Murthy, M. Neidig, T. Lompe, and S. Jochim, Phys. Rev. Lett. **114**, 230401 (2015).

[18] S. Stock, Z. Hadzibabic, B. Battelier, M. Cheneau, and J. Dalibard, Phys. Rev. Lett. **95**, 190403 (2005).

[19] K. Merloti, R. Dubessy, L. Longchambon, A. Perrin, P.-E. Pottie, V. Lorent, and H. Perrin, New J. Phys. **15**, 033007 (2013).

[20] J. I. Gillen, W. S. Bakr, A. Peng, P. Unterwaditzer, S. Fölling, and M. Greiner, Phys. Rev. A **80**, 021602 (2009).

[21] R. A. Williams, J. D. Pillet, S. Al-Assam, B. Fletcher, M. Shotter, and C. J. Foot, Opt. Express **16**, 16977 (2008).

[22] T. Li, H. Kelkar, D. Medellin, and M. Raizen, Opt. Express **16**, 5465 (2008).

[23] S. Al-Assam, R. A. Williams, and C. J. Foot, Phys. Rev. A **82**, 021604 (2010).

[24] M. Miranda, A. Nakamoto, Y. Okuyama, A. Noguchi, M. Ueda, and M. Kozuma, Phys. Rev. A **86**, 063615 (2012).

[25] D. Mitra, P. T. Brown, P. Schauß, S. S. Kondov, and W. S. Bakr, Phys. Rev. Lett. **117**, 093601 (2016).

[26] The variations of the beam position and angle induced by the motion of the translation stage were found to be less important than the defects of the tested lenses.

[27] We compensate the slow drift of the lattice by a feedback on the piezoelectric stack after each experimental sequence.

[28] N. Cooper, Adv. Phys. **57**, 539 (2008).

C

Clebsch-Gordan coefficients

The interaction Hamiltonian of a single-electron atom in an electromagnetic field is of the form (in Coulomb gauge) [300]

$$H = \frac{1}{2m}\left[\mathbf{P} - q\mathbf{A}(\mathbf{R},t)\right]^2 + V(R) - \frac{q}{m}\mathbf{S}\cdot\mathbf{B}(\mathbf{R},t), \tag{C.1}$$

where $\mathbf{R}$, $\mathbf{P}$ and $\mathbf{S}$ are the position, momentum and spin operators of the electron and $\mathbf{B}(\mathbf{R},t)$ and $\mathbf{A}(\mathbf{R},t)$ are the magnetic field and vector potential operators.
It can be split into a time independent and a time dependent part

$$H = H_0 + W(t), \tag{C.2}$$

with

$$H_0 = \frac{1}{2m}\mathbf{P}^2 + V(R), \tag{C.3}$$

and

$$W(t) = -\frac{q}{m}\mathbf{P}\cdot\mathbf{A}(\mathbf{R},t) - \frac{q}{m}\mathbf{S}\cdot\mathbf{B}(\mathbf{R},t) + \frac{q^2}{2m}\mathbf{A}^2(\mathbf{R},t). \tag{C.4}$$

The last term in C.4 can be neglected for small fields, and $W(t)$ can be expanded in electric dipole (ED), magnetic dipole (MD), electric quadrupole (EQ) and higher order terms:

$$W(t) = W_{\mathrm{ED}}(t) + W_{\mathrm{MD}}(t) + W_{\mathrm{EQ}}(t) + ... \tag{C.5}$$

The electric dipole is dominant by a factor λ/a_0 where a_0 is the Bohr radius and λ the wavelength of light, but the other terms become important when the transitions via the electric dipole are forbidden by selection rules.
A probability of transition from a state $|1\rangle$ to a state $|2\rangle$ which are eigenstates of the time independent Hamiltonian can be computed in the framework of time-dependent perturbation theory. The transition probability between two states if $W(t)$ varies sinusoidally at the frequency of the transition $\nu = (E_2 - E_1)/h$ is (see for example [300], chapter 13)

$$P_{12} \propto |\,\langle 2|\,W(t)\,|1\rangle\,|^2. \tag{C.6}$$

We compute the matrix elements in the case of an optical and a MW transitions to define the Clebsch-Gordan coefficients which are used in the main text.

C.1 Electric dipole

It can be shown that $W_{\mathrm{ED}} \propto \mathbf{R}$ [300]. The driving of an atom by a nearly-resonant optical radiation is thus characterized by the dipole matrix element $\langle F\, m_F|\, \mathbf{R}\, |F'\, m'_F\rangle$ between the two hyperfine sublevels, where the primed variables refer to the excited states and the unprimed ones to the ground states. It is possible to factorize this matrix element thanks to the Wigner-Eckart theorem in terms of a Wigner $3-j$ symbol (also called Clebsch-Gordan coefficient) as:

$$\langle F\, m_F|\, \mathbf{R}_q\, |F'\, m'_F\rangle = \langle F|\, \mathbf{R}\, |F'\rangle\, (-1)^{F'-1+m_F}\sqrt{2F+1}\begin{pmatrix} F' & 1 & F \\ m'_F & q & -m_F \end{pmatrix} \tag{C.7}$$

where q is labelling the component of $\mathbf{R}$ in the spherical basis. The computation of the coefficients have been performed in [124], and we report the modulus square of these coefficients normalized to the strongest transition in figure C.1.

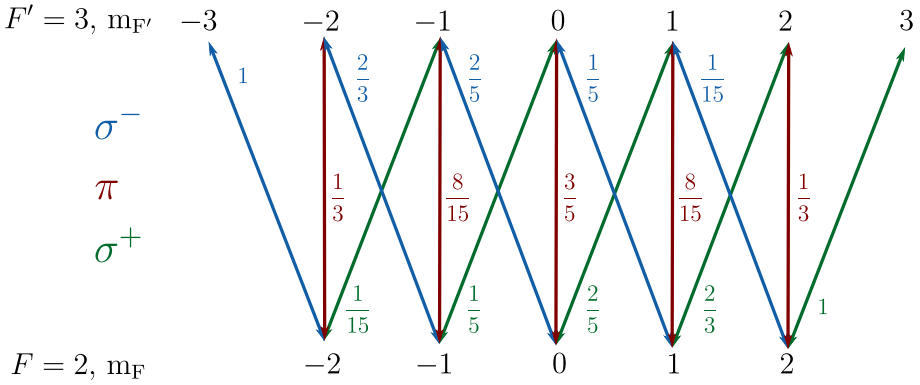

Figure C.1 *– Modulus square of the Clebsch-Gordan coefficients of the $F = 2 \to F' = 3$ transition normalized to the strongest transition.*

The average of the coefficients of the π transitions gives 7/15. This factor is used in this thesis to rescale the light cross-section of the atoms. It corresponds to assuming that the $|F, m_F\rangle$ states are all equally populated at the beginning of the imaging pulse and that these transitions are driven together[a].

C.2 Magnetic dipole

For the case of magnetic transitions, it can be shown that the relevant Hamiltonian is $W_{\mathrm{MD}} \propto (\mathbf{L} + 2\mathbf{S}) \cdot \boldsymbol{\epsilon}$, where $\boldsymbol{\epsilon}$ is along the polarization of the magnetic field. As for Alkali atoms $L = 0$, it can be computed as $W_{\mathrm{MD}} \propto \mathbf{S} \cdot \boldsymbol{\epsilon}$. The Clebsch-Gordan coefficients can then be found in [125], or computed by decomposing the $|F, m_F\rangle$ states on the $|I, m_I, S, m_S\rangle$ states. The result shown in figure C.2 is then obtained.

[a] This also assumes that the levels are degenerate, meaning that the magnetic field should be as small as possible on the experiment.

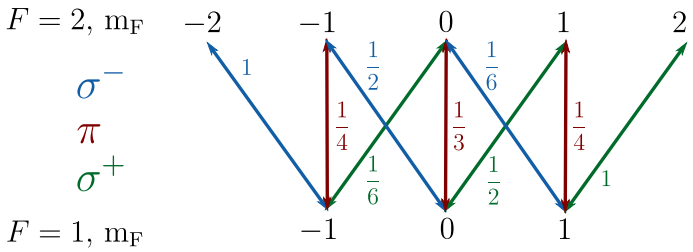

Figure C.2 – *Modulus square of the Clebsch-Gordan coefficients of the $F = 1 \rightarrow F = 2$ transition normalized to the strongest transition.*

D

Appendix of the atom number calibration

D.1 Monte Carlo simulations for checking validity of linearisation of noise

We describe here the simulations used in section 7.2.5 to validate the linearisation of the fluctuations. As the photonic shot noise has a non-trivial effect, which depends on the optical depth on the pixel, these simulations use photon numbers rather than optical depths. We keep here the notations of chapter 7. In absorption imaging, the mean number of photons after interaction with the atomic cloud is

$$\bar{N}_{p,1} = \bar{N}_{p,0} \exp\left(\frac{-\bar{N}_{\mathrm{a},1} \times \bar{n}}{\bar{N}_{p,0}}\right), \tag{D.1}$$

where $\bar{n}$ is the number of photons absorbed by each atom. The absorption imaging thus gives us only the value of the product $\bar{N}_{\mathrm{a}} \times \bar{n}$. The aim of these simulations is to simulate the expected noise on the number of collected photons for different $\bar{n}$ and to compare it to the experimental result to find the individual values $\bar{n}$ and $\bar{N}_{\mathrm{a}}$. More precisely, we compare the experimental data to Monte Carlo simulations following this procedure:

- We choose a region of interest and compute over all the iterations: the mean photon numbers on the three images and the variance of the number of photons for subimage 1 minus the one of subimage 2 (which is thus related to the variance of $N_{a,1} - N_{a,2}$).
- We then try to reproduce the experimental means and variance assuming a binomial law for the number of atoms $N_{a,1}$, due to a Bernoulli event for each atom, and a poissonian law for all the measured photon numbers, due to the coherence of the light.
  To do this, we fix the product $\bar{N}_{\mathrm{a}} \times \bar{n}$ according to the data as:

$$\bar{N}_{p,1} = \bar{N}_{p,0} \exp\left(\frac{-(\bar{N}_{\mathrm{a}}/2) \times \bar{n}}{\bar{N}_{p,0}}\right), \tag{D.2}$$

  As we already showed that taking the difference of two images gets rid of the fluctuations of the total atom number N_a, we consider in this analysis that $N_a = N_{a,1} + N_{a,2}$ does not fluctuate, whereas $N_{a,1}$ and $N_{a,2}$ of course fluctuate. We also check that adding a noise on N_a in the simulations does not change the result.

- The aim is to find a couple $(\bar{N}_\mathrm{a}, \bar{n})$ which has the good product, and for which the variance $\mathrm{Var}(N_{p,1} - N_{p,2})$ matches the experimental one.
  We thus implement a loop on $\bar{n}$. For each $\bar{n}$:
  - We calculate the corresponding $\bar{N}_\mathrm{a}$.
  - We pick $N_{\mathrm{a},1}$ according to a binomial law of parameter p. (We in fact only worked with $p = 1/2$).
  - We then should have $N_{\mathrm{a},2} = \bar{N}_\mathrm{a} - N_{\mathrm{a},1}$, but we noticed experimentally that there are always less atoms in the second pulse than in the first one. And this effect increases with the atomic density. To take this into account, we instead use

$$N_{\mathrm{a},2} = \gamma(\bar{N}_\mathrm{a} - N_{\mathrm{a},1}), \quad \text{with} \quad \gamma = \frac{\ln\left(\bar{N}_{p,0}/\bar{N}_{p,2}\right)}{\ln\left(\bar{N}_{p,0}/\bar{N}_{p,1}\right)}. \tag{D.3}$$

    The number of photons $N_{\mathrm{p},i}$ which should be detected on the camera are then picked following a poissonian law of mean $\bar{\mu}_i$ (for i= 1 or 2), with

$$\bar{\mu}_i = \bar{N}_{p,0} \exp\left(\frac{-N_{\mathrm{a},1} \times \bar{n}}{\bar{N}_{p,0}}\right). \tag{D.4}$$

  - For each value of $\bar{n}$, 100 000 values are computed and then averaged. We checked that the results were not different between 100 000 and 1 000 000.
- The couple $(\bar{N}_\mathrm{a}, \bar{n})$ giving the values closest to the experimental ones is selected.

D.2 Modelling the optical response

We present in this section the protocol developed in the team, that we used to extract the response function of the imaging system and to recover the correct atom number in a selected zone.

D.2.1 Correlations between pixels

To deconvolve the effect of the finite resolution of the imaging system, we compute the different covariances between pixels. We thus have to relate them to the model that we described in section 7.3.1.
We remind the equation (7.37)

$$d(\boldsymbol{q}, i) \approx \frac{1}{A_q} \sum_{\boldsymbol{q}'} \sigma(\boldsymbol{q} - \boldsymbol{q}')\ N_a(\boldsymbol{q}', i)\ +\ \text{photon noise}\ (\boldsymbol{q}, i),$$

which leads to:

$$\mathrm{Cov}[d(\boldsymbol{q}_A), d(\boldsymbol{q}_B)] = \frac{1}{A_q^2} \sum_{\boldsymbol{q}'_A} \sum_{\boldsymbol{q}'_B} \sigma(\boldsymbol{q}_A - \boldsymbol{q}'_A)\ \sigma(\boldsymbol{q}_B - \boldsymbol{q}'_B)\ \mathrm{Cov}[N_a(\boldsymbol{q}'_A), N_a(\boldsymbol{q}'_B)]. \tag{D.5}$$

We suppose that there are no significant correlations between the fluctuations of atom number in two different locations $\boldsymbol{q}'_A$ and $\boldsymbol{q}'_B$, so that

$$\mathrm{Cov}[N_a(\boldsymbol{q}'_A), N_a(\boldsymbol{q}'_B)] = \mathrm{Var}[N_a(\boldsymbol{q}'_A)]\ \delta_{\boldsymbol{q}'_A,\boldsymbol{q}'_B} \tag{D.6}$$

We thus get

$$\mathrm{Cov}[d(\boldsymbol{q}_A), d(\boldsymbol{q}_B)] = \frac{1}{A_q^2}\sum_{\boldsymbol{q}} \sigma(\boldsymbol{q}_A - \boldsymbol{q})\ \sigma(\boldsymbol{q}_B - \boldsymbol{q})\ \mathrm{Var}[N_a(\boldsymbol{q})] \tag{D.7}$$

which corresponds to what was discussed qualitatively in section 7.3: the fluctuations between pixels $\boldsymbol{q}_A$ and $\boldsymbol{q}_B$ are correlated because they are linked to the same source $\boldsymbol{q}$. Note that in the case $\boldsymbol{q}_A = \boldsymbol{q}_B$ one has to add the photonic and read-out noises to (D.7).
The process was explained for simplicity for a single image, but it is straightforward to extend it to the case of difference of ODs. We then get:

$$D(\boldsymbol{q}, i) \approx \frac{1}{A_q}\sum_{\boldsymbol{q}'} \sigma(\boldsymbol{q} - \boldsymbol{q}')\ [N_{a,1}(\boldsymbol{q}', i) - N_{a,2}(\boldsymbol{q}', i)]\ +\ \text{photon noise}(\boldsymbol{q}, i). \tag{D.8}$$

For $\boldsymbol{q}_A \neq \boldsymbol{q}_B$, this leads to the set of equations (7.38-7.39-7.40) of the main text which is copied here for convenience:

$$\begin{aligned}\mathrm{Cov}[D(\boldsymbol{q}_A), D(\boldsymbol{q}_B)] &= \frac{1}{A_q^2}\sum_{\boldsymbol{q}} \sigma(\boldsymbol{q}_A - \boldsymbol{q})\ \sigma(\boldsymbol{q}_B - \boldsymbol{q})\ \mathrm{Var}[(N_{a,1} - N_{a,2})(\boldsymbol{q})] \\ &= \frac{1}{A_q^2}\sum_{\boldsymbol{q}} \sigma(\boldsymbol{q}_A - \boldsymbol{q})\ \sigma(\boldsymbol{q}_B - \boldsymbol{q})\ \bar{N}_a(\boldsymbol{q}),\end{aligned} \tag{D.9}$$

$$\tilde{V}(\boldsymbol{q}_A) = \frac{1}{A_q^2}\sum_{\boldsymbol{q}} \sigma^2(\boldsymbol{q}_A - \boldsymbol{q})\ \bar{N}_a(\boldsymbol{q}), \tag{D.10}$$

where $\tilde{V}$ is obtained from $\mathrm{Var}[D]$ by subtracting photon shot noise and read-out noise as in (7.32). Also the sum of the two ODs reads

$$\bar{S}(\boldsymbol{q}_A) = \frac{1}{A_q}\sum_{\boldsymbol{q}} \sigma(\boldsymbol{q}_A - \boldsymbol{q})\ \bar{N}_a(\boldsymbol{q}). \tag{D.11}$$

This set of equations allows one to reconstruct the imaging transfer function $\sigma(\boldsymbol{q}-\boldsymbol{q}')$ as well as the pixel contents $N_a(\boldsymbol{q})$.

D.2.2 Computation of spatial correlations of the differences of ODs

Working on the same 8×8 quasi-uniform zone as in section 7.2.5, we determine the different $\mathrm{Cov}[D(\boldsymbol{q}_A), D(\boldsymbol{q}_B)]$. For a best signal to noise ratio, we average the obtained $\mathrm{Cov}[D(\boldsymbol{q}_A), D(\boldsymbol{q}_B)]$ when $\boldsymbol{Q} = \boldsymbol{q}_B - \boldsymbol{q}_A$ is the same, and obtain a matrix $\mathrm{Cov}[D](\boldsymbol{Q})$. More precisely:

- We choose $\boldsymbol{q}_A$ inside the inner 6×6 central window;
- We set $\boldsymbol{q}_B = \boldsymbol{q}_A + \boldsymbol{Q}$ with $-3 \leq Q_{x,y} \leq +3$ (we authorize to pick pixels outside of the 8×8 region for this averaging);

- We average the result over the 36 possible positions of $\boldsymbol{q}_A$ to obtain $\mathrm{Cov}[D](\boldsymbol{Q})$, which is a set of 7×7 values;
- For the central value $\boldsymbol{Q} = 0$, we subtract the photonic shot noise and the readout noise as in (7.32).

An example of obtained $\mathrm{Cov}[D](\boldsymbol{Q})$ matrix is shown in the main text in figure 7.8a. The imaging transfer function $\sigma(\boldsymbol{q} - \boldsymbol{q}')$ can in principle be reconstructed for the set of equations (7.38-7.39-7.40). It has however many unknowns, and the resolution is greatly improved by taking advantages of the symmetries visible in figure 7.8a: $x \to -x$ and $x \to y$. We chose to take advantage of these symmetries, and take the corresponding averages for the covariances, which are named $C_0, ..., C_5$ as shown in figure 7.8b.

Taking this into account, we model the response $\sigma(\boldsymbol{q}, \boldsymbol{q}')$ by 5 numbers:

- The on-site response

$$\sigma_0 = \sigma(\boldsymbol{q} - \boldsymbol{q}')) \quad \text{with } \boldsymbol{q}' = \boldsymbol{q}; \tag{D.12}$$

- The nearest-neighbour response

$$\sigma_1 = \sigma(\boldsymbol{q} - \boldsymbol{q}') \quad \text{with } q'_x = q_x \pm 1, q'_y = q_y \quad \text{or} \quad q'_x = q_x, q'_y = q_y \pm 1; \tag{D.13}$$

- The "corner" response

$$\sigma_2 = \sigma(\boldsymbol{q}, \boldsymbol{q}') \quad \text{with } q'_x = q_x \pm 1, q'_y = q_y \pm 1; \tag{D.14}$$

- And two further responses

$$\begin{aligned} \sigma_3 &= \sigma(\boldsymbol{q} - \boldsymbol{q}') \quad \text{with } q'_x = q_x \pm 2, q'_y = q_y \quad \text{or} \quad q'_x = q_x, q'_y = q_y \pm 2; \\ \sigma_4 &= \sigma(\boldsymbol{q} - \boldsymbol{q}') \quad \text{with } q'_x = q_x \pm 2, q'_y = q_y \pm 1 \quad \text{or} \quad q'_x = q_x \pm 1, q'_y = q_y \pm 2. \end{aligned} \tag{D.15}$$

With this parametrization and assuming a uniform atom distribution N_a in the selected zone, we obtain from the set (7.38-7.39-7.40) the following equations:

$$\bar{S} = \frac{1}{A_q}\left(\sigma_0 + 4\sigma_1 + 4\sigma_2 + 4\sigma_3 + 8\sigma_4\right)\bar{N}_a \equiv \frac{\sigma_{\mathrm{tot}}}{A_q}\bar{N}_a \tag{D.16}$$

$$\bar{V}(0,0) = \frac{1}{A_q^2}\left(\sigma_0^2 + 4\sigma_1^2 + 4\sigma_2^2 + 4\sigma_3^2 + 8\sigma_4^2\right)\bar{N}_a \tag{D.17}$$

$$\mathrm{Cov}[D](0,1) = \frac{1}{A_q^2}\left(2\sigma_0\sigma_1 + 4\sigma_1\sigma_2 + 2\sigma_1\sigma_3 + 4\sigma_2\sigma_4 + 4\sigma_3\sigma_4\right)\bar{N}_a \tag{D.18}$$

$$\mathrm{Cov}[D](1,1) = \frac{1}{A_q^2}\left(2\sigma_0\sigma_2 + 2\sigma_1^2 + 4\sigma_2\sigma_3 + 4\sigma_1\sigma_4 + 2\sigma_4^2\right)\bar{N}_a \tag{D.19}$$

$$\mathrm{Cov}[D](2,0) = \frac{1}{A_q^2}\left(\sigma_1^2 + 2\sigma_2^2 + 2\sigma_0\sigma_3 + 4\sigma_1\sigma_4 + 2\sigma_4^2\right)\bar{N}_a \tag{D.20}$$

$$\mathrm{Cov}[D](2,1) = \frac{1}{A_q^2}\left(2\sigma_1\sigma_2 + 2\sigma_1\sigma_3 + 2\sigma_0\sigma_4 + 2\sigma_2\sigma_4 + 2\sigma_3\sigma_4\right)\bar{N}_a \tag{D.21}$$

$$\mathrm{Cov}[D](2,2) = \frac{1}{A_q^2}\left(\sigma_2^2 + 2\sigma_3^2 + 4\sigma_1\sigma_4\right)\bar{N}_a \tag{D.22}$$

$$\tag{D.23}$$

The coefficients of equations (D.16) to (D.22) are determined from the set of equations (7.38-7.39-7.40). They arise from the computation of $\mathrm{Cov}[D(\boldsymbol{q}_A), D(\boldsymbol{q}_B)]$ with $\boldsymbol{q}_B = \boldsymbol{q}_A + \boldsymbol{Q}$. One has to count the number of possibility for going from $\boldsymbol{q}_A$ to the wanted $\boldsymbol{q}_A + \boldsymbol{Q}$ in two steps[a]. This can be shown graphically as done in figure D.1. We have 7 equations and 6 unknowns $(\sigma_0, \sigma_1, \sigma_2, \sigma_3, \sigma_4, \bar{N}_a)$.

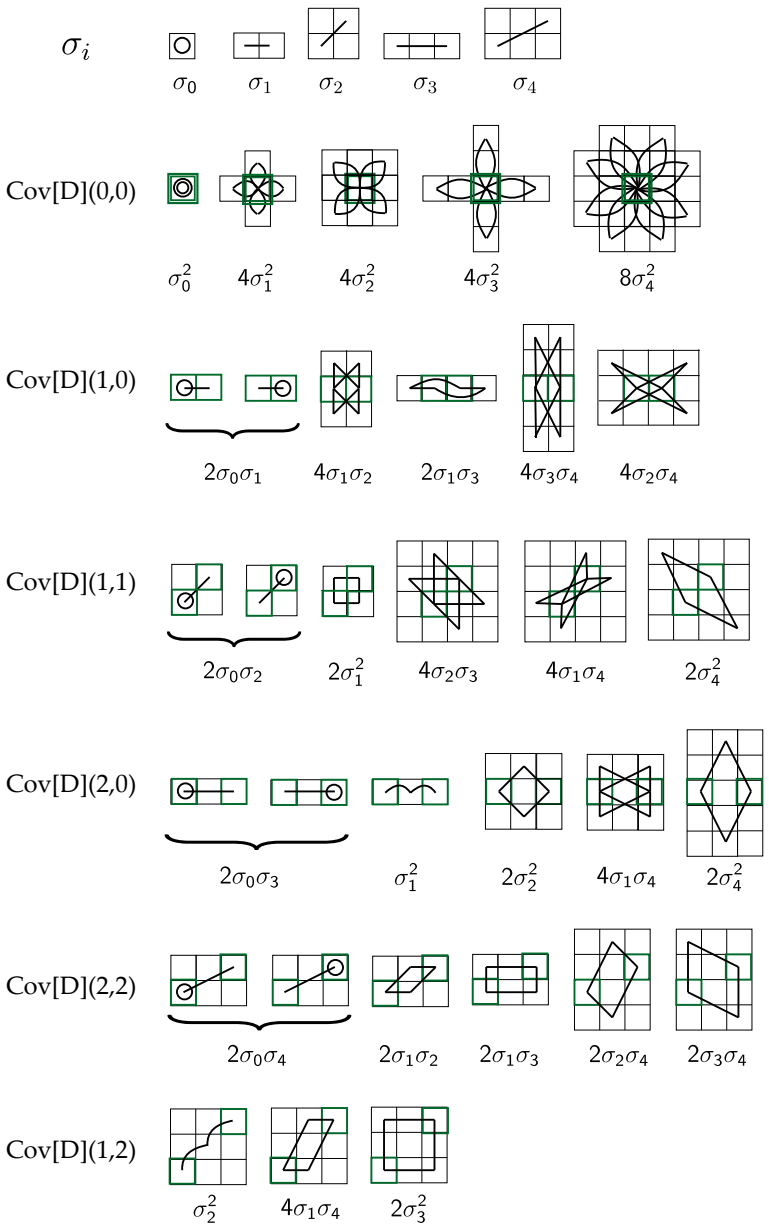

Figure D.1 *– Determination of the coefficients of equations (D.16) to (D.22). The σ_i are shown at the top of the picture. For each Cov[D](**Q**), one has to count the number of possible ways to make the vector **Q** (symbolized by the two green squares) using two σ_i.*

[a]We note that there should be more symmetrical coefficients such as $\mathrm{Cov}[D](1,0)$. We chose not to include them in the system of equations which is still valid, but to average them in the images. $\mathrm{Cov}[D](0,1)$ in table D.23 is in fact computed on the images as $[\mathrm{Cov}[D](0,1) + \mathrm{Cov}[D](1,0)]/2$.

Table D.1 *– Fitting parameters $\sigma_{0,1,2,3=4}$ and $\bar{N}_a$ for the correlations of the ODs on different pixels. Bottom: determination for a 6×6 central window.*

	σ_0/A_q	σ_1/A_q	σ_2/A_q	$\sigma_{3=4}/A_q$	σ_{tot} (μm^2)	F	$\bar{N}_a$
Run 1	0.0302	0.0082	0.0027	0.0002	0.0991	1.37	8.75
Run 2	0.0299	0.0073	0.0031	-0.0007	0.0818	1.66	6.07
Run 3	0.0252	0.0063	0.0022	-0.0001	0.0752	1.80	13.23

In principle σ_3 and σ_4 can be treated as independent and one needs to solve a non-linear system of 6 equations. However it turns out that the solution is not very stable for some runs. Since the distance between the two pixels for σ_3 and σ_4 are quite similar (2.0 vs.$\sqrt{5} \approx 2.2$), we impose in the following $\sigma_4 = \sigma_3$ and we are left with a system of 5 unknowns for the first 5 equations given above. The two remaining ones can be used as sanity check of the proposed solution. The results are given in table D.1 for three different runs, and shown in figure 7.8c for run 2 which is used as an example in this chapter. The robustness of the results can be checked looking at subsets of images, as it is done in section 7.3.3.

E

List of publications

- J.-L. Ville, T. Bienaimé, R. Saint-Jalm, L. Corman, M. Aidelsburger, L. Chomaz, K. Kleinlein, D. Perconte, S. Nascimbène, J. Dalibard, and J. Beugnon. Loading and compression of a single two-dimensional Bose gas in an optical accordion. *Physical Review A* **95**, 013632 (2017).

- L. Corman, J.-L. Ville, R. Saint-Jalm, M. Aidelsburger, T. Bienaimé, S. Nascimbène, J. Dalibard, and J. Beugnon. Transmission of near-resonant light through a dense slab of cold atoms. *Physical Review A*, **96**, 053629 (2017).

- M. Aidelsburger, J.-L. Ville, R. Saint-Jalm, S. Nascimbène, J. Dalibard, and J. Beugnon. Relaxation Dynamics in the Merging of N Independent Condensates. *Physical Review Letters* **119**, 190403 (2017).

- R. Saint-Jalm, M. Aidelsburger, J.-L. Ville, L. Corman, Z. Hadzibabic, D. Delande, S. Nascimbène, N. Cherroret, J. Dalibard, and J. Beugnon. Resonant-light diffusion in a disordered atomic layer. *Physical Review A* **97**, 061801(R) (2018).

- J.-L. Ville, R. Saint-Jalm, É. Le Cerf, M. Aidelsburger, S. Nascimbène, J. Dalibard, and J. Beugnon. Sound Propagation in a Uniform Superfluid Two-Dimensional Bose Gas. *Physical Review Letters* **121**, 145301 (2018).
  - Featured in APS Physics synopsis: *Sound Propagates in a 2D Bose Gas Despite Lack of Collisions*[a].

[a] url: https://physics.aps.org/synopsis-for/10.1103/PhysRevLett.121.145301

Bibliography

[1] R. Frisch. Experimenteller Nachweis des Einsteinschen Strahlungsrückstoßes. *Zeitschrift für Physik A Hadrons and Nuclei*, 86(1):42–48, 1933.

[2] A. Einstein. Quantentheorie des einatomigen idealen Gases. (German) [Quantum theory of monatomic ideal gases]. pages 261–267, 1924.

[3] M. H. Anderson, J. R. Ensher, M. R. Matthews, C. E. Wieman, E. A. Cornell, et al. Observation of Bose-Einstein condensation in a dilute atomic vapor. *science*, 269(5221):198–201, 1995.

[4] K. B. Davis, M.-O. Mewes, M. R. Andrews, N. J. Van Druten, D. S. Durfee, D. M. Kurn, and W. Ketterle. Bose-Einstein condensation in a gas of sodium atoms. *Physical review letters*, 75(22):3969, 1995.

[5] C. C. Bradley, C. A. Sackett, J. J. Tollett, and R. G. Hulet. Evidence of Bose-Einstein condensation in an atomic gas with attractive interactions. *Physical Review Letters*, 75(9):1687, 1995.

[6] V. F. Sears and E. C. Svensson. Pair Correlations and the Condensate Fraction in Superfluid He 4. *Physical Review Letters*, 43(27):2009, 1979.

[7] S. Bose. Plancks Gesetz und Lichtquantenhypothese. *Zeitschrift für Physik*, 26(1):178–181, 1924.

[8] E. P. Gross. Structure of a quantized vortex in boson systems. *Il Nuovo Cimento (1955-1965)*, 20(3):454–477, 1961.

[9] L. P. Pitaevskii. Vortex lines in an imperfect Bose gas. *Sov. Phys. JETP*, 13(2):451–454, 1961.

[10] M. R. Andrews, C. G. Townsend, H.-J. Miesner, D. S. Durfee, D. M. Kurn, and W. Ketterle. Observation of interference between two Bose condensates. *Science*, 275(5300):637–641, 1997.

[11] I. Bloch, T. W. Hänsch, and T. Esslinger. Measurement of the spatial coherence of a trapped Bose gas at the phase transition. *Nature*, 403(6766):166–170, 2000.

[12] B. P. Anderson and M. A. Kasevich. Macroscopic quantum interference from atomic tunnel arrays. *Science*, 282(5394):1686–1689, 1998.

[13] E. W. Hagley, L. Deng, M. Kozuma, J. Wen, K. Helmerson, S. L. Rolston, , and W. D. Phillips. A well-collimated quasi-continuous atom laser. *Science*, 283(5408):1706–1709, 1999.

[14] I. Bloch, T. W. Hänsch, and T. Esslinger. Atom laser with a cw output coupler. *Physical Review Letters*, 82(15):3008, 1999.

[15] N. Bogoliubov. On the theory of superfluidity. *J. Phys*, 11(1):23, 1947.

[16] J. Steinhauer, R. Ozeri, N. Katz, and N. Davidson. Excitation Spectrum of a Bose-Einstein Condensate. *Phys. Rev. Lett.*, 88:120407, 2002.

[17] M. R. Matthews, B. P. Anderson, P. C. Haljan, D. S. Hall, C. E. Wieman, and E. A. Cornell. Vortices in a Bose-Einstein condensate. *Physical Review Letters*, 83(13):2498, 1999.

[18] K. W. Madison, F. Chevy, W. Wohlleben, and J. Dalibard. Vortex formation in a stirred Bose-Einstein condensate. *Physical Review Letters*, 84(5):806, 2000.

[19] J. R. Abo-Shaeer, C. Raman, J. M. Vogels, and W. Ketterle. Observation of vortex lattices in Bose-Einstein condensates. *Science*, 292(5516):476–479, 2001.

[20] B. DeMarco and D. S. Jin. Onset of Fermi degeneracy in a trapped atomic gas. *Science*, 285(5434):1703–1706, 1999.

[21] A. G. Truscott, K. E. Strecker, W. I. McAlexander, G. B. Partridge, and R. G. Hulet. Observation of Fermi pressure in a gas of trapped atoms. *Science*, 291(5513):2570–2572, 2001.

[22] F. Schreck, L. Khaykovich, K. L. Corwin, G. Ferrari, T. Bourdel, J. Cubizolles, and C. Salomon. Quasipure Bose-Einstein condensate immersed in a Fermi sea. *Physical Review Letters*, 87(8):080403, 2001.

[23] I. Bloch, J. Dalibard, and W. Zwerger. Many-body physics with ultracold gases. *Rev. Mod. Phys*, 80(3):885, 2008.

[24] S. Inouye, M. R. Andrews, J. Stenger, H.-J. Miesner, D. M. Stamper-Kurn, and W. Ketterle. Observation of Feshbach resonances in a Bose-Einstein condensate. *Nature*, 392(6672):151–154, 1998.

[25] S. L. Cornish, N. R. Claussen, J. L. Roberts, E. A. Cornell, and C. E. Wieman. Stable 85 Rb Bose-Einstein condensates with widely tunable interactions. In *Collected Papers Of Carl Wieman*, pages 593–596. World Scientific, 2008.

[26] K. M. O'hara, S. L. Hemmer, M. E. Gehm, S. R. Granade, and J. E. Thomas. Observation of a strongly interacting degenerate Fermi gas of atoms. *Science*, 298(5601):2179–2182, 2002.

[27] T. Bourdel, L. Khaykovich, J. Cubizolles, J. Zhang, F. Chevy, M. Teichmann, L. Tarruell, S. J. J. M. F. Kokkelmans, and C. Salomon. Experimental study of the BEC-BCS crossover region in lithium 6. *Physical Review Letters*, 93(5):050401, 2004.

[28] M. Bartenstein, A. Altmeyer, S. Riedl, S. Jochim, C. Chin, J. H. Denschlag, and R. Grimm. Crossover from a molecular Bose-Einstein condensate to a degenerate Fermi gas. *Physical review letters*, 92(12):120401, 2004.

[29] N. D. Mermin and H. Wagner. Absence of ferromagnetism or antiferromagnetism in one-or two-dimensional isotropic Heisenberg models. *Physical Review Letters*, 17(22):1133, 1966.

[30] P. C. Hohenberg. Existence of long-range order in one and two dimensions. *Physical Review*, 158(2):383, 1967.

[31] N. D. Mermin. Crystalline order in two dimensions. *Physical Review*, 176(1):250, 1968.

[32] B. Paredes, A. Widera, V. Murg, O. Mandel, S. Fölling, I. Cirac, G. V. Shlyapnikov, T. W. Hänsch, and I. Bloch. Tonks-Girardeau gas of ultracold atoms in an optical lattice. *Nature*, 429(6989):277–281, 2004.

[33] T. Kinoshita, T. Wenger, and D. S. Weiss. Observation of a one-dimensional tonks-girardeau gas. *Science*, 305(5687):1125–1128, 2004.

[34] Z. Hadzibabic, P. Krüger, M. Cheneau, B. Battelier, and J. Dalibard. Berezinskii–Kosterlitz–Thouless crossover in a trapped atomic gas. *Nature*, 441(7097):1118–1121, 2006.

[35] J. Hubbard. Electron correlations in narrow energy bands. In *Proceedings of the royal society of london a: mathematical, physical and engineering sciences*, volume 276, pages 238–257. The Royal Society, 1963.

[36] M. Greiner, O. Mandel, T. Esslinger, T. W. Hänsch, and I. Bloch. Quantum phase transition from a superfluid to a Mott insulator in a gas of ultracold atoms. *nature*, 415(6867):39–44, 2002.

[37] T. Stöferle, H. Moritz, C. Schori, M. Köhl, and T. Esslinger. Transition from a strongly interacting 1D superfluid to a Mott insulator. *Physical review letters*, 92(13):130403, 2004.

[38] I. B. Spielman, W. D. Phillips, and J. V. Porto. Mott-insulator transition in a two-dimensional atomic Bose gas. *Physical Review Letters*, 98(8):080404, 2007.

[39] M. Köhl, H. Moritz, T. Stöferle, C. Schori, and T. Esslinger. Superfluid to Mott insulator transition in one, two, and three dimensions. *Journal of Low Temperature Physics*, 138(3):635–644, 2005.

[40] R. Jördens, N. Strohmaier, K. Günter, H. Moritz, and T. Esslinger. A Mott insulator of fermionic atoms in an optical lattice. *Nature*, 455(7210):204–207, 2008.

[41] U. Schneider, L. Hackermüller, S. Will, T. Best, I. Bloch, T. A. Costi, R. W. Helmes, D. Rasch, and A. Rosch. Metallic and insulating phases of repulsively interacting fermions in a 3d optical lattice. *Science*, 322(5907):1520–1525, 2008.

[42] M. Greiner, I. Bloch, O. Mandel, T. W. Hänsch, and T. Esslinger. Exploring phase coherence in a 2D lattice of Bose-Einstein condensates. *Physical Review Letters*, 87(16):160405, 2001.

[43] J. Sebby-Strabley, M. Anderlini, P. S. Jessen, and J. V. Porto. Lattice of double wells for manipulating pairs of cold atoms. *Physical Review A*, 73(3):033605, 2006.

[44] C. Becker, P. Soltan-Panahi, J. Kronjäger, S. Dörscher, K. Bongs, and K. Sengstock. Ultracold quantum gases in triangular optical lattices. *New Journal of Physics*, 12(6):065025, 2010.

[45] L. Tarruell, D. Greif, T. Uehlinger, G. Jotzu, and T. Esslinger. Creating, moving and merging Dirac points with a Fermi gas in a tunable honeycomb lattice. *Nature*, 483(7389):302–305, 2012.

[46] G.-B. Jo, J. Guzman, C. K. Thomas, P. Hosur, A. Vishwanath, and D. M. Stamper-Kurn. Ultracold atoms in a tunable optical kagome lattice. *Physical review letters*, 108(4):045305, 2012.

[47] D. Greif, M. F. Parsons, A. Mazurenko, C. S. Chiu, Se. Blatt, F. Huber, and M. Ji, G.and Greiner. Site-resolved imaging of a fermionic Mott insulator. *Science*, 351(6276):953–957, 2016.

[48] M. Boll, T. A. Hilker, G. Salomon, A. Omran, J. Nespolo, L. Pollet, I. Bloch, and C. Gross. Spin-and density-resolved microscopy of antiferromagnetic correlations in Fermi-Hubbard chains. *Science*, 353(6305):1257–1260, 2016.

[49] N. R. Cooper. Rapidly rotating atomic gases. *Advances in Physics*, 57(6):539–616, 2008.

[50] A. L. Fetter. Rotating trapped Bose-Einstein condensates. *Reviews of Modern Physics*, 81(2):647, 2009.

[51] J. Dalibard, F. Gerbier, G. Juzeliūnas, and P. Öhberg. Colloquium: Artificial gauge potentials for neutral atoms. *Reviews of Modern Physics*, 83(4):1523, 2011.

[52] N. Goldman, G. Juzeliūnas, P. Öhberg, and I. B. Spielman. Light-induced gauge fields for ultracold atoms. *Reports on Progress in Physics*, 77(12):126401, 2014.

[53] M. Aidelsburger, M. Atala, S. Nascimbène, St. Trotzky, Y.-A. Chen, and I. Bloch. Experimental realization of strong effective magnetic fields in an optical lattice. *Physical review letters*, 107(25):255301, 2011.

[54] T. Kovachy, P. Asenbaum, C. Overstreet, C. A. Donnelly, S. M. Dickerson, A. Sugarbaker, J. M. Hogan, and M. A. Kasevich. Quantum superposition at the half-metre scale. *Nature*, 528(7583):530–533, 2015.

[55] S. L. Campbell, R. B. Hutson, G. E. Marti, A. Goban, N. D. Oppong, R. L. McNally, L. Sonderhouse, J. M. Robinson, W. Zhang, B. J. Bloom, et al. A Fermi-degenerate three-dimensional optical lattice clock. *arXiv preprint arXiv:1702.01210*, 2017.

[56] A. Ramanathan, K. C. Wright, S. R. Muniz, M. Zelan, W. T. Hill III, C. J. Lobb, K. Helmerson, W. D. Phillips, and G. K. Campbell. Superflow in a toroidal Bose-Einstein condensate: an atom circuit with a tunable weak link. *Phys. Rev. Lett.*, 106:130401, 2011.

[57] T. Langen, R. Geiger, and J. Schmiedmayer. Ultracold atoms out of equilibrium. 2015.

[58] J.-P. Brantut, J. Meineke, D. Stadler, S. Krinner, and T. Esslinger. Conduction of ultracold fermions through a mesoscopic channel. *Science*, 337(6098):1069–1071, 2012.

[59] J.-P. Brantut, C. Grenier, J. Meineke, D. Stadler, S. Krinner, C. Kollath, T. Esslinger, and A. Georges. A thermoelectric heat engine with ultracold atoms. *Science*, 342(6159):713–715, 2013.

[60] S. Krinner, D. Stadler, D. Husmann, J.-P. Brantut, and T. Esslinger. Observation of quantized conductance in neutral matter. *Nature*, 517(7532):64–67, 2015.

[61] S. Eckel, J. G. Lee, F. Jendrzejewski, C. J. Lobb, G. K. Campbell, and W. T. Hill III. Contact resistance and phase slips in mesoscopic superfluid-atom transport. *Physical Review A*, 93(6):063619, 2016.

[62] B. T. Seaman, M. Krämer, D. Z. Anderson, and M. J. Holland. Atomtronics: Ultracold-atom analogs of electronic devices. *Physical Review A*, 75(2):023615, 2007.

[63] J.-Y. Choi, S. W. Seo, and Y.-I. Shin. Observation of thermally activated vortex pairs in a quasi-2D Bose gas. *Physical review letters*, 110(17):175302, 2013.

[64] T. Yefsah, R. Desbuquois, L. Chomaz, K. J. Günter, and J. Dalibard. Exploring the Thermodynamics of a Two-Dimensional Bose Gas. *Phys. Rev. Lett.*, 107:130401, 2011.

[65] R. Desbuquois, T. Yefsah, L. Chomaz, C. Weitenberg, L. Corman, S. Nascimbène, and J. Dalibard. Determination of Scale-Invariant Equations of State without Fitting Parameters: Application to the Two-Dimensional Bose Gas Across the Berezinskii-Kosterlitz-Thouless Transition. *Phys. Rev. Lett.*, 113:020404, 2014.

[66] C.-L. Hung, X. Z., N. Gemelke, and C. Chin. Observation of scale invariance and universality in two-dimensional Bose gases. *Nature*, 470:236, 2011.

[67] P. Cladé, C. Ryu, A. Ramanathan, K. Helmerson, and W. D. Phillips. Observation of a 2D Bose Gas: From Thermal to Quasicondensate to Superfluid. *Phys. Rev. Lett.*, 102:170401, 2009.

[68] S. Tung, G. Lamporesi, D. Lobser, L. Xia, and E. A. Cornell. Observation of the presuperfluid regime in a two-dimensional Bose gas. *Physical review letters*, 105(23):230408, 2010.

[69] T. Plisson, B. Allard, M. Holzmann, G. Salomon, A. Aspect, P. Bouyer, and T. Bourdel. Coherence properties of a two-dimensional trapped Bose gas around the superfluid transition. *Physical Review A*, 84(6):061606, 2011.

[70] C.-L. Hung, X. Zhang, L.-C. Ha, S.-K. Tung, N. Gemelke, and C. Chin. Extracting density–density correlations from in situ images of atomic quantum gases. *New Journal of Physics*, 13(7):075019, 2011.

[71] J.-Y. Choi, S. W. Seo, W. J. Kwon, and Y.-I. Shin. Probing phase fluctuations in a 2D degenerate Bose gas by free expansion. *Physical review letters*, 109(12):125301, 2012.

[72] S. W. Seo, J.-Y. Choi, and Y.-I. Shin. Scaling behavior of density fluctuations in an expanding quasi-two-dimensional degenerate Bose gas. *Physical Review A*, 89(4):043606, 2014.

[73] P. A. Murthy, I. Boettcher, L. Bayha, M. Holzmann, D. Kedar, M. Neidig, M. G. Ries, A. N. Wenz, G. Zürn, and S. Jochim. Observation of the Berezinskii-Kosterlitz-Thouless Phase Transition in an Ultracold Fermi Gas. *Phys. Rev. Lett.*, 115:010401, 2015.

[74] I. Boettcher and M. Holzmann. Quasi-long-range order in trapped two-dimensional Bose gases. *Physical Review A*, 94(1):011602, 2016.

[75] T. Ozawa and S. Stringari. Discontinuities in the First and Second Sound Velocities at the Berezinskii-Kosterlitz-Thouless Transition. *Physical review letters*, 112(2):025302, 2014.

[76] Z. Hadzibabic and J. Dalibard. Two-dimensional Bose fluids: An atomic physics perspective. *Riv. del Nuovo Cimento*, 34:389, 2011.

[77] J. Dalibard. Fluides quantiques de basse dimension et transition de Kosterlitz-Thouless, 2016-2017. Cours du Collège de France, available on `http://www.phys.ens.fr/ dalibard/`.

[78] O. Penrose and L. Onsager. Bose-Einstein Condensation and Liquid Helium. *Phys. Rev.*, 104:576–584, 1956.

[79] J. von Neumann. *Mathematische Grundlagen der Quantenmechanik*. 1932. Princeton University Press (1955).

[80] N. D. Mermin and H. Wagner. Absence of Ferromagnetism or Antiferromagnetism in One- or Two-Dimensional Isotropic Heisenberg Models. *Phys. Rev. Lett.*, 17:1133–1136, 1966.

[81] N. D. Mermin. Crystalline Order in Two Dimensions. *Phys. Rev.*, 176:250–254, 1968.

[82] P. C. Hohenberg. Existence of Long-Range Order in One and Two Dimensions. *Phys. Rev.*, 158:383–386, 1967.

[83] V. N. Popov. *Functional Integrals and Collective Modes*. Cambridge University Press, Cambridge, 1987.

[84] Y. Kagan, B. V. Svistunov, and G. V. Shlyapnikov. Influence on inelastic processes of the phase transition in a weakly collisional two-dimensional Bose gas. *Sov. Phys. JETP*, 66:314, 1987.

[85] D. S. Petrov, M. Holzmann, and G. V. Shlyapnikov. Bose-Einstein Condensation in Quasi-2D Trapped Gases. *Phys. Rev. Lett.*, 84:2551–2555, 2000.

[86] V. L. Berezinskii. Destruction of long-range order in one-dimensional and two-dimensional system possessing a continous symmetry group - II. quantum systems. *Soviet Physics JETP*, 34:610, 1971.

[87] J. M. Kosterlitz and D. J. Thouless. Ordering, metastability and phase transitions in two dimensional systems. *J. Phys. C: Solid State Physics*, 6:1181, 1973.

[88] J. M. Kosterlitz. The critical properties of the two-dimensional xy model. *Journal of Physics C: Solid State Physics*, 7(6):1046–1060, 1974.

[89] C. J. Pethick and H. Smith. *Bose-Einstein Condensation in Dilute Gases*. Cambridge University Press, 2 edition, 2008.

[90] M. Naraschewski and R. J. Glauber. Spatial coherence and density correlations of trapped Bose gases. *Phys. Rev. A*, 59:4595–4607, 1999.

[91] N. Navon, A. L. Gaunt, R. P. Smith, and Z. Hadzibabic. Critical dynamics of spontaneous symmetry breaking in a homogeneous Bose gas. *Science*, 347(6218):167–170, 2015.

[92] R. Desbuquois. *Thermal and superfluid properties of the two-dimensional Bose gas*. PhD thesis, Université Pierre et Marie Curie-Paris VI, 2013.

[93] J. Dalibard. Collisional dynamics of ultra-cold atomic gases. In *Proceedings of the International School of Physics-Enrico Fermi*, volume 321, page 14, 1999.

[94] M. Egorov, B. Opanchuk, P. Drummond, B. V. Hall, P. Hannaford, and A. I. Sidorov. Measurement of s-wave scattering lengths in a two-component Bose-Einstein condensate. *Phys. Rev. A*, 87:053614, 2013.

[95] T. Yefsah. *Thermodynamique du gaz de Bose à deux dimensions*. PhD thesis, Université Pierre et Marie Curie-Paris VI, 2011.

[96] D. S. Petrov and G. V. Shlyapnikov. Interatomic collisions in a tightly confined Bose gas. *Phys. Rev. A*, 64:012706, 2001.

[97] J.-Y. Choi, W. J. Kwon, and Y.-I. Shin. Observation of Topologically Stable 2D Skyrmions in an Antiferromagnetic Spinor Bose-Einstein Condensate. *Phys. Rev. Lett.*, 108:035301, 2012.

[98] I. Boettcher, L. Bayha, D. Kedar, P. A. Murthy, M. Neidig, M. G. Ries, A. N. Wenz, G. Zürn, S. Jochim, and T. Enss. Equation of State of Ultracold Fermions in the 2D BEC-BCS Crossover Region. *Phys. Rev. Lett.*, 116:045303, 2016.

[99] W. Weimer, K. Morgener, V. P. Singh, J. Siegl, K. Hueck, N. Luick, L. Mathey, and H. Moritz. Critical Velocity in the BEC-BCS Crossover. *Phys. Rev. Lett.*, 114:095301, 2015.

[100] L. D. Landau and E. M. Lifchitz. *Physique Statistique*. Editions Mir, 1984.

[101] C. Cohen-Tannoudji and C. Robilliard. Wave functions, relative phase and interference for atomic Bose-Einstein condensates. *Comptes Rendus de l'Académie des Sciences-Series IV-Physics*, 2(3):445–477, 2001.

[102] N. Prokof'ev, O. Ruebenacker, and B. Svistunov. Critical Point of a Weakly Interacting Two-Dimensional Bose Gas. *Phys. Rev. Lett.*, 87:270402, 2001.

[103] A. I. Safonov, S. A. Vasilyev, I. S. Yasnikov, I. I. Lukashevich, and S. Jaakkola. Observation of Quasicondensate in Two-Dimensional Atomic Hydrogen. *Phys. Rev. Lett.*, 81:4545–4548, 1998.

[104] C. Mora and Y. Castin. Extension of Bogoliubov theory to quasicondensates. *Phys. Rev. A*, 67:053615, 2003.

[105] Y. Castin. Simple theoretical tools for low dimension Bose gases. In *Journal de Physique IV (Proceedings)*, volume 116, pages 89–132. EDP sciences, 2004.

[106] A. J. Leggett. *Quantum Liquids*. Oxford University Press, 2006.

[107] S.-K. Ma. *Statistical Mechanics*. World Scientific, 1985.

[108] J. Dalibard. Cohérence et superfluidité dans les gaz atomiques, 2015-2016. Cours du Collège de France, available on `http://www.phys.ens.fr/ dalibard/`.

[109] M. Kardar. *Statistical physics of fields*. Cambridge University Press, 2007.

[110] D. R. Nelson and J. M. Kosterlitz. Universal Jump in the Superfluid Density of Two-Dimensional Superfluids. *Phys. Rev. Lett.*, 39:1201, 1977.

[111] D. S. Fisher and P. C. Hohenberg. Dilute Bose gas in two dimensions. *Phys. Rev. B*, 37:4936–4943, 1988.

[112] N. Metropolis, A. W. Rosenbluth, M. N. Rosenbluth, A. H. Teller, and E. Teller. Equation of State Calculations by Fast Computing Machines. *Journal of Chemical Physics*, 21:1087–1092, 1953.

[113] N. Proukakis, S. Gardiner, M. Davis, and M. Szymańska. *Quantum Gases: Finite temperature and non-equilibrium dynamics*, volume 1. World Scientific, 2013.

[114] B. V. Svistunov, E. S. Babaev, and N. V. Prokof'ev. *Superfluid states of matter*. Crc Press, 2015.

[115] R. J. Fletcher, J. Robert de Saint Vincent, M.and Man, N. Navon, R. P. Smith, K. G. Viebahn, and Z. Hadzibabic. Connecting Berezinskii-Kosterlitz-Thouless and BEC Phase Transitions by Tuning Interactions in a Trapped Gas. *Phys. Rev. Lett.*, 114:255302, 2015.

[116] J.-L. Ville, T. Bienaimé, R. Saint-Jalm, L. Corman, M. Aidelsburger, L. Chomaz, K. Kleinlein, D. Perconte, S. Nascimbène, J. Dalibard, and J. Beugnon. Loading and compression of a single two-dimensional Bose gas in an optical accordion. *Phys. Rev. A.*, 95:013632, 2017.

[117] L. Corman. *The two-dimensional Bose gas in box potentials*. PhD thesis, Université de recherche Paris Sciences et Lettres - PSL Research University, 2016.

[118] K. Kleinlein. Setting up a new experiment for investigating artificial magnetism of two-dimensional Bose gases. Master's thesis, Masterarbeit, 2014.

[119] M. Riedel. *Multi-particle entanglement on an atom chip*. PhD thesis, Fakultät für Physik der Ludwig-Maximilians-Universität München, 2010.

[120] K. Hueck, N. Luick, L. Sobirey, J. Siegl, T. Lompe, H. Moritz, L. W. Clark, and C. Chin. Calibrating high intensity absorption imaging of ultracold atoms. *Optics Express*, 25(8):8670–8679, 2017.

[121] T. C. Li, H. Kelkar, D. Medellin, and M. G. Raizen. Real-time control of the periodicity of a standing wave: an optical accordion. *Opt. Express*, 16(8):5465–5470, 2008.

[122] R. Saint-Jalm. Development of a dynamically tunable, bidimensionaly confining optical trap for ultracold rubidium atoms. Master's thesis, École normale supérieure, 2015.

[123] J.-L. Ville. Generation of highly tunable light potentials on a two-dimensional degenerate Bose gas. Master's thesis, Université de recherche Paris Sciences et Lettres - PSL Research University, 2014.

[124] D. A. Steck. Rubidium 87 D line data, 2001.

[125] P. Treutlein. *Coherent manipulation of ultracold atoms on atom chips*. PhD thesis, Fakultät für Physik der Ludwig-Maximilians-Universität München, 2010.

[126] K. Maussang. *États comprimés atomiques sur puce à atomes.* PhD thesis, Université Pierre et Marie Curie-Paris VI, 2010.

[127] A. Ramanathan, S. R. Muniz, K. C. Wright, R. P. Anderson, W. D. Phillips, K. Helmerson, and G. K. Campbell. Partial-transfer absorption imaging: A versatile technique for optimal imaging of ultracold gases. *Rev. Sci. Instrum.*, 83(8):083119, 2012.

[128] D. S. Kothari and B. N. Srivasava. Joule-Thomson Effect and Quantum Statistics. *Nature*, 140:970–971, 1937.

[129] T. F. Schmidutz, I. Gotlibovych, A. L. Gaunt, R. P. Smith, N. Navon, and Z. Hadzibabic. Quantum Joule-Thomson Effect in a Saturated Homogeneous Bose Gas. *Phys. Rev. Lett.*, 112:040403, 2014.

[130] I. Shvarchuck, Ch. Buggle, D. S. Petrov, K. Dieckmann, M. Zielonkowski, M. Kemmann, T. G. Tiecke, W. von Klitzing, G. V. Shlyapnikov, and J. T. M. Walraven. Bose-Einstein Condensation into Nonequilibrium States Studied by Condensate Focusing. *Phys. Rev. Lett.*, 89:270404, 2002.

[131] P. A Murthy, D. Kedar, T. Lompe, M. Neidig, M. G. Ries, A. N. Wenz, G. Zürn, and S. Jochim. Matter-wave Fourier optics with a strongly interacting two-dimensional Fermi gas. *Physical Review A*, 90(4):043611, 2014.

[132] K. Hueck, N. Luick, L. Sobirey, J. Siegl, T. Lompe, and H. Moritz. Two-dimensional homogeneous Fermi gases. *Physical Review Letters*, 120(6):060402, 2018.

[133] S. Tung. *Probing an interacting Bose gas in a quasi-two-dimensional trap.* PhD thesis, Faculty of the graduate school of the University of Colorado, 2010.

[134] L. Chomaz. *Coherence and superfluidity of Bose gases in reduced dimensions: from harmonic traps to uniform fluids.* PhD thesis, École Normale Supérieure, 2014.

[135] R. Olf, F. Fang, G. E. Marti, A. MacRae, and D. M. Stamper-Kurn. Thermometry and cooling of a Bose gas to 0.02 times the condensation temperature. *Nat. Phys.*, 11(9):720–723, 2015.

[136] C. Cohen-Tannoudji, J. Dupont-Roc, G. Grynberg, and P. Thickstun. *Atom-photon interactions: basic processes and applications.* Wiley Online Library, 1992.

[137] J.-M. Raimond and S. Haroche. *Exploring the quantum.* Oxford University Press, Oxford, 2006.

[138] P. W. H. Pinkse, T. Fischer, P. Maunz, and G. Rempe. Trapping an atom with single photons. *Nature*, 404(6776):365–368, 2000.

[139] B. Gouraud, D. Maxein, A. Nicolas, O. Morin, and J. Laurat. Demonstration of a memory for tightly guided light in an optical nanofiber. *Phys. Rev Lett.*, 114(18):180503, 2015.

[140] C. Sayrin, C. Junge, R. Mitsch, B. Albrecht, D. O'Shea, P. Schneeweiss, J. Volz, and A. Rauschenbeutel. Nanophotonic optical isolator controlled by the internal state of cold atoms. *Phys. Rev. X*, 5(4):041036, 2015.

[141] L. Britnell, R. M. Ribeiro, A. Eckmann, R. Jalil, B. D. Belle, A. Mishchenko, Y.-J. Kim, R. V. Gorbachev, T. Georgiou, S. V. Morozov, A. N. Grigorenko, A. K. Geim, C. Casiraghi, A. H. Castro Neto, and K. S. Novoselov. Strong light-matter interactions in heterostructures of atomically thin films. *Science*, 340(6138):1311–1314, 2013.

[142] Lord Rayleigh. Xxxiv. on the transmission of light through an atmosphere containing small particles in suspension, and on the origin of the blue of the sky. *The London, Edinburgh, and Dublin Philosophical Magazine and Journal of Science*, 47(287):375–384, 1899.

[143] N. Skribanowitz, I. P. Herman, J. C. MacGillivray, and M. S. Feld. Observation of Dicke Superradiance in Optically Pumped HF Gas. *Phys. Rev. Lett.*, 30:309–312, 1973.

[144] M. Gross, P. Goy, C. Fabre, S. Haroche, and J. M. Raimond. Maser Oscillation and Microwave Superradiance in Small Systems of Rydberg Atoms. *Phys. Rev. Lett.*, 43:343–346, 1979.

[145] R. Röhlsberger, K. Schlage, B. Sahoo, S. Couet, and R. Rüffer. Collective Lamb shift in single-photon superradiance. *Science*, 328(5983):1248–1251, 2010.

[146] S. Inouye, A. P. Chikkatur, D. M. Stamper-Kurn, J. Stenger, D. E. Pritchard, and W. Ketterle. Superradiant Rayleigh scattering from a Bose-Einstein condensate. *Science*, 285(5427):571–574, 1999.

[147] M. O. Araújo, I. Krešić, R. Kaiser, and W. Guerin. Superradiance in a large and dilute cloud of cold atoms in the linear-optics regime. *Phys. Rev. Lett.*, 117(7):073002, 2016.

[148] S. J. Roof, K. J. Kemp, M. D. Havey, and I. M. Sokolov. Observation of Single-Photon Superradiance and the Cooperative Lamb Shift in an Extended Sample of Cold Atoms. *Phys. Rev. Lett.*, 117:073003, 2016.

[149] D. Pavolini, A. Crubellier, P. Pillet, L. Cabaret, and S. Liberman. Experimental Evidence for Subradiance. *Phys. Rev. Lett.*, 54:1917–1920, 1985.

[150] W. Guerin, M. O. Araújo, and R. Kaiser. Subradiance in a large cloud of cold atoms. *Phys. Rev. Lett.*, 116(8):083601, 2016.

[151] R. H. Dicke. Coherence in spontaneous radiation processes. *Physical Review*, 93(1):99, 1954.

[152] M. P. V. Albada and A. Lagendijk. Observation of Weak Localization of Light in a Random Medium. *Phys. Rev. Lett.*, 55:2692–2695, 1985.

[153] P.-E. Wolf and G. Maret. Weak localization and coherent backscattering of photons in disordered media. *Physical review letters*, 55(24):2696, 1985.

[154] K. M. Yoo, G. C. Tang, and R. R. Alfano. Coherent backscattering of light from biological tissues. *Applied optics*, 29(22):3237–3239, 1990.

[155] G. Labeyrie, F. De Tomasi, J.-C. Bernard, C. A. Müller, C. Miniatura, and R. Kaiser. Coherent backscattering of light by cold atoms. *Physical Review Letters*, 83(25):5266, 1999.

[156] Y. Bidel, B. Klappauf, J. C. Bernard, D. Delande, G. Labeyrie, C. Miniatura, D. Wilkowski, and R. Kaiser. Coherent light transport in a cold strontium cloud. *Physical review letters*, 88(20):203902, 2002.

[157] B.i Zhu, J. Cooper, J. Ye, and A. M. Rey. Light scattering from dense cold atomic media. *Phys. Rev. A*, 94:023612, 2016.

[158] H. A. Bethe. The electromagnetic shift of energy levels. *Phys. Rev.*, 72:339–341, 1947.

[159] R. Friedberg, S. R. Hartmann, and J. T. Manassah. Frequency shifts in emission and absorption by resonant systems ot two-level atoms. *Physics Reports*, 7(3):101–179, 1973.

[160] J. Keaveney, A. Sargsyan, U. Krohn, I. G. Hughes, D. Sarkisyan, and C. S. Adams. Cooperative Lamb shift in an atomic vapor layer of nanometer thickness. *Phys. Rev. Lett.*, 108(17):173601, 2012.

[161] Z. Meir, O. Schwartz, E. Shahmoon, D. Oron, and R. Ozeri. Cooperative Lamb shift in a mesoscopic atomic array. *Phys. Rev. Lett.*, 113(19):193002, 2014.

[162] M. D. Lukin, M. Fleischhauer, R. Cote, L. M. Duan, D. Jaksch, J. I. Cirac, and P. Zoller. Dipole Blockade and Quantum Information Processing in Mesoscopic Atomic Ensembles. *Phys. Rev. Lett.*, 87:037901, 2001.

[163] R. Heidemann, U. Raitzsch, V. Bendkowsky, B. Butscher, R. Löw, L. Santos, and T. Pfau. Evidence for Coherent Collective Rydberg Excitation in the Strong Blockade Regime. *Phys. Rev. Lett.*, 99:163601, 2007.

[164] Y. Miroshnychenko, T. Wilk, A. Chotia, M. Viteau, D. Comparat, P. Pillet, A. Browaeys, P. Grangier, et al. Observation of collective excitation of two individual atoms in the Rydberg blockade regime. *Nature Physics*, 5(2):115–118, 2009.

[165] E. Urban, T. A. Johnson, T. Henage, L. Isenhower, D. D. Yavuz, T. G. Walker, and M. Saffman. Observation of Rydberg blockade between two atoms. *Nat. Phys.*, 5(2):110–114, 2009.

[166] C. Cohen-Tannoudji, J. Dupont-Roc, G. Grynberg, and P. Thickstun. *Atom-photon interactions: basic processes and applications*. Wiley Online Library, 1992.

[167] J. Javanainen, J. Ruostekoski, Y. Li, and S.-M. Yoo. Exact electrodynamics versus standard optics for a slab of cold dense gas. *Phys. Rev. A*, 96:033835, 2017.

[168] M. Chalony, R. Pierrat, D. Delande, and D. Wilkowski. Coherent flash of light emitted by a cold atomic cloud. *Physical Review A*, 84(1):011401, 2011.

[169] C. C. Kwong, T. Yang, M. S. Pramod, K. Pandey, D. Delande, R. Pierrat, and D. Wilkowski. Cooperative emission of a coherent superflash of light. *Phys. Rev. Lett.*, 113(22):223601, 2014.

[170] U. Frisch. Wave propagation in random media. *Probabilistic methods in applied mathematics*, pages 75–198, 1968.

[171] J. D. Jackson. *Classical electrodynamics*. Wiley, 1999.

[172] R. P. Feynman, R. B. Leighton, and M. Sands. *The Feynman lectures on physics 2. Mainly Electromagnetism and matter*. Addison-Wesley, 1969.

[173] H. C. Hulst and H. C. van de Hulst. *Light scattering by small particles*. Courier Corporation, 1957.

[174] J. Javanainen and J. Ruostekoski. Light propagation beyond the mean-field theory of standard optics. *Optics express*, 24(2):993–1001, 2016.

[175] J. Chabé, M.-T. Rouabah, L. Bellando, T. Bienaimé, N. Piovella, R. Bachelard, and R. Kaiser. Coherent and incoherent multiple scattering. *Physical Review A*, 89(4):043833, 2014.

[176] B. A. Lagendijk, A.and Van Tiggelen. Resonant multiple scattering of light. *Physics Reports*, 270(3):143–215, 1996.

[177] S. Chandrasekhar. *Radiative transfer*. Courier Corporation, 2013.

[178] B. Pierrat, R.and Gremaud and D. Delande. Enhancement of radiation trapping for quasiresonant scatterers at low temperature. *Physical Review A*, 80(1):013831, 2009.

[179] N. Cherroret, D. Delande, and B. A. van Tiggelen. Induced dipole-dipole interactions in light diffusion from point dipoles. *Phys. Rev. A*, 94:012702, 2016.

[180] S. Jennewein, M. Besbes, N. J. Schilder, S. D. Jenkins, C. Sauvan, J. Ruostekoski, J.-J. Greffet, Y. R. P. Sortais, and A. Browaeys. Coherent Scattering of Near-Resonant Light by a Dense Microscopic Cold Atomic Cloud. *Phys. Rev. Lett.*, 116(23):233601, 2016.

[181] L. Chomaz, L. Corman, T. Yefsah, R. Desbuquois, and J. Dalibard. Absorption imaging of a quasi-two-dimensional gas: a multiple scattering analysis. *New J. Phys.*, 14(5):055001, 2012.

[182] S. L. Bromley, B. Zhu, M. Bishof, X. Zhang, T. Bothwell, J. Schachenmayer, T. L. Nicholson, R. Kaiser, S. F. Yelin, M. D. Lukin, A. M. Rey, and J. Ye. Collective atomic scattering and motional effects in a dense coherent medium. *Nat. Commun.*, 7, 2016.

[183] M.-T. Rouabah, M. Samoylova, R. Bachelard, P. W. Courteille, R. Kaiser, and N. Piovella. Coherence effects in scattering order expansion of light by atomic clouds. *JOSA A*, 31(5):1031–1039, 2014.

[184] O. Morice, Y. Castin, and J. Dalibard. Refractive index of a dilute Bose gas. *Phys. Rev. A*, 51(5):3896, 1995.

[185] W. Guerin, M.T. Rouabah, and R. Kaiser. Light interacting with atomic ensembles: collective, cooperative and mesoscopic effects. *Journal of Modern Optics*, 64(9):895–907, 2017.

[186] L. Corman, J. L. Ville, R. Saint-Jalm, M. Aidelsburger, T. Bienaimé, S. Nascimbène, J. Dalibard, and J. Beugnon. Transmission of near-resonant light through a dense slab of cold atoms. *Phys. Rev. A*, 96:053629, 2017.

[187] R. Saint-Jalm, M. Aidelsburger, J.-L. Ville, L. Corman, Z. Hadzibabic, D. Delande, S. Nascimbene, N. Cherroret, J. Dalibard, and J. Beugnon. Resonant-light diffusion in a disordered atomic layer. *Physical Review A*, 97(6):061801, 2018.

[188] K. Kemp, S. J. Roof, M. D. Havey, I.M. Sokolov, and D.V. Kupriyanov. Cooperatively enhanced light transmission in cold atomic matter. *arXiv:1410.2497*, 2014.

[189] J. Pellegrino, R. Bourgain, S. Jennewein, Y. R. P. Sortais, A. Browaeys, S. D. Jenkins, and J. Ruostekoski. Observation of suppression of light scattering induced by dipole-dipole interactions in a cold-atom ensemble. *Phys. Rev. Lett.*, 113(13):133602, 2014.

[190] S. D. Jenkins, J. Ruostekoski, J. Javanainen, S. Jennewein, R. Bourgain, J. Pellegrino, Y. R. P. Sortais, and A. Browaeys. Collective resonance fluorescence in small and dense atom clouds: Comparison between theory and experiment. *Phys. Rev. A*, 94:023842, 2016.

[191] J. Javanainen, J. Ruostekoski, Y. Li, and S.-M. Yoo. Shifts of a resonance line in a dense atomic sample. *Phys. Rev. Lett.*, 112(11):113603, 2014.

[192] S. Jennewein, L. Brossard, Y. R. P. Sortais, A. Browaeys, P. Cheinet, J. Robert, and P. Pillet. Coherent Scattering of Near-Resonant Light by a Dense, Microscopic Cloud of Cold Two-Level Atoms: Experiment versus Theory. *arXiv preprint arXiv:1802.03563*, 2018.

[193] L. Chomaz, L. Corman, T. Bienaimé, R. Desbuquois, C. Weitenberg, S. Nascimbene, J. Beugnon, and J. Dalibard. Emergence of coherence via transverse condensation in a uniform quasi-two-dimensional Bose gas. *Nat. Commun.*, 6:6162, 2015.

[194] P. C. Bons, R. de Haas, D. de Jong, A. Groot, and P. van der Straten. Quantum Enhancement of the Index of Refraction in a Bose-Einstein Condensate. *Phys. Rev. Lett.*, 116:173602, 2016.

[195] P. W. Milonni and P. L. Knight. Retardation in the resonant interaction of two identical atoms. *Phys. Rev. A*, 10:1096–1108, 1974.

[196] J. Ruostekoski and J. Javanainen. Lorentz-Lorenz shift in a Bose-Einstein condensate. *Phys. Rev. A*, 56(3):2056, 1997.

[197] Y. Bidel, B. Klappauf, J. C. Bernard, D. Delande, G. Labeyrie, C. Miniatura, D. Wilkowski, and R. Kaiser. Coherent light transport in a cold strontium cloud. *Phys. Rev. Lett.*, 88:203902, 2002.

[198] D. J. Whiting, E. Bimbard, J. Keaveney, M. A. Zentile, C. S. Adams, and I. G. Hughes. Electromagnetically induced absorption in a nondegenerate three-level ladder system. *Opt. Lett.*, 40(18):4289–4292, 2015.

[199] D. J. Whiting, J. Keaveney, C. S. Adams, and I. G. Hughes. Direct measurement of excited-state dipole matrix elements using electromagnetically induced transparency in the hyperfine Paschen-Back regime. *Phys. Rev. A*, 93:043854, 2016.

[200] S. D. Jenkins and J. Ruostekoski. Controlled manipulation of light by cooperative response of atoms in an optical lattice. *Phys. Rev. A*, 86:031602, 2012.

[201] G. Hétet, L. Slodička, M. Hennrich, and R. Blatt. Single Atom as a Mirror of an Optical Cavity. *Phys. Rev. Lett.*, 107:133002, 2011.

[202] R.J. Bettles, S.A. Gardiner, and C.S. Adams. Enhanced optical cross section via collective coupling of atomic dipoles in a 2D array. *Phys. Rev. Lett.*, 116(10):103602, 2016.

[203] E. Shahmoon, D. S. Wild, M. D. Lukin, and S. F. Yelin. Cooperative resonances in light scattering from two-dimensional atomic arrays. *Phys. Rev. Lett.*, 118(11):113601, 2017.

[204] S. E. Skipetrov and I. M. Sokolov. Magnetic-field-driven localization of light in a cold-atom gas. *Phys. Rev. Lett.*, 114:053902, 2015.

[205] J. Pellegrino, R. Bourgain, S. Jennewein, Y. R. P. Sortais, A. Browaeys, S. D. Jenkins, and J. Ruostekoski. Observation of Suppression of Light Scattering Induced by Dipole-Dipole Interactions in a Cold-Atom Ensemble. *Phys. Rev. Lett.*, 113:133602, 2014.

[206] F. Riboli, F. Uccheddu, G. Monaco, N. Caselli, F. Intonti, M. Gurioli, and S. E. Skipetrov. Tailoring Correlations of the Local Density of States in Disordered Photonic Materials. *Phys. Rev. Lett.*, 119:043902, 2017.

[207] S.E. Skipetrov and J.H. Page. Red light for Anderson localization. *New J. Phys.*, 18(2):021001, 2016.

[208] S. E. Skipetrov and I. M. Sokolov. Absence of Anderson localization of light in a random ensemble of point scatterers. *Phys. Rev. Lett.*, 112:023905, 2014.

[209] N. Cherroret and S. E. Skipetrov. Microscopic derivation of self-consistent equations of Anderson localization in a disordered medium of finite size. *Phys. Rev. E*, 77:046608, 2008.

[210] W. H. Zurek. Cosmological experiments in superfluid helium? *Nature*, 317(6037):505–508, 1985.

[211] T. W. B. Kibble and A. Vilenkin. Phase equilibration in bubble collisions. *Phys. Rev. D*, 52(2):679–688, 1995.

[212] S. Rudaz, A. M. Srivastava, and S. Varma. Probing gauge string formation in a superconducting phase transition. *Int. J. Mod. Phys.*, 14(10):1591–1604, 1999.

[213] R. Monaco, J. Mygind, and R. J. Rivers. Zurek-Kibble domain structures: The dynamics of spontaneous vortex formation in annular Josephson tunnel junctions. *Phys. Rev. Lett.*, 89(8):080603, 2002.

[214] L. Corman, L. Chomaz, T. Bienaimé, R. Desbuquois, C. Weitenberg, S. Nascimbène, J. Dalibard, and J. Beugnon. Quench-Induced Supercurrents in an Annular Bose Gas. *Phys. Rev. Lett.*, 113(13):135302, 2014.

[215] V. M. H. Ruutu, M. Krusius, W. Xu, V. B. Eltsov, A. J. Gill, T. W. B. Kibble, Y. G. Makhlin, G. E. Volovik, and B. Placais. Vortex formation in neutron-irradiated superfluid ^{3}He as an analogue of cosmological defect formation. *Nature*, 382(6589):334–336, 1996.

[216] C. Bauerle, Y. M. Bunkov, S. N. Fisher, and H. Godfrin. Laboratory simulation of cosmic string formation in the early Universe using superfluid 3He. *Nature*, 382:332–334, 1996.

[217] M. E. Dodd, P. C. Hendry, N. S. Lawson, P. V. E. McClintock, and C. D. H. Williams. Nonappearance of Vortices in Fast Mechanical Expansions of Liquid ^{4}He through the Lambda Transition. *Phys. Rev. Lett.*, 81:3703–3706, 1998.

[218] I. Chuang, R. Durrer, N. Turok, and B. Yurke. Cosmology in the Laboratory: Defect Dynamics in Liquid Crystals. *Science*, 251(4999):1336–1342, 1991.

[219] K. Pyka, J. Keller, H. L. Partner, R. Nigmatullin, T. Burgermeister, D. M. Meier, K. Kuhlmann, A. Retzker, M. B. Plenio, W. H. Zurek, A. Del Campo, and T. E. Mehlstäubler. Topological defect formation and spontaneous symmetry breaking in ion Coulomb crystals. *Nature Communications*, 4:2291, 2013.

[220] S. Ulm, J. Roßnagel, G. Jacob, C. Degünther, S. T. Dawkins, U. G. Poschinger, R. Nigmatullin, A. Retzker, M. B. Plenio, F. Schmidt-Kaler, and K. Singer. Observation of the Kibble-Zurek scaling law for defect formation in ion crystals. *Nature Communications*, 4:2290, 2013.

[221] A. Del Campo, G. De Chiara, G. Morigi, and M. B. Plenio. Structural defects in ion chains by quenching the external potential: the inhomogeneous Kibble-Zurek mechanism. *Phys. Rev. Lett.*, 105:075701, 2010.

[222] S.-Z. Lin, X. Wang, Y. Kamiya, G.-W. Chern, F. Fan, D. Fan, B. Casas, Y. Liu, V. Kiryukhin, W. H. Zurek, et al. Topological defects as relics of emergent continuous symmetry and Higgs condensation of disorder in ferroelectrics. *Nature Physics*, 10(12):970, 2014.

[223] R. Carmi and E. Polturak. Search for spontaneous nucleation of magnetic flux during rapid cooling of $YBa_2Cu_3O_{7-\delta}$ films through T_c. *Phys. Rev. B*, 60:7595–7600, 1999.

[224] G. Labeyrie and R. Kaiser. Kibble-Zurek Mechanism in the Self-Organization of a Cold Atomic Cloud. *Phys. Rev. Lett.*, 117(27):275701, 2016.

[225] C. N. Weiler, T. W. Neely, D. R. Scherer, A. S. Bradley, M. J. Davis, and B. P. Anderson. Spontaneous vortices in the formation of Bose-Einstein condensates. *Nature*, 455(7215):948–951, 2008.

[226] G. Lamporesi, S. Donadello, S. Serafini, F. Dalfovo, and G. Ferrari. Spontaneous creation of Kibble-Zurek solitons in a Bose-Einstein condensate. *Nat. Phys.*, 9(10):656–660, 2013.

[227] S. Donadello, S. Serafini, T. Bienaimé, F. Dalfovo, G. Lamporesi, and G. Ferrari. Creation and counting of defects in a temperature-quenched Bose-Einstein condensate. *Phys. Rev. A*, 94(2):023628, 2016.

[228] J. Beugnon and N. Navon. Exploring the Kibble–Zurek mechanism with homogeneous Bose gases. *Journal of Physics B: Atomic, Molecular and Optical Physics*, 50(2):022002, 2017.

[229] G.-B. Jo, J.-H. Choi, C. A. Christensen, T. A. Pasquini, Y.-R. Lee, W. Ketterle, and D. E. Pritchard. Phase-Sensitive Recombination of Two Bose-Einstein Condensates on an Atom Chip. *Phys. Rev. Lett.*, 98:180401, 2007.

[230] D. R. Scherer, C. N. Weiler, T. W. Neely, and B.P. Anderson. Vortex Formation by Merging of Multiple Trapped Bose-Einstein Condensates. *Phys. Rev. Lett.*, 98(11):110402, 2007.

[231] V. Schweikhard, S. Tung, and E. A. Cornell. Vortex Proliferation in the Berezinskii-Kosterlitz-Thouless Regime on a Two-Dimensional Lattice of Bose-Einstein Condensates. *Phys. Rev. Lett.*, 99:030401, 2007.

[232] R. Carmi, E. Polturak, and G. Koren. Observation of spontaneous flux generation in a multi-Josephson-junction loop. *Phys. Rev. Lett.*, 84(21):4966–4969, 2000.

[233] M. Aidelsburger, J. L. Ville, R. Saint-Jalm, S. Nascimbène, J. Dalibard, and J. Beugnon. Relaxation Dynamics in the Merging of N Independent Condensates. *Phys. Rev. Lett.*, 119:190403, 2017.

[234] S. Eckel, F. Jendrzejewski, A. Kumar, C. J. Lobb, and G. K. Campbell. Interferometric Measurement of the Current-Phase Relationship of a Superfluid Weak Link. *Phys. Rev. X*, 4(3):031052, 2014.

[235] J. J. Chang, P. Engels, and M. A. Hoefer. Formation of Dispersive Shock Waves by Merging and Splitting Bose-Einstein Condensates. *Phys. Rev. Lett.*, 101(17):170404, 2008.

[236] R. Meppelink, S. B. Koller, J. M. Vogels, P. van der Straten, E. D. van Ooijen, N. R. Heckenberg, H. Rubinsztein-Dunlop, S. A. Haine, and M. J. Davis. Observation of shock waves in a large Bose-Einstein condensate. *Phys. Rev. A*, 80(4):043606, 2009.

[237] M. Bowick, L. Chandar, E. A. Schiff, and A. M. Srivastava. The Cosmological Kibble Mechanism in the Laboratory: String Formation in Liquid Crystals. *Science*, 263(5149):943–945, 1994.

[238] S. Janson. Euler-Frobenius numbers and rounding. *Online J Anal Comb*, 8, 2013.

[239] S. Burger, K. Bongs, S. Dettmer, W. Ertmer, K. Sengstock, A. Sanpera, G. V. Shlyapnikov, and M. Lewenstein. Dark Solitons in Bose-Einstein Condensates. *Phys. Rev. Lett.*, 83(25):5198–5201, 1999.

[240] J. Denschlag, J. E. Simsarian, D. L. Feder, C. W. Clark, L. A. Collins, J. Cubizolles, L. Deng, E. W. Hagley, K. Helmerson, W. P. Reinhardt, S. L. Rolston, B. I. Schneider, and W. D. Phillips. Generating Solitons by Phase Engineering of a Bose-Einstein Condensate. *Science*, 287(5450):97–101, 2000.

[241] C. Becker, S. Stellmer, P. Soltan-Panahi, S. Dörscher, M. Baumert, E.-M. Richter, J. Kronjäger, K. Bongs, and K. Sengstock. Oscillations and interactions of dark and dark–bright solitons in Bose–Einstein condensates. *Nat. Phys.*, 4(6):496–501, 2008.

[242] E. A. Kuznetsov and S. K. Turitsyn. Instability and collapse of solitons in media with a defocusing nonlinearity. *Sov Phys JETP*, 1988.

[243] C. Becker, K. Sengstock, P. Schmelcher, P. G. Kevrekidis, and R. Carretero-González. Inelastic collisions of solitary waves in anisotropic Bose–Einstein condensates: sling-shot events and expanding collision bubbles. *New Journal of Physics*, 15(11):113028, 2013.

[244] R. T. Bailey. Estimation from Zero-Failure Data. *Risk Analysis*, 17(3):375–380, 1997.

[245] M. F. Riedel, P. Böhi, Y. Li, T. W. Hänsch, A. Sinatra, and P. Treutlein. Atom-chip-based generation of entanglement for quantum metrology. *Nature*, 464(7292):1170, 2012.

[246] W. M. Itano, J. C. Bergquist, J. J. Bollinger, J. M. Gilligan, D. J. Heinzen, F. L. Moore, M. G. Raizen, and D. J. Wineland. Quantum projection noise: Population fluctuations in two-level systems. *Phys. Rev. A*, 47:3554–3570, 1993.

[247] R. J. Donnelly. The two-fluid theory and second sound in liquid helium. *Phys. Today*, 62(10):34–39, 2009.

[248] A. Griffin and E. Zaremba. First and second sound in a uniform Bose gas. *Phys. Rev. A*, 56:4839–4844, 1997.

[249] M. R. Andrews, D. M. Kurn, H.-J. Miesner, D. S. Durfee, C. G. Townsend, S. Inouye, and W. Ketterle. Propagation of sound in a Bose-Einstein condensate. *Phys. Rev. Lett.*, 79:553–556, 1997.

[250] R. Meppelink, S. B. Koller, and P. van der Straten. Sound propagation in a Bose-Einstein condensate at finite temperatures. *Phys. Rev. A*, 80:043605, 2009.

[251] B. Yang, Y.-Y. Chen, Y.-G. Zheng, H. Sun, H.-N. Dai, X.-W. Guan, Z.-S. Yuan, and J.-W. Pan. Quantum criticality and the Tomonaga-Luttinger liquid in one-dimensional Bose gases. *Phys. Rev. Lett.*, 119:165701, 2017.

[252] E. Taylor, H. Hu, X.-J. Liu, L. P. Pitaevskii, A. Griffin, and S. Stringari. First and second sound in a strongly interacting Fermi gas. *Phys. Rev. A*, 80:053601, 2009.

[253] J. Joseph, B. Clancy, L. Luo, J. Kinast, A. Turlapov, and J. E. Thomas. Measurement of sound velocity in a Fermi gas near a Feshbach resonance. *Phys. Rev. Lett.*, 98:170401, 2007.

[254] L.A. Sidorenkov, M.K. Tey, R. Grimm, Y.-H. Hou, L. Pitaevskii, and S. Stringari. Second sound and the superfluid fraction in a Fermi gas with resonant interactions. *Nature*, 498(7452):78–81, 2013.

[255] M. Ota and S. Stringari. Second sound in 2D Bose gas: from the weakly interacting to the strongly interacting regime. *arXiv:1712.05022*, 2017.

[256] D.J. Bishop and J.D. Reppy. Study of the superfluid transition in two-dimensional ^{4}He films. *Phys. Rev. Lett.*, 40:1727–1730, 1978.

[257] L. P. Pitaevskii and S. Stringari. Bose-Einstein Condensation, 2003.

[258] A. Rançon and N. Dupuis. Universal thermodynamics of a two-dimensional Bose gas. *Phys. Rev. A*, 85:063607, 2012.

[259] N. Prokof'ev and B. Svistunov. Two-dimensional weakly interacting Bose gas in the fluctuation region. *Phys. Rev. A*, 66:043608, 2002.

[260] J.-L Ville, R. Saint-Jalm, É. Le Cerf, M. Aidelsburger, S. Nascimbène, J. Dalibard, and J. Beugnon. Sound propagation in a uniform superfluid two-dimensional Bose gas. *Phys. Rev. Lett.*, 121:145301, 2018.

[261] L. P. Pitaevskii and S. Stringari. Landau damping in dilute Bose gases. *Phys. Lett. A*, 235(4):398–402, 1997.

[262] N. Navon, A. L. Gaunt, R. P. Smith, and Z. Hadzibabic. Emergence of a turbulent cascade in a quantum gas. *Nature*, 539(7627):72–75, 2016.

[263] N. Prokof'ev and B. Svistunov. Two-dimensional weakly interacting Bose gas in the fluctuation region. *Phys. Rev. A*, 66:043608, 2002.

[264] M. Ota and S. Stringari. Second sound in a two-dimensional Bose gas: From the weakly to the strongly interacting regime. *Phys. Rev. A*, 97:033604, 2018.

[265] M.-C. Chung and A. B. Bhattacherjee. Damping in 2D and 3D dilute Bose gases. *New J. Phys.*, 11(12):123012, 2009.

[266] A. Griffin, Wen-Chin Wu, and S. Stringari. Hydrodynamic modes in a trapped bose gas above the Bose-Einstein transition. *Phys. Rev. Lett.*, 78:1838–1841, 1997.

[267] D.M. Stamper-Kurn, H.-J. Miesner, S. Inouye, M.R. Andrews, and W. Ketterle. Collisionless and hydrodynamic excitations of a Bose-Einstein condensate. *Phys. Rev. Lett.*, 81:500–503, 1998.

[268] D. Guéry-Odelin, F. Zambelli, J. Dalibard, and S. Stringari. Collective oscillations of a classical gas confined in harmonic traps. *Phys. Rev. A*, 60:4851–4856, 1999.

[269] L. Pitaevskii and S. Stringari. *Bose-Einstein condensation and superfluidity*, volume 164. Oxford University Press, 2016.

[270] M. Ota, F. Larcher, F. Dalfovo, L. Pitaevskii, N.P. Proukakis, and S. Stringari. Collisionless sound in a uniform two-dimensional Bose gas. *arXiv:1804.04032*, 2018.

[271] A. Cappellaro, F. Toigo, and L. Salasnich. Collisionless dynamics in two-dimensional bosonic gases. *arXiv:1807.02541*, 2018.

[272] R. Meppelink, S. B. Koller, J. M. Vogels, H. T. C. Stoof, and P. van der Straten. Damping of superfluid flow by a thermal cloud. *Phys. Rev. Lett.*, 103:265301, 2009.

[273] Y.-H. Wang, A. Kumar, F. Jendrzejewski, R.M. Wilson, M. Edwards, S. Eckel, G.K. Campbell, and C.W. Clark. Resonant wavepackets and shock waves in an atomtronic SQUID. *New J. Phys.*, 17(12):125012, 2015.

[274] K. Hueck, N. Luick, L. Sobirey, J. Siegl, T. Lompe, and H. Moritz. Two-dimensional homogeneous Fermi gases. *Phys. Rev. Lett.*, 120:060402, Feb 2018.

[275] M. F. Riedel, P. Böhi, Y. Li, T. W. Hänsch, A. Sinatra, and P. Treutlein. Atom-chip-based generation of entanglement for quantum metrology. *Nature*, 464(7292):1170, 2012.

[276] V. Pastukhov. Damping of Bogoliubov excitations at finite temperatures. *J. Phys. A: Math. Theor.*, 48(40):405002, 2015.

[277] P.C. Hohenberg and P.C. Martin. Microscopic theory of superfluid helium. *Ann. Phys.*, 34(2):291–359, 1965.

[278] Sandro Stringari. Private communication.

[279] R. Desbuquois, L. Chomaz, T. Yefsah, J. Léonard, J. Beugnon, C. Weitenberg, and J. Dalibard. Superfluid behaviour of a two-dimensional Bose gas. *Nature Physics*, 8(9):645, 2012.

[280] C. De Rossi, R. Dubessy, K. Merloti, M. de Goër de Herve, T. Badr, A. Perrin, L. Longchambon, and H. Perrin. Probing superfluidity in a quasi two-dimensional Bose gas through its local dynamics. *New Journal of Physics*, 18(6):062001, 2016.

[281] N. R. Cooper and Z. Hadzibabic. Measuring the superfluid fraction of an ultracold atomic gas. *Physical review letters*, 104(3):030401, 2010.

[282] S. T. John, Z. Hadzibabic, and N. R. Cooper. Spectroscopic method to measure the superfluid fraction of an ultracold atomic gas. *Physical Review A*, 83(2):023610, 2011.

[283] I. Carusotto and Y. Castin. Nonequilibrium and local detection of the normal fraction of a trapped two-dimensional Bose gas. *Physical Review A*, 84(5):053637, 2011.

[284] D. S. Hall, M. R. Matthews, J. R. Ensher, C. E. Wieman, and E. A. Cornell. Dynamics of component separation in a binary mixture of Bose-Einstein condensates. *Physical Review Letters*, 81(8):1539, 1998.

[285] S. B. Papp, J. M. Pino, and CE Wieman. Tunable miscibility in a dual-species Bose-Einstein condensate. *Physical review letters*, 101(4):040402, 2008.

[286] J. Kronjäger, C. Becker, P. Soltan-Panahi, K. Bongs, and K. Sengstock. Spontaneous pattern formation in an antiferromagnetic quantum gas. *Physical review letters*, 105(9):090402, 2010.

[287] M. Gring, M. Kuhnert, T. Langen, T. Kitagawa, B. Rauer, M. Schreitl, I. Mazets, D. A. Smith, E. Demler, and J. Schmiedmayer. Relaxation and prethermalization in an isolated quantum system. *Science*, page 1224953, 2012.

[288] T. Langen, S. Erne, R. Geiger, B. Rauer, T. Schweigler, M. Kuhnert, W. Rohringer, I. E. Mazets, T. Gasenzer, and J. Schmiedmayer. Experimental observation of a generalized gibbs ensemble. *Science*, 348(6231):207–211, 2015.

[289] D. Stadler, S. Krinner, J. Meineke, J.-P. Brantut, and T. Esslinger. Observing the drop of resistance in the flow of a superfluid Fermi gas. *Nature*, 491(7426):736, 2012.

[290] R. P. Feynman. *Progress in low temperature physics*, volume 1. North-Holland, Amsterdam, 1955.

[291] D. J. Papoular, L. P. Pitaevskii, and S. Stringari. Fast thermalization and Helmholtz oscillations of an ultracold Bose gas. *Physical review letters*, 113(17):170601, 2014.

[292] N. R. Cooper. Optical flux lattices for ultracold atomic gases. *Physical review letters*, 106(17):175301, 2011.

[293] N. R. Cooper and J. Dalibard. Reaching fractional quantum hall states with optical flux lattices. *Physical review letters*, 110(18):185301, 2013.

[294] Y-J Lin, R. L. Compton, K. Jimenez-Garcia, J. V. Porto, and I. B. Spielman. Synthetic magnetic fields for ultracold neutral atoms. *Nature*, 462(7273):628, 2009.

[295] J. Struck, C. Ölschläger, R. Le Targat, P. Soltan-Panahi, A. Eckardt, M. Lewenstein, P. Windpassinger, and K. Sengstock. Quantum simulation of frustrated classical magnetism in triangular optical lattices. *Science*, 333(6045):996–999, 2011.

[296] G. Jotzu, M. Messer, R. Desbuquois, M. Lebrat, T. Uehlinger, D. Greif, and T. Esslinger. Experimental realization of the topological Haldane model with ultracold fermions. *Nature*, 515(7526):237–240, 2014.

[297] M. Mancini, G. Pagano, G. Cappellini, L. Livi, M. Rider, J. Catani, C. Sias, P. Zoller, M. Inguscio, M. Dalmonte, et al. Observation of chiral edge states with neutral fermions in synthetic Hall ribbons. *Science*, 349(6255):1510–1513, 2015.

[298] B. K. Stuhl, H.-I. Lu, L. M. Aycock, D. Genkina, and I. B. Spielman. Visualizing edge states with an atomic Bose gas in the quantum Hall regime. *Science*, 349(6255):1514–1518, 2015.

[299] L. Giorgetti, I. Carusotto, and Y. Castin. Semiclassical field method for the equilibrium Bose gas and application to thermal vortices in two dimensions. *Phys. Rev. A*, 76(1):013613, 2007.

[300] C. Cohen-Tannoudji, B. Diu, and F. Laloë. *Mécanique quantique, Tome II*. Éditions Hermann, 1973.

Résumé

Les atomes ultrafroids constituent depuis une vingtaine d'années un domaine fructueux pour l'étude de la physique à N corps. Cependant l'inhomogénéité des nuages atomiques, induite par les méthodes de piégeage utilisées habituellement, constitue une limite pour les études portant sur de grandes échelles de longueur. Nous reportons ici la mise en place d'un nouveau dispositif expérimental, combinant un potentiel modulable à bords raides et fond plat dans le plan atomique, avec un confinement versatile dans la troisième direction. Nous nous intéressons à différentes excitations du système, premièrement des degrés de liberté internes des atomes via leur interaction avec la lumière, puis deuxièmement de leur mouvement collectif avec la propagation de phonons.

La répartition des atomes dans un plan est particulièrement adaptée aux études de diffusion de la lumière. Elle permet en effet de sonder de fortes densités atomiques, entraînant de fortes interactions dipôle-dipôle induites, tout en gardant un signal transmis suffisant pour effectuer des mesures. Nous avons mesuré la déviation au comportement d'un atome isolé pour de la lumière proche de résonance lorsque la densité atomique est modifiée. Nous avons également étudié la diffusion de photons dans un disque d'atomes en injectant de la lumière seulement au centre du disque.

Nous nous sommes ensuite intéressés aux excitations collectives du gaz. Nous avons mesuré la vitesse du son dans le milieu, qui est liée à la fraction superfluide du système, et comparé nos résultats aux prédictions d'un modèle hydrodynamique à deux fluides. En utilisant une géométrie adaptée, nous avons en outre étudié la dynamique de retour à l'équilibre d'un système isolé, en imageant la phase du condensat de Bose-Einstein résultant de la fusion de jusqu'à douze condensats.

Mots Clés :

condensat de Bose-Einstein, basse dimension, interaction lumière-matière, superfluidité, systèmes hors-équilibre, atomtronique

Abstract

Ultracold atoms have proven to be a powerful platform for studying many-body physics. However the inhomegeneity of atomic clouds induced by potentials commonly used to trap the atoms constitutes a limitation for studies probing large length scales. Here we present the implementation of a new versatile setup to study two-dimensional Bose gases, combining a tunable in-plane box potential with a strong and efficient confinement along the third direction. We study different excitations of the system, either of internal degrees of freedom of the atoms with light scattering, or of their collective motion with phonon propagation.

The slab geometry is particularly well suited for light scattering studies. It allows one to probe high atomic densities, leading to strong induced dipole-dipole interactions, while keeping a good enough light transmission for measurements. We monitor the deviation from the single atom behavior for near resonant light by varying the atomic density. We additionally monitor the spreading of photons inside the slab by injecting light only at the center of a disk of atoms.

We also investigate collective excitations of the atomic gas. We measure the speed of sound which is linked to the superfluid density of the cloud and compare our results to a two-fluid hydrodynamic model predictions. Using a relevant geometry, we additionally study how an isolated system goes back to equilibrium. This is done by imaging the phase of the resulting Bose-Einstein condensate (BEC) after merging up to twelve BECs.

Keywords :

Bose-Einstein condensate, low dimensionality, light-matter interaction, superfluidity, out-of-equilibrium systems, atomtronics